# Transition State Analysis of the α-Carboxyketose Synthases

## NeuB and DAHP Synthase

# Transition State Analysis of the α-Carboxyketose Synthases NeuB and DAHP Synthase

By

PALLAVI MUKHERJEE

A Thesis

Submitted to the School of Graduate Studies

In Partial Fulfilment of the Requirements

for the Degree

Doctor of Philosophy

DOCTOR OF PHILOSOPHY McMaster University

(Chemistry Graduate Program) Hamilton, Ontario

TITLE: TRANSITION STATE ANALYSIS OF THE α-CARBOXYKETOSE SYNTHASES NEUB AND DAHP SYNTHASE

AUTHOR: Pallavi Mukherjee

SUPERVISOR: Dr. Paul J. Berti

NUMBER OF PAGES: xv, 163

**Lay Abstract**

Antibiotic resistance is a global public health emergency. ESKAPE pathogens are capable of "escaping" the action of antibiotics and are responsible for the majority of hospital infections. Therefore, there is an urgent need for new antibiotics. αCKSs are enzymes that catalyze PEP-utilizing reactions essential for bacterial survival and virulence, making them attractive antibiotic targets. Several αCKS inhibitors have been reported, but few are potent, and it is not clear how to improve their affinity. Enzymes function by binding extremely tightly to their transition states (TSs), where the transition state is the energetic barrier that a reaction must cross to get from reactants to products. This thesis uses kinetic isotope effects (KIEs), that is, the change in reaction rates for reactants containing heavy isotopes, to determine the TS structures for two αCKS enzymes, NeuB and DAHPS. The KIEs demonstrate that both enzymes stabilize TS structures in which the enzyme is forming a carbon-carbon bond between PEP and the aldose reactant. TS mimics are stable chemical compounds that mimic the charge and geometric features of the TS structure. If we can capture even a fraction of the TS binding energy, it will result in a potent inhibitor. The TS structures for the NeuB- and DAHPS-catalyzed reactions revealed in this thesis are new blueprints for inhibitor design.

**Abstract**

Antibiotic resistance is a global public health challenge. On current trends, antibiotic-resistant infections could cause an additional 10 million deaths per year by 2050, surpassing cancer. New antimicrobial compounds are desperately needed. The α-carboxyketose synthases (αCKSs) are antibiotic targets that catalyze aldol-like reactions of phosphoenolpyruvate (PEP) and aldoses to form sugars essential to bacterial survival or virulence. These include 3-deoxy-*D*-*arabino*-heptulosonate 7-phosphate synthase (DAHPS) (amino acid synthesis) and a sialic acid synthase, NeuB (immune evasion). More than 40 years of inhibitor design has yielded few potent inhibitors and no rational basis for improving them. We have performed transition state (TS) analysis on NeuB and DAHPS using multiple kinetic isotope effects (KIEs) to reveal the TS structure and provide a target for rational inhibitor design. We developed new methods of KIE measurement by NMR and measured the 3-$^{13}$C-, 2-$^{13}$C-, and 2-$^{18}$O KIEs for NeuB and DAHPS. For NeuB, the 3-$^{13}$C KIE is normal, while the 2-$^{13}$C, and 2-$^{18}$O KIEs are close to unity. This reveals that the first irreversible transition state is for formation of the tetrahedral intermediate (THI), rather than its breakdown and that the TS involves formation of the C3···C1’ bond with no involvement of the water nucleophile, and little charge development. This TS structure explains the ineffectiveness of previous cationic inhibitors and suggests a route forward for inhibitor design. For DAHPS, the 3-$^{13}$C KIE is normal; the 2-$^{18}$O KIE is close to unity, and the 2-$^{13}$C KIE is inverse. The DAHPS TS is therefore similar to NeuB’s, with similar implications for inhibitor design, but further optimization is needed to fully understand the inverse KIE at C2.

**Acknowledgements**

I would like to thank Dr. Berti for giving me the opportunity to work in his lab. Thank you for guiding me throughout my PhD, for giving me the opportunity to try new things, for teaching me to have confidence in my own capabilities, for motivating me when research got challenging, and for providing me with support throughout COVID-19. I have learnt so much from you, and I am very fortunate to have you as my supervisor for 5+ years.

I would like to thank my committee members, Dr. Harrison and Dr. Rullo for their constant support and guidance throughout my PhD journey.

Also, I would also like to thank Dr. Hilary Jenkins and Dr. Bob Berno (NMR facility) for their extensive help and advice for all my NMR measurements. A shoutout to Dr. Hilary Jenkins for always ensuring that my experiments ran smoothly and for answering all my questions. I would also like to thank Dr. Kirk Green for helping me out with the MassLynx software.

I would like to thank all the great humans in the Berti lab, both past and present. Dr. Balachandran, Dr. Heimhalt, and Dr. Gama, whose theses formed the groundwork and helped me understand all the research done previously in the Berti lab, Nick to teach me how to be brave in the lab, Alvin for helping me get started with my research and giving me so many moments to laugh both inside and outside the lab, Laraib for her incredible sense of humour and nostalgic conversations, and Weronika for her support and for making the last leg of my PhD journey in the lab awesome.

Additionally, I would like to thank my friends Dipankar and Nikita for not only supporting me as I started out my PhD in Canada but also ensuring that I have a life outside the

lab, and for being there for me throughout this journey. I would also like to thank Meg for always listening to me and teaching me how to navigate through periods of stress and anxiety that I felt during my PhD.

Bapi, amar shob kotha shonar jonno, amar shob dukho, bhoi, brithi, shob shomaye amar shaat devar jonno. Amake constantly motivate korar jono. Amar mono hoi na ami eta akdom korte partam jodi tumi na thakte. Aaj eta ami shesh korte pere chi karon tumi amar shob kotha shune cho, tomar shate kotha bolte bolte amar koto jinish realize houche. Aaj eta tomar chara hoto e na. Thank you, amar dukho ar kushi, shobe te shaat devar jono, thank you ki ami eyi jibone tomake baba pe chi. Dada, for always being there for me. Mami, thank you for your listening to me and motivating to perform well every day. Ar amake - eyi puro journey ta k complete korar jono.

Sofi, my beautiful partner, thank you. Thank you for your endless support, love and companionship, thank you for everything that you have done for me. Thank you for giving me the space to think, to allow myself to be, for giving me infinite moments of happiness and love. Thank you for being my biggest support system and cheerleader throughout this all. Te amo para siempre, Miju.

**Table of Contents**

## List of Figures

## List of Abbreviations

| | |
|---|---|
| αCKS | α-carboxyketose synthase |
| A5P | arabinose 5-phosphate |
| ADP | adenosine diphosphate |
| ATP | adenosine triphosphate |
| apk | automated phase correction |
| AQ | acquisition period |
| ATP | adenosine triphosphate |
| BSA | bovine serum albumin |
| CI | confidence interval |
| CV | column volume |
| DAHP | 3-deoxy-*D*-*arabino*-heptulosonate 7-phosphate |
| DAHPS | DAHP synthase |
| DIPEA | *N*,*N*-diisopropylethylamine acetate |
| DXR | 1-deoxy-*D*-xylulose 5-phosphate reductoisomerase |
| d1 | delay time |
| E4P | erythrose 4-phosphate |
| EDTA | ethylenediaminetetraacetic acid |
| ESI-MS | electrospray ionization mass spectrometry |
| EXC | contribution from vibrationally excited states to an IE |
| FBDD | fragment-based drug discovery |
| FID | free induction decay |
| G3P | glyceraldehyde 3-phosphate |
| G6P | glucose 6-phosphate |
| Gro3P | glycerol 3-phosphate |
| HPLC | high-performance liquid chromatography |
| $I^{‡}$ | TS inhibitor |
| IE | isotope effect |
| ImmH | immucillin H |
| Kdo | 3-deoxy-*D*-*manno*-octulosonate |
| Kdo8P | Kdo 8-phosphate |
| Kdo8PS | Kdo8P synthase |
| K-HEPES | 4-(2-Hydroxyethyl)piperazine-1-ethane-sulfonic acid-KOH |
| KIE | kinetic isotope effect |
| LDH | lactate dehydrogenase |
| lb | line broadening |
| LB | lysogeny broth |
| LFER | Linear free energy relationship |
| LPS | Lipopolysaccharide |
| ManNAc | *N*-acetylmannosamine |
| MGAM | Malachite green/ammonium molybdate |
| MMI | mass and moments of inertia contribution to an IE |
| MMP | monomethylphosphate |
| NADH | nicotinamide adenine dinucleotide |

| | |
|---|---|
| NeuB | sialic acid synthase |
| NeuNAc | *N*-acetylneuraminic acid |
| NMR | nuclear magnetic resonance |
| NOE | nuclear Overhauser effect |
| o1p | left spectral limits |
| o2p | right spectral limits |
| pABA | *p*-aminobenzoic acid |
| PEP | Phosphoenolpyruvate |
| PK | pyruvate kinase |
| PNP | purine nucleoside phosphorylase |
| ppsA | phosphoenolpyruvate synthase |
| rManNAc | reduced ManNAc (*N*-acetylmannitolamine) |
| RSA | reducing sugar assay |
| SI | sensitivity improved |
| S/N | signal to noise ratio |
| SW | sweep width |
| TFP | trifluoropyruvyl |
| TFPHEE | Trifluoropyruvate hydrazone ethyl ester |
| TRIS | tris(hydroxymethyl)aminomethane |
| TS | transition state |
| ZPE | zero-point energy contribution to an IE |

# 1 Introduction

## 1.1 Antibiotic Resistance

Antibiotic resistance is one of the greatest global public health challenges of our time. The CDC estimates that 2.8 million antibiotic-resistant infections led to 35,000 deaths in the US alone in 2019[1]. It is predicted that antibiotic-resistant infections could cause an additional 10 million deaths per year globally by 2050, which surpasses the current annual worldwide deaths from cancer and HIV[1].

The discovery of penicillin from the culture filtrate of a fungus *Penicillium notatum* in 1928 by Alexander Fleming revolutionized the treatment of bacterial infections[2]. The golden age of antibiotic discovery (1940 -1960) witnessed the isolation of most of the major classes of antibiotics[3]. Antibiotics not only treated bacterial infections, but improved medical care for surgeries, organ transplantation and cancer treatment, but this was quickly impaired by the emergence of resistant bacterial strains[4]. In the 1940s, penicillin was the drug of choice, but the resistance against penicillin became a significant clinical challenge[4]. New β-lactam antibiotics were developed to overcome penicillin resistance[4]; however, methicillin-resistant *Staphylococcus aureus* (MRSA) emerged by 1961[5]. In order to fight bacterial infections, there must be a balance between discovery of novel antibiotics, and the emergence of resistant strains. However, after the golden age, subsequent research mainly focused on modifying existing antibiotics to deal with the onset of resistance, and no new classes of antibiotics were discovered until the fluoroquinolone class in 1962 and oxazolidinones in 2000[3].

Bacterial resistance to antibiotics appears in many forms, including enzymatic modification of the drug, mutations within the target enzyme, and efflux pumps[6]. The ability of bacteria to evolve resistance to antibiotics increases antibiotic use, which leads to a vicious cycle of resistance and increased use, contributed to by the inherent ability of bacteria to adapt to their environment, exposure to antibiotics in hospitals, and poor sewerage disposal systems, among many others[1, 7]. While antibiotic resistance has been increasing, pharmaceutical companies like Eli Lily, Roche, and GSK have abandoned their antibiotic portfolios[8]. The primary reason for this is low profitability and return on investment due to short-term use of antibiotic treatments, lack of novel therapeutic targets in clinical development, and growing scientific challenges of antibacterial research[8, 9]. The growing number of antibacterial-resistant pathogens, especially those associated with hospital-acquired infections, place a substantial burden on the clinical and global healthcare economy[10]. The "ESKAPE" pathogens are six pathogens that cause most antibiotic-resistant infections[11, 12]. These are *Enterococcus faecium*, *Staphylococcus aureus*, *Klebsiella pneumoniae* (and *E. coli*), *Acinetobacter baumannii*, *Pseudomonas aeruginosa*, and *Enterobacter* species[13]. The World Health Organization has also recently listed ESKAPE pathogens in the list of 12 bacteria against which new antibiotics are urgently needed[14]. Therefore, there is an urgent need to improve antibacterial therapies and strategies, discover new drug targets, and design novel and potent inhibitors to combat bacterial infections.

## 1.2 α-Carboxyketose synthase family

The α-carboxyketose synthases (αCKSs) are enzymes that catalyze aldol-like reactions of phosphoenolpyruvate (PEP) and an aldose to form α-carboxyketose sugars that are essential to bacterial survival or virulence[15] (**Figure 1.1**). They are absent in mammals, which minimizes the potential for side effects from αCKS inhibitors, making them promising targets for the

development of broad-spectrum antibiotics[16, 17]. Although, αCKSs have been a target for ~40 years, no clinically useful antibiotics have been developed against them. The three main αCKSs are 3-deoxy-*D*-*manno*-octulosonate 8-phosphate (Kdo8P) synthase (Kdo8PS), 3-deoxy-*D*-*arabino*-heptulosonate 7-phosphate (DAHP) synthase (DAHPS) and *N*-acetylneuraminic acid (NeuNAc) synthase (NeuB).

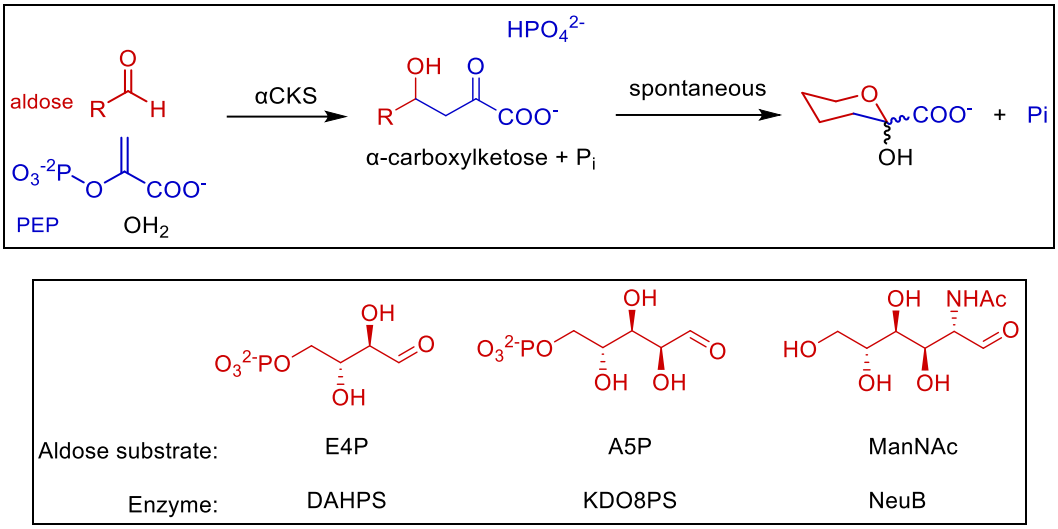


Figure 1.1. αCKS catalyzed reactions

αCKSs catalyzes the reaction between PEP and an aldose. DAHP synthase catalyzes the reaction with an Erythrose-4-phosohate (E4P) , Kdo8P synthase with arabinose 5-phosphate (A5P) and NeuB with *N*-acetylmannosamine (ManNAc) by the αCKS superfamily of enzymes.

### *1.2.1 αCKSs reaction mechanisms*

αCKSs catalyze two-step, stereoselective aldol-like condensation reactions between PEP and an aldose via a tetrahedral intermediate (THI)[18] to form a linear αCKS product that readily cyclizes to its cyclic hemiketal form (**Figure 1.2**). THI formation is an addition step, forming new C3−C1' and C2−O2' bonds across PEP's double bond. THI breakdown is an elimination step, with C2−O2 bond breakage and O2'−H deprotonation leading to C2=O2' bond formation.

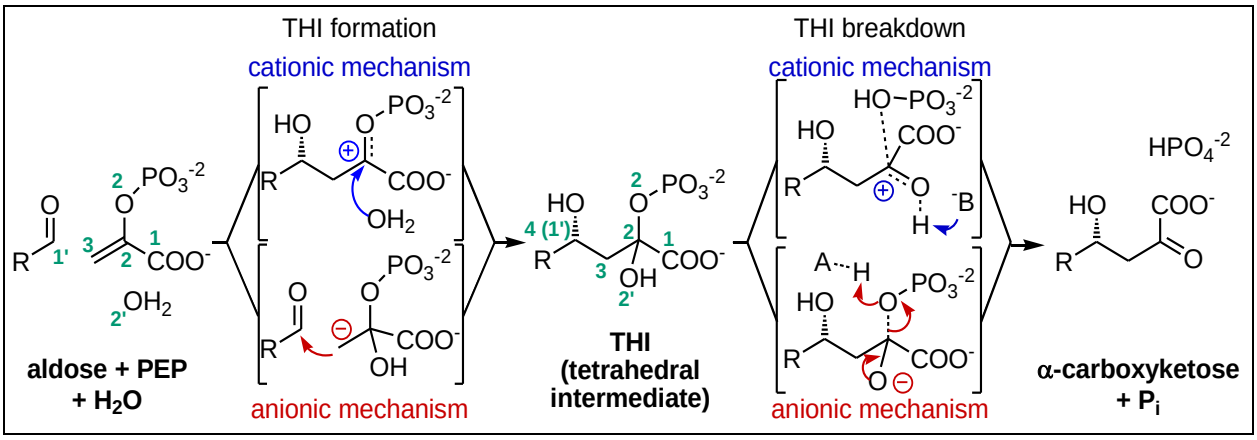


Figure 1.2. Proposed mechanism of αCKS catalytic reactions

Proposed mechanisms for the aldol-like condensation between PEP and an aldose (E4P in case of DAHPS-catalyzed reaction) to form an α-carboxyketose (DAHP) and $P_i$.

*THI formation:* THI formation has been observed in the Kdo8PS reaction by mass spectrometric detection using rapid chemical quench methodology[18] and ESI-MS[19]. In the first study, an acyclic bisphosphate intermediate[19] was observed while in the second study, a labile hemiketal phosphate intermediate[19] was reported. Isotopic labelling studies with [2-$^{18}$O]PEP showed that the $^{18}$O label appears in the [$^{18}$O]$P_i$ product rather than DAHP or NeuNAc, confirming C−O bond cleavage.[15, 20]. The fact that $P_i$ departure occurs via C2−O2 bond cleavage rather than P−O bond cleavage in both the DAHPS- and NeuB-catalyzed reactions is further evidence for a THI since it is the only plausible reaction pathway that leads to C2−O2 bond cleavage.

*Proposed THI formation mechanisms:* Proposed catalytic mechanisms tend to fall into the broad categories of cationic and anionic mechanisms (**Figure 1.2**).

If the reaction proceeds via a cationic mechanism, THI formation would occur via with the nucleophilic attack of PEP's C3 on the aldose's electrophilic carbonyl carbon (C1'), leading to the formation of an oxacarbenium ion species[15,21]. Both THI formation and breakdown could

be either stepwise or concerted for both cationic and anionic mechanisms. For example, for cationic THI formation, if water attack on C2 begins before the C3−C1' bond has completely formed, it will be a concerted mechanism. If C3−C1'bond formation is complete before water attack begins, then the reaction is stepwise. The existence of an oxocarbenium ion THI/transition state can be supported by the potent, bisubstrate inhibitor of Kdo8PS ($K_i$ = 0.4 μM)[22-25] **(Figure 1.3).** This step is followed by the nucleophilic attack of water that leads to the formation of the THI. The anionic mechanism involves the nucleophilic attack of water or hydroxide on PEP's C2, forming a carbanion intermediate which then attacks the aldose carbonyl carbon. This could be either stepwise or concerted[15]. It has been observed that nucleophilic attack on an unactivated enolpyruvyl group does not occur even under extreme conditions, which makes the anionic mechanism unlikely[26].

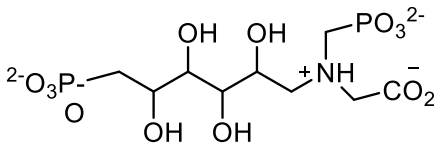


**8**

$K_i$* = 0.4 μM

Figure 1.3: Kdo8PS inhibitor, compound **8**.

*THI breakdown*: THI breakdown involves departure of $P_i$ via cleavage of the C2−O2 bond, formation of the C2−O2' double bond, and deprotonation of O2', leading to the open chain form of the α-carboxyketose. Once the product is released, it spontaneously cyclizes to its pyranose form in solution[16,27-29].

*Kinetic mechanism:* For DAHPS and Kdo8PS, a rapid equilibrium sequential ter ter kinetic mechanism was reported[17, 30] In this mechanism, the substrates bind in order: $Mn^{2+}$

followed by PEP, then the aldose (E4P for DAHPS; A5P for Kdo8PS)[17]. We can assume that NeuB follows the same sequential ordered ter ter kinetic mechanism, though it has not been demonstrated experimentally whether the rapid equilibrium assumption is valid; that is, whether substrate binding is in equilibrium or whether the steady state assumption needs to be used[31].

*Active site residues:* Mutation of key residues in the active site of DAHPS has a very small effect on $k_{cat}$ (≤100-fold)[32]. It wasn't clear why mutating key catalytic residues had such a small effect on the rate-limiting step[32]. It is possible that DAHPS could be catalyzing the reaction largely through catalysis by approximation[32, 33].

### *1.2.2 DAHPS*

3-Deoxy-*D*-*arabino*-heptulosonate 7-phosphate synthase (DAHPS) catalyzes the first step in the shikimate biosynthetic pathway, using the glycolytic intermediate, PEP, and the pentose phosphate pathway intermediate, *D*-erythrose 4-phosphate (E4P) to form the seven carbon sugar DAHP, and inorganic phosphate ($P_i$)[34].

#### *1.2.2.1 Shikimate pathway*

The shikimate pathway is a seven-step metabolic pathway in bacteria, plants and fungi that leads to biosynthesis of a variety of aromatic metabolites, including the aromatic amino acids phenylalanine (Phe), tryptophan (Trp) and tyrosine (Tyr), and folate. Chorismate, a central intermediate in the pathway, branches off to anthranilate and prephenate, which in turn leads to the aromatic amino acids, and *para*-aminobenzoic acid, a precursor for folate synthesis[35]. The shikimate pathway, which is found only in microorganisms and plants is essential for their

survival. Its absence in mammals makes it a suitable target for designing enzyme inhibitors[36-41] (**Figure 1.4**).

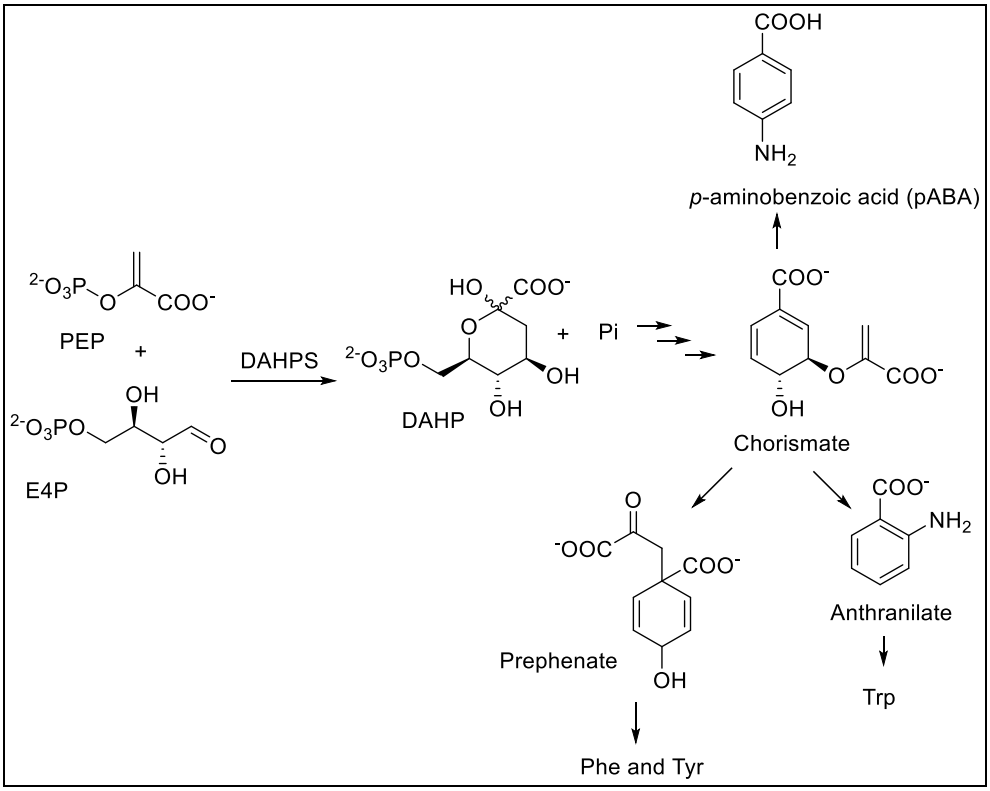


Figure 1.4: Shikimate pathway

DAHPS catalyzes the first step of the shikimate pathway leading to chorismate. Chorismate then branches to anthranilate, which ultimately leads to Trp. Prephenate leads to Phe and Tyr, and *p*-aminobenzoic acid, which leads to folate.

DAHPS activity is regulated by transcriptional control and allosteric feedback inhibition, with allosteric feedback being the major regulatory mechanism in vivo. Bacteria and fungi have multiple DAHPS isoforms that differ from each other mainly based on their feedback inhibition. *E.coli* has three DAHPS isozymes, one each feedback regulated by Phe, Tyr, and Trp[40]. *E. coli* DAHPS(Phe) was used in this thesis.

### *1.2.2.2 Structure of E.coli DAHPS (Phe)*

The DAHPSs are divided into three major subtypes, namely Class Iα, Iβ and II, based upon their phylogenetic classification[41]. The *E.coli* DAHPSs belong to Class Iα, with monomeric masses ≈ 40 kDa. DAHPS (Tyr) and DAHPS (Trp) are homodimers in solution, while DAHPS(Phe) is a homotetramer[42, 43]. Each monomer consists of eight parallel β-barrel fold surrounded by eight α-helices, a $(\beta/\alpha)_8$-fold making up a TIM barrel (exemplified by triose phosphate isomerase structure)[44] with the active site of the DAHPS located at the C-terminal end of the barrel[15, 44, 45]. The DAHPS(Phe) homotetramer has a dimer-of-dimers quaternary structure with tight A:B and C:D dimers and a looser interface between the tight dimers (**Figure 1.5 a**) [44]. Multiple lines of evidence point to half-of-sites reactivity across the αCKS superfamily[45-58] and many DAHPS(Phe) structures display pseudo-twofold symmetry in the crystal structures, with diagonal subunits B and C adopting identical conformations while subunits A and D adopt different conformations[17].For example, in the DAHP oxime-inhibited structure, only subunits B and C bound inhibitor, while subunits A and D adopted an unbound conformation. These conformational differences involve three loops making up 8% of the amino acid sequence (**Figure 1.5 b**).

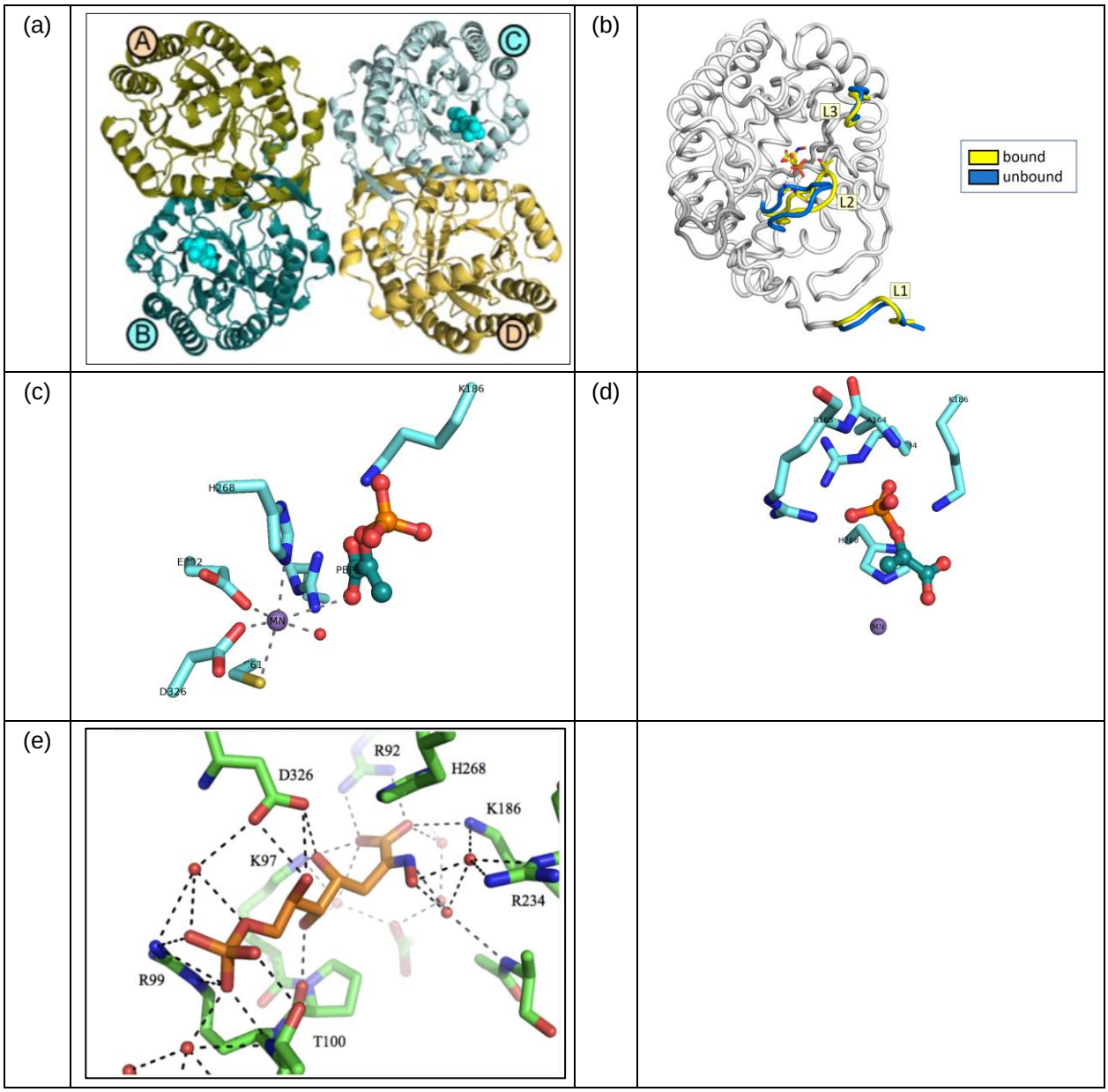


Figure 1.5: DAHPS(Phe) X-ray crystal structure

(**a**) Ribbon diagram of the inhibitor-bound complex DAHPS(Phe)·DAHP oxime$_2$ (PDBID: 5CKS)[17] showing pseudo-twofold symmetry. The inhibitor is bound to subunits B and C, while subunits A and D are in an unbound conformation. (**b**) Monomer structures of DAHPS(Phe)·DAHP oxime$_2$ showing bound (subunit B) and unbound (subunit A) conformations of DAHPS(Phe).[46] (**c**) Metal ion binding site in *E. coli* DAHPS(Phe) (PDBID: 8E0X)[46](**d**) Residues Ala164, Arg165, Lys186, and Arg234 interacting with the phosphate group of PEP (PDBID: 8E0X[46]). (**e**) Residues Arg99 and Thr100 interacting with the distal phosphate group of DAHP oxime[17]. (Figures 4b,c,e from reference 17, 46, used with permission from the American Chemical Society, ©2017, 2022).

Each DAHPS subunit contains an active site. The binding site has been identified in multiple crystal structures, including the DAHPS(Phe)·$Mn^{2+}$·PEP·$P_i$ structure (PDBID: 8E0X), in which $P_i$ occupies the presumed binding site for E4P's phosphate group. The DAHPS(Phe)·DAHP $oxime_2$ crystal structure occupied the full active site, with the oxime group in the PEP/THI phosphate binding site (PDBID: 5CKS),[17] and DAHPS(Phe) complexed with combinations of $Mn^{2+}$, PEP, $P_i$ and $SO_4^{2-}$ in different subunits (PDBID: 8E0Y[46], 1KFL[50]).

The metal ion coordination sphere includes residues Cys61, His268, Glu302, Asp326, a water molecule, and the PEP carboxylate[44, 50, 46] (**Figure 1.5 c**). The PEP phosphate group forms salt bridges with Arg165 $N^{\eta 1}$, Lys186 $N^{\zeta}$, Arg234 $N^{\varepsilon}$, and the Ala164 backbone NH (**Figure 1.5 d**). The PEP $COO^-$ forms two salt bridges with Arg92 Nη, Lys97 $N^{\zeta}$ and Lys186 $N^{\zeta}$. The E4P binding site has been inferred from the DAHP oxime, $P_i$, and sulfate, G3P binding sites[50, 21, 46]. E4P's phosphate group appears to interact with Arg99 and Thr100[17] (**Figure 1.5 e)**. In yeast DAHPS·$Co^{2+}$·PEP·G3P complex modelled by replacing G3P by E4P, the E4P O1' group was 2.4 Å away from $Co^{2+}$, which would facilitate electrophilic catalysis for a *re* face attack by the *si* face of C2=C3 of PEP, after which the proton transfer can take place between E4P O1' and the highly conserved Lys112 or Lys97 in *E. coli* DAHPS(Phe) acting a general acid catalyst[21].

### *1.2.3 NeuB*

NeuB catalyzes the condensation of PEP with *N*-acetylmannosamine (ManNAc) to give the sialic acid *N*-acetylneuraminic acid (NeuNAc) (Figure 1.1). [59, 60] Sialic acids are a family of high carbon sugars that are distributed in mammalian cells, viruses and some microbial organisms[60, 61]. Sialic acids plays an important role in animal cell recognition, development and cell adhesion[15]. Most bacteria do not use sialic acids; those that do are neuroinvasive, including

*Neisseria meningitidis*[59], *Campylobacter jejuni*[62, 63], and a neuroinvasive strains of *E. coli* K1[64, 65] that seek to evade the host's immune system by mimicking host cells[15]. Some bacteria salvage sialic acids, while others synthesise it[66].

### *1.2.3.1 Structure and active site of NeuB*

*N. meningitidis* NeuB exists as a domain-swapped dimer in solution consisting of an *N*-terminal $(\beta/\alpha)_8$ TIM barrel domain and a C-terminal domain that is related to antifreeze proteins[15]. NeuB shows less than 10% sequence identity with *E.coli* DAHPS(Phe)[15] (**Figure 1.6**). Although, there is a low sequence identity between the *N*-terminal domain of NeuB and its homolog DAHPS(Phe), the two enzymes have similar supersecondary structures (with root mean square deviation of 2.1 Å on 273 Cα atoms)[15]. This could suggest a similarity in their function and enzymatic mechanism[15].

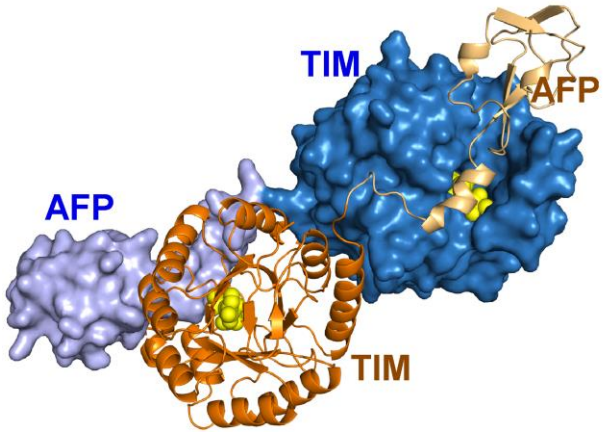


Figure 1.6: NeuB X-ray crystal structure

NeuB·NeuNAc oxime dimer crystal structure (PDBID: 6PPY)[31] contains one subunit per asymmetric unit. NeuB consists of an *N*-terminal TIM barrel domain (dark blue/orange), a C-terminal domain, homologous to a type III antifreeze protein (AFP) (light blue/orange), and a linker that contributes the R314 side chain to the active site of the other monomer. NeuNAc oxime's location is shown as yellow spheres[31]. (Figure from reference 31, used with permission from the American Chemical Society, ©2019).

### *1.2.3.2 Sialic acid biosynthesis*

The first step in the biosynthesis of sialic acid in both mammals and bacteria is the epimerisation and hydrolysis of uridine diphosphate *N*-acetylglucosamine (UDP-GlcNAc) to *N*-acetylmannosamine (ManNAc)[29, 67, 68]. However, after the first step, synthesis of NeuNAc follows a different route between mammalian and bacterial cells[15, 69] (**Figure 1.7**).

In mammals, ManNAc is phosphorylated to *N*-acetylmannosamine 6-phosphate[68]. In the next step, NeuNAc 9-phosphate synthase catalyzes the condensation of PEP with ManNAc 6-P to give NeuNAc 9-phosphate, which is then dephosphorylated by NeuNAc 9-phosphate phosphatase to NeuNAc[68, 69]. In contrast, in bacteria, NeuB catalyzes the condensation of PEP and ManNAc to directly from NeuNAc[15, 67] (**Figure 1.7**).

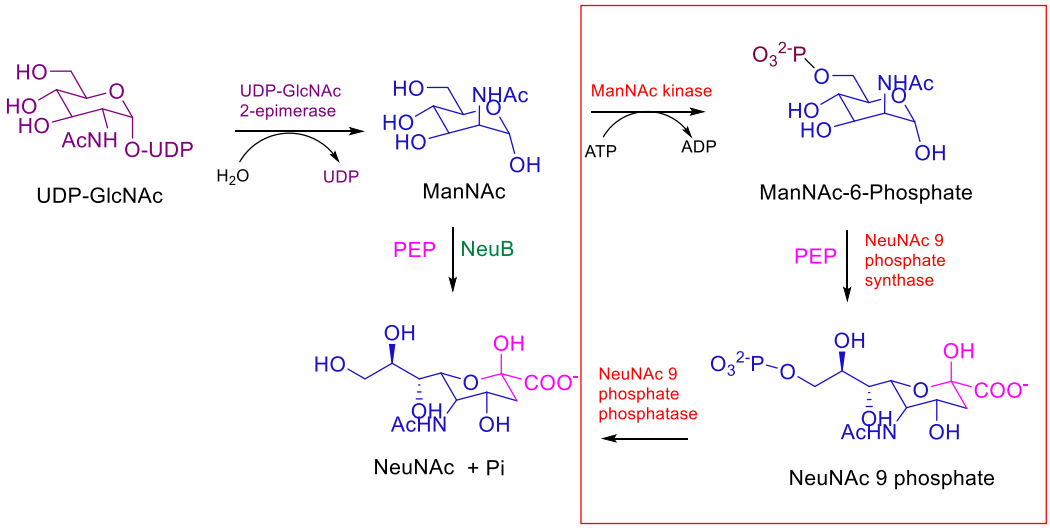


Figure 1.7: Biosynthesis of sialic acid in animal and bacterial cells

Steps in the red box on occur in mammals but not bacteria. There is no mammalian equivalent of NeuB.

The NeuB active site is situated in a deep crevice at the *C*-terminal end of the TIM barrel[15] that contains most of the key residues, while the *C*-terminal domain seals the active site from the bulk solvent[15]. Three residues (Thr285', Phe288', Arg314') from C-terminal domain of

the opposite monomer are positioned within the active site cavity of the *N*-terminal domain, where they play an active role in substrate binding[15]. In the active site, the divalent metal ion forms an octahedral complex with two key His residues, two water molecules, a non-bridging phosphate oxygen of PEP and the aldehyde oxygen of ManNAc. The PEP phosphate groups forms hydrogen bonds to highly conserved serine residues (Ser-132, -154, -213)[15] . These interactions are different from DAHPS where PEP mostly interacts with DAHPS through cationic Lys and Arg side chains[15]. The PEP carboxylate group forms interactions with Lys-129 and Lys-53. However, the C2=C3 double bond of PEP does not interact with any residues, making it easier for it to attack the aldose. There are multiple hydrogen bonds ManNAc and the side chains of Asp247, Gln55, and Tyr186[15]. ManNAc's O7 and O4 form direct and indirect (water-mediated) hydrogen bonds to Arg314' from the opposite subunit, in addition to forming several favorable non-covalent interactions[15] (**Figure 1.6**).

### *1.2.4 Kdo8PS*

Kdo8PS catalyzes the reaction between PEP and *D*-arabinose 5-phosphate (A5P) to form the eight-carbon sugar 3-deoxy-*D*-*manno*-octulosonate 8-phosphate (Kdo8P)[18], which is dephosphorylated to Kdo. Kdo is an essential component of lipopolysaccharide (LPS) of most Gram-negative bacteria[70] and is essential in assembling LPS[71, 72]. LPS plays an important role in maintaining outer membrane stability and integrity, bacterial pathogenicity, and in providing an additional barrier to antibiotic entry[71-73]. LPS is made up of lipid A, the inner and outer cores, and the *O*-antigen repeat (**Figure 1.8**). Lipid A is a hydrophobic component consisting of fatty acid tail that links the LPS to the outer membrane. The inner core links the lipid A to the outer membrane and consists of two Kdo moieties and two heptose sugars. The outer core is made of

different types, including heptoses and glucose serving as the attachment site for O-antigen repeat[73].

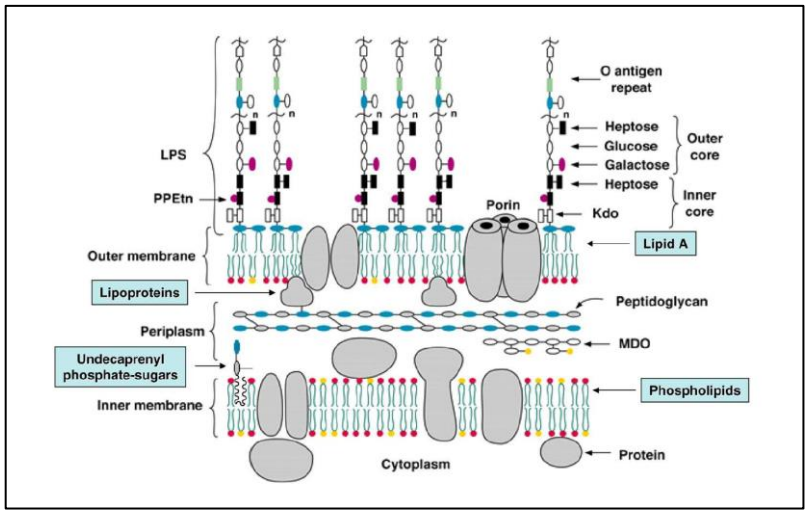


Figure 1.8: Kdo in the *E. coli* cell wall

Kdo-lipid A regions of LPS are required for the growth of *E. coli* and other Gram-negative bacteria. Figure from reference [70]. (Figures from reference 70, used with permission from Annual Review of Biochemistry, ©2002).

Crystal structures of the *A. aeolicus* Kdo8PS·PEP·A5P complex (PDB: 1FXQ) and *A. aeolicus* Kdo8PS·$Cd^{2+}$ (PDB:1FXP)[74] show Kdo8PS is a homotetramer containing four distinct active site regions [74]. The active site is open in the absence of substrates, or when only one substrate is present but closes when PEP and A5P are both present[74]. In the active site, PEP C2 adopts a distorted geometry, with two water molecules located at the *si* and *re* sides; one of these could be the water nucleophile that would attack C2 to form the THI. Although Kdo8PS catalyzes a reaction similar to DAHPS, there are key mechanistic differences, particularly in the requirement of a metal cofactor and the orientation of E4P/A5P in the active site[75]. Notably, for some Kdo8PS enzymes, the metal ion is not essential for catalysis, whereas all known DAHPS enzymes require a metal ion for activity[21, 74, 76-79]. In Kdo8PS, a direct catalytic role of the metal ion is unlikely as metal ion-dependent Kdo8PSs can be made metal ion-independent with a

single point Cys to Asn mutation[80, 81] that removes metal ion dependence with only a ~10-fold decrease in $k_{cat}$.

### *1.2.5 αCKSs dependence on metal ions*

The role of metal ions in αCKS catalysis is an open question. All known DAHPSs[49, 82] and NeuBs[15,63, 83] are divalent metal ion-dependant, while both metal ion-dependant and -independent Kdo8PSs are known[76, 78, 80, 84]. There are contradictory proposals about the metal ions' role in catalysis. In one view, the divalent metal ion does not directly participate in catalysis, but rather provides structural support by maintaining the correct orientation of substrates and key active site residues to facilitate the delivery of water[49, 79, 80]. In other proposals, the metal ion facilitates by electrostatic catalysis by polarizing the carbonyl (C=O) bond of the aldose substrate[15, 63]. The metal ion could also catalyze THI formation by making one of the water nucleophile's protons more acidic, thereby aiding $^{-}$OH formation, and increasing the water nucleophile's nucleophilicity.

#### *1.2.5.1 DAHPS*

DAHPS requires a divalent metal ion for its activity[76]. The metal activator *in vivo* is not known, but some studies suggest $Fe^{2+}$ [42, 78, 82], $Co^{2+}$ [85, 86] , $Cu^{2+}$ [87], or $Zn^{2+}$[82]. A wide range of divalent metal ions have been tested in vitro that could activate DAHPS, including $Mn^{2+}$> $Cd^{2+}$> $Fe^{2+}$>$Co^{2+}$> $Ni^{2+}$> $Cu^{2+}$>$Zn^{2+}$>$Ca^{2+}$.[82] Metal ions such as $Ni^{2+}$, $Cu^{2+}$, and $Ca^{2+}$ were slow in activating the enzyme. If these metal ions were preincubated with the enzyme for a few minutes at 23 °C and added to the reaction mixture, the rate improved significantly[82]. Competition experiment with sequential addition of different metal ions demonstrated that $Fe^{2+}$, $Co^{2+}$, and $Zn^{2+}$ could not be easily displaced by other metal ions ($Mn^{2+}$, $Cu^{2+}$, and $Ca^{2+}$) when bound to

DAHPS[82]. The concentration of the metal ion bound to the active site of DAHPS was found to be 30% for $Mn^{2+}$, 52% for $Zn^{2+}$, and 88% $Cu^{2+}$.[49] Moreover, it has been shown that the identity of the metal ion could affect the rate of product release step[49].

The metal ion binding site consists of four residues (Cys61, His 268, Glu302 and Asp326), PEP and a water bridging to Lys97[44, 88] forming a trigonal bipyramidal coordination[21]. Our lab has reported crystal structures showing the interaction between the metal ion with PEP and $P_i$ in the DAHPS active site (**Figure 1.9**)[46] which shows that all the subunits are fully occupied only when crystal structures contain a metal ion in the active site[46]. In *Thermotoga maritima* DAHPS, the E4P carbonyl C1' interacts with Lys131 but it is too far from the $Cd^{2+}$ metal ion. [79] This is supported by the steady-state and presteady-state kinetic studies that suggests metal ion plays a structural role, bringing the water molecule in a more favourable orientation for the nucleophilic attack[49]. When a model of the active site was created by replacing glyceraldehyde 3-phosphate (G3P) in the crystal structure (DAHPS·$Co^{2+}$·PEP·G3P) with E4P showed that E4P's carbonyl group coordinates with the metal ion at a distance of 2.4 Å, close enough to act as an electrophilic catalyst[21]. Direct interaction between the metal ion and E4P is further supported by the fact that $K_{M,E4P}$ depends on the metal ion's identity[82].

DAHPS crystal structures have been studied with $Pb^{2+}$, $Mn^{2+}$, $Co^{2+}$, and $Cd^{2+}$ (PDBID: 1OF8[21], 1KFL[50], 1N8F[89], 1QR7[44], 1RZM[79], 8E0V[46], 8E0X[46], 8E0Y[46], 7RUE[90]). The active site interaction depends on the nature of the metal ion. While $Mn^{2+}$ gave highest rate, it interacted more with oxygen donors like Glu302 and Asp326 while $Fe^{2+}$, $Co^{2+}$, and $Zn^{2+}$ formed stronger interactions with nitrogen or thiol groups like Cys61 and His268[49, 82]. Cys61 has been reported to play a catalytic role as it is involved in metal binding[82]. .

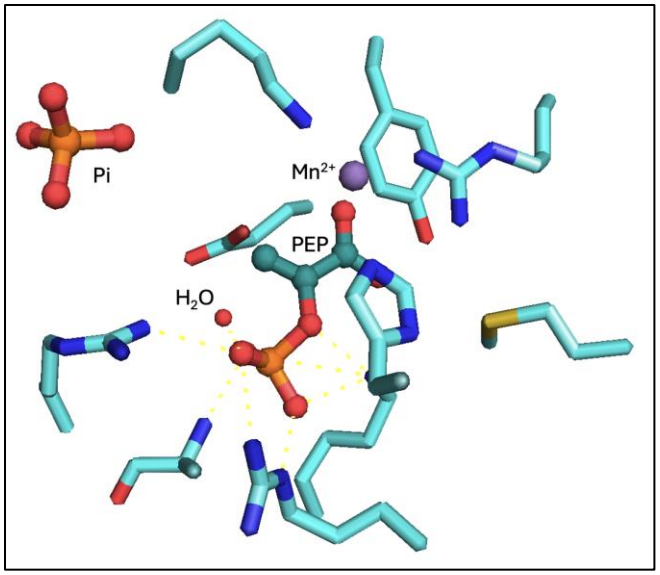


Figure 1.9: DAHPS·$Mn^{2+}$·PEP·$P_i$ crystal structure
DAHPS·$Mn^{2+}$·PEP·$P_i$ crystal structure (PDBID: 8E0X) from reference 46.

### *1.2.5.2 NeuB*

NeuB requires a divalent metal ion for its activity, as the metal ion is proposed to play both structural and catalytic roles[15, 29]. In *C. jejuni* NeuB, $Mn^{2+}$ and $Co^{2+}$ increased enzymatic activity, $Mg^{2+}$ had no effect on NeuB's activity at all, but $Zn^{2+}$ inhibited enzyme activity at pH 7.5[15, 63]. Our studies have showed that in *N. meningitidis* NeuB, $Mg^{2+}$ shows comparable rates to $Mn^{2+}$. The *N. meningitidis* NeuB·$Mn^{2+}$·PEP·rManNAc crystal structure, where rManNAc is reduced ManNAc (*N*-acetylmannositolamine), had the C1 hydroxyl group of rManNAc within 2.5 Å of $Mn^{2+}$. If the carbonyl oxygen of ManNAc bound in the same location, it would be close to both $Mn^{2+}$ and PEP C3.[15]. Our lab reported crystal structures of the NeuB·$Mn^{2+}$·$P_i$·ManNAc (PDBID: 6PPZ) and NeuB·$Mg^{2+}$·malate (PDBID:6PPW) complexes (**Figure 1.10**)[31]. In the NeuB·$Mn^{2+}$·$P_i$·ManNAc complex, the phosphate group formed multiple contacts with the enzyme's active site especially with K129[31]. ManNAc bound in an open chain form but its

carbonyl oxygen atom bound in a non-productive orientation, being oriented to occupy then PEP C3 binding site[31].

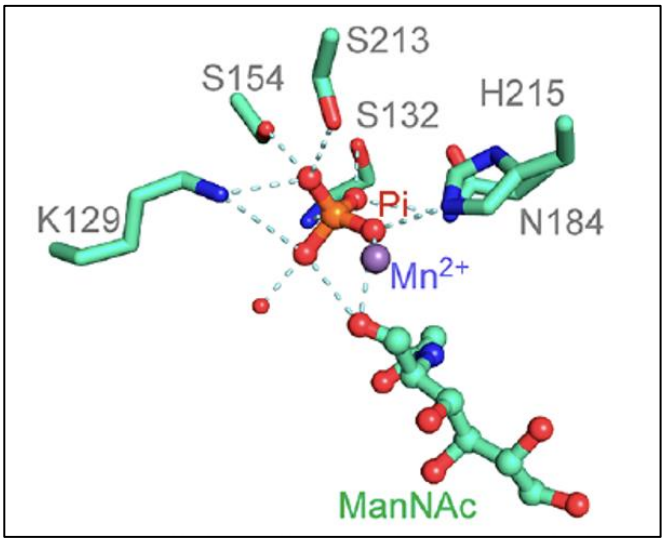


Figure 1.10: NeuB·$Mn^{2+}$·Pi·ManNAc crystal structure

NeuB·$Mn^{2+}$·Pi·ManNAc crystal structure (PDBID:6PPY)[31] (Figures from reference 31, used with permission from Biochemistry, ©2009).

### *1.2.5.3 Kdo8PS*

Based on their divalent metal ion requirements, Kdo8PS is divided in two classes[78, 91, 92]: Class I Kdo8PSs are metal ion-independent, including from *E. coli*[78], *N. meningitidis*[93], and the plant *A. thaliana*[76]. Class II Kdo8PS are metal ion-dependent including *C. jejuni*[30], *A. aeolicus*[77], *Acidithiobacillus ferrooxidans*[94], *Aquifex pyrophilus*[95], and *Helicobacter pylori*[84]. It is possible that Class II metal dependent Kdo8PS diverged from metal dependent type Iβ DAHPS[91], or they share a common ancestral metal-dependent protein[28, 77, 91, 96]. In the metal dependent form of the enzyme, four conserved amino acid residues (Cys, Asp, Glu and His) coordinate with the metal ion. The Cys residue is substituted by Asn in metal-independent Kdo8PSs[97]. Metal-dependent versions of Kdo8PS have been converted to being metal-independent[81, 98]. Metal dependent *A. aeolicus* Kdo8PS was made metal independent with a single amino acid mutation, C11N[81].

C11N was catalytically more efficient than the wild type counterpart and bound to PEP more tightly[81]. A metal binding site was introduced into the metal independent *E. coli* Kdo8PS using a single amino acid mutation, N26C, and a double amino acid mutation M25P/N26C[98]. The mutant enzymes had increased $k_{cat}$ values in presence of $Mn^{2+}$., while The C11N mutant of metal ion-dependent *A. pyrophilus* Kdo8PS retained ~10% of the wild-type activity[80]. The N26C mutant of metal ion-independent *E. coli* Kdo8PS had only a decrease ~12-fold in $k_{cat}/K_M$ but it did not become metal ion-dependent[80].

Crystal structure and comparative studies between *E.coli* DAHPS(Phe), metal independent *E.coli* Kdo8PS, and metal dependent *A.aeolicus* Kdo8PS have conserved His and Glu residues[98]. Studies done on the metal-dependent Class II Kdo8P synthase from *H. pylori* using $Zn^{2+}$, $Cd^{2+}$, $Cu^{2+}$, $Co^{2+}$, $Mn^{2+}$, and $Ni^{2+}$ revealed that it showed highest activity, specificity and cooperativity with $Cd^{2+}$.[99] The degree of metal ion occupancy at concentrations >> $K_{M,metal}$, was often less than 100%, indicating partial active site occupancy of 79% for $Cu^{2+}$, 29% for $Co^{2+}$, 55% for $Cd^{2+}$ enzymes[99]. The rate-limiting step was product release with $Cd^{2+}$, $Cu^{2+}$, and $Co^{2+}$, but enzyme chemistry for $Mn^{2+}$ and $Ni^{2+}$ [99]. These differences could be due to differences in the size of the metal ion and nature of the ligands resulting in different coordination geometries[99]. Divalent metal ions were proposed to be involved in catalysis in the Class II Kdo8PS, as well as a structural role[99]. In metal dependent Kdo8PS enzymes, the metal ion does not interact with the carbonyl oxygen of A5P, but coordinates with the hydroxyl oxygen at C2 via a water molecule[74, 75].

### *1.2.6 αCKS inhibitors*

Nearly half of the orally administered drugs are enzyme inhibitors[100]. Enzyme inhibitors are used to treat a plethora of diseases including infectious, metabolic, cardiovascular, neurological disorders, and cancer[101-103]. For example, galantamine, used to treat Alzheimer's, both inhibits acetylcholinesterase and allosterically modulates nicotine acetylcholine receptors[104]. Enzymes as targeted in drug therapy because enzyme activity is essential for all life processes which often get altered in disease conditions, and the natural ligand binding site on enzymes easily interact with small, drug-like molecules, making enzymes particularly susceptible to drug modulation[105]. For example, penicillin works by inhibiting the enzyme transpeptidase that catalyzes the final step in cell-wall biosynthesis[106].

Most potent inhibitors take advantage of the enzymatic chemistry to achieve inhibition[107]. Enzyme inhibitors can be covalent and irreversible, or non-covalent and reversible[102, 108, 109]. Inhibitors can bind to any of the enzyme forms (**Figure 1.11**) and the modes of inhibition can be competitive, noncompetitive, and uncompetitive based on how inhibitor binding affects substrate binding[102, 105, 108]. In competitive inhibition, inhibitor can bind to the free enzyme (E), blocking the substrate from binding. As binding is competitive, inhibition can be relieved by higher substrate concentrations. Therefore, competitive inhibitors increase the apparent $K_M$ values without changing $k_{cat}$. In noncompetitive inhibition, the inhibitor binds in a separate site and decreases $k_{cat}$ without affecting $K_M$. That is, the inhibitor can bind equally to the free enzyme (E) to form E·I complex or to the enzyme-substrate (E·S) complex to form E·S·I. Uncompetitive inhibitors only bind to the E·S complex to form an inactive E·S·I complex. Uncompetitive inhibitors decrease both the apparent $K_M$ and $k_{cat}$ values.

In multi-substrate reactions an inhibitor's mode of inhibition can be different for each substrate. For example, the MurA inhibitor fosfomycin binds only after the first substrate, UDP-GlcNAc, has bound, and blocks binding of the second substrate, PEP. In this case, inhibition is uncompetitive with respect to UDP-GlcNAc and competitive with respect to PEP[110].

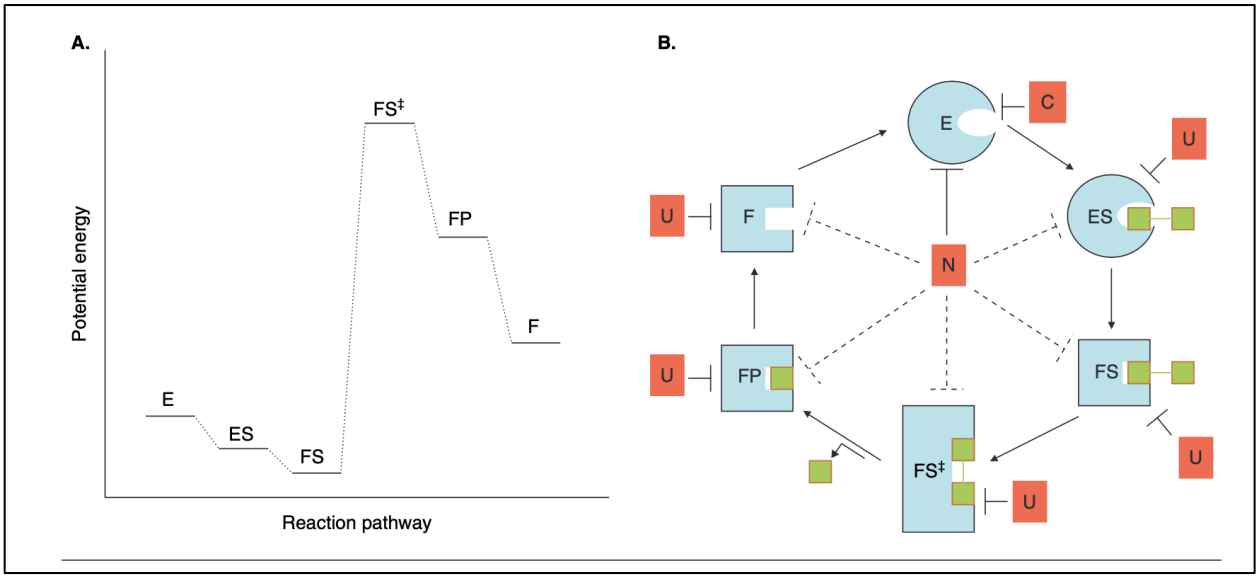


Figure 1.11: Energy level diagram for enzyme catalysis and inhibition

(**A**) Energy profile of an enzyme catalyzed reaction; E = enzyme, S= substrate(s), ES = enzyme-substrate complex, FS = enzyme– substrate complex in an altered conformation of the protein, FS = enzyme–transition state complex, FP = enzyme with one product bound, F: free enzyme in an altered conformation of the protein. (**B**) Cartoon of the conformational states that an enzyme may access during catalytic turnover; C, U and N represent competitive, uncompetitive and non-competitive inhibition. Figure from reference 105. (Figures from reference 105, used with permission from Expert Opinion on Therapeutic Targets, ©2007).

### *1.2.7 DAHPS inhibitors*

Several inhibitors against DAHPS have been reported[16, 111-113,90]. The inhibitors are designed to mimic the substrates, intermediates, and presumed transition state (TS) structures. Due to the unique outer membrane in Gram negative bacteria, containing multiple negative charges, inhibitors designed to mimic the anionic DAHPS substrates E4P and PEP may have poor cell permeability and *in vivo* effectiveness[114]. However, these inhibitors can be optimized to

improve cell permeability. Inhibitors based on the DAHPS intermediate and TS structures can provide deep insight into the enzyme catalytic mechanisms.

### *1.2.7.1 Substrate mimics*

Fosmidomycin inhibits DAHPS competitively with to respect PEP and uncompetitively with respect to E4P, with a $K_i$ of 35μM (**Figure 1.12**). This suggests that the inhibitor binds to the PEP binding site, with E4P also bound[111]. The extent of inhibition depends on the identity of the metal cofactor, with inhibition being 2-fold greater with $Mn^{2+}$ and $Fe^{2+}$ than with $Co^{2+}$[111]. This suggests that the bound inhibitor also interacts with the bound metal ion[111]. Fosmidomycin is also a potent inhibitor of 1-deoxy-*D*-xylulose 5-phosphate reductoisomerase (DXR). It interacts with DXR's metal cofactor through its hydroxyamino and aldehyde functional groups, so it may engage in the same types of interactions with DAHPS.

The substrate mimic sulfoenolpyruvate (**1**) did not inhibit DAHPS significantly despite its resemblance to PEP, while allylic phosphonate (**2**) competitively inhibited DAHPS with $K_i$= 154 μM[111] (Figure 1.12).

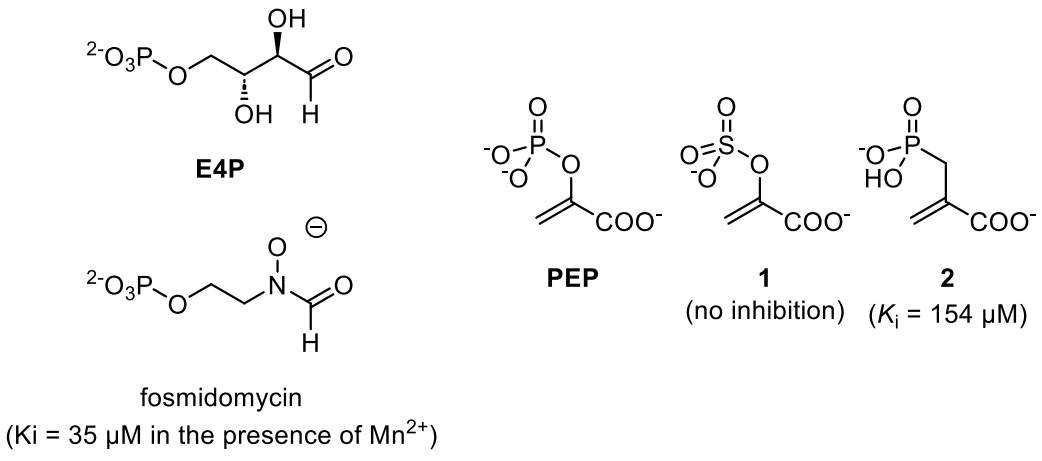


Figure 1.12: Substrate mimics of PEP and E4P

Fosmidomycin is competitive with respect to PEP but uncompetitive to E4P. The $K_i$ = 35 μM with $Mn^{2+}$. **1** and **2** are PEP substrate mimics[111].

### *1.2.8 Oxacarbenium ion mimics*

If the DAHPS-catalyzed reaction proceeds via a cationic mechanism, an oxacarbenium ion will be formed. Multiple DAHPS inhibitors have attempted to mimic this putative intermediate (**Figure 1.13**).

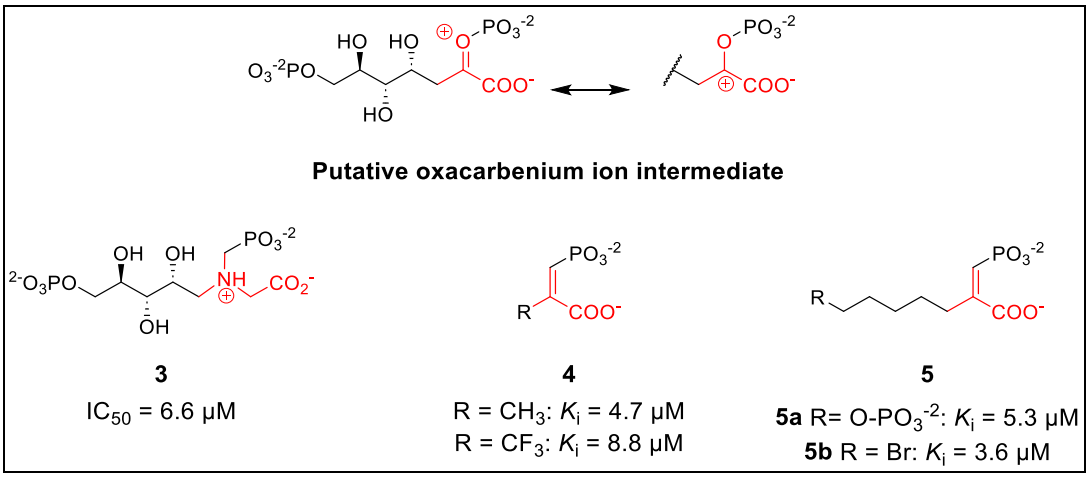


Figure 1.13: Oxacarbenium ion mimic inhibitors

DAHPS inhibitors mimicking an oxacarbenium ion[113].

The aminophosphonate group of compound **3** was designed to mimic the positive charge on the oxacarbenium ion, based on a Kdo8PS inhibitor, but inhibition was not notably strong[113]. The vinyl phosphonate inhibitor **4** was designed to mimic the partial double bond character on C2 of PEP and O2 of phosphate. The *E*-configuration resembles DAHPS-bound PEP[111]. Adding an electronegative $CF_3$ group did not improve binding[111]. Extending the inhibitor to occupy E4P's phosphate binding site with phosphate (**5a**) or Br (**5b**) did not significantly improve binding[112].

### *1.2.9 Tetrahedral intermediate (THI) mimics*

Several inhibitors were designed to mimic the THI (**Figure 1.14**)[17]. In compound **6** the THI C−O bond was replaced with a stable C-C bond. Ethyl phosphate groups were used to allow the compound to enter bacterial cells. It was reported to inhibit the growth of several Gram-negative bacteria including *E.coli*, though no $IC_{50}$ values were reported[115].

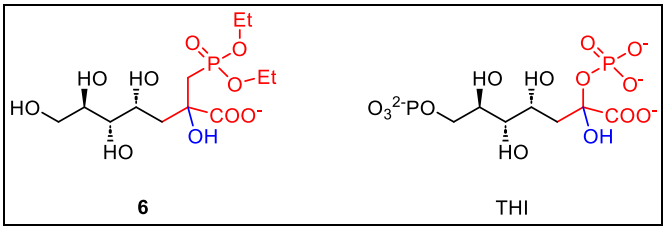


Figure 1.14: THI mimic inhibitor

Compound **6** was designed as THI mimic, but no $K_i$ value or $IC_{50}$ for bacterial growth inhibition was reported[115].

### *1.2.10 DAHP oxime*

DAHP oxime is a potent slow-binding inhibitor of DAHPS with $K_i$ = 1.5 μM and a residence time of 83 min.[17] The DAHPS·DAHP oxime crystal structure revealed that the oxime functional group, in combination with two crystallographic waters, occupies the THI / PEP phosphate binding site. It is bound in only two of DAHPS's four active sites in the crystal structure. Linear free energy relationship (LFER) analysis of inhibition demonstrated that it is a TS mimic[32], so DAHP oxime is both a structural and functional mimic of the phosphate group of the THI. DAHP oxime binds competitively with respect to $Mn^{2+}$, PEP and E4P in subunits B and C, and has a mixed mode of inhibition with respect to all substrates in subunits A and D[17] (**Figure 1.5**). When subunits B and D are occupied by DAHP oxime at [DAHP oxime] ≥ 50μM, $K_{M,E4P}$ decreases, indicating that DAHP oxime occupying subunits B and C increases E4P

binding to subunits A and D. This positive cooperativity is the dominant cause of incomplete inhibition[17].

The coordination of the phosphate group in the THI intermediate and that of oxime group of DAHP oxime in combination with two water molecules suggests that the oxime group mimics phosphate group's functionality at the binding site (**Figure 1.15)**[17].

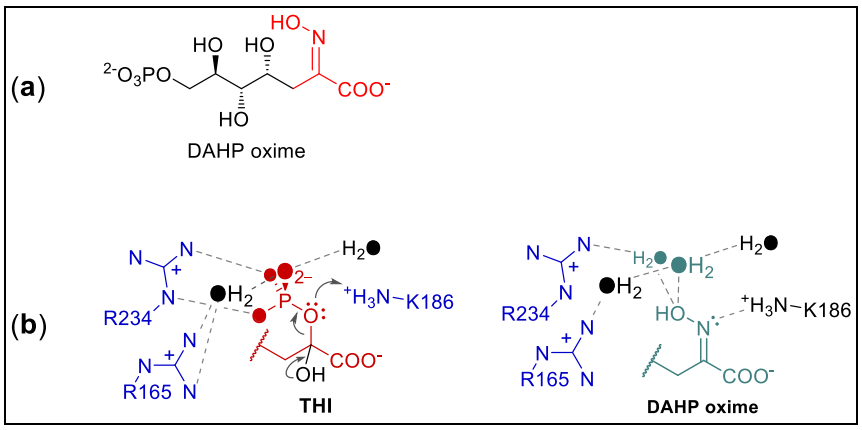


Figure 1.15: DAHP oxime inhibition of DAHPS

(**a**) DAPH oxime. (**b**) The THI's presumed active site interactions and crystallographically observed interactions of DAHP oxime with DAHPS[17].

### *1.2.11 Other Imine-Based Inhibitors*

An "inhibitor-in-pieces" approach was used to optimize DAHP inhibitors[90]. In this method, fragment-based inhibitor design[116] was combined with the substrate-in-pieces[117] approach. Initially, pyruvate oxime and Gro3P were used to mimic DAHP oxime with the missing C4-O4H group[17] (**Figure 1.16 a**) which inhibited DAHPS with modest a $K_i$ = 1.3 mM[90], and pyruvate hydrazone and Gro3P inhibited DAHPS with a $K_i$ = 35 µM (**Figure 1.16 b**) [90]. This led to the synthesis of the most potent DAHPS inhibitor to date, DAHP hydrazone[90] (Chapter 2). The pyruvate-based fragments were synthesized with fluoro-substituents (**Figure 1.16 c**). Increasing the number of fluorine atoms decreased the p$K_a$ of the oxime's functional group and

improved $K_i$. 3,3,3-trifluoropyruvate oxime (TFP oxime) inhibited DAHPS with a $K_i$ = 300 µM[90]. TFP semicarbazone inhibited DAHPS with $K_i$ = 320 µM (**Figure 1.16 c**)[90]. Both TFP oxime and TFP semicarbazone ethyl ester inhibited *E.coli* growth in culture[90]. The crystal structures of DAHPS with bound TFP oxime and TFP semicarbazone demonstrated that these inhibitors bound upside down in the active site compared with DAHP oxime (**Figure 1.16 d**). In the ball and stick model (**Figure 1.16 d**), the TFP based inhibitors are shown in different colours while DAHP oxime in gray. The C=N group in the TFP based inhibitors was upside and sideways with respect to the oxime group for DAHP oxime's group. The $CF_3$ and the carboxylate group of the TFP based inhibitors occupied the same locations as the two crystallographic waters in the DAHP oxime complex[90]. This introduced new direction for developing inhibitors[90].

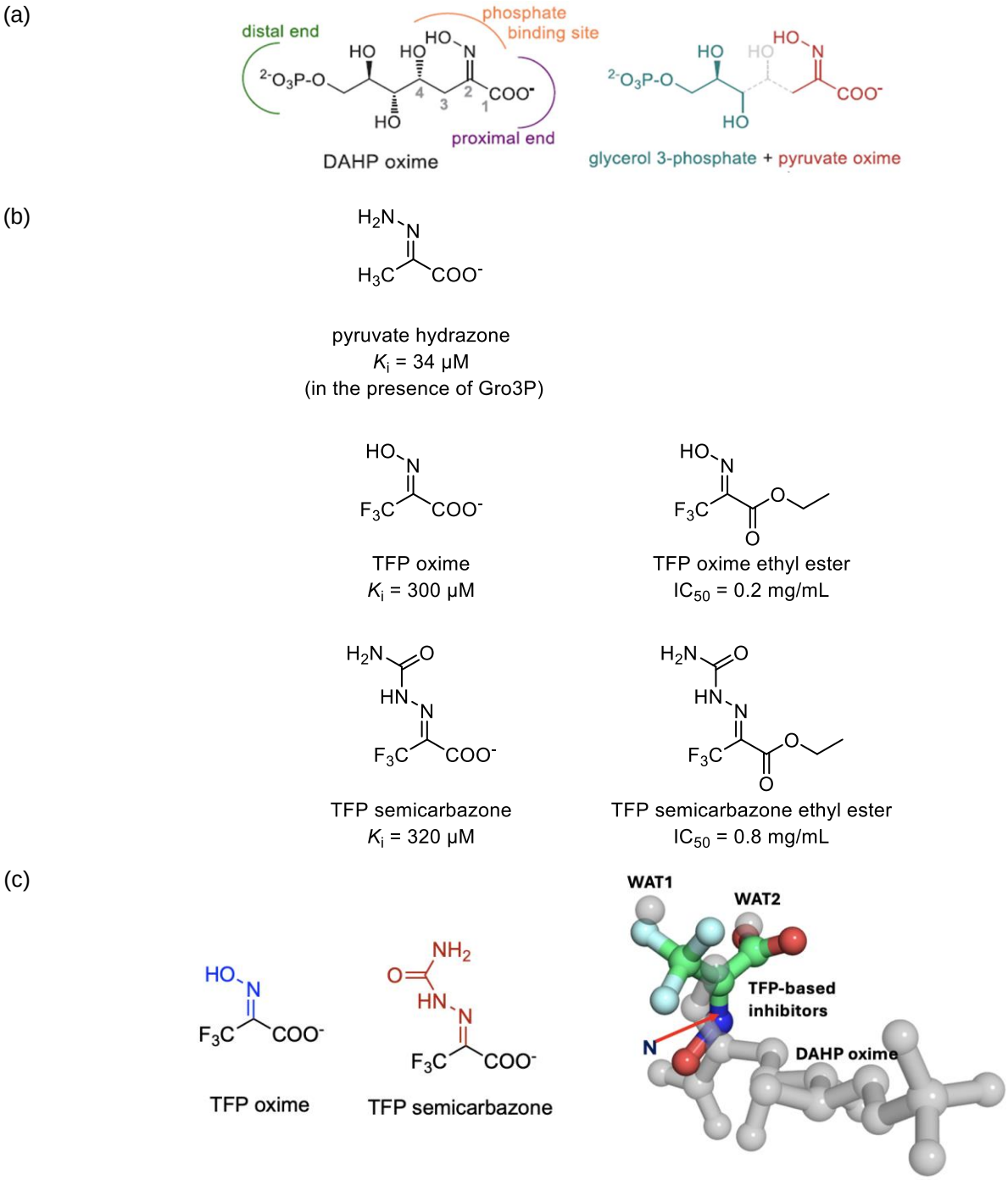


Figure 1.16: Inhibitor-in-pieces approach to designing inhibitors against DAHPS

(**a**) Comparing DAHP oxime and pyruvate oxime + Gro3P binding. (**b**) Pyruvate hydrazone and TFP-based inhibitors. (**c**) Upside-down binding of TFP-based inhibitors relative to DAHP oxime[90].(Figures from reference 90, used with permission from ACS Infectious Disease ©2021).

### *1.2.12 NeuB inhibitor - NeuNAc oxime*

Two inhibitors of NeuB have been reported, a THI mimic inhibitor with $K_i$* of 3 μM[29] and NeuNAc oxime[118] (**Figure 1.17**). NeuNAc oxime had a modest initial $K_i$ of 36 μM[118], but it bound slowly over ≈10 h and the dissocation rate constant was too low to measure, < 2.5 × $10^{-7}$ $s^{-1}$, giving a residence time ($t_R$) of over 47 days, much longer than the lifetime of a bacterial cell. This made NeuNAc oxime an effectively irreversible inhibitor[31]. It is competitive with respect to $Mn^{2+}$, PEP and ManNAc.

NeuNAc oxime shows 10% residual rate even at high inhibitor concentration, indicating that the inhibitor binds to only one of the subunits of the homodimer[31]. The half-of-site binding could be attributed to either negative cooperativity between inhibitor molecules, or positive cooperativity between substrate and inhibitor[31]. NeuNAc oxime does not inhibit NeuB immediately but only after a short period of incubation and inhibition becomes stronger over ≈10 h[31]. NeuNAc oxime formed fewer interactions in the NeuB phosphate binding site than DAHP oxime did with DAHPS, and fewer than PEP with NeuB, forming only three out of the six neutral interactions that PEP[31]. Nonetheless, it did achieve an exceptional residence time. Complete inhibition occurs when NeuNAc oxime is incubated with NeuB for 4 h while catalyzing the reaction, i.e., when all the three substrates are present, suggesting successful inhibition is possible *in vivo*[31].

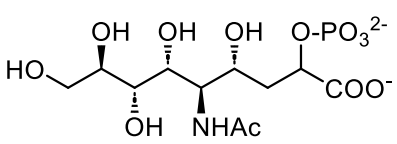


**7**
($K_i$ = 3 μM)

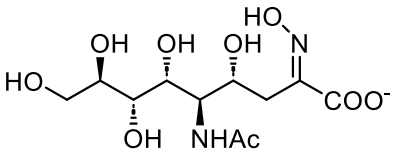


NeuNAc oxime
$K_i^*$ ≈ 0

Figure 1.17: NeuB Inhibitors

A THI mimic inhibitor of NeuB, **7** and NeuNAc oxime, the oxime equivalent of DAHP oxime[29,31].

### *1.2.13 Kdo8PS inhibitors*

Several inhibitors have been reported for Kdo8PS (**Figure 1.18**) generally using the same design principles as for DAHPS and NeuB inhibition.

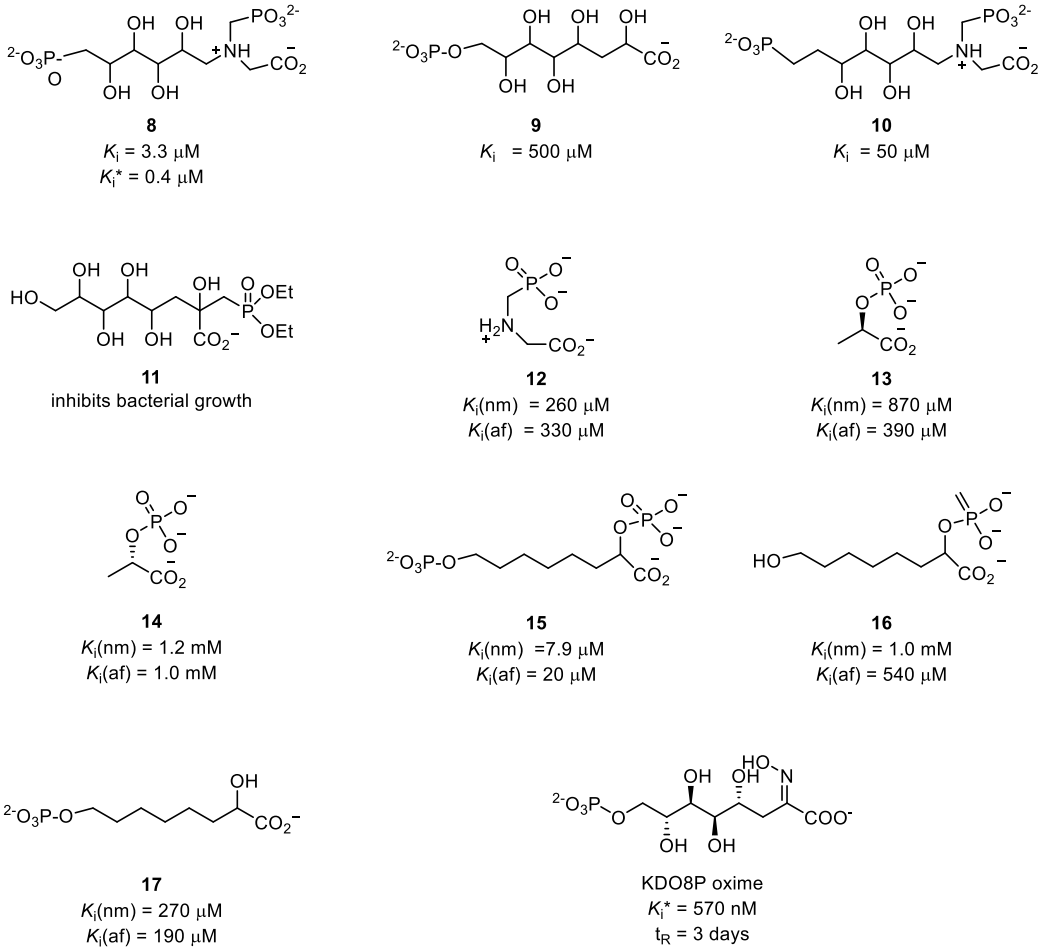


Figure 1.18: Kdo8PS inhibitors

Kdo8PS inhibitors. The residence time, $t_R$, is the time the inhibitor remains in the active site once bound; inhibitors **12** to **17** were tested against metal-independent *N. meningitidis* Kdo8PS (nm) and metal-dependent *A. ferrooxidans* Kdo8PS (af).[119, 25, 120, 115, 121]

Compounds **8** and **9** were similar to the DAHPS inhibitors (**Figure 1.13**) meant to mimic the presumed oxacarbenium ion intermediate. Compound **8** was competitive with respect to PEP

with $K$i = 3.3 µM[119] under fast binding conditions, and $K$i$^*$ = 0.4 µM[25] under slow binding conditions. Compound **9** was a derivative of compound **8** with $K_i$ = 50 µM[120]. Compound **10** mimicked the acyclic Kdo8P intermediate with a $K_i$ = 500 µM[25]. There was no reported $K_i$ for compound **11** or $IC_{50}$ though it was reported to inhibit Gram-negative bacterial growth[115]. Compound **12** mimicked the PEP part of compound **8**.[121] Compounds **13** and **14** had similar features to some parts of the THI[121]. Compound **15** was intended to mimic the THI, but without any of the hydroxyl groups[121]. Compounds **16** and **17** was designed to understand the role of the A5P/PEP-derived phosphate groups[121]. Kdo8P oxime, inhibited *C. jejuni* Kdo8PS[30]. Kdo8P oxime is analogous to DAHP oxime, the TS mimic of DAHPS[17, 32]. It inhibited Kdo8PS uncompetitively with respect to $Mn^{2+}$, and competitively with respect to A5P and PEP[30]. It displayed a fast-binding inhibition with a $K_i$ of 10 µM and slow-binding inhibition with an ultimate $K_i^*$ of 0.57 µM, with a $t_R$ ranging from 27 min to up to ~3 days depending on the concentration of excess Kdo8P oxime[30]. Similar to DAHP oxime, Kdo8P oxime displayed residual rate at high inhibitor concentrations[30]. This may result from negative cooperativity between the inhibitor molecules and different subunits, causing some subunits to remain unoccupied, or due to positive cooperativity between the inhibitor and substrates bound to different subunits[30].

## 1.3 Reaction space

The αCKSs catalyze a two-step reaction; an addition step to form the THI, and an elimination step to form the ketone product. Each individual step can be visualized using a More O'Ferrall-Jencks plot, a two-dimensional representation of the bonds being formed or broken in a given reaction step (**Figure 1.19**) [33, 122].

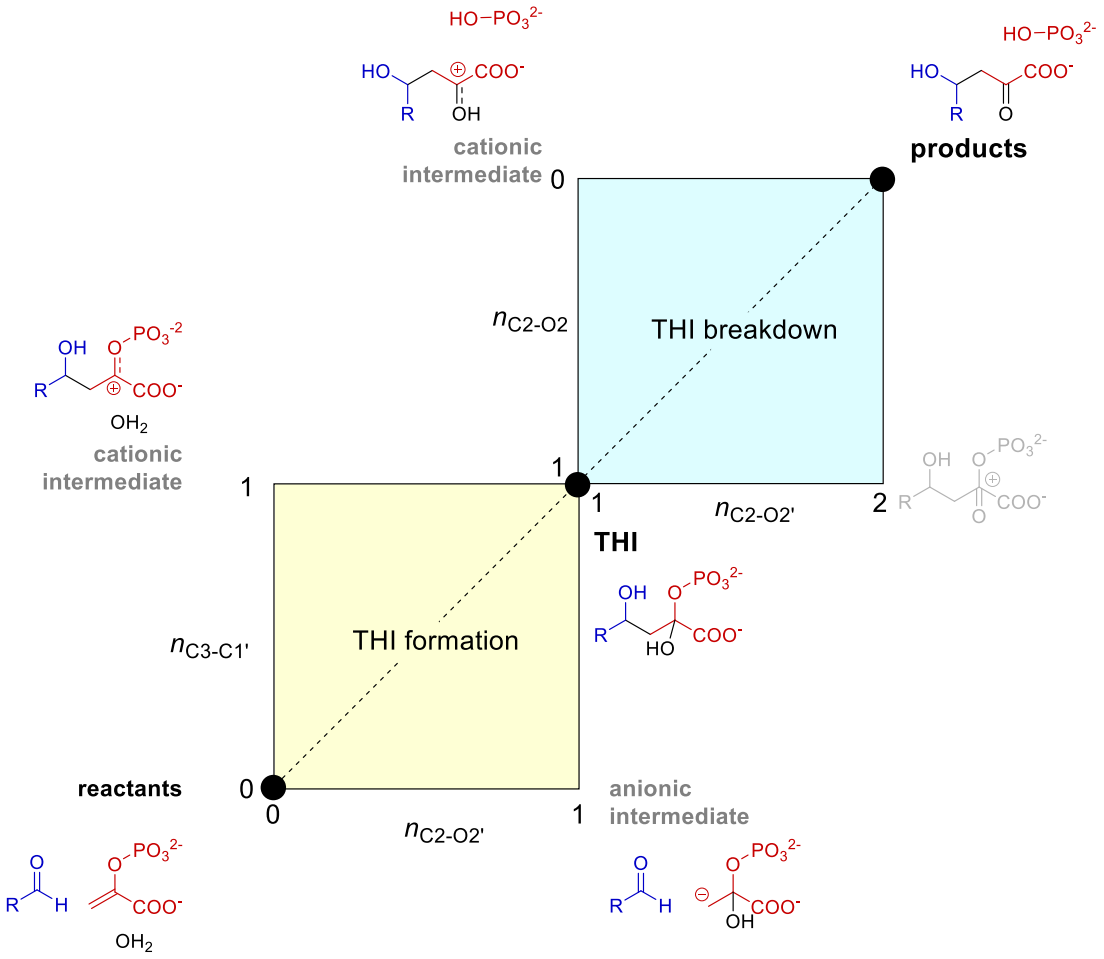


Figure 1.19: αCKS reaction space

This is a reaction space diagram for αCKS reactions. For THI formation (yellow square) the axes correspond to the bond orders (*n*) for forming the new C3-C1' and C2-O2' bonds; that is, $n_{C3\text{-}C1'}$ and $n_{C2\text{-}O2}$. The aldose, PEP, and $H_2O$ reactants (lower left) and the THI (upper right) are shown. THI formation can follow (*i*) a stepwise, cationic mechanism, forming a cationic intermediate (upper left), (*ii*) a stepwise, anionic mechanism with an anionic intermediate (lower right), or (*iii*) a concerted mechanism (diagonal) with the C3-C1' and C2-O2' bonds forming simultaneously. For THI breakdown (blue square), the axes show the bond order (*n*) for breaking the C2-O2 bond and forming the C2-O2' double bond, that is, $n_{C2\text{-}O2}$ and $n_{C2\text{-}O2'}$. The THI (lower left) breaks down to the products (upper right). THI breakdown can follow (*i*) a cationic pathway with the protonation of the bridging oxygen and cleavage of the C2-O2 bond to form a cationic intermediate (upper left), (*ii*) an unrealistic anionic mechanism with the formation of a pentavalent carbon intermediate (lower right), or (*iii*) a concerted mechanism.

The reaction space for THI formation (yellow) has the reactants in the bottom left corner, and the THI on the top right corner. The *y*-axis corresponds to the C3−C1' bond order ($n_{C3-C1'}$) for the new bond between PEP and the aldose. The *x*-axis corresponds to the bond order for the formation of the new C2−O2' bond ($n_{C2-O2'}$) between PEP and the water nucleophile. If THI

formation is stepwise, then only C3-C1’ bond will be forming at the transition state, proceeding to the cationic intermediate at the top left corner of the reaction space. However, if the addition reaction is concerted, there will be simultaneous formation of both the C3−C1’ and C2−O2’ bonds in the reaction coordinate motion, and no intermediates (**Figure 1.19**). In principle, C2−O2’ bond formation and an anionic intermediate is possible, but this is not expected to be realistic (see below) [26].

The reaction space for THI breakdown (blue) starts from the THI . The *y*-axis corresponds to $n_{C2\text{-}O2}$ as the C2−O2 bond in the THI breaks during phosphate group departure, and the bond order decreases from 1 to 0. The *x*-axis corresponds to $n_{C2\text{-}O2'}$ for the formation of the C2=O2’ double bond in the keto product. As the double bond forms, the bond order increases from 1 to 2. If THI breakdown follows a cationic pathway, i.e., the cleavage of the C2−O2 bond in presence of a general acid catalyst and phosphate departure, then it will form a cationic intermediate, located at the top left corner. If the C2=O2’ double bond forms first, an unrealistic pentavalent carbon intermediate would be formed in the lower right corner (**Figure 1.19**).

## 1.4 Transition states

All chemical reactions proceed through a high energy state that is located between the substrates and products, the transition state[123]. The transition state is the top of the energy barrier in the reaction coordinate diagram (**Figure 1.20**).

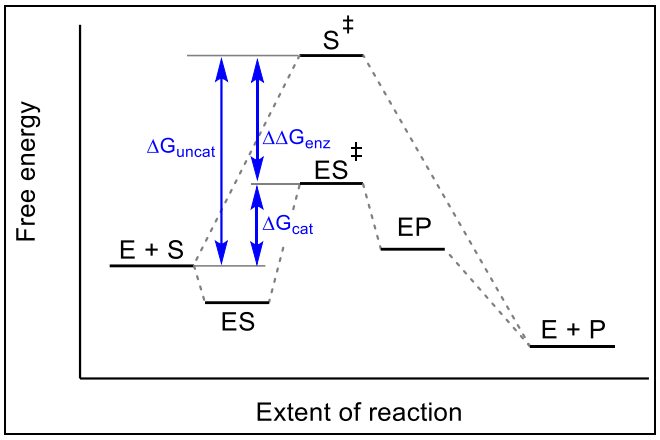


Figure 1.20: Energy level diagram of enzyme-catalyzed and uncatalyzed reactions

This figure represents the reaction coordinate diagram of a catalyzed versus uncatalyzed reaction where E = enzyme, S = substrate, S‡= non-enzymatic transition state, ES‡ = enzyme-transition state complex, P = product, EP = enzyme·product complex. In this figure [S] > $K_{d,S}$, and as a result ES has lower energy than E + S. If [S] < $K_{d,S}$, then the ES energy would be higher than the E + S state[102, 108]. For a reaction to proceed, the reactants must cross the TS, i.e., ES‡ (for catalyzed) and S‡ (for uncatalyzed)[102].

In 1946, Pauling proposed that enzymes catalyze reactions by binding to and stabilizing a strained form of the substrate, i.e. the "activated complex". This lowers the energy of the enzymatic TS, ES‡, thus stabilizing it. This in turn decreases the energy required to cross this high energy barrier ($E_a$) and increases the reaction rate[124, 125]. The extent of lowering the TS energy is a reflection of TS binding and is given by $\Delta\Delta G_{enz} = \Delta G_{uncat} - \Delta G_{cat}$ [34,126] Enzymes can enhance reaction rates by up to $10^{19}$-fold, implying $\Delta\Delta G_{enz}$ values of up to -26 kcal/mol[108]. The estimated dissociation constants for E·S‡ complexes, $K_d$‡, are typically in the range of $10^{-15}$ to $10^{-24}$ M, while enzymatic-substrate dissociation constants $K_s$, for most enzymes are in the range $10^{-3}$ to $10^{-6}$ M[102]. Thus, enzymes accelerate reactions by binding to the transition state more tightly than any other species[127]. Enzymes' preferential binding of transition states and very low $K_d$‡ values show the value of designing inhibitors that mimic the charge and geometry of the transition state[124]. TS analogues have the potential to bind more tightly than substrates, proportional to the catalytic rate enhancement imposed by the enzyme[128].

## 1.5 Transition state analysis

In the search for potent enzyme inhibitors, knowledge of the TS structure can provide useful information to designing new compounds[102]. Understanding the TS structure allows for further characterization of the mechanisms by which the enzyme stabilizes the TS complex during catalysis[129]. However, the lack of detailed, experimentally determined transition states for enzyme-catalyzed reactions is a major barrier to inhibitor design[128]. Experimental determination of TS structures is difficult. Spectroscopic techniques are incapable of detecting enzymatic TS complexes because of their short lifetimes, $10^{-13}$ s, and effectively zero concentrations[130] . The only experimental technique that can determine TS structures in detail is TS analysis, i.e., measuring multiple kinetic isotope effects (KIEs) throughout the substrates, then computationally interpreting the KIEs to yield the TS structure.

## 1.6 Kinetic Isotope Effects

A KIE is the ratio of rate constants for two reactants with different isotopes at a specific location in the molecule **(Equation 1**), and it reflects any change in the molecular structure between the reactant and the transition[123, 131]. Similarly, equilibrium isotope effects (EIEs) reflect the effect of an isotopic label on a chemical equilibrium (Equation 2)[108].

Equation 1:

$$KIE = {}^{light}k/{}^{heavy}k$$

Equation 2:

$$EIE = {}^{light}K/{}^{heavy}K$$

KIEs are primary if they involve an atom undergoing bond making/breaking during the reaction, or secondary for atoms remote from the site of chemistry[108, 131, 132, 124].

KIEs are vibrational phenomena which arise due to changes in an atom's "vibrational environment" between the reactant and the transition state[132]. "Vibrational environment" is the combined effect of bond strengths and molecular geometry on an atom's vibrational frequencies. Vibrational frequencies depend on atomic mass and the bonding force constants (bond stretch, bend, torsion and out-of-plane bend), and force constants depend, in turn, on a molecule's structure. Thus, any change in molecular structure in the vicinity of an isotopic label will cause changes in the vibrational frequencies between the reactant and the TS, which will result in an isotope effect[128, 131].

KIEs are conceptualized and modeled computationally using a harmonic oscillator model where a bond is modeled two masses connected through a spring (**Figure 1.21**).

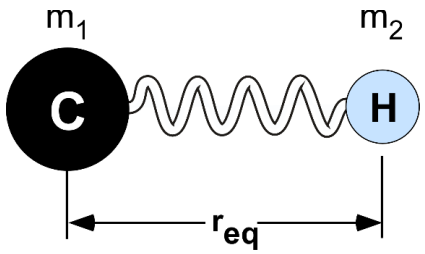


Figure 1.21. Ball and spring model of C-H bond

The ball-and-spring model of a C-H bond with masses $m_1$ and $m_2$ respectively. The atoms are represented by balls, and the chemical bond by an ideal massless spring with a defined strength.

At the equilibrium bond length, $r_{eq}$, the system is at rest, but if the spring is stretched or compressed, it obeys Hooke's law (**Equation 3**):

Equation 3

$$F = -k\Delta r$$

where $F$ = restoring force acting in the opposite direction to the change in the bond length, $\Delta r$ = change in bond length, and $k$ = spring constant, which corresponds to the bond strength.

The vibrational frequency, ν, of a bond is (**Equation 4**):

Equation 4:

$$\nu = \frac{1}{2\pi}\sqrt{\frac{k}{\mu}}$$

where $\mu = \frac{m_1 m_2}{m_1 + m_2}$ is the reduced mass.

Thus, the vibrational energy of a bond depends on its frequency, which varies directly with the spring constant of the bond, $k$, and inversely with its reduced mass μ.

The vibrational energy ($E_v$) is expressed as (**Equation 5**):

Equation 5:

$$E_v = \left(\mathrm{v} + \frac{1}{2}\right) h\nu$$

where, v = vibrational quantum number, $h$ = Planck constant and ν = frequency.

In accordance with Heisenberg uncertainty principle, an atom in a molecule cannot be at rest, even at 0 K, and thus molecules possess a vibrational energy even at 0 K, the zero point energy[133]. The zero-point energy, when v = 0, and is given by **(Equation 6):**

Equation 6:

$$E_0 = \frac{1}{2} h\nu$$

Heavy isotopes always have lower zero-point energies than light isotopes, but the energy difference between isotopes depends on vibrational frequency, and therefore the bond strength **(Figure 1.22).** We observe a normal KIE if the force constant decreases since the zero point energy decreases more for the lighter isotope ($^1$H) than for the heavier ($^2$H); that is, the vibrational environment becomes looser[124131]. If there is no change in the force constant, then the zero-point energy remains the same and the observed KIE is unity.

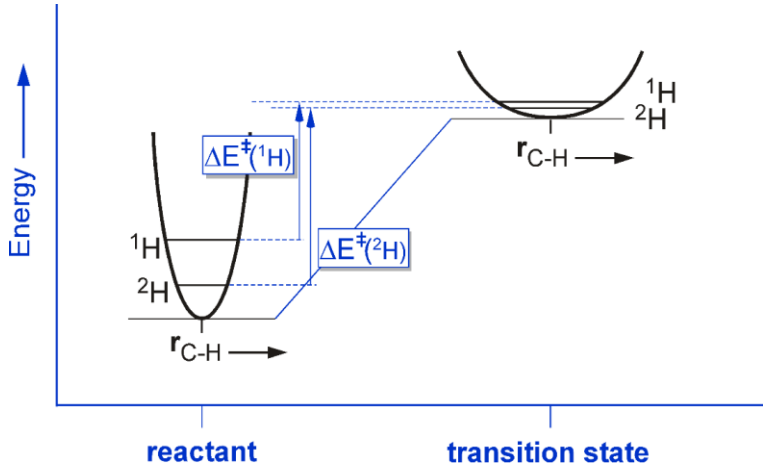


Figure 1.22. ZPE contribution to KIE

The zero-point energies of $^1$H and $^2$H (horizontal lines) depend on the reduced mass, μ, and the vibrational frequency, ν. The parabolic curve shows how energy varies when a C-H bond is stretched or compressed from its equilibrium bond length both in the reactant and the transition state. This illustrates a secondary IE. For a primary KIE of C−H bond cleavage, there would be no restoring force for the C−H stretch at the transition state, and therefore no harmonic oscillator[123].

Three factors contribute to KIEs (**Equation 7**):

Equation 7:

$$KIE = MMI \times ZPE \times EXC$$

MMI is the contribution caused by isotopic labelling changing the mass and moments of inertia of a molecule. Increasing the mass of a molecule lowers its overall translation and rotation energy[133,134]. ZPE is the contribution from zero point energies and it reflects changes in

vibrational frequencies upon isotopic substitution[124131]. ZPE is generally the largest contributor to secondary KIEs[124]. EXC represents the contribution from vibrationally excited states when, the vibrational quantum number, is > 0. It is generally small at physiological temperatures[134,135].

For regular bonds acting like harmonic oscillators, any disturbance in the equilibrium position leads to a positive restoring force to bring the system back to its equilibrium position. However, the TS, being located at the top of the energy profile, does not experience a restoring force along the reaction coordinate; any movement along the reaction coordinate leads to a force pushing the molecule either forward to form products or back towards the reactants[128, 131, 136]. This force is the equivalent of a harmonic oscillator with a negative force constant, and it results in an imaginary vibrational frequency, e.g., 200*i* $cm^{-1}$, which is often written as a negative frequency, e.g., -200 $cm^{-1}$. The reaction coordinate normal mode of vibration does not contribute to the ZPE and EXC terms in equation **7,** but it does contribute to the MMI term[124].

The reaction coordinate contribution to the KIE is $^{light}\nu^{\ddagger}/^{heavy}\nu^{\ddagger}$, the ratio of reaction coordinate frequencies for the light and heavy isotopes. Since vibrational frequencies are always lower with heavy isotopes, $^{light}\nu^{\ddagger}/^{heavy}\nu^{\ddagger}$ is always > 1, and it can be a dominant contributor to the KIE, meaning that most primary KIEs are normal even if the atoms involved in bond making and breaking have a tighter vibrational environment than the reactant state.

### *1.6.1 Normal vs Inverse KIEs*

Atoms that become vibrationally less constrained in the transition state show a normal KIE, with the light isotope reacting faster than the heavy, i.e., KIE = $^{light}k/^{heavy}k > 1$ [132]. This arises because the change in zero point energies means that the activation energy for the light isotope, $\Delta E^{\ddagger}(^{1}H)$, is less than the heavy isotope, $\Delta E^{\ddagger}(^{2}H)$[124,133] (Figure 1.22). On the other hand,

when the atoms become more vibrationally constrained in the TS the heavy isotope reacts faster giving rise to an inverse KIE, i.e., KIE < 1.[131, 132]

The acid-catalyzed hydrolysis of dAMP illustrates these points. The C1'−N9 bond is almost completely broken at the transition state (**Figure 1.23**)[133]. This loss in bond order is partially compensated by protonation at N7, which results in an increased π-bonding between C8-N9, but the overall bond order to N9 decreases, and a normal 9-$^{15}$N KIE is observed[133]. An inverse KIE is observed at O4'. As the C1'-N9 bond breaks, a high oxacarbenium ion character develops at C1'. This positive charge is stabilized by π-bond formation between the lone pair of O4' and C1', increasing the C1'-O4' bond order at the transition state[133].

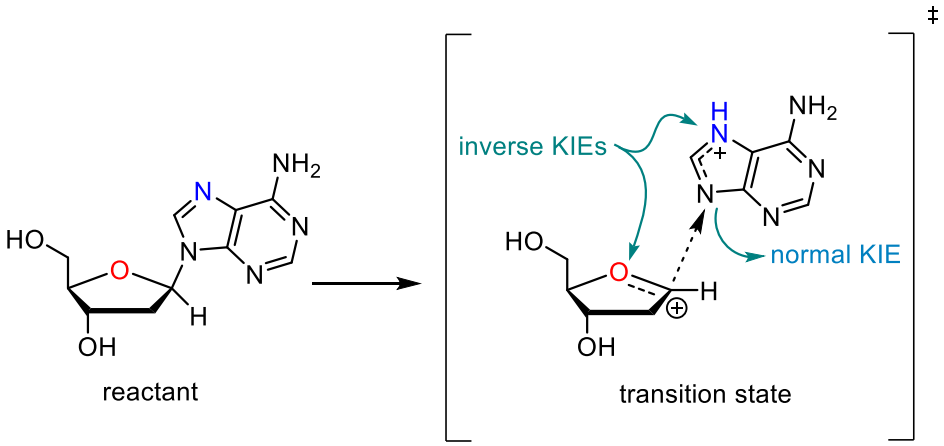


Figure 1.23. Normal vs. Inverse KIEs

In acid-catalyzed dAMP hydrolysis the C1'−N9 bond is breaking in the transition state, so the 9-$^{15}$N KIE is normal. The increased bond order between the ring oxygen and C1' leads to an inverse 5'-$^{18}$O KIE. N7 is protonated before C1'−N9 bond cleavage, leading to an inverse 7-$^{15}$N KIE[133].

### *1.6.2 Non-competitive and Competitive KIEs*

KIEs can be measured using (i) direct, non-competitive measurements, or (ii) internal competition methods. For non-competitive KIE measurements, the reactions are carried out separately for the labelled and unlabelled substrates and the ratio of the rate constants is

calculated[131,137]. This limits the accuracy of non-competitive KIE measurements, and they are not generally used for TS analysis. In competitive KIE measurements, both labelled and unlabelled substrates are present in the reaction mixture, and the KIE is measured as the ratio of rate constants. This removes many sources of error and allows KIEs to be measured with the precision needed for TS analysis, in the ± 0.002 to ± 0.010 range. The isotopic compounds compete as substrates to react with the enzyme, so the ratio of rate constants reflects the specificity constant, $k_{cat}/K_M$[131]. Competitive KIEs can be measured by various techniques such as isotope ratio mass spectrometry[129], liquid scintillation counting of radioisotopes, or NMR[138].

### *1.6.3 KIEs on the First Irreversible Step*

Competitive KIEs are KIEs on the specificity constant, $k_{cat}/K_M$[108]. That is, KIE = $^{light}(k_{cat}/K_M)/(^{heavy}k_{cat}/K_M)$. Since $k_{cat}/K_M$ reflects the change between the free enzyme and substrate in solution (E + S) and the enzyme·TS complex (E·S$^{‡}$), competitive KIEs reflect that step[123, 133]. If a reaction involves more than one step, $k_{cat}/K_M$ reflects the first irreversible step, which is not necessarily the same as the rate-limiting step[139]. αCKS-catalyzed reactions involve at least two steps, THI formation and breakdown (Figure 1.2). If THI formation is irreversible, that is, if $k_3/k_2 \gg 1$, then the KIEs will reflect THI formation only. The observable KIEs will be $KIE_{formation} = \alpha_1$, where $\alpha_1$ is the KIE on step $k_1$. In this case, once the THI is formed, the reaction is committed to proceed forward and there is no longer any discrimination between the isotopic labels in steps $k_3$ or $k_4$. If THI formation is fully reversible and THI breakdown is the first irreversible step, that is, if $k_3/k_2 \approx 0$, then the observable KIEs will reflect THI breakdown, $KIE_{breakdown} = \alpha_1\alpha_3/\alpha_2$. If the THI partitions both forward and backward, that is, if THI formation

is "partially irreversible", then the KIEs will reflect both steps and depend on the partitioning ratio, $k_3/k_2$ (**Equation 8**).

Equation 8

$$\mathrm{KIE} = \frac{\alpha_1\left(\alpha_3/\alpha_2 + \frac{k_3}{k_2}\right)}{1 + \frac{k_3}{k_2}}$$

In this case, the experimentally observable KIE will vary between $\mathrm{KIE}_{\mathrm{formation}}$ and $\mathrm{KIE}_{\mathrm{breakdown}}$ (**Figure 1.24**).

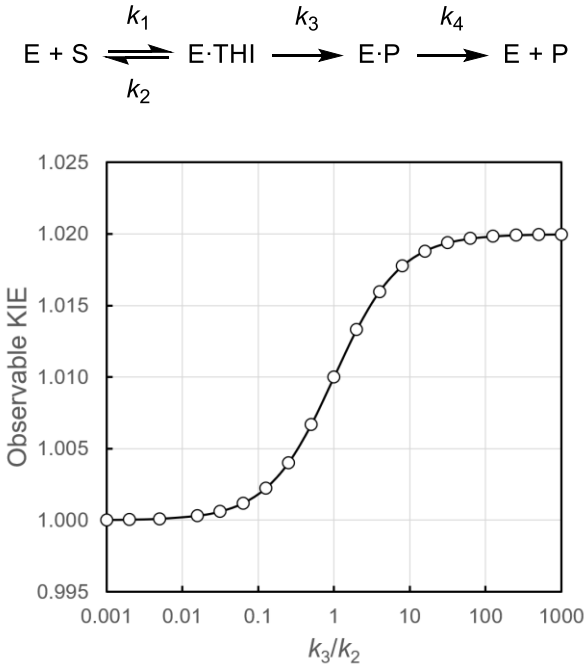


Figure 1.24: Observable KIE as a function of THI partitioning

THI partitioning is $k_3/k_2$, the ratio of rates of the THI breaking down to products or back to substrates. If the THI partitions only forward to products, then $k_3/k_2$ is large and the first irreversible step is THI formation. Conversely, if the THI partitions primarily back to the substrates, then $k_3/k_2$ is small and the first irreversible step is THI breakdown. In this example, with hypothetical KIEs of $\mathrm{KIE}_{\mathrm{formation}}$ = 1.02 and $\mathrm{KIE}_{\mathrm{breakdown}}$ = 1.00, if $k_3/k_2 < 0.1$ or $> 10$, the observable KIE will be experimentally indistinguishable from $\mathrm{KIE}_{\mathrm{breakdown}}$ or $\mathrm{KIE}_{\mathrm{formation}}$, respectively. In between these values, the observable KIE will be a combination of the individual KIEs.

For DAHPS, there is evidence for product release being rate-limiting under most conditions[18, 49, 140] however, since the chemical steps of αCKS reactions are irreversible, no step after $k_3$ will affect the observable KIEs. The specificity constant for metal-dependent αCKSs is a fourth order rate constant $k_{cat}/(K_{M,metal}\times K_{M,PEP}\times K_{M,aldose})$[17]. That does not affect the above discussion about the first irreversible step, and for simplicity it will be called simply $k_{cat}/K_M$.

### *1.6.4 Measuring KIEs using NMR*

In 1980s, Pascal *et al*. measured deuterium KIEs using NMR spectroscopy[141]. In 1995, Singleton and Thomas developed a method to measure competitive KIEs for the Diels-Alder reaction at natural abundance using NMR spectroscopy[138]. Using natural abundance reactants avoided the need to synthesize labelled reactants, but it did require multi-mole scale reactions owing to the low abundance of $^{13}C$ and $^{2}H$. Additionally, this method could not be used to measure NMR inactive KIEs such $^{18}O$.

A direct measurement method was developed by Bennet's group to measure competitive KIEs[142] (**Figure 1.25**). It uses an NMR active nucleus as a reporter nucleus to probe the isotopic composition of adjacent nuclei. If the reporter nucleus (e.g., $^{13}C$) is adjacent to an NMR active nucleus (e.g., $^{13}C$), the isotopes at the site of interest ($^{13}C$ and $^{12}C$) can be differentiated based on their one bond coupling constants[142]. However, if the reporter nucleus (e.g., $^{13}C$) is adjacent to an NMR inactive nuclei at the site of interest (e.g., $^{16}O$ and $^{18}O$) then the difference in the chemical shift due to isotopic effect can be used to measure the isotope ratios (**Figure 1.25**)[142]. For example, to measure the [2-$^{13}C$]PEP KIE, the 3-$^{13}C$ label would be used as the reporter nucleus to detect the $^{13}C/^{12}C$ ratio at C2. The 2-$^{13}C$ KIE reaction mixture would contain a mixture of [3-$^{13}C$]- and [2,3-$^{13}C$]PEPs. The $^{13}C3$ peak in [3-$^{13}C$]PEP reflects the presence of $^{12}C2$, while in

[2,3-$^{13}$C]PEP it reflects the presence of $^{13}$C2, which splits the $^{13}$C3 peak with $J_1$ = 80 Hz. In this way, the $^{13}$C/$^{12}$C ratio at C2 can be measured. Measuring the 3-$^{13}$C KIE is similar, except that the 2-$^{13}$C reporter is also split by coupling with $^{31}$P with $J_3$ = 7.5 Hz (**Figure 3.7**). For 2-$^{18}$O KIE measurements using $^{13}$C NMR, a mixture of [2-$^{13}$C,2-$^{18}$O]PEP and [2-$^{13}$C]PEP is used, with the $^{13}$C2 peak reporting on the adjacent $^{18}$O2 or $^{16}$O2 atom. The same principles are used for measuring the 2-$^{18}$O KIE using $^{31}$P NMR and for measuring $^{13}$C KIEs using isotope ratios in the NeuNAc or DAHP products.

The advantages of this method include the use of milligram amounts of starting material rather than multi-grams with natural abundance isotopes, being able to measure KIEs on NMR-inactive nuclei like $^{18}$O, the ability to measure KIEs from isotope ratios in both the reactants and products, and extending the technique to include other probe nuclei such as $^{31}$P, $^{19}$F etc. in addition to $^{13}$C[142].

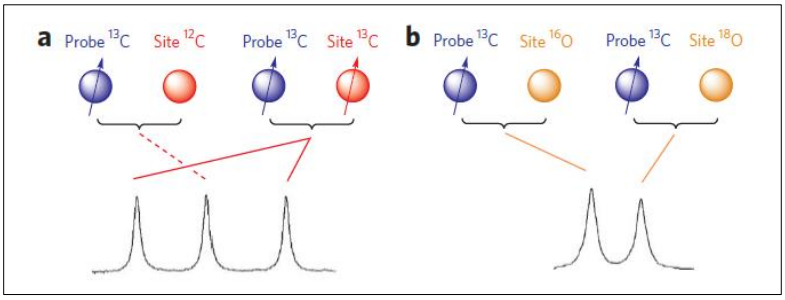


Figure 1.25. KIE measurement by NMR

Competitive KIEs were measured using $^{13}$C- and $^{18}$O KIE using a reporter nucleus e.g., (**a**) $^{13}$C is adjacent to an NMR active nucleus (e.g., $^{13}$C), the isotopes at the site of interest ($^{13}$C and $^{12}$C) can be differentiated based on their one bond coupling constants. (**b**) If $^{31}$P is adjacent to two NMR inactive nucleus (e.g., $^{18}$O), then the isotopes at the site of interest ($^{16}$O and $^{18}$O) can be differentiated based on their chemical shift. Figure from reference 142. (Figures from reference 142, used with permission from Nature Chemical Biology , ©2010).

### *1.6.5 Free Induction Decay*

When an NMR-active nucleus like $^{13}C$ is placed an external magnetic field, $B_0$, in an NMR spectrometer and a 90° radiofrequency (rf) pulse is applied, the rf electromagnetic field rotates the $^{13}C$ atom's magnetization vector from the z-axis to the x-y plane (**Figure 1.26**).[143, 144] Precession of this magnetization vector in the x-y plane is the signal that is detected as the free induction decay (FID)[143]. The FID represents the decay of the non-equilibrated magnetization vector precessing in the transverse plane as a function of time after the rf pulse[143, 144].

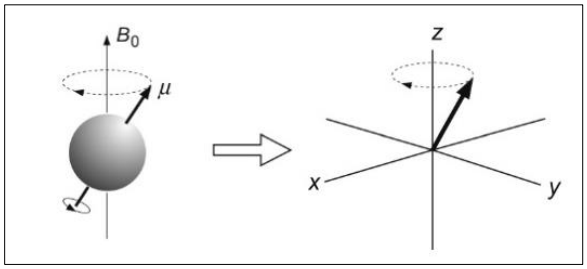


Figure 1.26: Larmor precession

When an NMR-active nucleus is placed in an external magnetic field, $B_0$, applied along the z-axis, and its magnetization vector is flipped into the x-y plane, the magnetization vector precesses at a rate proportional to the strength of the external magnetic field[143]. (Figure from reference 143, used with permission from Elsevier, ©2016).

A mathematical method called Fourier transform is applied to interpret the FID by converting the time domain FID to a frequency domain signal (**Figure 1.27**)[145, 146]. Different parts of the FID store information about the NMR spectrum such as intensity and phase correction, signal to noise ratio (S/N) and resolution[144].

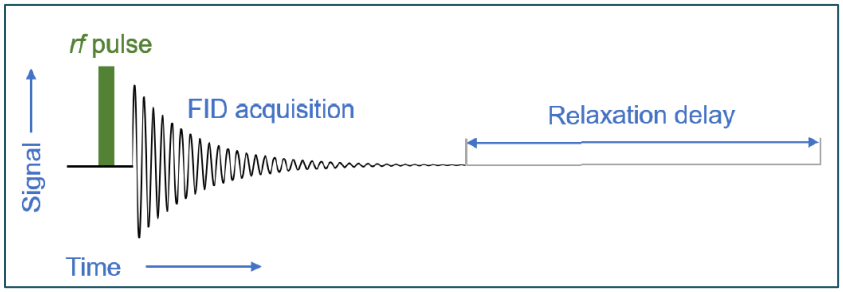

Figure 1.27: 90° rf pulse and FID

Fourier transform is applied to interpret the FID by converting the time domain FID to a frequency domain signal. Different part of the FID gives different information about the NMR spectrum e.g., it is important to for the NMR signal to fully relax before another pulse to ensure good signal to noise ratio and good resolution[144, 146 143, 146].

After the excitation of the non-equilibrated net magnetization vector to the x-y plane, it relaxes to its state of equilibrium, i.e., along the z-axis[143]. There are two modes of relaxation, namely longitudinal and transverse relaxation.

*Longitudinal relaxation:* The return of the net magnetization vector along the z-axis is called longitudinal relaxation and it is the characterized by the time constant $T_1$[143]. It reflects the return of the magnetization vector to the *z*-axis.

*Transverse relaxation:* The net magnetization vector is the sum of microscopic vectors representing the individual nuclei. After the rf pulse and excitation of the net magnetization to the x-y plane, small differences in the magnetic field cause individual nuclei to precess at slightly different frequencies[143]. This results in the loss of phase coherence and therefore, the net magnetization vector along the x-y plane[143]. This is called the transverse relaxation. Transverse relaxation occurs more quickly than longitudinal relaxation, and since the width of NMR peaks is inversely related to the relaxation time, $T_2$ governs the peak width.

Differences in the magnetic field in the sample can arise due to two reasons[143]. First, it could be due to static magnetic field inhomogeneity throughout the sample volume due to instrument imperfection[143]. This can be minimized for each sample when optimizing or shimming the static magnetic field[143]. Second, it could arise from local magnetic fields due to intramolecular or intermolecular interactions in the sample[143]. The experimentally observed

transverse relaxation time, $T_2$*, contains contributions from both factors (**Equation 9**). $T_2$* is inversely proportional to the NMR peak width (**Equation 10**)[143], $\Delta\nu_{1/2}$[143].

Equation 9:

$$\frac{1}{T_2^*} = \frac{1}{T_2} + \frac{1}{T_{2(\Delta B_0)}}$$

Where $T_{2(\Delta B0)}$ = contribution to the relaxation from inhomogeneity in the magnetic field.

Equation 10:

$$\Delta\nu_{½} = \frac{1}{\Pi} T_2^*$$

Traditionally, it was considered that the FID was decayed sufficiently after 3 × $T_2$* to avoid the truncation of the FID that is known to cause deterioration in resolution, and at the same time avoid accumulating noise that worsens the signal to noise ratio (S/N)[147]. However, longitudinal relaxation, $T_1$, has traditionally been the dominating factor in determining relaxation times in quantitative NMR.

### *1.6.5.1 Relaxation times*

Transverse relaxation ($T_2$) is faster than longitudinal relaxation ($T_1$), which means that the FID signal will decay to baseline before the excited nuclei are fully relaxed. For traditional quantitative NMR, the excited nuclei must be fully longitudinally relaxed before the next rf pulse is applied. If a nucleus is not fully relaxed when the next rf pulse is applied, the next 90° rf pulse is superimposed on the residual longitudinal excitation, leading to a flip angle > 90° and a signal that is no longer quantitative. A relaxation time of 7 × $T_1$ allows for the recovery of 99.99 % magnetization when using a flip angle of 90°[148]. However, it can take several minutes for the $^{13}$C

nuclei to completely relax, making data acquisition quite time consuming. For general use, NMR spectra are collected with more frequent pulses at a smaller flip angle (≈ 30°).[147] This increases S/N at the expense of peak intensities not being quantitative at different sites in the molecule. Dr. Andrew Murkin (University of Buffalo) proposed using incomplete relaxation when measuring isotopic ratios[149]. The rationale is that because a single nucleus (e.g., $^{13}$C2 of PEP) is being observed and its $T_1$ value will not be affected by the isotope at the adjacent site ($^{12}$C3 or $^{13}$C3), it is possible accurately measure the $^{12}$C3/$^{13}$C3 ratio without complete $T_1$ relaxation at $^{13}$C2. The effect of incomplete relaxation will be the same with either isotope at C3. Using the two approaches, Alvin Niu from the Berti Lab showed that (i) any variation in $T_1$ affected the $^{31}$P signal equally for $^{16}$O-$^{31}$P and $^{18}$O-$^{31}$P in PEP[146], and therefore the standard error wasn't affected significantly, (ii) it was possible to decrease the acquisition time for measuring KIEs by 9-fold, from 6 h to 40 min[146].

Using short intervals between rf pulses without complete $T_1$ relaxation makes faster isotope ratio measurement possible; however, the interval between rf pulses must allow complete transverse relaxation ($T_2$*). If $T_2$* is incomplete and the FID not fully decayed, peak ringing (or 'sinc wiggles') will be observed, so intervals between rf pulses of 5 × $T_2$* were used[150, 151].

### *1.6.6 NMR acquisition parameters for measuring KIEs*

An internal standard is needed in KIE measurement to determine the extent of the reaction ($F_1$)[152]. It is important to ensure that the internal standard: (a) is inert to the KIE reaction conditions, or placed within a capillary tube, and (b) peak of interest does not overlap with the internal standard[152]. For $^{13}$C- and $^{18}$O-KIE measurements, the enzymatic reactions were run until 70 – 80 % completion that took 8 -12 h. This gave sufficient time to collect enough spectra (20 –

40 spectra) with a S/N > 10[152]. As the reaction reaches completion, $R/R_o$ becomes more accurate while the S/N worsens. To improve S/N in the spectra as the reaction neared completion, the FIDs from successive spectra were co-added[152]. Similarly, for isotope ratios from the products, FIDs from early spectra were co-added to improve their S/N. It was important to set the acquisition parameters to minimize the time required to collect each spectrum while also obtaining suitable S/N and resolution with no ringing in the spectrum.

For peaks to be quantitative, through-space coupling through the Nuclear Overhauser Effect (NOE) must be avoided.[150, 151, 153]. NOEs are observed when spin excitation of one nucleus is transferred to another, increasing its intensity. This increase in intensity is not quantifiable, so it is suppressed during data collection using inverse-gated decoupling[153]. Inverse-gated (i.e., during acquisition), as opposed to gated (between rf pulses) or power-gated decoupling (constant decoupling), reduces sample heating during decoupling[153].

Obtaining quantitative NMR data requires optimizing acquisition parameters, the number of scans per spectrum (typically 512 for $^{13}C$, 600 for $^{31}P$), and post-acquisition processing parameters such as phasing, Lorentzian multiplication, and the number data points[152]. To obtain a balance between resolution and S/N, the line broadening (lb) for the peak is adjusted to 75 % of line width at half height of the narrowest line of interest[154]. The shimming of the sample was changed to automatic shimming during data collection to maintain consistent peak shape. Shimming provides a homogeneous magnetic field to and has a direct effect on the peak shape. Obtaining symmetrical peak shape is critical for quantitative NMR, especially when measuring $^{18}O$ KIEs, where the peaks overlap and require peak deconvolution[152].

Converting the experimentally observed isotope ratios to a KIE requires compensating for the reactant becoming depleted in the faster-reacting isotope as the reaction proceeds[138, 142, 155, 156]. This requires measuring the fractional extent of reaction, $F_1$, along with each isotope ratio measurement, and converting the observed isotope ratios to KIEs (**Equation 11**)[157].

Equation 11

$$\frac{R}{R_0} = (1 - F_1)^{\frac{1}{\mathrm{KIE}}-1}$$

where $F_1$ is the fractional extent of reaction for isotope 1, and $R$ and $R_0$ are the isotope ratios $^{heavy}S/^{light}S$ (e.g., $^{13}C/^{12}C$) at time = i and 0 respectively (**Equation 12Equation 13**).

Equation 12

$$R = \frac{\sum peak\ areas\ for\ ^{heavy}S}{\sum peak\ areas\ for\ ^{light}S}$$

Equation 13

$$F_1 = 1 - \frac{P_i/Ref_i}{P_0/Ref_0}$$

It is also possible to determine KIEs from the isotope ratios in the products (**Equation 14**):

Equation 14

$$\frac{RP_i}{RP_\infty} = \frac{1 - (1 - F_1)^{\frac{1}{KIE}}}{F_1}$$

where $RP_i$ and $RP_\infty$ are the product isotope ratios $^{heavy}P/^{light}P$ (e.g., $^{13}C/^{12}C$) at time = i and ∞, respectively.

## 1.7 Computations

The free energy surface around a transition state is at a saddle point; that is, it is the highest energy point on the lowest energy pathway between reactant and product[123]. The experimental transition state cannot be calculated directly from the experimental KIEs[123, 133]. Rather, the computational transition state whose calculated KIEs that most closely match the experimental KIEs is the experimental transition state. The rationale is that while computational transition states are often not accurate because of limitations of the computational methods and because solvent and enzymes change TS structures, vibrational frequencies for a given computational TS structure *are* accurate[158-160] and therefore the computational TS structure whose calculated KIEs best match the experimental values is the true experimental transition state.

Interpreting experimental KIEs therefore involves creating computational models of the reaction. This was done previously using bond order vibrational analysis methods[123] but as computational power has increased over time, it has become increasingly feasible to use electronic structure calculations (e.g., in Gaussian 16) to model KIEs[161]. Computational models are created for each plausible mechanism. For αCKS reactions, that would include the cationic and anionic stepwise mechanisms of THI formation and breakdown (**Figure 1.2**), as well as concerted THI formation and breakdown.

For reactions that are not well understood, it is not possible to make reasonable initial guesses at a TS structure. Instead, a potential energy scan is used to understand how energies vary throughout reaction space (**Figure 3.15**). For example, for THI formation, as series of constrained optimizations are performed with fixed bond lengths for the bonds being formed,

namely C3···C1' and C2···O2'. The energies of these constrained structures show which mechanisms are reasonable or unreasonable and guide further TS optimization calculations.

## 1.8 Transition States and Inhibitor Design

### *1.8.1 TS analogues*

A TS analogue is a stable chemical compound that resembles an enzymatic transition state [162]. TS analogues are often potent inhibitors because they mimic the charge and geometry of the species to which an enzyme binds most tightly[136]. Potent TS inhibitors include coformycin and pentostatin (inhibitors of adenosine deaminase)[163] and phosphonamidate inhibitors of thermolysin[164]. Many compounds are designed with TS mimicry in mind, but experimentally demonstrating TS mimicry is not straightforward. One experimental technique is LFER analysis to demonstrate a linear relationship between $\log(K_M/k_{cat})$ vs $\log(K_i)$. If a linear relationship exists, then any perturbation in the free energy of TS stabilization has an equal or a proportional effect on the free energy of inhibitor binding, meaning that the inhibitor is interacting with the enzyme as the TS does[32].

### *1.8.2 Example of a TS inhibitor*

Forodesine (immucillin H, ImmH), which is used to treat leukemias, is a TS inhibitor of purine nucleoside phosphorylate (PNP) that was developed based on TS analysis[165]. Human PNP catalyzes the phosphorylation of purine 2'-deoxyribonucleosides to the purine base and α-*D*-ribose 1-phosphate[166,167]. The purine base products are salvaged for nucleoside synthesis or further metabolized to uric acid[166]. Inhibiting PNP in dividing T cells leads to an accumulation of

dGTP, an allosteric inhibitor of ribonucleotide reductase, which inhibits formation of dCTP and dUTP thus, preventing DNA synthesis and repair, ultimately leading to T-cell apoptosis[168].

TS analysis of bovine PNP demonstrated a dissociative $S_N2$ ($A_ND_N$) mechanism in which the leaving group and nucleophile were both in the reaction coordinate[168-170]. The leaving group purine had mostly departed and the bond to the nucleophile had barely started to form, leaving a significant positive charge on the ribosyl ring. At the transition state, there is loss of bond order between the C1'-N9 of the purine base which generates a partial positive charge on C1' of ribosyl group, making the purine base a good leaving group[169, 170]. There is also protonation at the N7 position of the purine ring which can be seen in the electrostatic potential map[169, 170]. The electron potential map of the TS of bovine PNP shows the distribution of the partial positive charge between the leaving group and the ribosyl carbocation (shown in blue), while the electron density map of inosine (reactant) in the ground state is neutral (**Figure 1.28**) [168-170]. The nucleophile (arsenate was used) participates only weakly, the loss of bond order much ahead of the nucleophilic attack[169, 170].

TS analysis of bovine PNP led to the development of the TS inhibitor ImmH[168]. The oxacarbenium ion-like ribosyl group was mimicked in ImmH with an iminoribitol structure with a nitrogen p$K_a$ of 6.9 that provides partial positive charge (32% protonated) at physiological pH[166, 168]. Chemical stability was introduced into the inhibitor by using a C1'−C9 bond in 9-deazahypoxanthine[168]. This also increased the N7 p$K_a$ value, leading to N7 being protonated[168]. The C1' carbon of ImmH is $sp^3$-hybridized while it is largely $sp^2$ -hybridized in the bovine PNP transition state, nonetheless ImmH still is an extremely potent inhibitor, with $K_i$ = 36 pM[166, 168] (**Figure 1.28**).

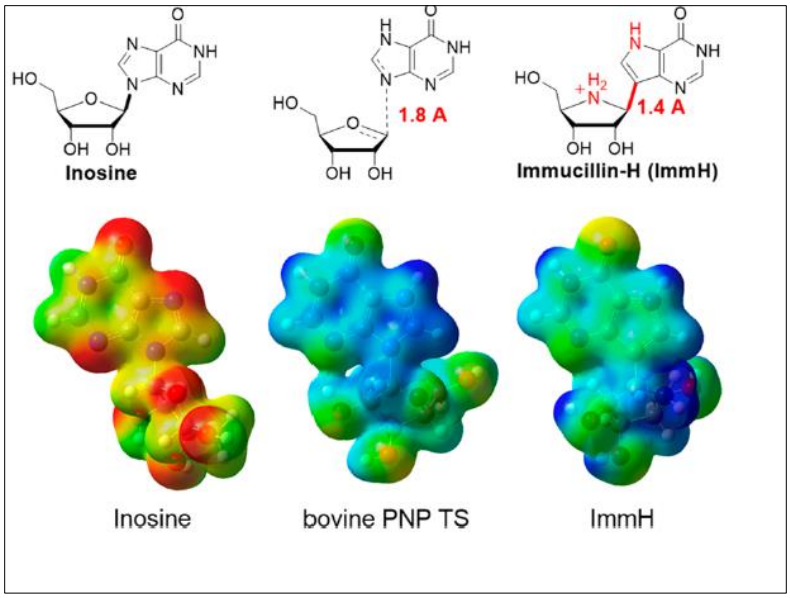


Figure 1.28. TS mimic inhibition of PNP

The PNP TS structure revealed partial positive charges near the N7-protonated hypoxanthine leaving group and the ribosyl cation[166]. The electrostatic potential surface of ImmH resembles the transition state more than the reactant inosine[166]. (Figures from reference 166, used with permission from the American Chemical Society, ©2018).

### *1.8.3 Slow-binding TS mimic inhibitors*

TS inhibitors are also commonly slow-binding inhibitors[167]. This observation has been rationalized in terms of TS mimic inhibitors rapidly forming weaker interactions with the enzyme reminiscent of substrate binding to form the Michaelis complex. The enzyme has been optimized by evolution to form the highly stabilized TS complex, $E \cdot S^{\ddagger}$. However, because it is not similarly optimized for interacting with the TS mimic inhibitor, there may be a significant kinetic barrier to conversion of the weakly bound E·I complex to the tighter $E \cdot I^{*}$ complex which more closely resembles the $E \cdot S^{\ddagger}$ complex.

## 1.9 Research objectives

The objective of this work was to perform TS analysis on NeuB and DAHPS by measuring KIEs in order to understand their catalytic mechanisms, leading ultimately to the

design of TS mimics based on the experimental transition states. KIEs were measured using NMR spectroscopy. Using the direct NMR method initially developed by Bennet's group[142], we measured the [2-$^{13}$C]-, [3-$^{13}$C]-, and [2-$^{18}$O]PEP KIEs. Using the method recently extended to using $^{31}$P by Alvin Niu of the Berti lab, we also measured the [2–$^{18}$O]PEP KIE using $^{31}$P nuclei as the reporter nucleus.

The experimental transition state for both enzymes had THI formation as the first irreversible step, proceeding through a stepwise mechanism with the C3−C1' bond being formed in the transition state, and no participation from the water nucleophile. Computational TS structures were found and the KIEs were calculated. The experimental TS was found by matching the calculated and experimental KIEs. This TS structure explained the ineffectiveness of previous cationic inhibitors and suggests a route forward for inhibitor design. The inverse 2-$^{13}$C for the DAHPS-catalyzed reaction may indicate some accumulation of more positive charge on C2 in the DAHPS transition state.

# 2 TFP and DAHP hydrazone

Although DAHP oxime is a potent inhibitor of DAHPS ($K_i$ = 1.5 µM), there was 15% residual activity, which would be sufficient for bacterial survival[17]. This prompted the need to optimize DAHPS inhibitors. Fragment based drug discovery (FBDD) is a technique increasingly used in pharmaceutical companies and medicinal chemistry[171, 172]. FBDD finds low molecular weight ligands (~150 Da) to bind to biological targets[171]. Even though it results in poorer $K_i$ values, it allows a more efficient exploration of chemical space in more detail using small molecules, increasing the likelihood of hits.[173]. Hits obtained can then be optimized by growing, linking or merging fragments to make the full length potent inhibitor[174].

Dr. Maren Heimhalt from the Berti lab used "inhibitor-in-pieces" approach to test inhibitor fragments that led to DAHP hydrazone, the most potent αCKS inhibitor to date[90]. In addition to working on TS analysis, I synthesized two compounds, DAHP hydrazone and trifluoropyruvate hydrazone ethyl ester (TFPHEE) to complete this manuscript for DAHPS inhibition and for future studies[90]. DAHP hydrazone was synthesized from PEP and E4P to make DAHP, then reacting DAHP with hydrazine to yield DAHP hydrazone. This first required synthesizing E4P. TFPHEE was more challenging since the originally reported synthesis did not yield the expected product, and it was necessary to extensively troubleshoot the synthesis to demonstrate that it could not have worked as originally reported.

## 2.1 Materials and Methods

### *2.1.1 E4P Synthesis and Purification*

E4P was synthesized by the oxidative degradation of glucose 6-phosphate (G6P) using lead tetraacetate ($Pb(OAc)_4$) based on the method by Sieben et al[175] and modified by Naresh

Balachandran of the Berti Lab[176]. G6P (200 µmol) was dissolved in 50 mL of acetic acid and 680 µmol lead tetraacetate was dissolved in 20 mL of acetic acid containing 700 µmol of $H_2SO_4$. The G6P was titrated with 500 µL aliquots of $Pb(OAc)_4$ every minute. The reaction was monitored using starch-iodide paper test until the reaction mixture contained a slight excess of $Pb(OAc)_4$. The principle is that Pb(IV) oxidizes $I^-$ to $I_2$, which then forms a deep blue/purple complex with starch. The starch-iodide paper was made by adding 2.5 g starch into 250 mL boiling water and 0.5 g sodium iodide to this cooled solution. Whatman Filter paper was cut, dipped into the solution, and dried. A drop of dd$H_2O$ and of the crude reaction mixture was spotted onto the testing paper while titrating it. This was continued until the purple colour did not fade, indicating that all the G6P had been consumed and a small excess of Pb(IV) was present. An additional 10 µmol of G6P was then added to consume the residual $Pb(OAc)_4$ to avoid over-oxidation of E4P to glyceraldehyde 3-phosphate , a DAHPS inhibitor[146].

The solution was filtered through a Celite filter and washed with 100 mL of dd$H_2O$. The flow-through was concentrated under vacuum to less than 5 mL at 5 °C. The crude product was purified on a Q-Sepharose anion exchange column (GE Healthcare; column volume was 12 mL), and eluted with a gradient of 0.1 M to 0.8 M sodium formate over 70 min at 1 mL/min. The 70 fractions collected were examined using the reducing sugar assay (RSA) to detect aldehyde groups[177]. The RSA measures the concentration of aldehyde sugars like E4P and G6P by detecting the reduction of $Cu^{2+}$ to $Cu^+$ produced by aldehyde oxidation[178] and complexing of $Cu^+$ by neocuproine[179]. The assay was performed in 1 mL with glucose standards by adding 0 – 100 µL of 1 mM glucose (prepared in 0.8 M sodium formate) into a 375 µL solution containing 187.5 µL of solution A (4% $Na_2CO_3$, 1.6% glycine, 0.045% anhydrous $CuSO_4$) and 187.5 µL of solution B (0.12% neocuproine·HCl) at pH 10 - 10.5. The 70 fractions were prepared with 5-10

µL fraction aliquot, 187.5 µL solution A, 187.5 µL of solution B, and 610 - 615 µL of $ddH_2O$ to a final volume of 1 mL. The solution was heated at 95 °C for 8 min and the $A_{450}$ was read. The fractions containing E4P were pooled and lyophilized to 2.5 mL and injected onto the SP-Sepharose column (GE Healthcare) to exchange $Na^+$ ions to $H^+$, and eluted with water over 30 min at 2 mL/min. The final fractions containing E4P were examined again using RSA, pooled, lyophilized and quantified using the DAHPS reaction. The purified E4P was dried down and stored in 50 mM HEPES buffer (pH 7.0) at -20 °C.

The lyophilized E4P was quantified using the RSA and MGAM assay. To quantify E4P using MGAM assay, different volumes of unknown E4P (0 to 100 µL) were added to 1 mM PEP, 100 µM $MnCl_2$, 100 µM TCEP, and 20 nM DAHPS in 50 mM K-HEPES at pH 7.0 in a final volume of 200 µL. Aliquots of 20 µL of reaction mixture were added to 96 well plate containing 100 µL MGAM solution and 80 µL $ddH_2O$ every 60 s and each reaction was quenched with 10 µL 34% citrate solution after 90 s.

### *2.1.2 DAHP hydrazone*

DAHP hydrazone was synthesized by first synthesizing and purifying DAHP by the reaction between PEP and E4P with DAHPS. DAHP was then reacted with hydrazine hydrate at pH 8 for 5 days. DAHP was synthesized as described previously[114], with some modifications. DAHP was synthesized by incubating 4.2 mM PEP, 80% of 4 mM E4P, 0.01 mM $Mn^{2+}$ and 400 nM DAHPS in 2.5 mL of 10 mM K-HEPES (pH 7.0) for 3 h at 25 °C. The final concentration of PEP after 3 h was determined using the lactate dehydrogenase (LDH) assay and pyruvate kinase (PK) assays, respectively. In the LDH assay, pyruvate is reduced to lactate with a concomitant oxidation of NADH to $NAD^+$, which is detected by a decrease in $A_{340}$ as NADH is consumed,

with $\Delta\varepsilon_{340} = -6220\ M^{-1}\ s^{-1}$.[180] The pyruvate kinase reaction converts PEP + ADP to pyruvate + ATP, and the pyruvate then enters the LDH reaction. A 96 assay well plate contained 5 µL of the DAHP reaction mixture, 400 nmols of adenosine diphosphate (ADP), 60 nmoles of NADH in 300 µL volume of (50 mM of 0.05 M Tris-HCl, pH 7.6 containing 0.12 M KCl and 0.062 M $MgSO_4$). To start the reaction, 5 mg/mL LDH was added which catalyzed the reduction of the unreacted sodium pyruvate to lactate and NADH oxidized to $NAD^+$. Addition of 1.3 µL of pyruvate kinase (PK) converts PEP and ADP to pyruvate and ATP. Concentrations were calculated using $\Delta\varepsilon_{340} = 6220\ M^{-1}\ cm^{-1}$. The excess PEP was titrated with the remaining 20% of E4P. After the reaction was completed, an Amicon Ultra 0.5 mL centrifugal filter was used to remove the enzyme. The crude DAHP reaction mixture was purified on a Q-Sepharose column (GE Healthcare; column volume was 12 mL), and eluted with a gradient of 0.1 M to 0.8 M sodium formate over 65 – 70 min at 1 mL/min. Fractions containing DAHP were assayed (see below), pooled, dried down to < 5 mL, and injected onto the SP-Sepharose column (GE Healthcare; column volume was 12 mL) to exchange $Na^+$ ions to $H^+$ and eluted with water over 30 min at 2 mL/min. The DAHP assay was repeated to determine the fractions containing DAHP, which were then pooled and dried down completely. A $^{13}C$-NMR was run on the purified product before making DAHP hydrazone.

*DAHP assay*: DAHP was detected by hydrolyzing its phosphate group using alkaline phosphatase and measuring the released $P_i$ with the Malachite green/ammonium molybdate (MGAM) colorimetric assay. Free $P_i$ in the fractions was also detected with the MGAM assay before alkaline phosphatase treatment. A 15 µL aliquot of DAHP was combined with 15 µL of 39 U/mL of alkaline phosphatase in 25 mM Tris-HCl, pH 7.6, 1 mM $MgCl_2$, 0.1 mM $ZnCl_2$, 50% w/v glycerol fraction, in a final volume of 200 µL $ddH_2O$, incubated for 10 min, and a 20

µL aliquot was added to the 96 well plate containing 50 µL MGAM solution + 30 µL dd$H_2O$ and the reaction was quenched by adding 10 µL of 34% citrate after 90 s[181]. The absorbance was read at 660 nm using the microplate reader. Prior to running the DAHP assay, a standard was run using 250 µM PEP.

The DAHP hydrazone synthetic method was previously established in our lab by Jenny Zheng and Jennifer Wild, undergraduate thesis students[114]. To 0.02 mmol of purified DAHP, 0.2 mmol hydrazine hydrate was added in 1 mL dd$H_2O$ and the pH was adjusted to pH 8. The reaction was left for 5 days at 25 °C. The excess hydrazine was removed via lyophilization, and a $^{13}$C-NMR was run to confirm the product's identity.

### *2.1.3 TFPHEE synthesis and purification*

3,3,3-Triflouropyruvate hydrazone ethyl ester (TFPHEE) was synthesized as previously,[114] with some modifications as the reaction proceeded. A solution containing 0.28 mmol of 3,3,3-triflouropyruvate ethyl ester, 3.2 mmol of hydrazine monohydrate, 3.2 mmol of acetic acid (pH 6.3) dissolved in anhydrous ethanol was first refluxed for 16 h. The crude reaction mixture was purified using silica gel column chromatography and two solvent systems (i) *Solvent system A*: 88% DCM : 10% methanol : 2% acetic acid (ii) *Solvent system B*: 80% ethyl acetate : 20% hexanes. A total of 35 - 40 fractions containing 1 mL samples were collected. Thin layer column chromatography was run on alternate fractions using the same solvent system used to purify the product. Based on the TLC data, the fractions likely containing the product were taken for $^{19}$F-, $^{1}$H- and $^{13}$C-NMR.

## 2.2 Results

### *2.2.1 E4P*

E4P, DAHPS's second substrate, was synthesized by oxidative degradation of glucose 6-phosphate with $Pb(OAc)_4$[175], then purified by anion exchange chromatography. This was originally done with a volatile buffer, ammonium formate. However, removing the buffer by lyophilization took two weeks, and ammonium ions tended to react with E4P's aldehyde group. A new anion exchange purification was developed using a gradient 0.1 to 0.8 M sodium formate on a Q-Sepharose column. The $Na^+$ ions were then exchanged to $H^+$ by cation exchange on an SP-Sepharose column to obtain pure E4P and formic acid. Formic acid was removed by lyophilization. E4P synthesized using this method was purified in batches as described above and the contents of the eluted fractions were confirmed by the RSA, quantified by reaction with DAHPS, then used to synthesize DAHP hydrazone, the most potent DAHPS inhibitor to date [43]. The revised method was used for all subsequent E4P syntheses.

### *2.2.2 DAHP hydrazone*

DAHP hydrazone, a 10 nM inhibitor of DAHPS, was needed to complete a manuscript on DAHPS inhibitors[43,90], and for future crystallization trials. Prior to making DAHP hydrazone, DAHP was synthesized by incubating 4.2 mM PEP, 4 mM E4P and 0.01 mM $MnCl_2$ in presence of 400 nM DAHPS enzyme in 2.5 mL of 10 mM K-HEPES (pH 7.0) for 3 h at 25 °C[114]. During the synthesis, the DAHP reaction mixture was titrated with a slight excess of E4P to avoid co-elution of PEP and DAHP. The reaction was monitored using the LDH/PK assay to confirm that all PEP was consumed. If there was excess E4P in the crude DAHP reaction mixture, it would elute before DAHP (based on the charge features of E4P and DAHP). To confirm that no E4P

co-eluted with DAHP, an RSA assay was run on the fractions containing DAHP. The crude DAHP reaction mixture was purified like E4P, using anion exchange chromatography on a Q-Sepharose column to obtain the purified sodium salt of DAHP. $Na^+$ ions were removed by cation exchange on a $H^+$-charged SP-Sepharose column. Purified DAHP was then lyophilized to remove formic acid. Unlike PEP it contains no chromophores, so DAHP was detected in fractions by hydrolyzing its phosphate monoester group with alkaline phosphatase and detecting any $P_i$ released using the MGAM colorimetric assay for $P_i$[181]. Fractions containing DAHP were pooled, lyophilized, and its identity confirmed by $^{13}$C-NMR.

DAHP hydrazone was synthesized by adding 0.02 mmol of purified DAHP, 0.2 mmol hydrazine hydrate in 1 mL dd$H_2O$ and the pH adjusted to 8 and incubating for 5 days at room temperature[114] (**Figure 2.1**). It was then lyophilized, and its identity confirmed by $^{13}$C-NMR (**Figure 2.2**). The hydrazone group was assumed to have an *E*-stereochemistry by analogy to DAHP oxime and other oximes<<references – Balachandran 2016 and More O'Ferrall et al. (2004) Rate and equilibrium constants for hydrolysis and isomerization of (E)- and (Z)-p-methoxybenzaldehyde oximes, *J. Phys. Org. Chem. 17*, 631-640. 10.1002/poc.780>>.

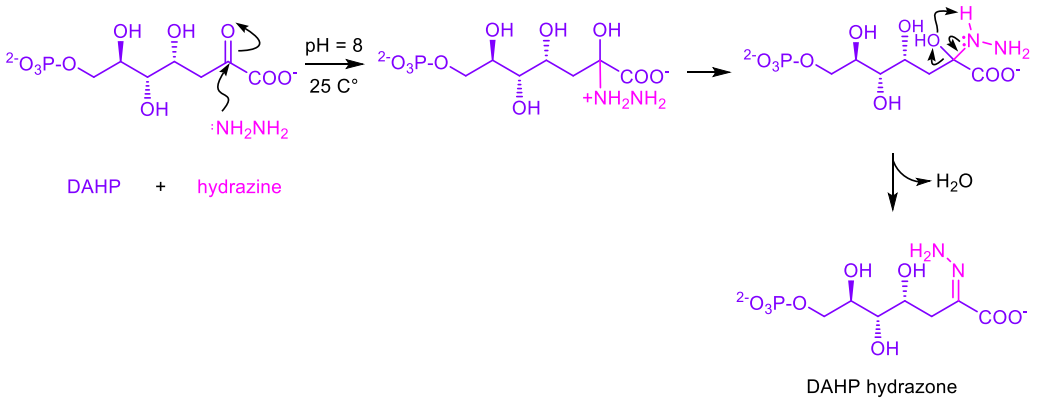


Figure 2.1: DAHP hydrazone synthesis

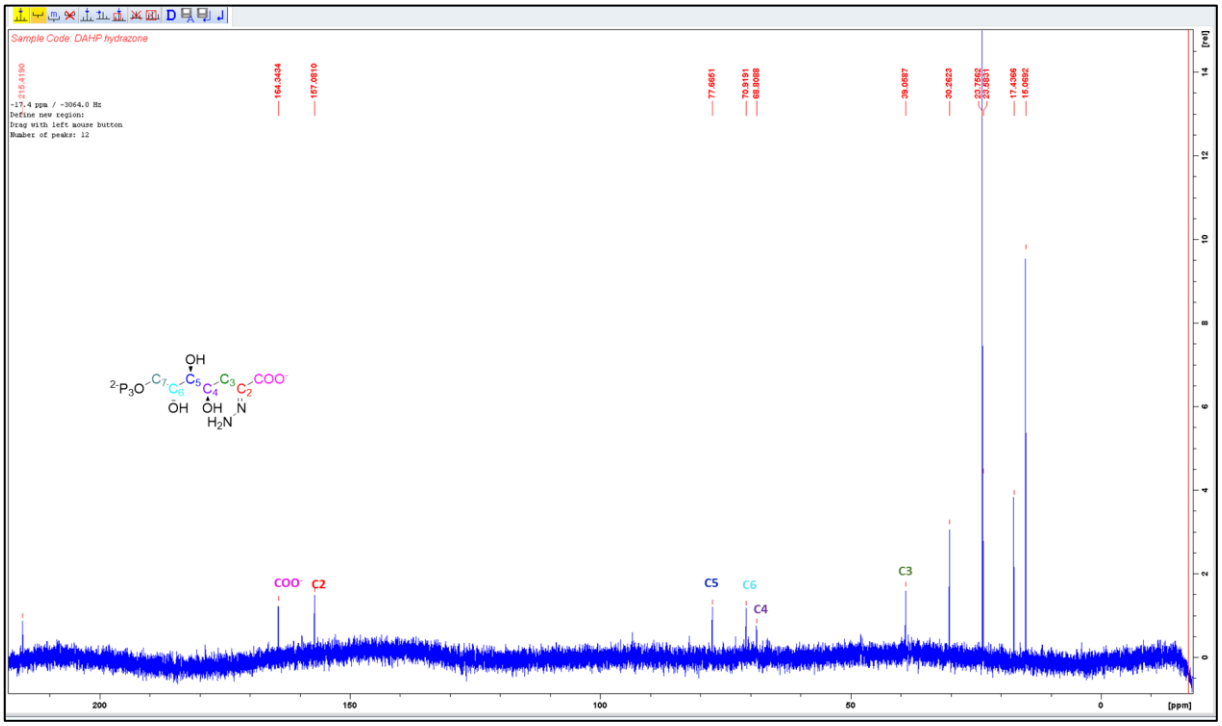


Figure 2.2: $^{13}$C-NMR of DAHP hydrazone

DAHP hydrazone (150 MHz, D2O) δ: 165.3 (C1), 157.0 (C2), 39.0 (C3), 68.8 (C4), 70.9 (C5) and 77.6 (C6).

### *2.2.3 TFP Hydrazone ethyl ester (TFPHEE)*

The first attempted TFPHEE synthesis used the previously reported conditions[114], namely combining 0.28 mmol trifluoropyruvate ethyl ester with 1.6 mmol hydrazine hydrate and 1.6 mmol of acetic acid in 2 mL EtOH was refluxed for 7 h (**Figure 2.3)**.

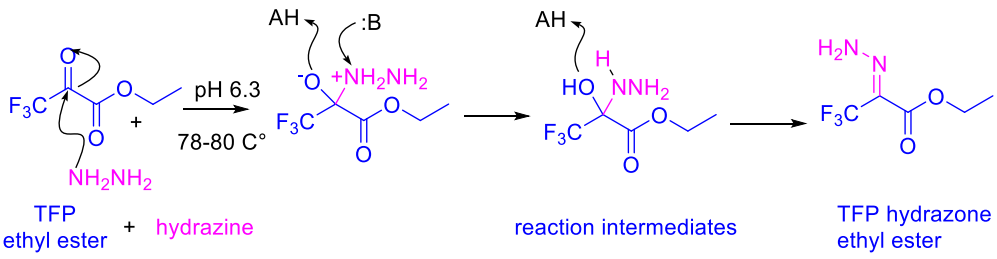


Figure 2.3: TFPHEE Synthesis.

However, based on the $^{19}$F-NMR, 7 h of reflux time did not yield the product, as its $^{19}$F-NMR chemical shift was expected to be between -64 ppm to -66 ppm. The reaction was then monitored using $^{19}$F-NMR from 0 to 42 h, and the optimal refluxing time was found to be between 14 -17 h (**Figure 2.4**). The singlet either at -64 ppm or -65 ppm were likely to be the product peak that was to be purified.

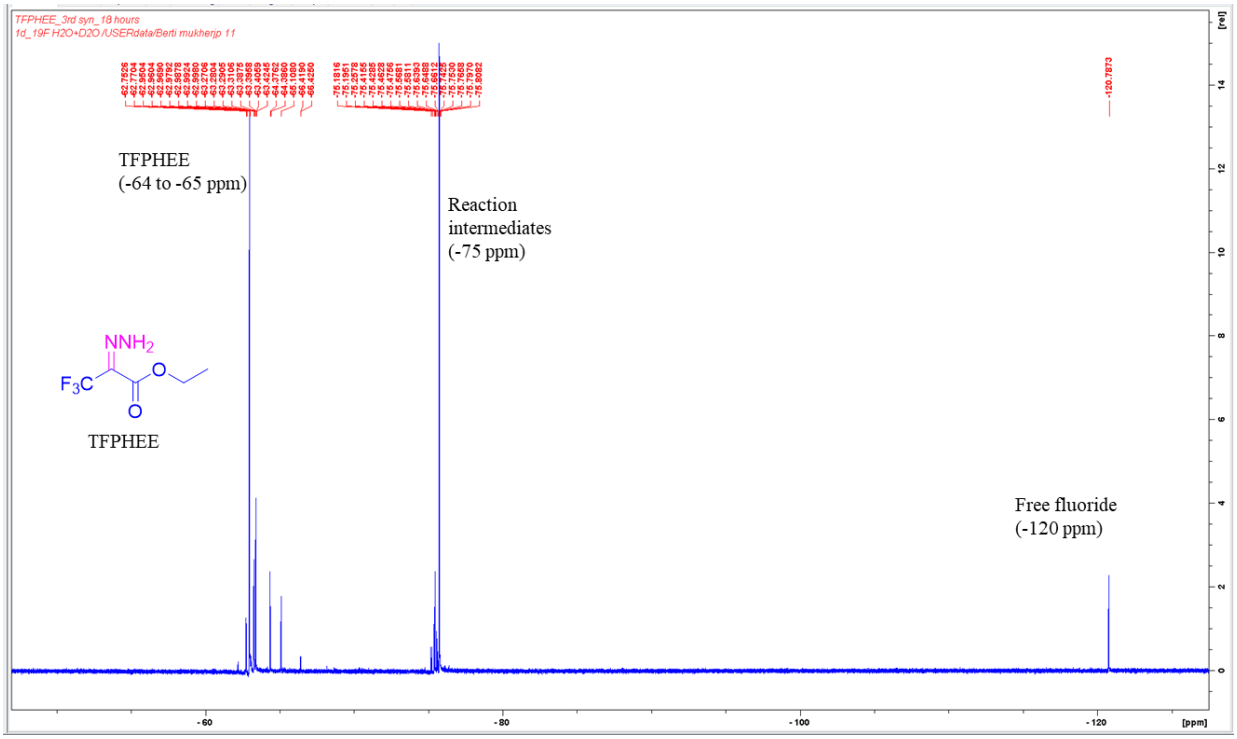


Figure 2.4: $^{19}$F-NMR of TFPHEE reaction mixture after 18 h of refluxing.

TFPHEE was initially reported to be purified by silica gel chromatography using 88 DCM : 10 Methanol : 2 acetic acid. Fractions containing a compound with a -64.3 ppm peak in $^{19}$F NMR were pooled and dried (**Figure 2.5**). However, after drying the $^{19}$F and $^{13}$C spectra did not contain the expected peaks.

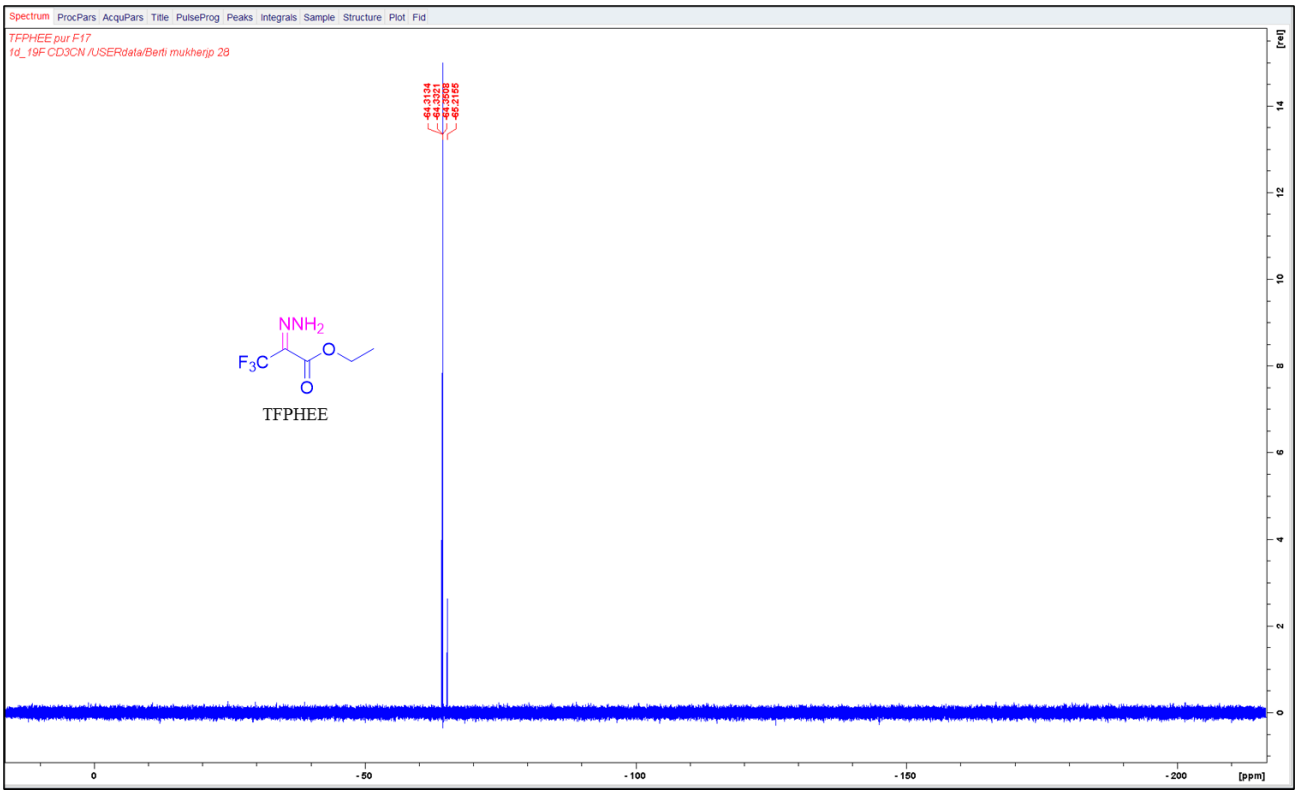


Figure 2.5: $^{19}$F-NMR of purified TFP hydrazone ethyl ester.

$^{19}$F NMR spectrum of Fraction 17 from the silica gel column using solvent system A with a chemical shift of -64.3 ppm, likely to be TFP hydrazone ethyl ester, but this peak disappeared after the product was dried.

A modified protocol was tried, namely combining 0.28 mmol trifluoropyruvate ethyl ester with 3.2 mmol hydrazine hydrate and 3.2 mmol of acetic acid (pH 6.3) in 2 mL ethanol was refluxed for 16 h. Again, TFPHEE appeared to have been purified; however, though the $^{19}$F-NMR continued to show a product peak at -63 ppm (**Figure 2.6)**, it also showed a significant peak at ~-66.7 ppm while $^{1}$H- and $^{13}$C-NMR primary showed only the solvent peaks (not shown).

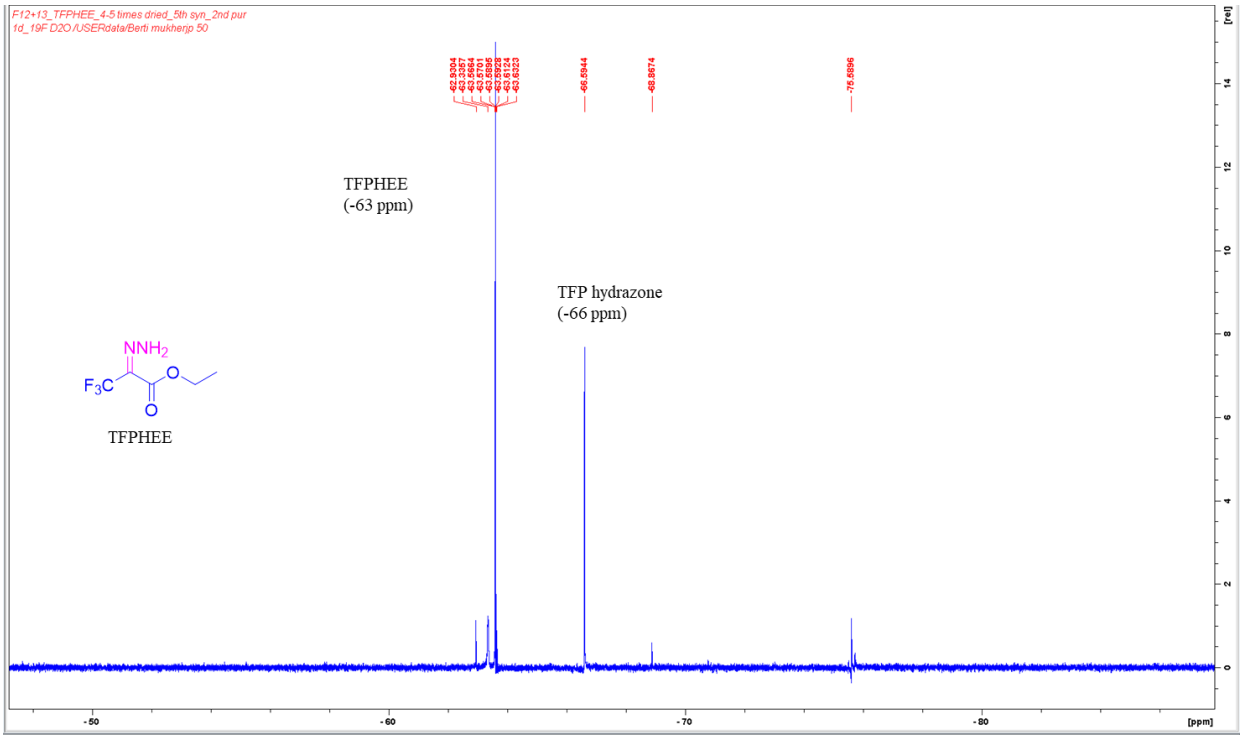


Figure 2.6: TFPHEE $^{19}$F NMR.

$^{19}$F-NMR for fractions 12 & 13 after purification of TFPHEE on the silica gel column using solvent system B

Based on the two preceding reactions it appeared that the product was being lost at some point during the purification. In order to investigate this further, the crude reaction mixture was dried down completely and $^{19}$F-, $^{1}$H- and $^{13}$C-NMR spectra were collected (**Figure 2.7 a-c)**. While the $^{19}$F-NMR spectrum showed a dominant peak at -63.3 ppm (most likely a reaction intermediate) and a singlet at -65 ppm (most likely the product peak), the $^{1}$H-NMR showed three quartets between 3.20 to 3.26 ppm (one of them could be the -$CH_2$ group), but no triplet (confirming the -$CH_3$ group) could be found in the upfield region. The $^{13}$C-NMR showed several peaks, some of which could be product peaks, however without the support of $^{1}$H-NMR, the compound identity was inconclusive. Whether or not it is possible to synthesize TFPHEE under modified conditions, it became clear that the previously reported synthesis would not yield product. It was therefore removed from the manuscript on DAHPS inhibition[90]. It had previously

been reported not to inhibit *E. coli* growth and to be water insoluble; deleting this did not change the manuscript's conclusions.

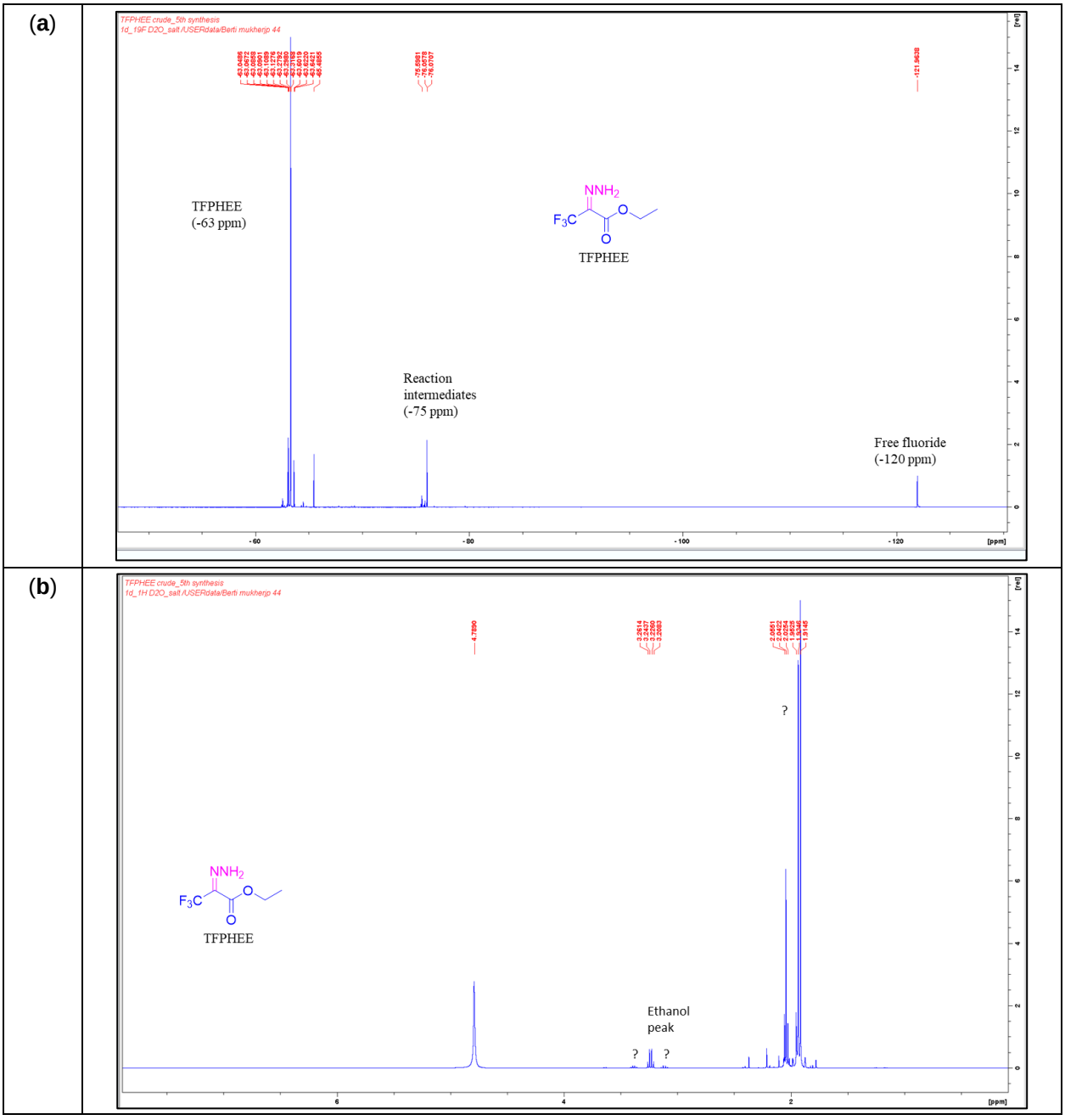

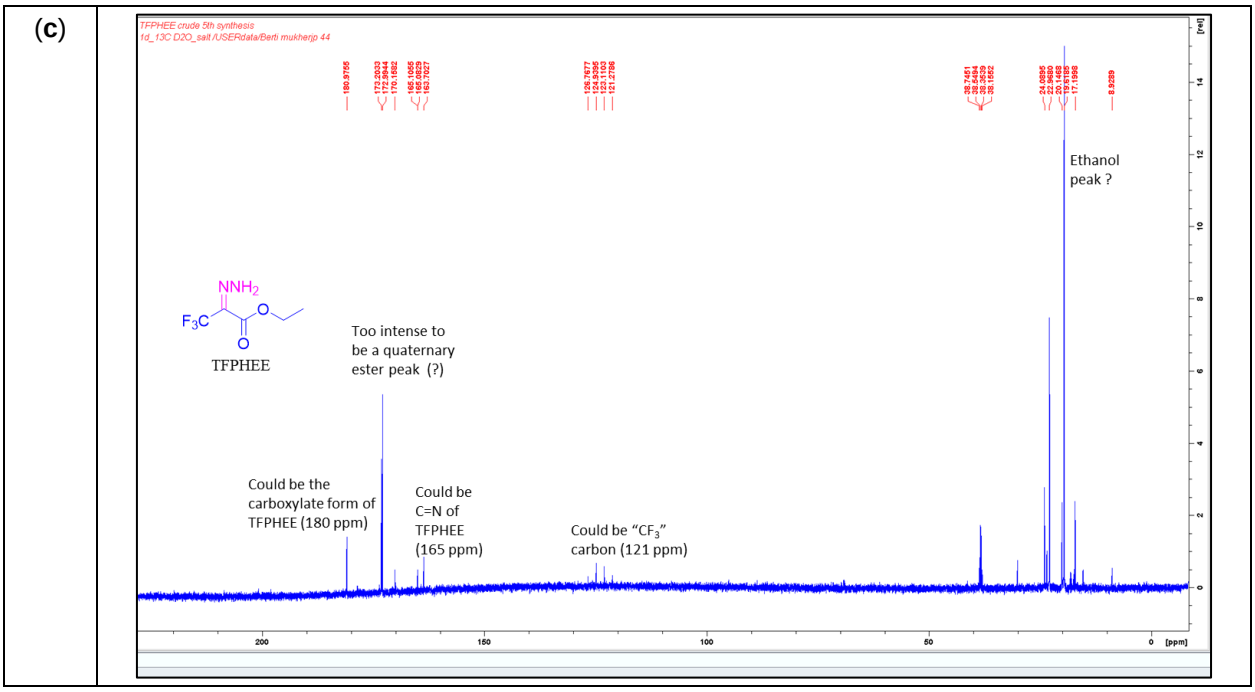


Figure 2.7: NMR spectra of crude TFPHEE reaction mixture
(**a**) $^{19}$F-NMR, (**b**) $^{1}$H-NMR, and (**c**) $^{13}$C-NMR of the crude TFPHEE.

## 2.3 Discussion

The DAHP hydrazone synthesis confirmed the identity and validity of the reported DAHP hydrazone synthesis. The method previously used to purify DAHP hydrazone was modified to remove the need for extended lyophilization in the presence of ammonium formate and reduce the potential for product loss. The Berti lab had solved the DAHPS·DAHP hydrazone crystal structure previously, but the electron density was difficult to interpret (**Figure 2.8**).

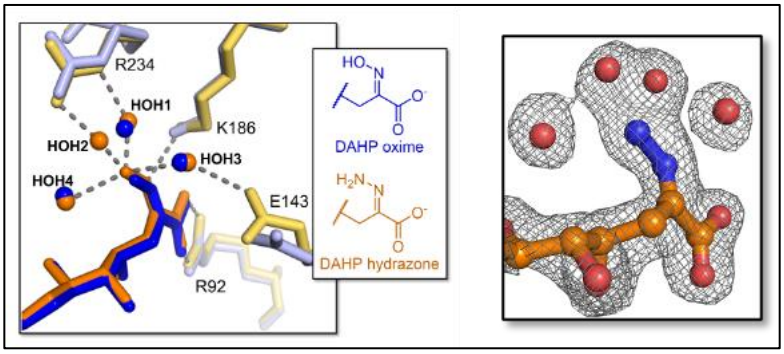

Figure 2.8: DAHP hydrazone and DAHP oxime crystal structures

Comparing DAHP hydrazone (blue) and DAHP oxime (orange) crystal structures ; electron density fitted well to three crystallographic waters around the hydrazone functional group. (Figure created by Paul Berti.)

The electron density fitted well to three crystallographic waters around the hydrazone functional group, reminiscent of the crystallographic waters in the DAHP oxime structure, and the added water would be consistent with the improved $K_i$. However, the hydrazone $-NH_2\cdots$HOH2 distance was 2.04 Å, unrealistically short for a N···O distance[182]. An alternative explanation was advanced by our collaborators that the DAHP hydrazone had undergone a formyl-group addition to yield the formyl-hydrazone compound, which also fit the electron density (**Figure 2.9**). There is no precedent in the chemical literature[183] and mass spectrometry of a redissolved crystal found DAHP hydrazone. However, in order to satisfy our collaborators and confirm the identity of the inhibitory species, it was necessary to purify DAHP hydrazone without weeks-long lyophilization in the presence of formate. This will allow us to redetermine the $K_i$ value in the future and re-crystallize the complex to confirm the identity of the inhibitor species.

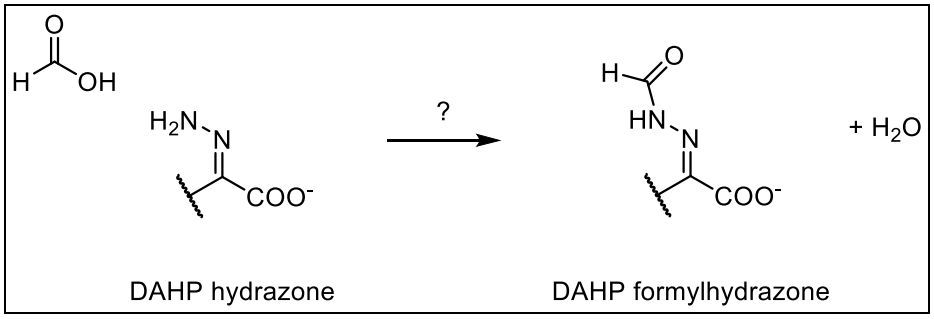


Figure 2.9: DAHP formylhydrazone

This reaction has not been observed experimentally, but the formylated product would match the observed electron density in the DAHPS·DAHP hydrazone crystal structure.

# 3 Transition state analysis of NeuB

## 3.1 Introduction

I performed TS analysis on NeuB by measuring multiple KIEs to understand its catalytic mechanism and to determine the TS structure, which will lead ultimately to the design of TS mimics based on the TS structure. $^{13}C$ KIEs were measured using the direct NMR method developed by Bennet's group[142], based on Singleton's method[138] as described previously. For example, to measure [3-$^{13}C$]KIE the 2-$^{13}C$ peak was monitored as the reporter isotope. Using a mixture of [2-$^{13}C$]- and [2,3-$^{13}C$]PEPs in the reaction mixture, the isotope ratio i.e.,$^{13}C/^{12}C$ at C3 was acquired continuously using quantitative $^{13}C$-NMR (**Figure 3.1**).

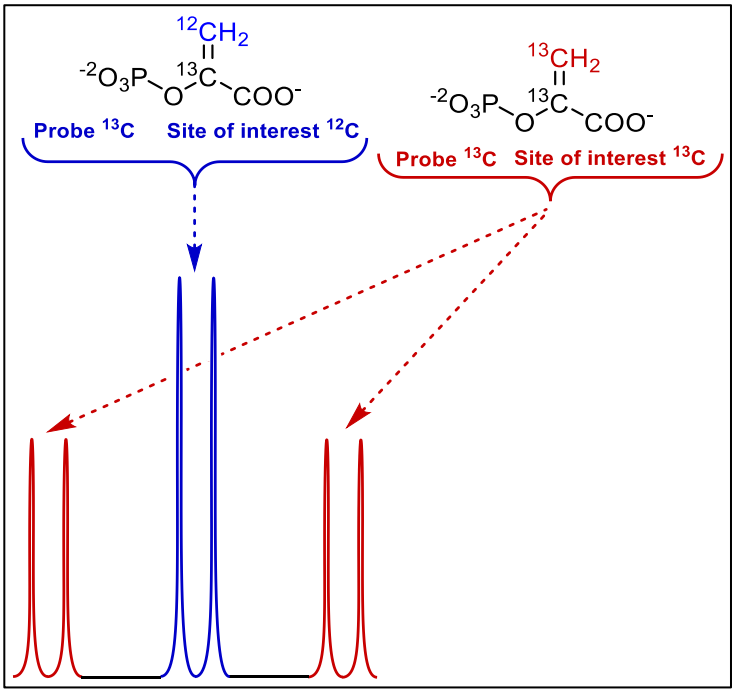


Figure 3.1: Measuring [3-$^{13}C$]KIE using quantitative $^{13}C$-NMR

The 3-$^{13}C$ KIE is measured by monitoring the 2-$^{13}C$ peak as the reporter isotope using a mixture of [2-$^{13}C$]- and [2,3-$^{13}C_2$]PEPs. 3-$^{13}C$ splits the 2-$^{13}C$ peak through one bond coupling with $^1J_{C\text{-}C}$ = 40 Hz, while $^{31}P$-$^{13}C$ coupling further splits the peaks with $^3J_{P\text{-}C}$ = 7 Hz.

This method was recently extended to using $^{31}P$ by Alvin Niu of the Berti lab to use [2-$^{18}O$]PEP to measure $^{18}O$ KIEs using $^{31}P$ nuclei as the reporter nucleus[146] (**Figure 3.2 a**). The $^{16}O/^{18}O$-induced chemical shift difference in $^{31}P$ NMR has been used previously to monitor positional isotope exchange[184, 185], ligand binding experiments [186, 187], and other mechanistic studies[188, 189], but to our knowledge, it has only been used once previously for high accuracy KIE measurements[190]. Part of this is likely due to $^{31}P$'s long relaxation times, which lengthens measurement times, and its sensitivity to metal ions (broadening or suppressing peaks). Alvin Niu demonstrated that it is possible to measure $^{18}O$ KIEs using $^{31}P$ NMR and to reduce the data collection time 9-fold by not allowing complete $T_1$ relaxation (**Figure 3.2 b**)[146].

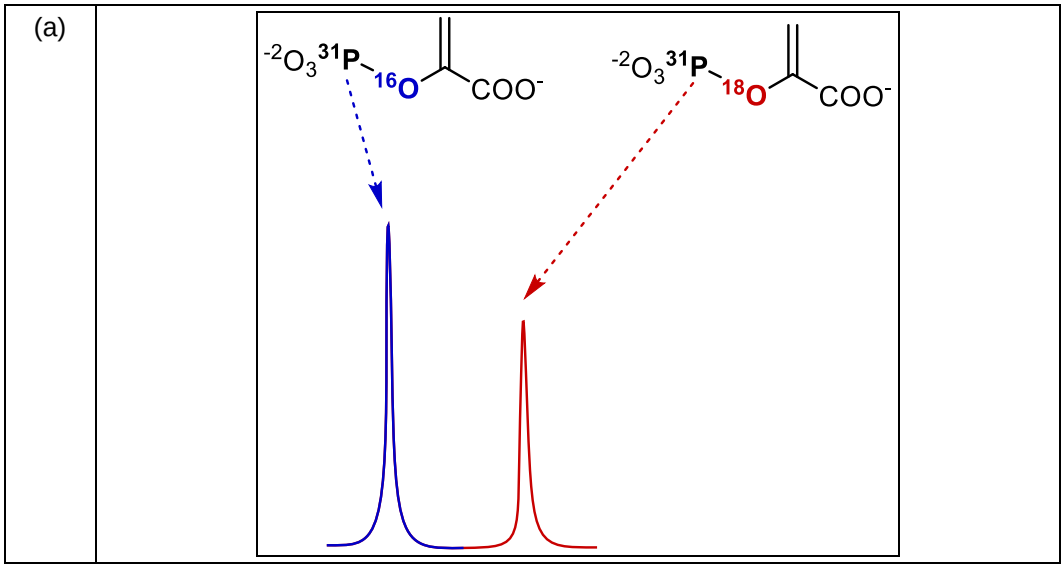

(b)

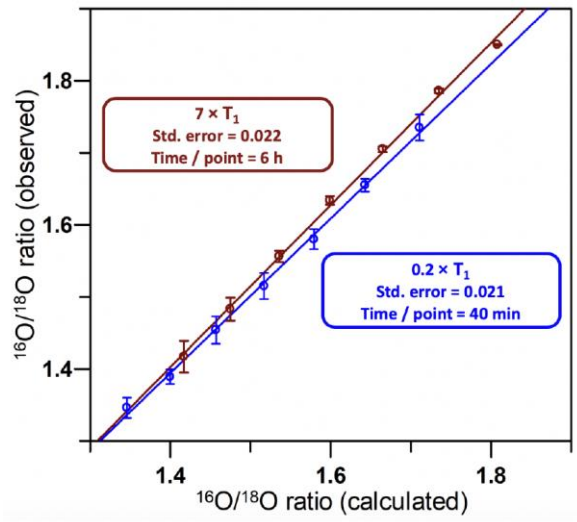


Figure 3.2: Quantitative $^{31}$P-NMR of [2-$^{18}$O]PEP

(**a**) $^{18}$O isotope ratio measurement using quantitative $^{31}$P NMR with a mixture of [2-$^{18}$O]- and [2-$^{16}$O]PEPs. (**b**) Standard curves of $^{16}$O/$^{18}$O ratios in labelled $P_i$ using conventional (complete) and incomplete relaxation pulse programs. Aliquots of $P^{16}O_4$ were added to $^{18}$O-labelled $P_i$ and spectra were collected using relaxation times of 7 × $T_1$ (red) or 0.2 × $T_1$. (blue). 7 × $T_1$ (119 s), 90° pulses, slope = 1.126 ± 0.022. 0.2 × $T_1$ (3.5 s), 30° pulses, slope = 1.073 ± 0.021[146]. The differences in slope would lead to a change of 0.05% in a 1% KIE (i.e., 1.0100 becomes 1.0105), an insignificant difference. (Figures from reference 146, used with permission from Alvin Niu, ©2020).

## 3.2 Materials and methods

### *3.2.1 Wild Type NeuB$_{H6}$*

The pET-30Xa/LIC plasmid encoding the *N. meningitidis* His$_6$-tagged *neuB* gene (NeuB$_{H6}$) was a kind gift from Martin Tanner (U. British Columbia)[15]. The plasmid was transformed into chemically competent *E.coli* DH5α cells, plated on agar plates containing 50 μg/mL kanamycin and incubated overnight at 37 °C. A single colony was introduced into 5 mL of lysogeny broth (LB) medium containing 50 μg/mL kanamycin and incubated at 37 °C overnight. The transformed cells were lysed, and the plasmid isolated using Thermo Scientific DNA Miniprep Kit. The plasmid was subsequently sequenced at the MOBIX sequencing facility (McMaster University). The purified plasmid was further transformed into *E. coli* BL21*(DE3)

cells, grown overnight in 50 mL LB medium with 50 μg/mL kanamycin at 37 °C, subcultured into 1 L LB containing 50 μg/mL of kanamycin and grown to a cell density of $OD_{600}$ ~ 0.6. Overexpression was induced by 1 mM isopropyl β-*D*-1thiogalactopyranoside (IPTG) and incubated for an additional 4 h. Cells were harvested by centrifugation, resuspended in 30 mM triethanolamine-HCl buffer (pH 7.5) and lysed using CelLytic B cell lysis reagent (Sigma-Alridch). The cell lysate was filtered through a 0.45 μm filter, and the supernatant was loaded onto a 1 mL pre-washed $Ni^{2+}$-charged Chelating-Sepharose Hi-trap (GE Life Sciences) column. The crude protein was purified using Elution Buffer A (30 mM triethanolamine, 10 mM imidazole buffer pH 7.5) and elution Buffer B (30 mM triethanolamine, 50 mM imidazole buffer pH 7.5) to remove unwanted proteins, then $NeuB_{H6}$ was eluted using elution Buffer C (30 mM triethanolamine, 500 mM imidazole buffer pH 7.5)[15]. The purified protein was dialyzed in 30 mM triethanolamine pH 7.5, 10% glycerol and 1mM tris(2-carboxyethyl) phosphine (TCEP) for 24 h. The purified protein was concentrated by ultrafiltration, flash frozen and stored at -80 °C. The protein concentration was determined using an $\varepsilon_{280} = 2.20 \times 10^4\ M^{-1}\ cm^{-1}$.

### *3.2.2 Wild type phosphoenolpyruvate synthetase (ppsA)*

A pET24b plasmid encoding phosphoenolpyruvate synthetase (ppsA) was a gift from Dr. David Jakeman (Dalhousie University).The plasmid was transformed into chemically competent *E.coli* DH5α cells, plated on agar plates containing 50 μg/mL kanamycin and incubated overnight at 37 °C. A single colony was introduced into 5 mL of lysogeny broth (LB) medium containing 50 μg/mL kanamycin and incubated at 37 °C overnight. The transformed cells were lysed, and the plasmid isolated using Thermo Scientific DNA Miniprep Kit. The plasmid was subsequently sequenced at the MOBIX sequencing facility (McMaster University). The purified plasmid was further transformed into chemically competent BL21(DE3) cells, plated on agar

plates containing 50 μg/mL kanamycin and incubated overnight at 37 °C. A single colony was introduced into 50 mL of lysogeny broth (LB) medium containing 50 μg/mL kanamycin and incubated overnight at 37 °C. The 50 mL overnight culture was transferred to 1 L of LB containing 50 μg/mL of kanamycin and grown at 37 °C to a cell density of $OD_{600}$ = 0.6. Overexpression of ppsA was induced by adding 0.2mM IPTG. It was incubated at 17 °C overnight. The cell pellet was resuspended in 35 mL of Buffer A (75 mM imidazole, 20 mM Tris-Cl, pH 8.0, 0.3 M NaCl) and protease cocktail inhibitor, and lysed in preliminary experiments by using CelLytic B (Sigma Aldrich). When this caused problems with protein activity, later preparations used a continuous cell-disruptor at 10,000 psi. The lysate was centrifuged at 8,000 rpm for 30 minutes at 4°C. The cell lysate was filtered through a 0.45 μm filter, and the supernatant was loaded onto a 1 mL pre-washed $Ni^{2+}$-charged Chelating-Sepharose Hi-trap (GE Life Sciences) column. The column was washed with 10 column volumes (CV) of Buffer A to remove non-specifically bound proteins and eluted with 5 × 10 CV aliquots of Buffer B (250 mM imidazole, 20 mM Tris-Cl, pH 8.0, 0.3 M NaCl). The eluted protein was examined by SDS-PAGE and dialyzed against 1 L of dialysis buffer (50 mM Tris-Cl, pH 8.0, 5% glycerol, 1 mM EDTA) over 48 h. The final concentration of ppsA was determined from $A_{280}$ using $\varepsilon_{280}$ = 69,720 $M^{-1}cm^{-1}$.

### *3.2.3 Rate assays*

The Malachite green/ammonium molybdate (MGAM) colorimetric assay[15] was used to measure the NeuB initial velocities ($v_0$) by following $P_i$ production. Typical reaction conditions were 500 nM NeuB with 3 mM PEP, 15 mM *N*-acetylmannosamine (ManNAc), 12.5 mM $MnCl_2$,100 μM TCEP, 0.1 mg/mL bovine serum albumin (BSA) in 50 mM Tris-acetate, pH 7.0,

in 300 µL. Aliquots of 20 µL of reaction mixture were added to 96 well plate containing 100 µL MGAM solution and 80 µL dd$H_2O$ every 60 s and each reaction was quenched with 10 µL of 34% trisodium citrate solution after 90 s. Some rate assays were run under the same conditions as the KIE reactions, namely higher PEP concentrations and using a diamagnetic divalent metal ion:15 mM PEP, 20 mM ManNAc, 200 – 500 nM NeuB, 1 mM ultrapure $MgCl_2$ (99.99% trace metal basis), 100 µM TCEP, 0.1 mg/mL BSA in 50 mM Tris-acetate, pH 7.0, in 300 µL. All buffers and substrates were treated with Chelex 100 (BioRad) except for $MgCl_2$ and enzymes.

### *3.2.4 Measuring competitive KIEs*

KIEs were measured competitively using quantitative $^{13}C$ and $^{31}P$ NMR. **Equation 11Equation 14** were used to fit the competitive KIEs from the isotope ratio ($R_i$ or $RP_i$) **Equation 12** vs. extent of reaction ($F_1$) **Equation 13** data on the reactant and product, respectively[142, 146, 156].

#### *3.2.4.1 Labelled PEP synthesis*

**[2-$^{13}$C]-, [3-$^{13}$C]-, [2-$^{13}$C,2-$^{18}$O]-, and [2-$^{18}$O]PEP syntheses**. $^{13}C$-labelled PEPs were synthesized enzymatically by dissolving 20 mM $^{13}C$ sodium pyruvate, 20 mM $MgCl_2$, 20 mM ATP, and 300 µL of ppsA in 2 mL of 300 mM Tris-acetate, pH 8.4 at 25 °C for 4 h (**Figure 3.3**) (**Table 3.1**). The pH was checked periodically during the reaction and re-adjusted with KOH as necessary.

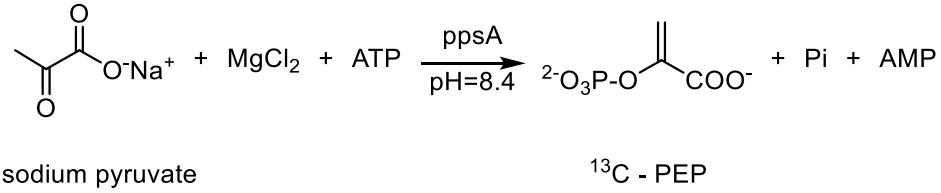

Figure 3.3: $^{13}C$ PEP synthesis

Reaction of sodium pyruvate with 20 mM ATP in presence of 300 µL ppsA and 20 mM MgCl2 at pH 8.4 to give 20 mM PEP, 20 mM AMP and 20 mM Pi.

The extent of reaction was followed by determining the concentrations of residual sodium pyruvate and synthesized PEPs using LDH assay and PK assays, respectively. In the LDH assay, pyruvate is reduced to lactate with a concomitant oxidation of NADH to $NAD^+$, which is detected by a decrease in $A_{340}$ as NADH is consumed, with $\Delta\varepsilon_{340} = 6220\ M^{-1}\ s^{-1}$.[180] The pyruvate kinase reaction converts PEP + ADP to pyruvate + ATP, and the pyruvate then enters the LDH reaction. A 96 assay well plate contained 10 µL of 360 times diluted labelled PEP, 400 nmols of adenosine diphosphate (ADP), 60 nmoles of NADH in 300 µL volume of (50 mM of 0.05 M Tris-HCl, pH 7.6 containing 0.12 M KCl and 0.062 M $MgSO_4$). To start the reaction, 5 mg/mL LDH was added which catalyzed the reduction of the unreacted sodium pyruvate to lactate and NADH oxidized to $NAD^+$. Addition of 1.3 µL of pyruvate kinase (PK) converts PEP and ADP to pyruvate and ATP.

[2-$^{18}O$]PEP and [2-$^{13}C$,2-$^{18}O$]PEP was synthesized using the same method except in $H_2{}^{18}O$ using unlabelled sodium pyruvate and [2-$^{13}C$] sodium pyruvate, respectively (Table 3.1). $H_2{}^{18}O$ was recovered via lyophilization and reused for future syntheses. The reaction mixture was dissolved in 2 mL $ddH_2O$. ppsA was removed by heating the PEP reaction mixture at 94 °C for 5 min, then removing precipitated protein by centrifugation. Labelled PEPs were initially purified using ion-paired reverse phase HPLC. The labelled PEP (500 µL) was loaded onto two C18 HPLC columns (Waters, 300 × 7.8 mm ID) connected in series and washed with 25 mM *N*,*N*-diisopropylethylamine acetate (DIPEA), pH 6.3 at a flow rate of 2 mL/min and $A_{232}$ detection. Labelled PEP was concentrated to 5 mL by rotary evaporation and injected onto a cation exchange column volume of 12 mL, SP-Sepharose (GE Life Sciences) in the $H^+$ form, to

remove DIPEA cations. This was time consuming as we could only inject 500 µL and the column required extensive washing before each injection. Labelled PEPs were subsequently purified by anion exchange chromatography on a 12 mL Q-Sepharose column and eluted with a gradient of 0.1 M to 0.8 M ammonium formate over 60 min at 2 mL/min with $A_{232}$ detection. Fractions containing PEP were pooled and lyophilized to < 4 mL, quantified using the LDH/PK assay, and injected onto a $H^+$-charged SP-Sepharose with a 120 mL column volume and eluted with water over 30 min at 3 mL/min to remove ammonium ions. The purified PEPs were quantified using LDH/PK assay and confirmed using $^{13}C$ and $^{31}P$ NMR. Labelled PEPs were stored at −20 °C. [2,3-$^{13}C$]PEP was purchased from Cambridge Isotope Labs (Tewksbury, MA).

Table 3.1:Starting material used for synthesizing $^{13}C$- and $^{18}O$-labelled PEPs.

| Starting material | Product |
|---|---|
| [2-$^{13}C$]sodium pyruvate | [2-$^{13}C$]PEP |
| [3-$^{13}C$]sodium pyruvate | [3-$^{13}C$]PEP |
| Sodium pyruvate (unlabelled) in $H_2{}^{18}O$ | [2-$^{18}O$]PEP |
| [2-$^{13}C$]sodium pyruvate in $H_2{}^{18}O$ | [2-$^{13}C$,2-$^{18}O$]PEP |

### *3.2.4.2 Measuring KIEs using $^{13}C$ and $^{31}P$ NMR*

Paramagnetic metal ions interfere with NMR spectra because the unpaired electrons increase the longitudinal relaxation rates ($T_1$) of nearby nuclei, making the peaks broader. As $MnCl_2$ is diamagnetic, $MgCl_2$ was used instead. To ensure that the $MgCl_2$ was responsible for the rate, ultrapure $MgCl_2$ was used. To decide the final KIE reaction conditions, NeuB reaction was run and followed using both the MGAM assay and NMR every 2 h for 6 – 8 h. The final reaction mixtures for KIE measurement contained a total PEP concentration of 10 mM, with 20 mM ManNAc, 1 mM $MgCl_2$, 0.1 mM TCEP, 250 – 500 nM NeuB (freshly thawed from -80 °C storage), 0.1 mg/mL BSA, and 10% $D_2O$ in 50 mM Tris-acetate, pH 7.0 in a 600 µL total

volume. For $^{13}C$ KIE measurements, $^{13}C$ methanol was used initially as the internal reference; however, it was later replaced by the Tris peak at ~60 ppm since the reaction mixture already contained 50 mM Tris-acetate and it is not volatile, unlike methanol. For 2-$^{13}C$ KIE measurements, the reaction mixture contained 5 mM [2,3-$^{13}C_2$]PEP and 5 mM [3-$^{13}C$]PEP. For 3-$^{13}C$ KIE measurements, the reaction mixture contained 5 mM [2,3-$^{13}C_2$]PEP and 5 mM [2-$^{13}C$]PEP. For 2-$^{18}O$ KIE measurements using $^{13}C$ NMR, 5 mM [2-$^{13}C$]PEP and 5 mM [2-$^{13}C$,2-$^{18}O$]PEP were used.

Prior to each KIE measurement, a small-scale KIE reaction in 50 µL volume was run at the same concentration as the NMR reaction using MGAM assay to ensure the enzyme was fully active. The KIE reaction mixtures were initially degassed for 30 min and kept under vacuum for 1 h for 3 cycles, as dissolved $O_2$ is paramagnetic and can shorten longitudinal relaxation times and lead to peak broadening. This was later discontinued as it was found that degassing did not improve the S/N. The samples were run on a Bruker 600 MHz spectrometer under the conditions in **Table 3.2** using a 30° pulse, a spectral width of 236 ppm, and a delay time (d1) of 0.5 s. To suppress NOEs, inverse-gated $^1H$ decoupling was used. The "autoshim" function in TopSpin was used after every spectrum to maintain symmetrical peak shapes. For each KIE measurement, a $^{13}C$ NMR spectrum was obtained before adding the enzyme, i.e., at time t = 0 h at an acquisition time (AQ) of 3.7 s to find $T_2$* (**Equation 9**). From this, the acquisition period, AQ, was adjusted to 5 × $T_2$*, and all subsequent spectra were collected using these parameters (**Table 3.2).** NeuB was added and $^{13}C$-NMR was collected every 30 – 35 min on the live reaction until its completion. The NMR data was processed using Bruker software TopSpin. The data was autophased, baseline corrected, FIDs were zero-filled to 512k and a Lorentzian multiplication using lb between 0.2 - 0.6 was applied to improve the S/N.

Table 3.2: Acquisition parameters for measuring KIEs with $^{13}C$ NMR

| Flip angle | Number of scans (NS) per spectrum | TD | O1p (ppm) | 1SW (ppm) | AQ (s) | Delay time (d1, s) |
|---|---|---|---|---|---|---|
| 30° | 512 | 262144 | 109 | 236 | 3.7 s | 0.5 |

For 2-$^{18}O$ KIE measurements using $^{31}P$ NMR, the reaction mixture was the same as above but using 5 mM [2-$^{18}O$]PEP and 5 mM unlabelled PEP, and 60 mM glyphosate (*N*-(phosphonomethyl)glycine) as an internal $^{31}P$ standard for determining the extent of reaction, $F_1$. Initially, the $^{16}O$- and $^{18}O$ PEP peaks in the 2-$^{18}O$ KIE reaction mixture had poor peak resolution. A number of solutions were tested to alleviate this problem, including adding substoichiometric EDTA to chelate any contaminating paramagnetic metal ions. This improved the peak resolution without affecting the reaction rate in small-scale reactions as monitored using the MGAM assay. $^{18}O$ KIEs using $^{31}P$ NMR were therefore measured in reaction mixtures containing 0.5 mM EDTA. As EDTA was successful in improving peak resolution, it was also added to the 3-$^{13}C$ KIE reaction mixtures to improve peak shape.

The data acquisition method used 30° pulses, a spectral width of 40 ppm, and a delay time, d1, of 0.5 s. Inverse-gated $^{1}H$ decoupling and autoshimming were used as for $^{13}C$ spectra. A $^{31}P$-NMR spectrum was obtained without enzyme, i.e., at time t = 0 h, with an acquisition time (AQ) of 2.55 s. From this, AQ was adjusted to obtain $5 \times T_2^*$ (**Equation 9**). NeuB was added and $^{31}P$-NMR was collected every 30 – 35 min on the live reaction until its completion. The $^{31}P$ NMR data were processed similarly to the $^{13}C$ NMR data.

Table 3.3: Acquisition conditions parameters for measuring KIEs with $^{31}P$ NMR.

| Flip angle | Number of scans (NS) per spectrum | TD | O1p (ppm) | 1SW (ppm) | AQ (s) | Delay time (d1, s) |
|---|---|---|---|---|---|---|

| | | | | | | |
|---|---|---|---|---|---|---|
| 30° | 600 | 49152 | 0 | 40 | 2.55 | 0.5 |

$^{13}C$ and $^{31}P$ KIEs were calculated by measuring the change in isotope ratios at multiple points as the reaction proceeded from 0% to ~80% reaction[142]. The isotopologue ratios $R_i$ or $RP_i$ and $R_0$ at t = i and t = 0, i.e.,$^{13}C/^{12}C$ and $^{18}O/^{16}O$, were measured by fitting the normalized peak intensities of PEP (reactant) and NeuNAc (product) using Voigt peak deconvolution in the program PeakFit (Systat Software, Inc.). The calculated peak areas were converted to isotope ratios, $R_i$ or $RP_i$ (**Equation 12**). $F_1$ was calculated from the ratio of the PEP peak to the Tris ~60 ppm peak as the internal reference in the $^{13}C$ NMR spectra, and glyphosate in $^{31}P$ spectra (**Equation 13**).

Experimental KIEs were found by fitting the reactant isotope ratios ($R_i/R_0$) vs. $F_1$ values to **Equation 11**[142] and the product isotope ratios, $RP_i/RP_\infty$ vs. $F_1$ to **Equation 14**. Chan et al.'s equation using the isotope ratio ($R = {}^{13}C/{}^{12}C$) and extent of reaction ($F_1$) was modified to fit the KIE from isotope ratios in the residual substrate (**Equation 15 & Equation** 16)[142].

Equation 15

$$R_i = 1 - F_1^{\frac{1}{(KIE-1)}} \times R_0$$

Equation 16

$$RP_i = \frac{\left(1 - (1 - F_1)^{\frac{1}{KIE}}\right) \times RP_\infty}{F_1}$$

### *3.2.4.3 Ninhydrin assay*

In some early KIE measurements, NeuB lost activity over the course the reaction. This was eventually traced to high ammonium formate concentrations in the labelled PEPs.

Thereafter, labelled PEPs were routinely assayed for $NH_4^+$ with the ninhydrin assay to check for the presence of ammonium formate. The assay reaction mixture contained different volumes (0 to 8 µL) of labelled PEP and 30 µL of 20 % ninhydrin in EtOH, made to a final volume 300 µL in 25 mM sodium bicarbonate, sodium carbonate buffer (pH 10). Reaction mixtures were allowed to stand for 20 min at 25 °C. The $A_{470}$ values were read and the concentration of ammonium formate in the labelled PEP was calculated. This was discontinued after the PEP purification method was changed to include a larger cation exchange column to completely remove ammonium formate.

#### *3.2.4.4 Integration and deconvolution*

In principle, numerical integration is the easiest method of determining peak areas. It involves adding together the height of each "slice" of a peak of interest. Accurate numerical integration requires fulfilling a number of criteria, including separation of the peaks of interest by at least 20 × line width, which was not possible in this study[146]. Therefore, we used Voigt peak deconvolution. Deconvolution involves fitting the experimental spectrum to a defined peak shape, then using the fitted values of peak height, width and asymmetry to analytically calculate the peak area. The main advantage of peak deconvolution is the ability to use it with overlapping peaks. Ideally, liquid NMR resonances have a Lorentzian shape, but practically, this is difficult to achieve as the NMR spectrometer itself also contributes to the peak shape, as the spectrometer's contribution has a Gaussian peak shape[191, 192]. Under this circumstance, Voigt deconvolution, that is, a mixed Lorentzian-Gaussian peak shaping function, is commonly used to fit peaks, especially asymmetrical peaks caused by poor shimming[137,138], or small chemical shift differences.

### *3.2.5 Computations*

All quantum mechanical calculations were performed in Gaussian 16[193] using hybrid density functional theory (DFT) with Becke's exchange functional[194], and Perdew and Wang's correlation functional[195] with either a 6-31G basis set (B3PW91/6-31G) or a 6-31+G** basis set (B3PW91/6-31+G**). This level of theory yields more reliable vibrational frequencies than other levels of theory with comparable computational cost[160, 196]. Solvent effects were modeled in some structures with a conductor-like polarizable continuum model (CPCM)[197] using a dielectric constant equal to water's. Early computational studies examined the potential energy surface by performing constrained optimizations with fixed bond lengths for the bonds being formed or broken in simplified computational models of THI formation and breakdown. This provided information on plausible reaction mechanisms and identified initial guesses for TS optimization calculations. TS optimizations were performed at the same level of theory, generally using the QST3 keyword[198]. QST3 optimizations require reactant and product structures and an initial estimate of the TS structure as input, then finds the optimized TS structure. Once several TS structures for THI formation and breakdown had been found, Dr. Berti further varied the computational models to generate other computational TS structures. For simple structural variations it was often possible to find new TS structures using the much simpler "opt=ts" keyword. In these cases, it was not necessary to run a full QST3 optimization or potential energy surface scan.

The computational KIEs for each TS structure were calculated using the program QUIVER[199] to converts a molecule's vibrational frequencies to the isotopic partition functions ($Q$) for its isotopologues, with the Cartesian force constants scaled by 0.9139 (= $0.956^2$) to match

harmonic frequency scaling of 0.956[196]. *Q* is essentially 1/KIE or 1/EIE for the atom of interest relative to a free, unbound atom (**Equation 17**).

Equation 17

$$KIE = Q_{reactant}/Q^{\ddagger} \times {}^{light}\nu^{\ddagger}/{}^{heavy}\nu^{\ddagger} \times Q_{Bell}$$

where $Q_{reactant}$ and $Q^{\ddagger}$ are the partition functions calculated with the 3N-6 normal vibrations modes of the reactant, and 3N-7 normal modes of the transition state, respectively; ${}^{light}\nu^{\ddagger}$ and ${}^{heavy}\nu^{\ddagger}$ are the reaction coordinate (imaginary) frequencies, and $Q_{Bell}$ is the Bell tunneling correction (Equation 18)[200, 201].

Equation 18

$$Q_{Bell} = \frac{|{}^{light}u^{\ddagger}|/2 \,/\, \sin\left(|{}^{light}u^{\ddagger}|/2\right)}{|{}^{heavy}u^{\ddagger}|/2 \,/\, \sin\left(|{}^{heavy}u^{\ddagger}|/2\right)}, \; u^{\ddagger} = h\nu^{\ddagger}/k_B T$$

Quantum tunneling corrections are important in heavy atom KIEs, particularly when the KIE > 1.01[202], even when the tunneling contribution is small[203]. The match between frequencies generated by QUIVER from the Cartesian force constants, and the scaled Gaussian 16 frequencies was checked routinely.

## 3.3 Results

### *3.3.1 ppsA*

ppsA was expressed and purified, and its purity was verified by SDS-PAGE (**Figure 3.4**). Initially, ppsA was lysed using the cell disruptor at 10, 000 psi in a common facility in MDCL; however, during the Covid-19 lockdowns, cells were chemically lysed in the Berti lab using

CelLytic B (Sigma Aldrich), as had been used previously for other enzymes. A small-scale lysis was done prior to the full-scale cell lysis process. In the first attempt at purifying ppsA after CelLytic B cell lysis, the protein eluted earlier than expected from the $Ni^{2+}$-Sepharose column, in the flow-through and with Buffer A. Neither the flowthrough nor the Buffer A eluate had any ppsA activity. The plasmid was sequenced, and it was observed that the $His_6$-tag was not present in the sequence. Another batch of ppsA plasmid was purified using the DNA miniprep kit and the sequence was confirmed. The second attempt at purifying ppsA using CelLytic B failed again for the same reason. This suggested that the component of the lysing buffer was denaturing the protein. Finally, ppsA was lysed using the cell disruptor and purified using the Ni-Sepharose column. The SDS-PAGE (**Figure 3.4**) confirmed a successful purification of ppsA with Buffer B. The purified protein showed high enzyme activity.

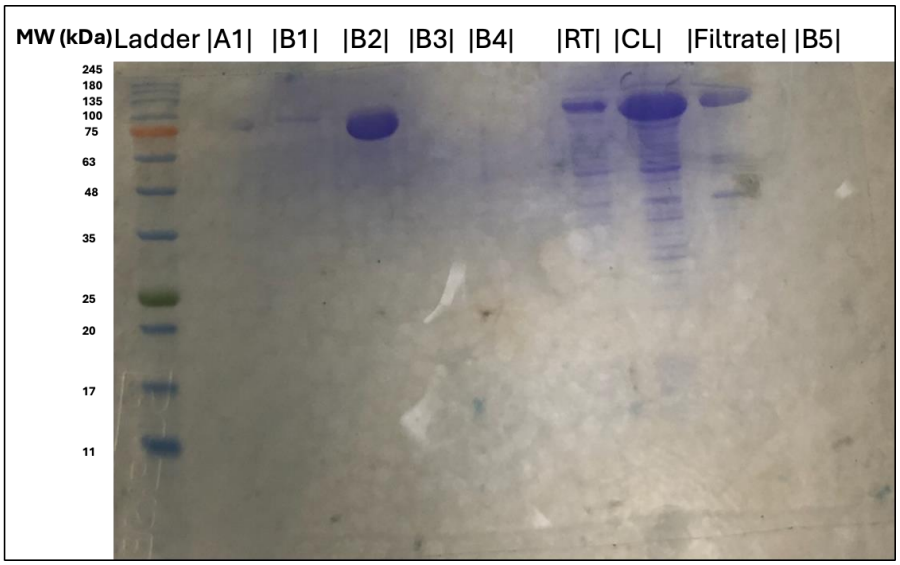


Figure 3.4: SDS-PAGE of ppsA

Lanes (left to right): Ladder: Protein standards; Lane A1: wash buffer; Lanes B1 – B4: Elution buffer; Lane RT: column run through; Lane CL: cell lysate, Lane cell lysate after 0.2 µm filtration; Lane B5: Elution buffer.

### *3.3.2 NeuB*

The $NeuB_{H6}$ plasmid was purified using DNA MINIprep kit (Qiagen) and sequenced to check its identity, then NeuB was expressed. The cells were lysed using CelLytic B cell lysis reagent (Sigma-Alridch). NeuB was purified using a $Ni^{+}$-charged Chelating-Sepharose column (**Figure 3.5**), eluted using 500 mM imidazole (Elution Buffer C), flash frozen and stored at -80 °C.

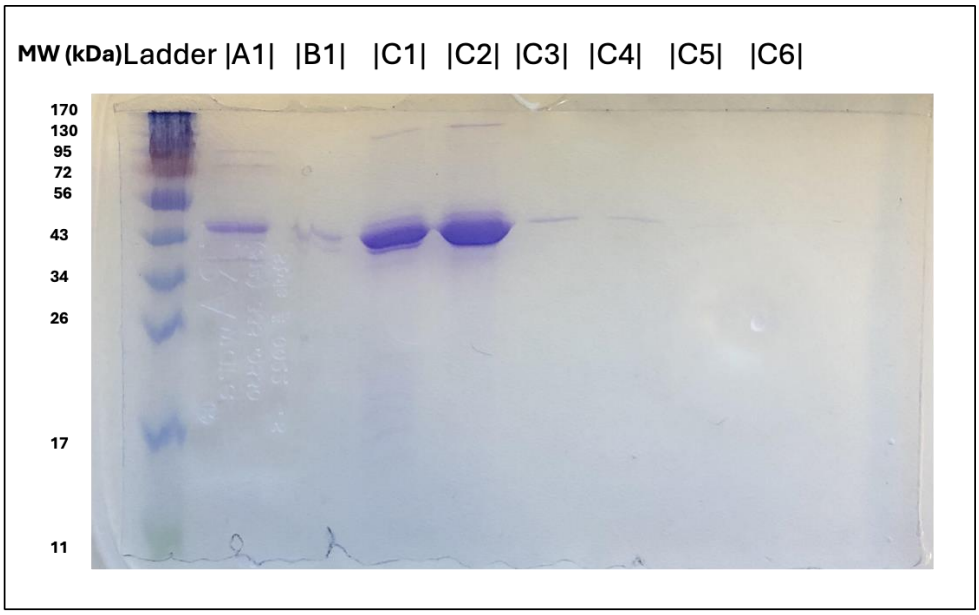


Figure 3.5: SDS-PAGE of NeuB

Lanes: Ladder: Protein standards; Lane A1: Wash buffer A; Lane B1: Wash buffer B; Lane C1 – C6: Elution buffer C.

### *3.3.3 Labelled PEPs*

Labelled PEPs were synthesized and purified as described in Materials & Methods section. The identities of the labelled PEPs were confirmed using $^{13}C$ and $^{31}P$ NMR, and their concentrations determined using the PK/LDH assay.

### *3.3.4 Experimental KIEs*

The 2-$^{13}$C, 3-$^{13}$C, and 2-$^{18}$O PEP KIEs in the NeuB reaction were measured using $^{13}$C- and $^{31}$P reporter nuclei. Competitive KIEs[204], wherein both the light and heavy isotopologues are present in the same reaction mixture, reflect the mechanism up to and including the first irreversible transition state[205], or if there are partially irreversible steps, the KIEs encompass all transition states leading up to the first fully irreversible step[205].

Experiments were run to determine whether KIEs could be measured using continuous monitoring of the isotope ratios in a live reaction in the NMR tube, or whether a single-point measurement (i.e., at a single $F_1$ value) would be required[151]. Continuous monitoring has the advantage that the change in isotope ratio can be observed as the reaction proceeds (**Figure 3.6**) and if the experimental data fit the expected curve (Equation 15Equation 16), there is greater confidence in the experimental KIEs. Conversely, since the enzyme must remain active in the NMR tube for multiple hours, the reaction must run predictably without stalling, and the S/N must high enough to give reliable isotope ratios with limited data collection times. A single point measurement, as traditionally used in NMR, scintillation counting and mass spectrometric methods, allows data to be collected as long as needed to achieve sufficient S/N, but lacks $R_i/R_0$ vs. $F_1$ data. This makes the experiments more difficult to troubleshoot[152, 204].

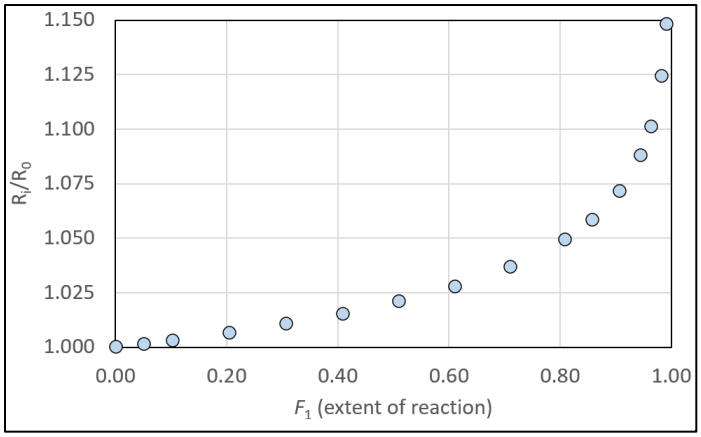


Figure 3.6: Plot of $R_i/R_0$ vs. $F_1$

The variation in isotope ratio, $R_i/R_0$, as a function of the extent of reaction, $F_1$, is fitted to equation **15** to determine the experimental KIE. In this hypothetical example, KIE = 1.030.

Small-scale test KIE reactions were run using the MGAM assay, and simultaneously, the enzymatic reaction was run in the NMR tube under the same reaction conditions and monitored every 2 h until the reaction neared completion. These experiments showed that KIE measurement using continuous monitoring of the isotopologue ratio was possible, but four problems needed to be solved:

(1) The reaction rate with labelled PEPs was unpredictable, sometimes running too fast, and sometimes not at all. This was eventually traced to NeuB being sensitive to high residual formate from the anion exchange purification of labelled PEPs using an ammonium formate gradient. As formate could not be quantified directly, the ninhydrin assay was used to quantify the ammonium ions to indirectly determine [formate]. From the rate assays, [formate] $\geq$ 0.8 M inhibited the NeuB-catalyzed reaction. The ninhydrin assay was introduced to routinely check labelled PEPs for ammonium formate. This assay was run until the source of formate was traced back to the use of a smaller 20 mL SP-Sepharose column which had lower resin capacity to exchange all the ammonium ions. Therefore, we replaced it by a 120 mL-SP Sepharose column that allowed for the easy exchange of all the ammonium ions from the labelled PEP. To ensure

that all the ammonium ions were exchanged, we also lyophilized the labelled PEP reaction mixture post the Q-Sepharose column for longer hours before injecting it on the SP-Sepharose column.

(2) NeuB stock solutions lost activity over time. It became standard practice to run small scale test reactions at the same concentrations as the NMR reaction immediately beforehand to ensure that the enzyme was fully active, and that residual ammonium formate was not interfering with the reaction.

(3) The NMR peak shapes became asymmetrical after repeated 30 min spectra as the reaction progressed. Automatic shimming during $^{13}C$ NMR spectrum acquisition was added, plus manual re-shimming every few hours.

(4) $MgCl_2$ at 1 mM resulted in broader peaks and poorer resolution, even using ultrapure $MgCl_2$ (99.99% trace metal basis). Adding 0.5 mM EDTA to the reaction mixture, which still contained 1 mM $MgCl_2$ did not affect the reaction rate, but significantly improved the peak shape. The fact that sub-stoichiometric EDTA improved the spectrum suggests that trace paramagnetic metal ions were interacting with PEP's phosphate group and affecting its peak shape. KIEs were measured under these conditions thereafter.

#### *3.3.4.1 Measuring 3-$^{13}C$ KIEs*

The 3-$^{13}C$ KIE was measured using a mixture of [2-$^{13}C$]- and [2,3-$^{13}C$]PEPs and monitoring the reactant PEP C2 peaks at 149.6 ppm, and the product NeuNAc C2 peaks at 96.4 and 97.2 ppm. The other minor forms of NeuNAc in solution, namely the acyclic, enol, and keto hydrate, were not observed and would not have affected the observed isotope ratios[206]. The NMR

data was processed on TopSpin. The data was autophased using the command 'apkf' over the range 152 to 148 ppm. The spectrum was baseline corrected, zero-filled using 512k or 1024k points, and 'lb' was adjusted to 75% of the peak width at half height[154]**(Figure 3.7).**

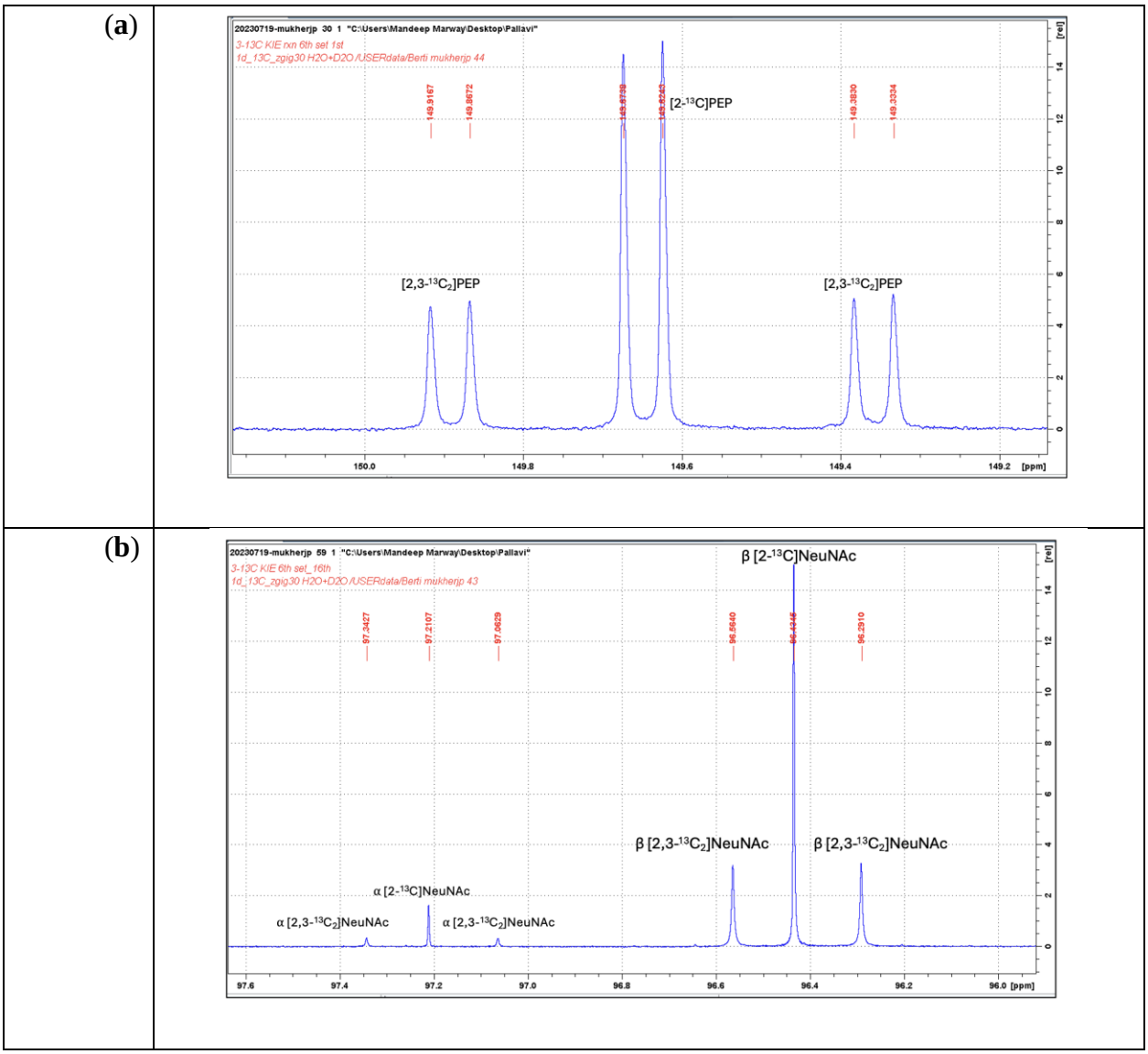


Figure 3.7: $^{13}$C-NMR of the NeuB 3-$^{13}$C KIE reaction

(**a**) Substrate peaks, with [2,3-$^{13}C_2$]PEP at 149.92 & 149.86 ppm and 149.38 & 149.33 ppm and [2-$^{13}$C]PEP at 149.67 & 149.62 ppm. (**b**) The product peaks of α- and β-anomers[207] of [2-$^{13}$C]NeuNAc at 97.34, 97.21 & 97.063 ppm, and 96.56, 96.43 & 96.30 ppm.

The $^{13}C/^{12}C$ isotope ratio ($R_i$) was measured in the reactant and product by calculating the peak areas for the reactant, product and Tris (internal reference) using peak deconvolution in the

program PeakFit (**Equation 12**). The extent of the reaction ($F_1$) was calculated using the peak areas for the light isotopologue and Tris (**Equation 13**). Fitting the isotope ratio data to (**Equation 15 & Equation** 16**)** gave an overall large, normal 3-$^{13}$C KIE of 1.023 ± 0.002 (**Table 3.4**). A typical progress curve of isotope ratio versus $F_1$ is shown for reactant and product peaks (**Figure 3.8**).

| | |
|---|---|
| (**a**) | 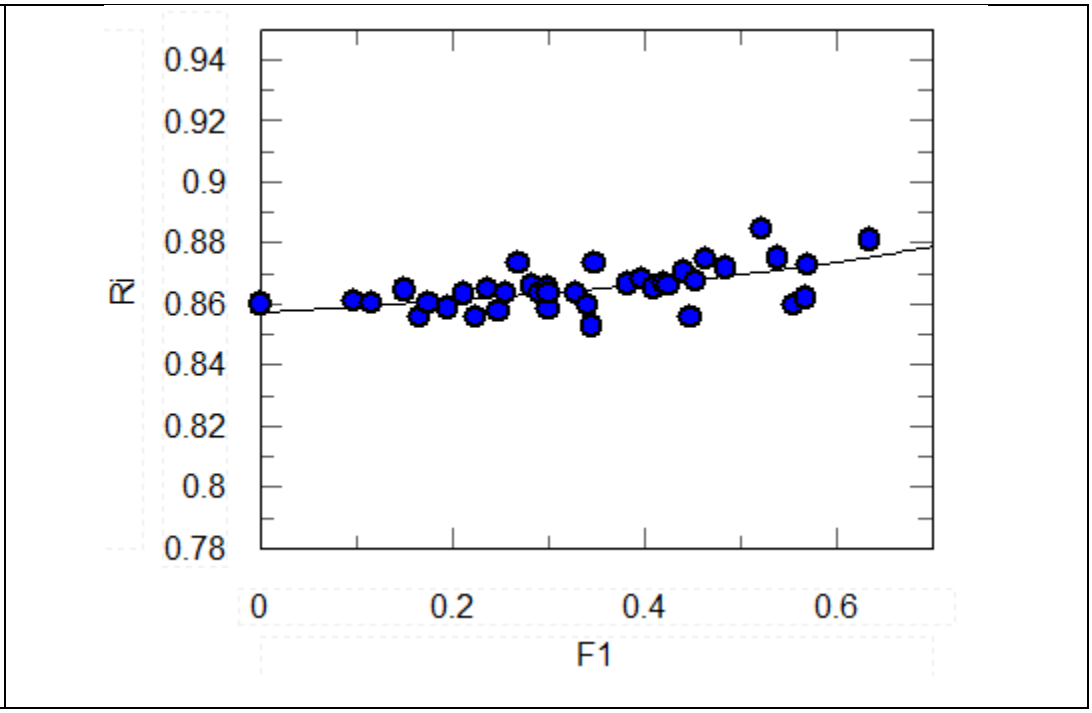 |

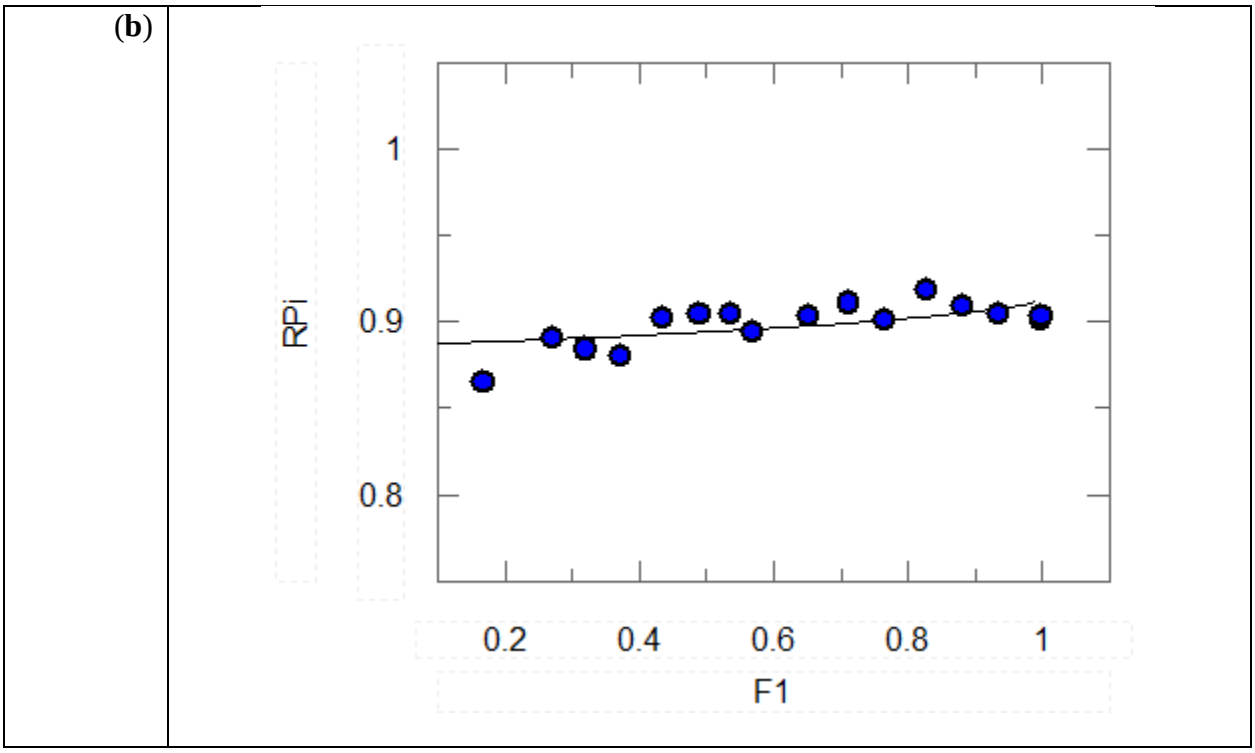


Figure 3.8: 3-$^{13}$C KIE measurements: isotope ratios vs. extent of reaction

Isotope ratios for 3-$^{13}$C KIE measurement showing (a) $R_i$ vs $F_1$ for the PEP reactant and (b) $RP_i$ vs. $F_1$ for the NeuNAc product.

Table 3.4 3-$^{13}$C Experimental KIEs

| | 3-$^{13}$C KIEs[a] | |
|---|---|---|
| Experiment no. | Reactant (**Equation 15**) | Product (**Equation 16**) |
| 1 | 1.0215 ± 0.005 | 1.0295 ± 0.027 |
| 2 | 1.0212 ± 0.004 | 1.0246 ± 0.017 |
| 3 | 1.0204 ± 0.004 | 1.0209 ± 0.009 |
| Mean (± 95% C. I.) | 1.023 ± 0.002 | |

a For individual experiments, the reported experimental error is the standard error on the fitted KIE value in Equation 15 & 16. The overall experimental error is the 95% confidence interval on the mean of all measurements.

A normal 3-$^{13}$C KIE indicates that THI formation is the first irreversible step of the NeuB reaction, i.e., the C3 of PEP is forming a bond with C1' of ManNAc at the transition state (**Figure 3.9**). An inverse KIE would have been expected if the transition state was water attack on the cationic intermediate during THI formation, or if it was THI breakdown. This is because

C3 would become more vibrationally constrained upon being converted from $sp^2$-hybridization with planar geometry in the reactant to $sp^3$-hybridization with tetrahedral geometry in the intermediates.

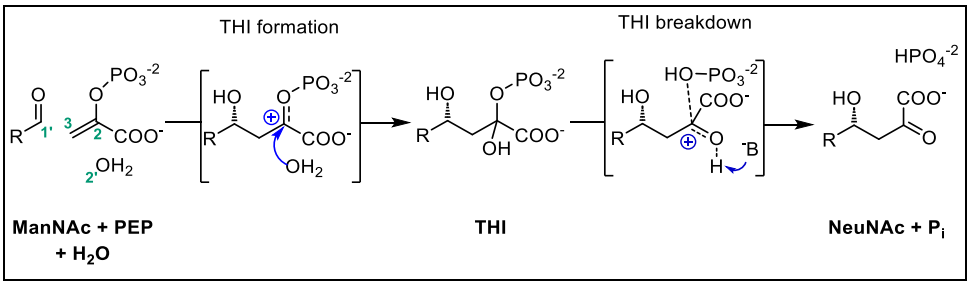


Figure 3.9. Simplified model of the NeuB catalytic reaction

Simplified mechanisms for the NeuB-catalyzed reaction between PEP and ManNAc to form NeuNAc and $P_i$.

### *3.3.5 Measuring 2-$^{13}$C-KIEs*

The 2-$^{13}$C KIE was measured using a mixture of [3-$^{13}$C]- and [2,3-$^{13}C_2$]PEPs (**Figure 3.10).** The 2-$^{13}$C KIE data was processed and KIE calculated like the 3-$^{13}$C KIE data except using lb = 0 & 0.2 (**Table 3.5**)

(a)

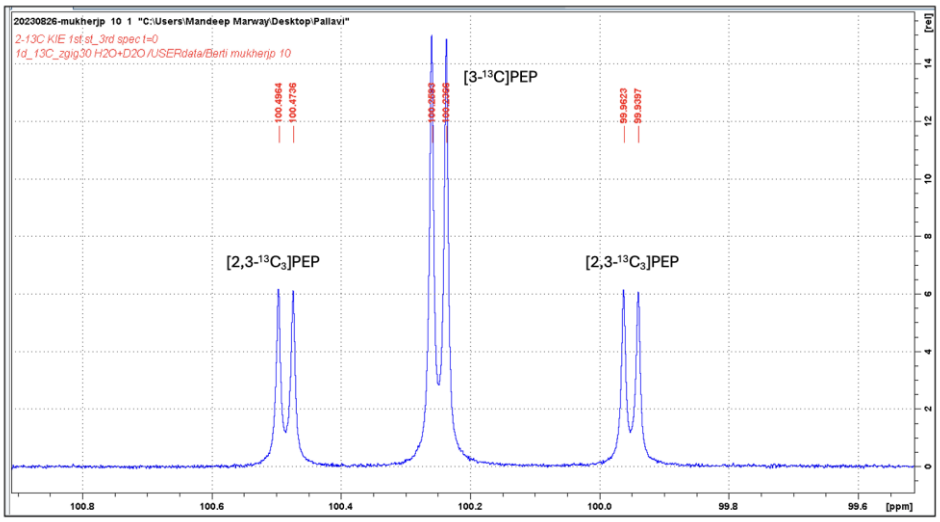

(b)

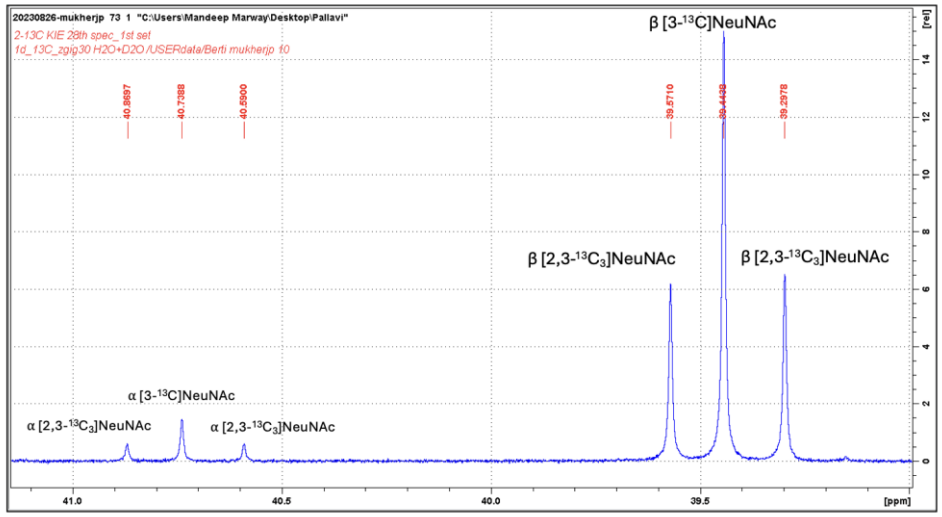


Figure 3.10: $^{13}$C-NMR of the 2-$^{13}$C KIE reaction mixture

(**a**) Substrate peaks, [2,3-$^{13}C_2$]PEP at 100.496 & 100.473 ppm & 99.96 & 99.94 ppm, and [3-$^{13}$C]PEP at 100.25 & 100.24 ppm, (**b**) Product peaks of α-anomers of [2,3-$^{13}C_3$]NeuNAc at 40.87 & 40.59 ppm, [3-$^{13}$C]NeuNAc at 40.74 ppm, and β-anomers of [2,3-$^{13}C_3$]NeuNAc 39.52 & 39.30 ppm, and [3-$^{13}$C]NeuNAc at 39.44 ppm.

Three KIE reactions, fitting both substrate and product isotope ratios to give six independent 2-$^{13}$C KIE measurements gave an inverse value of 2-$^{13}$C KIE = 0.994 ± 0.007 (**Table 3.5, Figure 3.11**). The slightly inverse 2-$^{13}$C KIE indicates that C2 is not part of the reaction coordinate, i.e., that the C2−O2' bond is not in the process of being formed. A large, inverse KIE would be expected during THI breakdown (see Section 3.3.7.2), so this KIE is also not consistent with THI breakdown being the first irreversible step.

Table 3.5: 2-$^{13}$C Experimental KIEs

| | 2-$^{13}$C KIEs [a] | |
|---|---|---|
| Experiment no. | Reactant (**Equation 15**) | Product (**Equation 16**) |
| 1 | 0.995 ± 0.001 | 1.001 ± 0.007 |
| 2 | 0.990 ± 0.005 | 0.996 ± 0.007 |
| 3 | 0.999 ± 0.006 | 0.983 ± 0.009 |
| Mean (± 95% C. I.) | 0.994 ± 0.007 | |

a For individual experiments, the reported experimental error is the standard error on the fitted KIE value in Equation 15 & 16. The overall experimental error is the 95% confidence interval on the mean of all measurements.

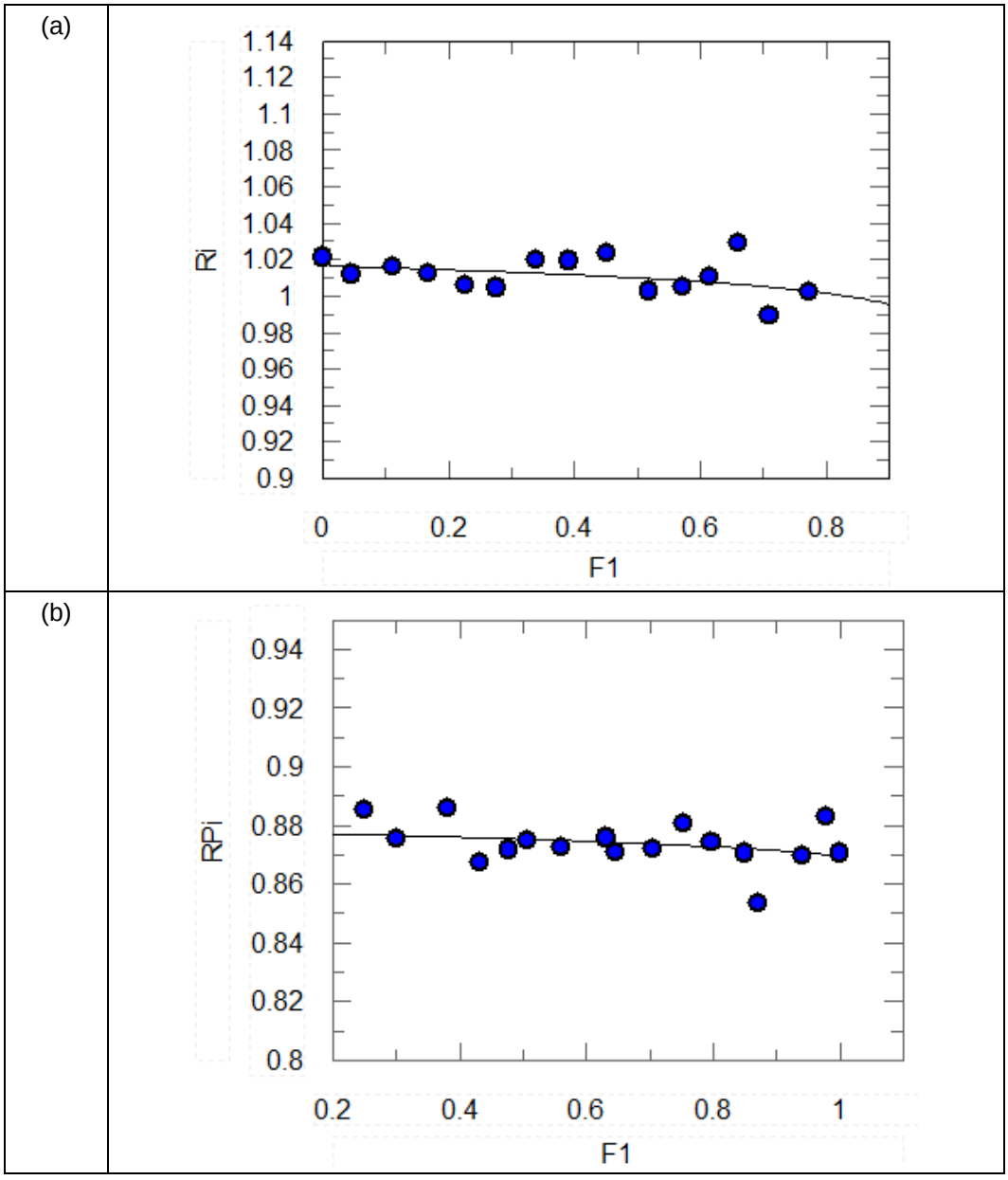


Figure 3.11: 2-$^{13}$C KIE measurements: isotope ratios vs. extent of reaction

Isotope ratios for 2-$^{13}$C KIE measurement showing (a) $R_i$ vs $F_1$ for the PEP reactant and (b) $RP_i$ vs. $F_1$ for the NeuNAc product.

### *3.3.5.1 Measuring 2-$^{18}$O KIE*

Several attempted 2-$^{18}$O KIE measurements failed before the experimental conditions were optimized. The 2-$^{18}$O KIE measurement was first attempted using $^{31}$P as the reporter nucleus with a mixture of [2-$^{18}$O]PEP and unlabelled ([2-$^{16}$O]) PEP. The difference in the chemical shift between the [2-$^{18}$O]- and [2-$^{16}$O]PEPs allows each isotopologue to be observed. The first attempt did not work due first to a slow reaction rate caused by either high ammonium formate or low NeuB activity. In the second attempt, the $^{31}$P peaks were not well-resolved and the peak shape changed significantly between the spectra. Before attempting another measurement using $^{31}$P NMR, the 2-$^{18}$O KIE was measured using $^{13}$C-NMR to eliminate the problem of peak broadening and poor resolution, making it easier to fit the peaks.

For measuring the 2-$^{18}$O KIE using $^{13}$C-NMR, [2-$^{13}$C,2-$^{18}$O]PEP was synthesized using the ppsA reaction with [2-$^{13}$C] sodium pyruvate dissolved in $H_2{}^{18}O$-containing Tris-acetate buffer. The pyruvate keto oxygen spontaneously exchanges with $H_2{}^{18}O$[146]. The product's identity was confirmed by $^{13}$C-NMR **(Figure 3.12)**.

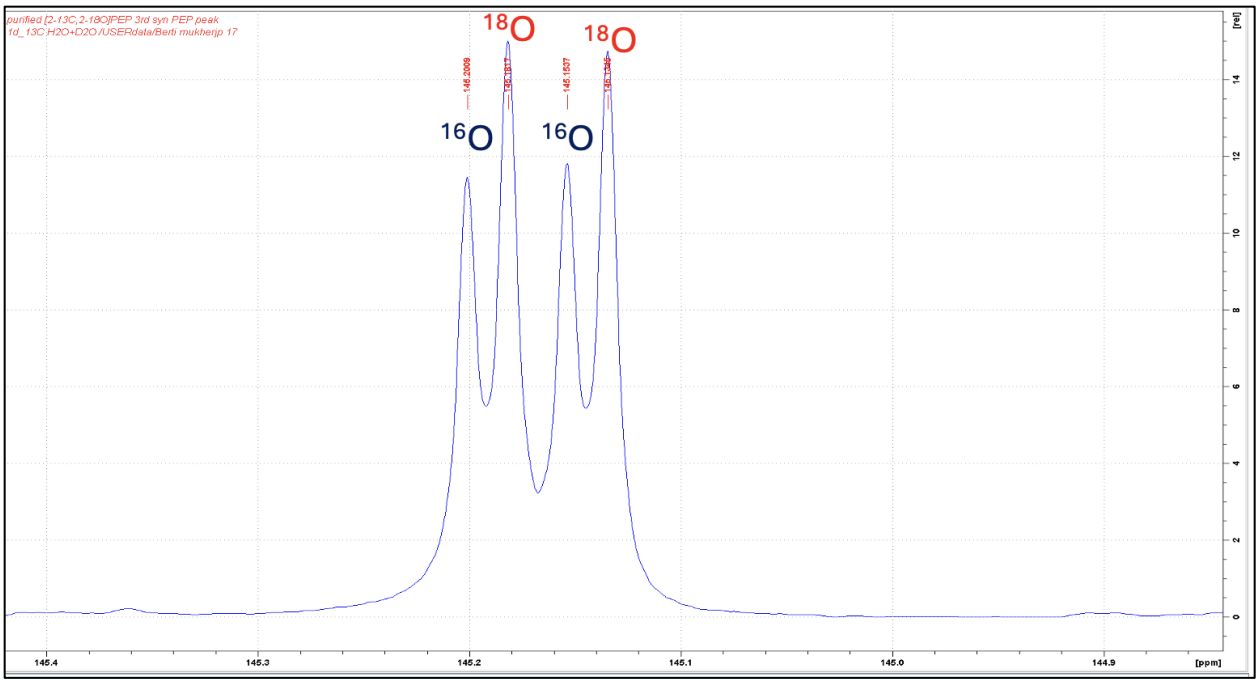


Figure 3.12: $^{13}$C-NMR of [2-$^{13}$C, 2-$^{18}$O]PEP

[2-$^{13}$C, 2-$^{18}$O]PEP in 10% $D_2O$ under KIE conditions; chemical shift (ppm): $^{13}$C-$^{16}$O PEP: 145.20, 145.15 ppm, $^{13}$C -$^{18}$O PEP: 145.18, 145.13 ppm.

As the 2-$^{18}$O KIE measurement was successful using $^{13}$C NMR (**Figure 3.14**), it was tried again using $^{31}$P NMR; however, the $^{18}$O- and $^{16}$O PEP peaks had extremely poor peak resolution **(Figure 3.13a).** Peak resolution is crucial due to a very small difference in chemical shifts between [2-$^{18}$O]- and [2-$^{16}$O]PEP. When repeated degassing of the sample and autoshimming did not improve peak resolution, one remaining possibility was that some trace metal ion could be interacting with PEP's phosphate group and affecting the $^{31}$P peak. Adding 0.5 mM EDTA in the presence of 1 mM ultrapure $MgCl_2$ to chelate any trace metal ions in small-scale reactions improved the peak resolution significantly (**Figure 3.13b**) without affecting the reaction rate, and the reaction ran to completion. The peak areas were subsequently calculated using PeakFit and $^{18}$O KIE was measured successfully using $^{31}$P-NMR. The measurement to repeated for accuracy and reproducibility.

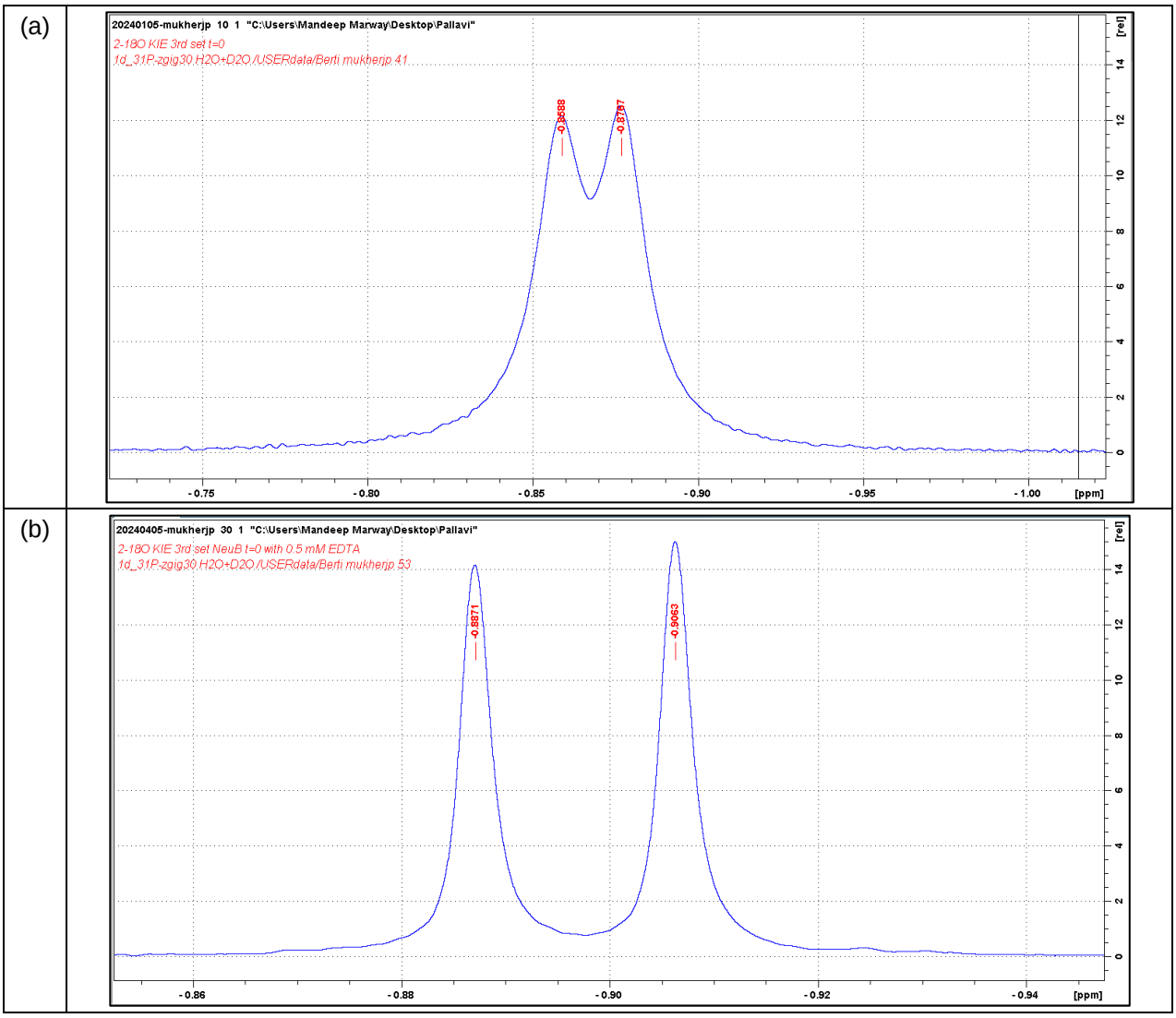


Figure 3.13: $^{31}$P NMR peak resolution in the absence and presence of EDTA

$^{31}$P NMR spectra on the same sample of a mixture of [2-$^{18}$O]- and [2-$^{16}$O]PEP (**a**) before and (**b**) after adding 0.5 mM EDTA to the reaction mixture containing 1 mM ultrapure $MgCl_2$.

The [2-$^{18}$O]PEP KIE was measured using both $^{13}$C- and $^{31}$P NMR spectra (**Figure 3.14**). Experiments number 1 and 2 used $^{13}$C NMR while experiments 3 and 4 used $^{31}$P NMR **(Table 3.6**). The experimental 2-$^{18}$O KIE was 0.999 ± 0.006. This showed that the $^{18}$O KIEs can be successfully measured irrespective of which atom was used as the reporter nucleus. A unity 2-$^{18}$O KIE demonstrates that THI breakdown is not the first irreversible step since C2−O2 bond cleavage would result in a large, normal KIE.

Table 3.6: 2-$^{18}$O Experimental KIEs

| Experiment no. | 2-$^{18}$O KIEs [a] Reactant (**Equation 15**) | Reporter nucleus |
|---|---|---|
| 1 | 1.002 ± 0.012 | 2-$^{13}$C |
| 2 | 0.995 ± 0.016 | 2-$^{13}$C |
| 3 | 0.996 ± 0.007 | $^{31}$P |
| 4 | 1.002 ± 0.006 | $^{31}$P |
| Mean (± 95% C. I.) | 0.999 ± 0.006 | |

a For individual experiments, the reported experimental error is the standard error on the fitted KIE value in Equation 15. The overall experimental error is the 95% confidence interval on the mean of all measurements.

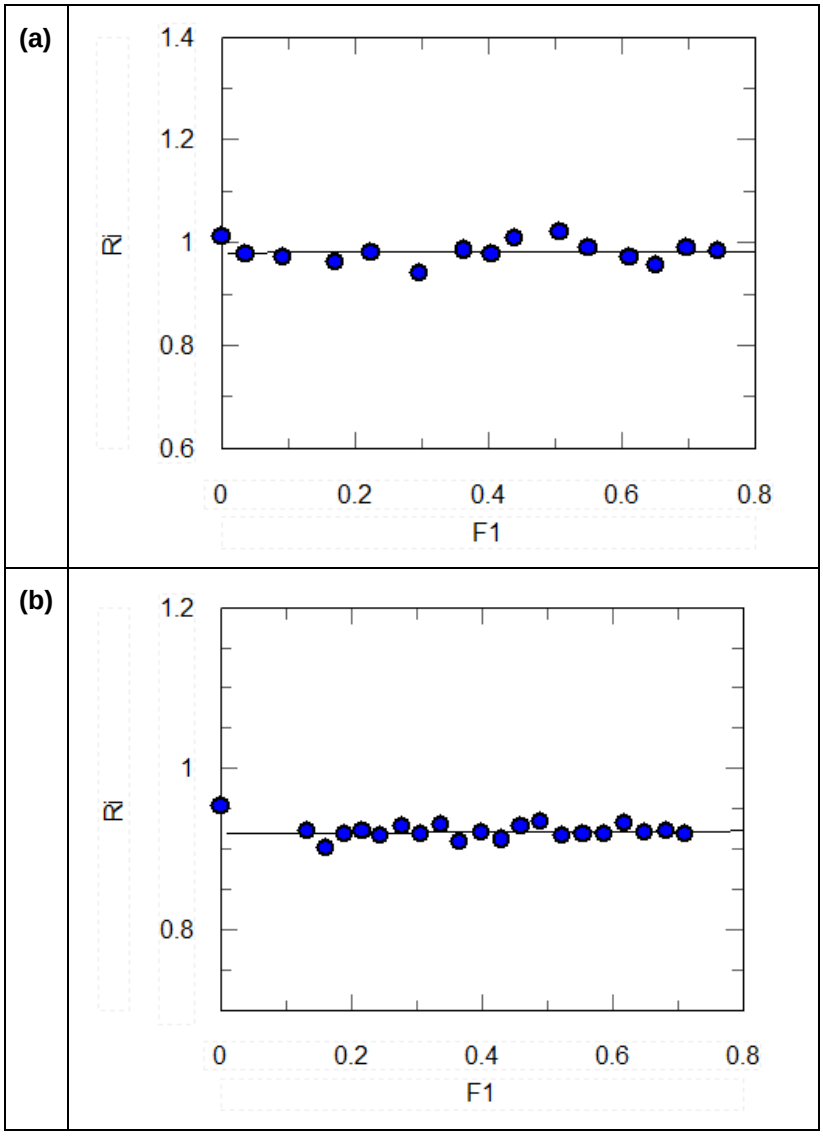


Figure 3.14: 2-$^{18}$O KIE measurement using $^{13}$C and $^{31}$P reporter nuclei

$R_i$ vs $F_1$ plots for 2-$^{18}$O KIE measurement for the NeuB catalyzed reaction using (**a**) 2-$^{13}$C, and (**b**) $^{31}$P as the reporter nuclei.

The experimental KIEs for the NeuB-catalyzed reaction are consolidated in **Table 4.4**.

Table 3.7: Experimental KIEs for the NeuB-catalyzed reaction.

| Isotopic label | Experimental KIE[a] | *n*[b] |
|---|---|---|
| 2-$^{13}$C | 0.994 ± 0.007 | 6 |
| 3-$^{13}$C | 1.022 ± 0.002 | 6 |
| 2-$^{18}$O | 0.999 ± 0.006 | 4 |

[a] Experimental error reported as the 95% confidence interval.

b Number of independent trials. For the 2-$^{13}$C and 3-$^{13}$C KIEs, this reflects three replicate reactions with KIEs calculated separately from isotope ratios on both the residual reactant and products. For 2-$^{18}$O KIE, the KIE was measured in four independent reactions, with two each using 2-$^{13}$C and $^{31}$P as the reporter nucleus.

### *3.3.6 Computations*

Interpreting experimental KIEs requires finding computational TS structures whose calculated KIEs match the experimental values to reveal the experimental TS structure[123, 133]. The nature of electronic structure calculations is that while computational transition states' energies and structures often do not match reality, the calculated vibrational frequencies for a given structure, and by extension the calculated KIEs, accurately reflect the expected KIEs for that TS structure. Therefore, the goal of KIE interpretation is to find a computational TS structure whose calculated KIEs match the experimental values. This can be done by creating a computational model of the reaction, then varying the reactant, solvation, acid/base catalysts, nucleophiles, and counterions until a computational TS structure with the correct KIEs is found.

In this study, the computational models needed to generate computational KIEs were built up from simple models into more complete ones. The reactant PEP was initially modelled as 2-methoxypropene (**18**) (**Figure 3.15a**), vinyl phosphate (**19**) (**Figure 3.16**) and later expanded to PEP (**25**) in its two protonation states at pH 7 (23% dianion and 77% trianion)[208].

ManNAc was modelled as acetaldehyde with various catalytic metals, including $Li^+$, $Mg^{2+}$, and $Ca^{2+}$. The nucleophilic water was modelled using $H_2O$, $^-OH$, or LiOH. In computational models, LiOH does not dissociate, and has nucleophilicity between $H_2O$ and $^-OH$. A variety of small molecules or ions were used to mimic active site residues, including formate, acetate, hydroxymethyammonium ion, methylenediammonium ion, $Li^+$ and $Cl^-$. Computational TS structures were found for both THI formation and breakdown.

#### *3.3.6.1 THI formation*

For THI formation, attempts were made to find TS structures via the two previously proposed pathways, namely anionic and cationic (**Figure 3.15 a**). To understand the energy profile, a potential energy surface (PES) was obtained using constrained optimizations (**Figure 3.15 b**). The C2−C3 bond length was fixed, and structures were optimized at increasing C2−O2' bond lengths. Then the C2−C3 bond length was increased and the C2−O2' was scanned out again (**Figure 3.15 b**). The PES showed a high energetic cost along the anionic pathway (**22**), so the anionic mechanism not further investigated. This was in good agreement with the Berti lab's previous experimental results that nucleophilic attack by $^-OH$ on an unactivated enolpyruvyl group (C2 of PEP) is not possible,[26] and the fact that PEP is extremely base stable[26].

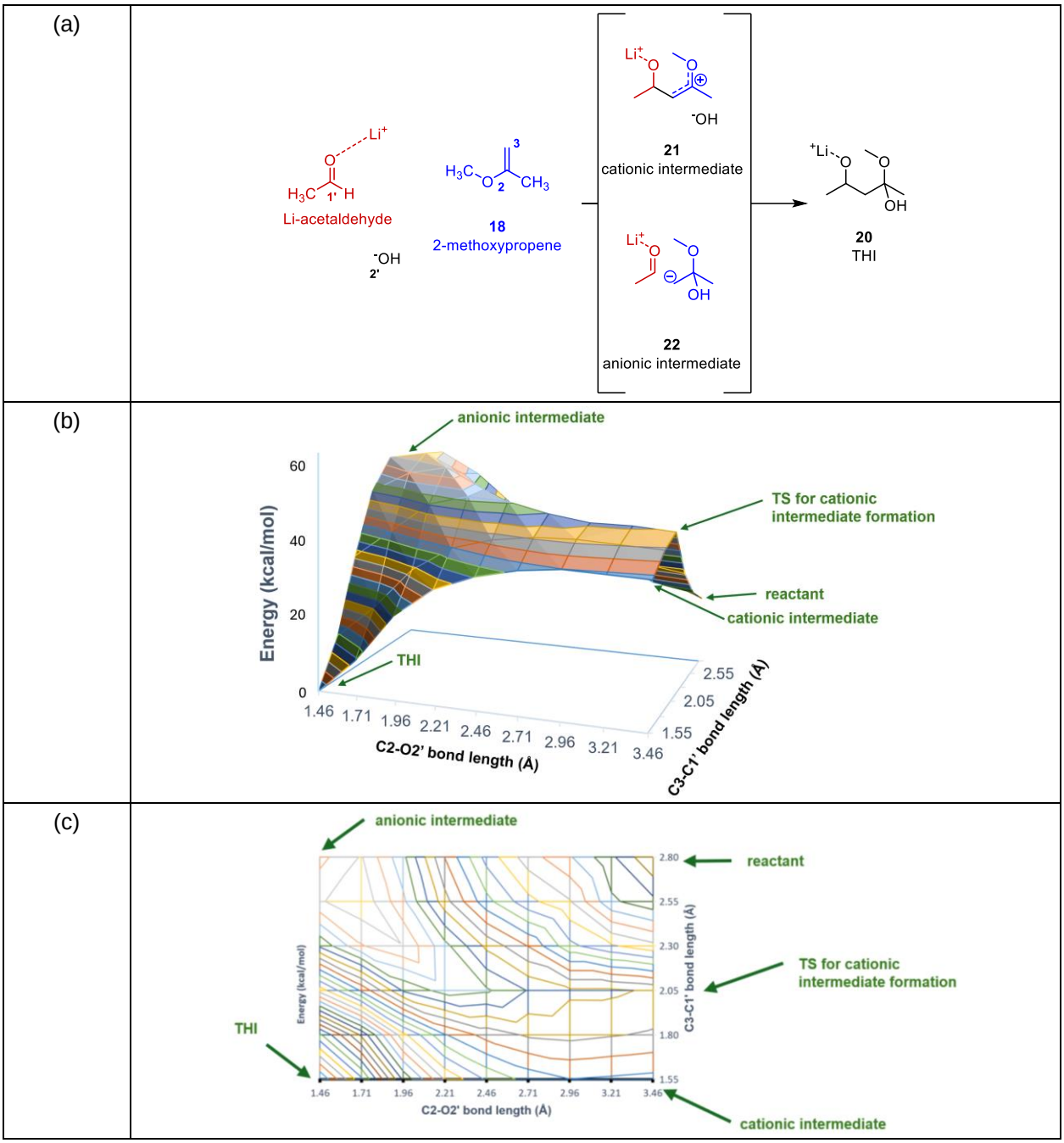


Figure 3.15: 3D-PES plot for model reactions

(**a**) Reaction of between **18** and Li acetaldehyde with $^{-}$OH via a cationic (**21**) or anionic mechanism (**22**) to form a THI (**20**). (**b**) Potential energy surface of energy (kcal/mol) vs C2-C3 bond length (Å) at fixed, increasing C2-O2' bond length (Å). (**c**) Energy contours for the same potential energy surface.

The PES showed a much lower energetic barrier for a cationic versus anionic mechanism.

A cationic intermediate was favoured over a concerted mechanism but given the shallowness of

the PES in the region of the cationic intermediate (**21**), concerted mechanisms were also plausible. The THI (**23**) was optimized for the model reaction between vinyl phosphate (**19**) and Li acetaldehyde with LiOH as the nucleophile. The C2−O2' bond of the THI (**23**) was scanned out from 1.43 Å at increasing C1'-C2 bond lengths. A full TS optimization gave a TS structure (**24**‡) with a reaction coordinate (imaginary) frequency of -500 $cm^{-1}$ (**Figure 3.16**).

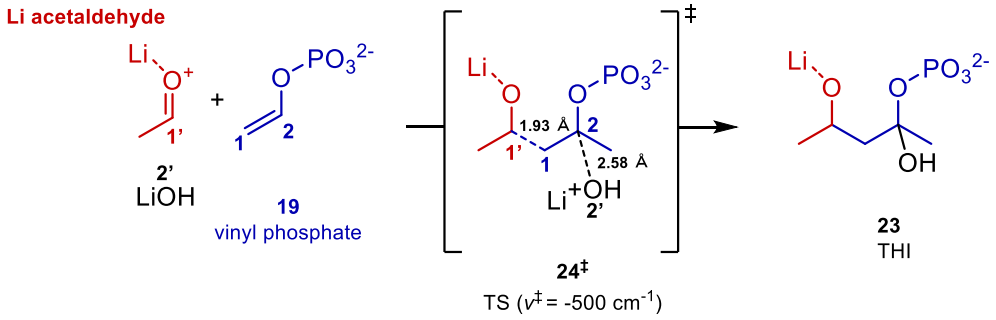


Figure 3.16: Computational TS (**24**‡) structure

TS structure (**24**‡) for THI formation (**23**) from vinyl phosphate (**19**), Li acetaldehyde, and LiOH.

The model reactants were expanded to PEP (**25**) with Li acetaldehyde, and LiOH as the nucleophile. Starting from the THI (**26**), the C3-C1'bond (Å) was scanned out at fixed C2-O2' bond length (Å) in search of plausible guesses at the TS. A TS structure (**27**‡) with an imaginary frequency of -439 $cm^{-1}$ was found with C3-C1' bond length of 1.98 Å and C2-O2' bond length of 2.13 Å **(Figure 3.17)**. This TS structure corresponds to a concerted mechanism, with both the C3-C1' and C2−O2' bonds are being formed in the reaction coordinate. The calculated 3-$^{13}$C and 2-$^{13}$C KIEs are both normal (**Table 3.8**). However, this contrasts with the experimental 2-$^{13}$C KIE of 0.994 (**Table 3.9).** Exploring various computational reaction models can result in finding computational TS structures with different KIE values at specific position of the reactant. This allows us to differentiate between a stepwise and concerted mechanism.

Table 3.8: List of all the calculated KIEs corresponding to each TS structure for THI formation

| | Calculated KIE | | |
|---|---|---|---|
| TS number | 3-$^{13}$C | 2-$^{13}$C | 2-$^{18}$O |
| **27‡** | 1.026 | 1.012 | 0.999 |
| **28‡** | 1.029 | 1.000 | 1.007 |
| **29‡** | 1.010 | 1.001 | 1.003 |
| **30‡** | 1.027 | 0.997 | 1.000 |
| **31‡** | 1.027 | 0.996 | 0.999 |
| **32‡** | 1.025 | 0.995 | 1.000 |
| **33‡**[a] | 1.022 | 0.995 | 0.999 |
| **34‡** | 0.996 | 1.001 | 0.997 |
| **35‡** | 0.985 | 1.017 | 0.996 |
| **36‡** | 0.986 | 1.015 | 0.995 |
| **37‡** | 0.995 | 1.013 | 0.995 |
| **38‡** | 0.992 | 1.015 | 0.995 |
| **39‡** | 0.990 | 1.016 | 0.997 |
| **40‡** | 0.989 | 1.018 | 0.998 |

[a] Model optimized at the M062X/6-31+G** level of theory. All others were at the B3P91/6-31+G** level of theory.

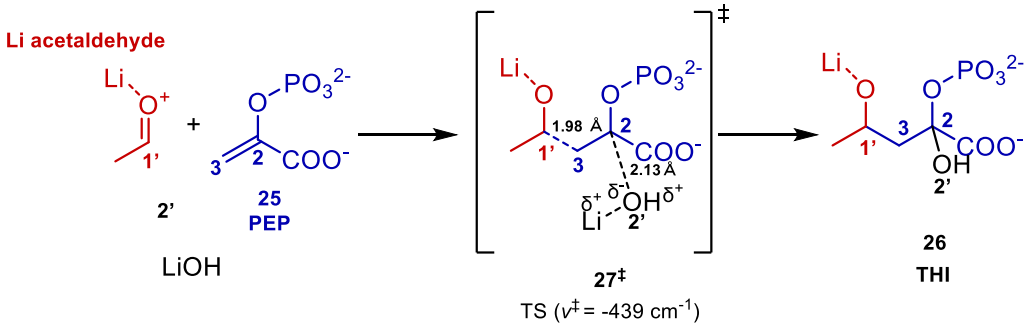


Figure 3.17: Computational TS structure **27‡** for THI formation

TS structure (**27‡**) for THI formation (**26**) from PEP (**25**), Li acetaldehyde, and LiOH.

Based on TS structure **27‡** (**Figure 3.17**), Dr. Berti varied the counterions and solvating molecules to create other TS structures. It is only after a TS structure has been optimized and the reaction coordinate visualized that is possible to determine what type of transition state it is. Several TS structures were for forming the cationic intermediate in a stepwise mechanism (**28‡**,

**29**‡, **30**‡, **31**‡, **32**‡, **33**‡) (**Figure 3.18 a)**, others were for concerted THI formation (**27**‡, **34**‡) (**Figure 3.18 c)** and others were for breakdown of the cationic intermediate to form the THI (**35**‡, **36**‡, **37**‡, **38**‡, **39**‡, **40**‡). In the latter structures the C3−C1' bond is fully formed, and the reaction coordinate involves only C2···O2' bond formation. These TS structures are characterized by inverse 3-$^{13}$C KIEs and normal 2-$^{13}$C KIEs of ~1.015 reflecting C2···O2' bond formation (**Table 3.9**) (**Figure 3.18 b**).

(a)

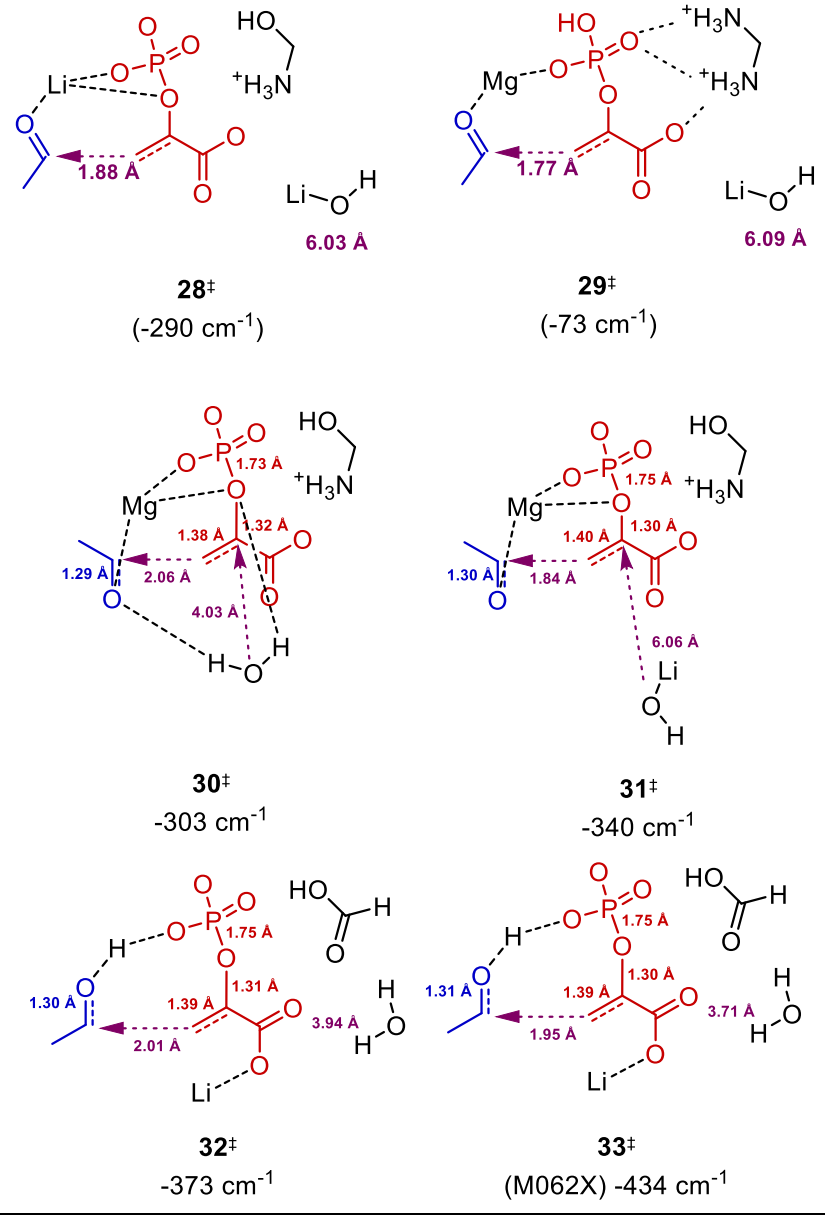

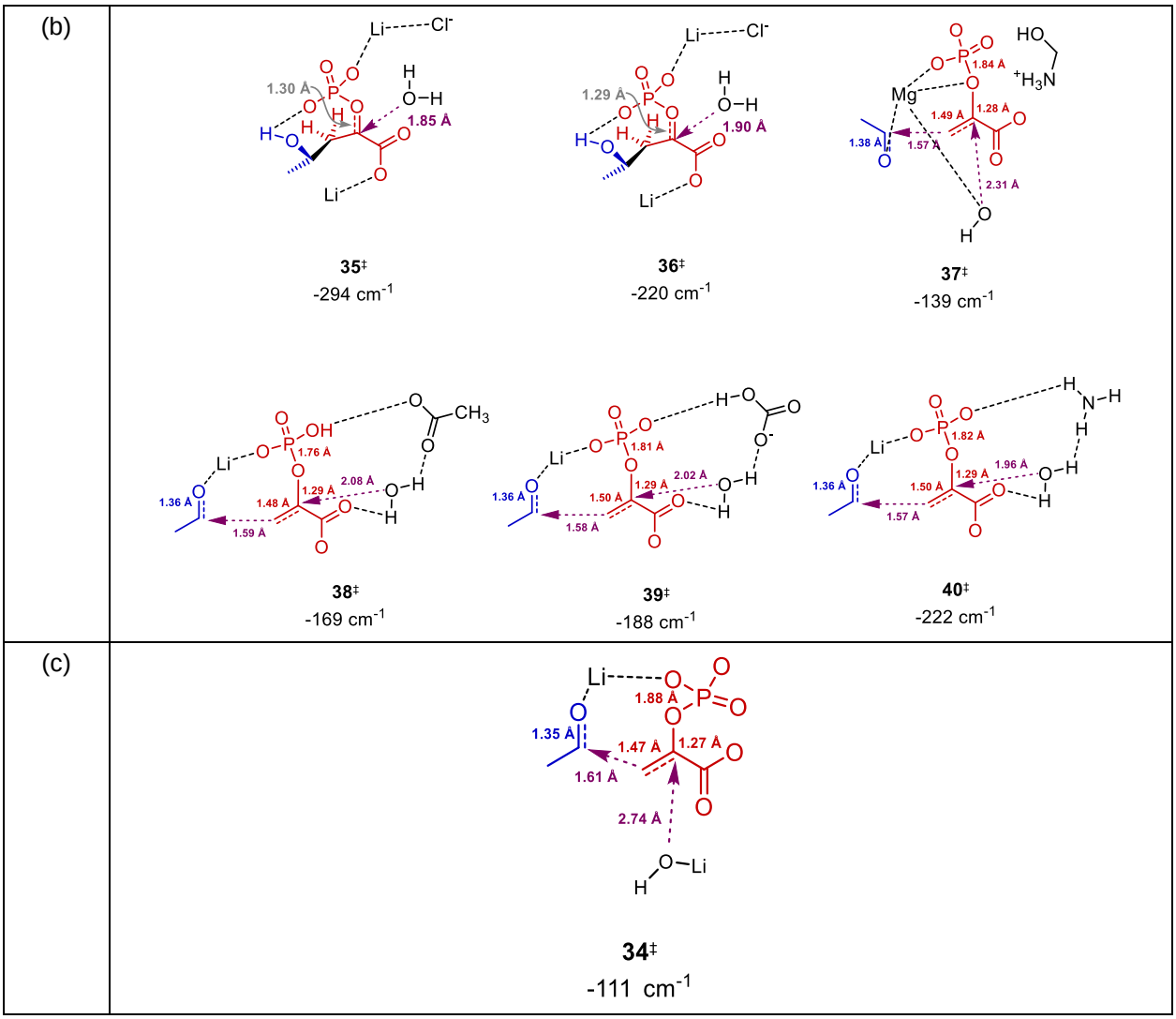


Figure 3.18: Computational TS structures for THI formation

(**a**) Structures **28‡**, **29‡**, **30‡**, **31‡**, **32‡**, **33‡** had only C3···C1' bond formation in the reaction coordinate. There were therefore transition states for formation of a cationic intermediate in a stepwise cationic mechanism of THI formation. (**b**) Structures **35‡**, **36‡**, **37‡**, **38‡**, **39‡**, **40‡** had only C2···O2' bond formation in the reaction coordinate. There were therefore transition states for breakdown of the cationic intermediate in a stepwise cationic mechanism of THI formation. (**c**) Structure **34‡** had both C3···C1' and C2···O2' bond formation in the reaction coordinate so it was a transition state for concerted THI formation.

A More O'Ferrall-Jencks plot was created for THI formation (**Figure 3.19 a).**The plot shows 16 computational TS structures with the symbol colours indicating how well the computational KIEs match the experimental values. White symbolizes a calculated KIE that matches the experimental KIE within experimental error. Calculated KIEs that are too low or too

high are coloured darker shades of blue and red, respectively, depending on how far they are from the experimental value **(Figure 3.19 b to d)**.

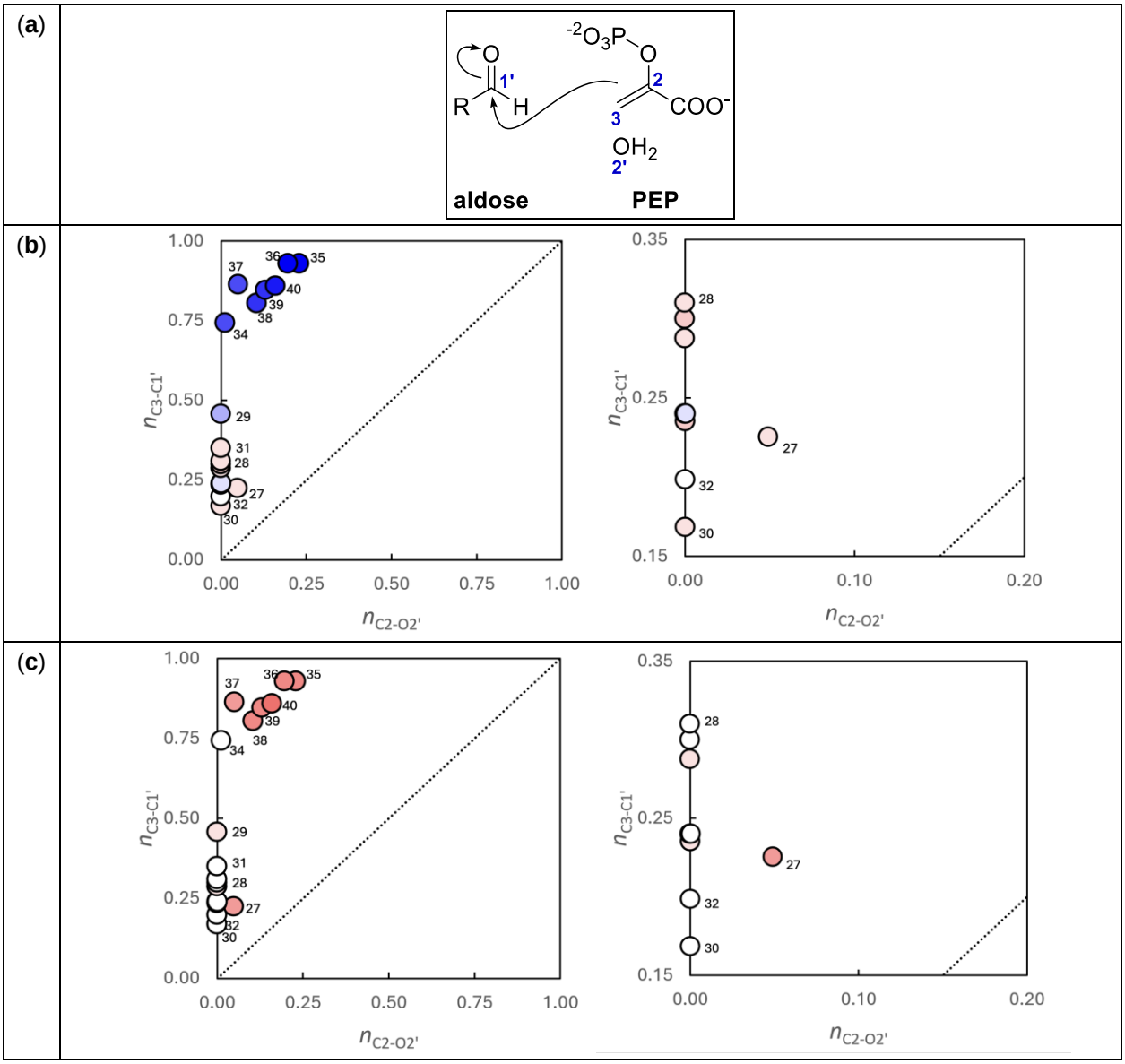

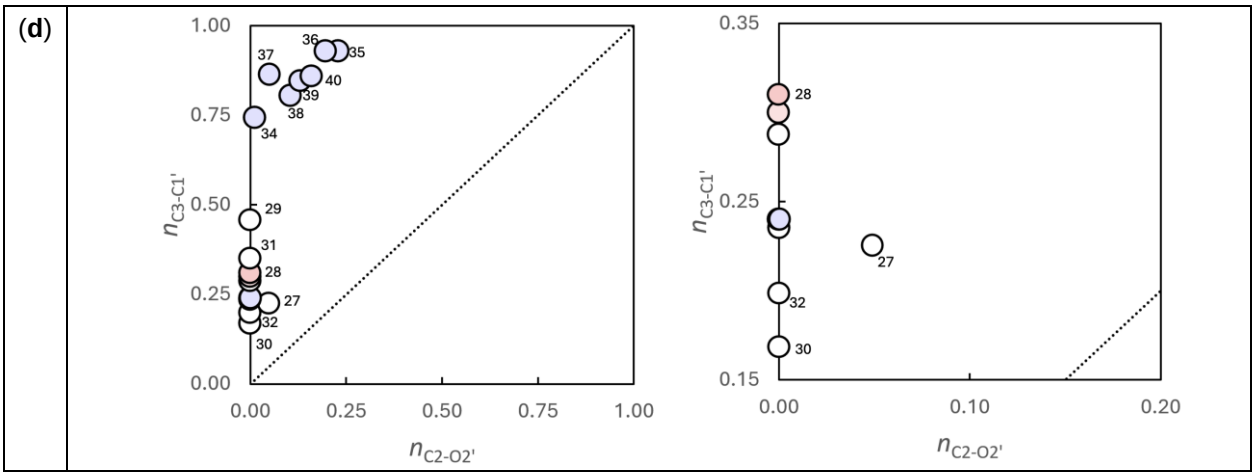


Figure 3.19: More O'Ferrall–Jencks plots for THI formation

More O'Ferrall–Jencks showing the attack of PEP C3 on the aldose C1' and of nucleophilic $H_2O$ on PEP C2 are shown. Pauling bond orders are shown: $n_{ij}=e^{(r_1-r_{ij})/0.3}$ where $r_1$ is the bond length of a single bond between atoms of type i and j and $r_{ij}$ is the observed bond length.[209] Here, white symbols mean that the calculated KIE matches the experimental value. Red and blue showing the deviation between the experimental and calculated KIEs. (a) 3-$^{13}$C KIEs: The white symbol range was expanded to 1.023 ± 0.004 since there were too few matching calculated KIEs in the 95% confidence interval of the experimental KIE. . Full range is 0.98 (blue) to 1.06 (red); the right graph is the same data but over a narrower range of bond orders (**b**) 2-$^{13}$C KIEs: white symbol range = 0.994 ± 0.007; full range = 0.95 (blue) to 1.03 (red) (**c**) 2-$^{18}$O KIEs: white symbol range = 0.999 ± 0.006; full range = 0.96 (blue) to 1.04 (red).

From the More O'Ferrall-Jencks plot, THI formation adopting a cationic, stepwise mechanism includes only the formation of the C3−C1' bond at the transition state. This will give a normal 3-$^{13}$C KIE since C3 is in the reaction coordinate as the bond is formed. There is no bond formation between the nucleophilic $H_2O2'$ and C2 of PEP, so the 2-$^{13}$C KIE will be unity or slightly inverse due to increases in the C2−O2 bond order as the cationic intermediate is formed. The extent of C3−C1' bond order and any π-bond formation with O2 will determine whether there is a cationic centre at C2. However, THI formation can also employ a concerted mechanism with the simultaneous attack of C3 on C1' and attack of the nucleophile, O2', on C2. The real determining factor to differentiate concerted vs. stepwise is whether C2-O2' bond formation is in the reaction coordinate, and that, in turn, is demonstrated by the 2-$^{13}$C KIE. In a concerted transition state, both 2-$^{13}$C and 3-$^{13}$C are in the reaction coordinate, so both KIEs are

normal. In this case, the transition state is expected to be neutral around the reactive center and located more towards the centre of the More O'Ferrall-Jencks plot.

From the 16 computational TS structures found, the ones that best match the experimental KIEs were **30‡**,**31‡**, **32‡, 33‡** (**Table 3.9).** These TS structures are in the lower left quadrant of the reaction space and involve only C3−C1' bond formation with C3-C1' bond orders ranging between 0.17 to 0.93 i.e., between 1.84 to 2.06 Å. Therefore, the best match of calculated with the experimental KIEs shows that the first irreversible transition state is for stepwise THI formation (**Table 3.9)**.

Table 3.9: Summary of experimental and calculated KIEs for THI formation for the NeuB catalyzed reaction.

| Position | Exptl. KIE | Calc KIEs (30‡, 31‡, 32‡) | Calc KIEs (27‡) |
|---|---|---|---|
| 3-$^{13}$C | 1.023 ± 0.002 | 1.025 → 1.027 | 1.026 |
| 2-$^{13}$C | 0.994 ± 0.004 | 0.995 → 0.997 | 1.012 |
| 2-$^{18}$O | 0.999 ± 0.006 | 0.999 → 1.000 | 0.999 |

Three TS structures (**30‡**,**31‡**,**32‡)** with similar geometric and charge features were found for THI formation via a stepwise, cationic mechanism **(Figure 3.18).** TS structures **30‡** and **31‡** were obtained by modelling the same reaction between $Mg^{2+}$·acetaldehyde and PEP, but, using LiOH and $H_2O$, respectively, as nucleophiles. $H_2O$ was a very weak nucleophile, while LiOH was significantly stronger. In the computational models, the $Li^+$ ion does not dissociate. Hydroxymethylammonium ion was used to mimic the interaction with Ser154 and Lys129 sidechains with the phosphate group of PEP in model **30‡** and **31‡** (**Figure 3.18**).[15] TS structure **32‡** was modelled using acetaldehyde hydrogen bonded to one of the phosphate non-bridging oxygens (**Figure 3.18**). Formate was intended to activate the water nucleophile via deprotonation, but that did not occur in the computational TS structure.

### *3.3.6.2 THI breakdown*

Initial computational models of THI breakdown investigated (i) an anionic mechanism via O2' deprotonation and (ii) a cationic mechanism via protonation of the phosphate bridging oxygen, O2 (**Figure 3.15)**. These two mechanisms emphasize different driving forces for THI breakdown. In the anionic pathway, deprotonating O2' will drive C2=O2' double-bond formation, which will drive C2−O2 bond breakage and phosphate group departure. In the cationic mechanism, protonating the phosphate bridging oxygen promotes C2−O2 bond cleavage and phosphate departure. Previous computational studies showed that protonating the non-bridging phosphate oxygens will not promote phosphate group departure[210]. For the anionic mechanism, a TS structure was sought by scanning out the THI to products, and a transition state, **41**‡, was found with an imaginary frequency of -166 $cm^{-1}$ (**Figure 3.20**).

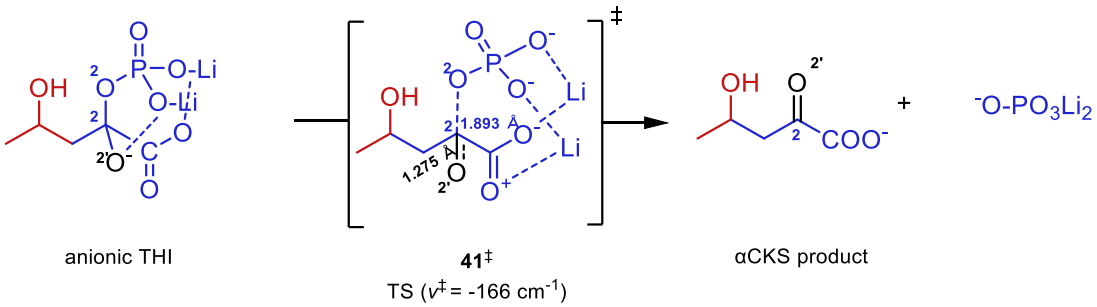


Figure 3.20: THI breakdown via a stepwise, anionic pathway mechanism

An anionic THI was scanned out to products and a TS was found first at a lower level of theory and then at a higher-level theory (**41‡)** with an imaginary frequency of -166 $cm^{-1}$.

The cationic pathway was modeled by optimizing both the THI and the cationic intermediate formed by protonating the phosphate bridging oxygen. A constrained scan was performed with increasing C2−O2 bond lengths to create a potential energy profile and initial guess at the TS structure. A TS structure, **42**‡, with an imaginary frequency of -92 $cm^{-1}$ was found **(Figure 3.21).**

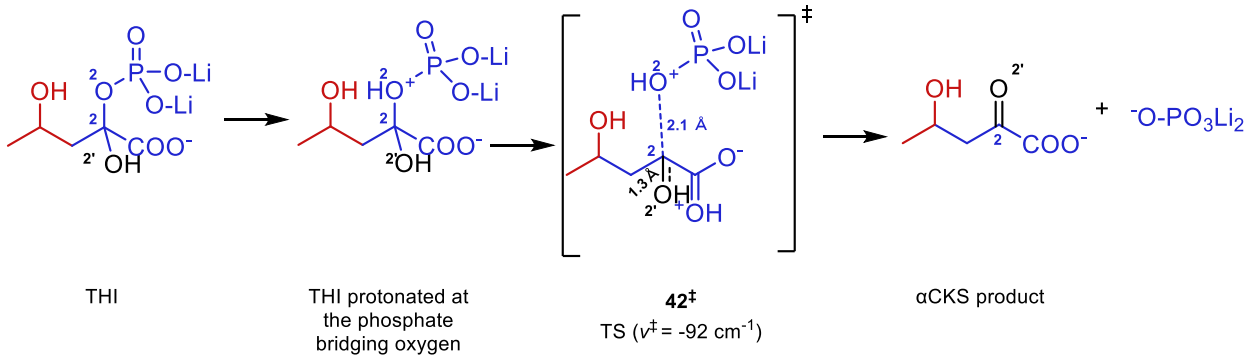


Figure 3.21: THI breakdown via a stepwise, cationic pathway

A cationic THI was scanned out to products and a TS structure (**42‡**) was found with an imaginary frequency -92 $cm^{-1}$.

Further TS structures were found for both cationic (**42‡**, **43‡**, **44‡**, **45‡**) and anionic (**46‡**, **47‡**) pathways by varying the counterions, protonation states, and presence of general acid/base catalysts. A More O'Ferrall-Jencks diagram was plotted for THI breakdown starting from THI to the product **(Figure 3.22 a)**. The *y*-axis corresponds to the $n_{C2\text{-}O2}$ bond order. As the C2-O2 bond in the THI breaks to release $P_i$, the bond order varies from 1 to 0. The *x*-axis corresponds to the $n_{C2\text{-}O2'}$ bond order for the formation of the new C=O bond, to form the product. As the double bond is forming, the bond order varies from 1 to 2. The plot shows eight computational TS structures corresponding to their bond orders in coloured circles ranging from red to white to blue. The colour range is based on the calculated KIEs (*z*-axis) using a middle value and defining a range (**Figure 3.22 b to d)**.

| (**a**) | 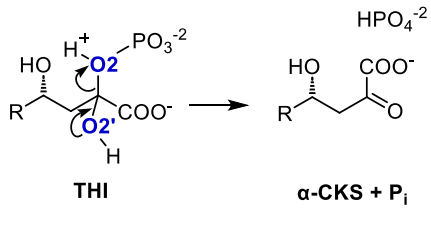 |
|---|---|

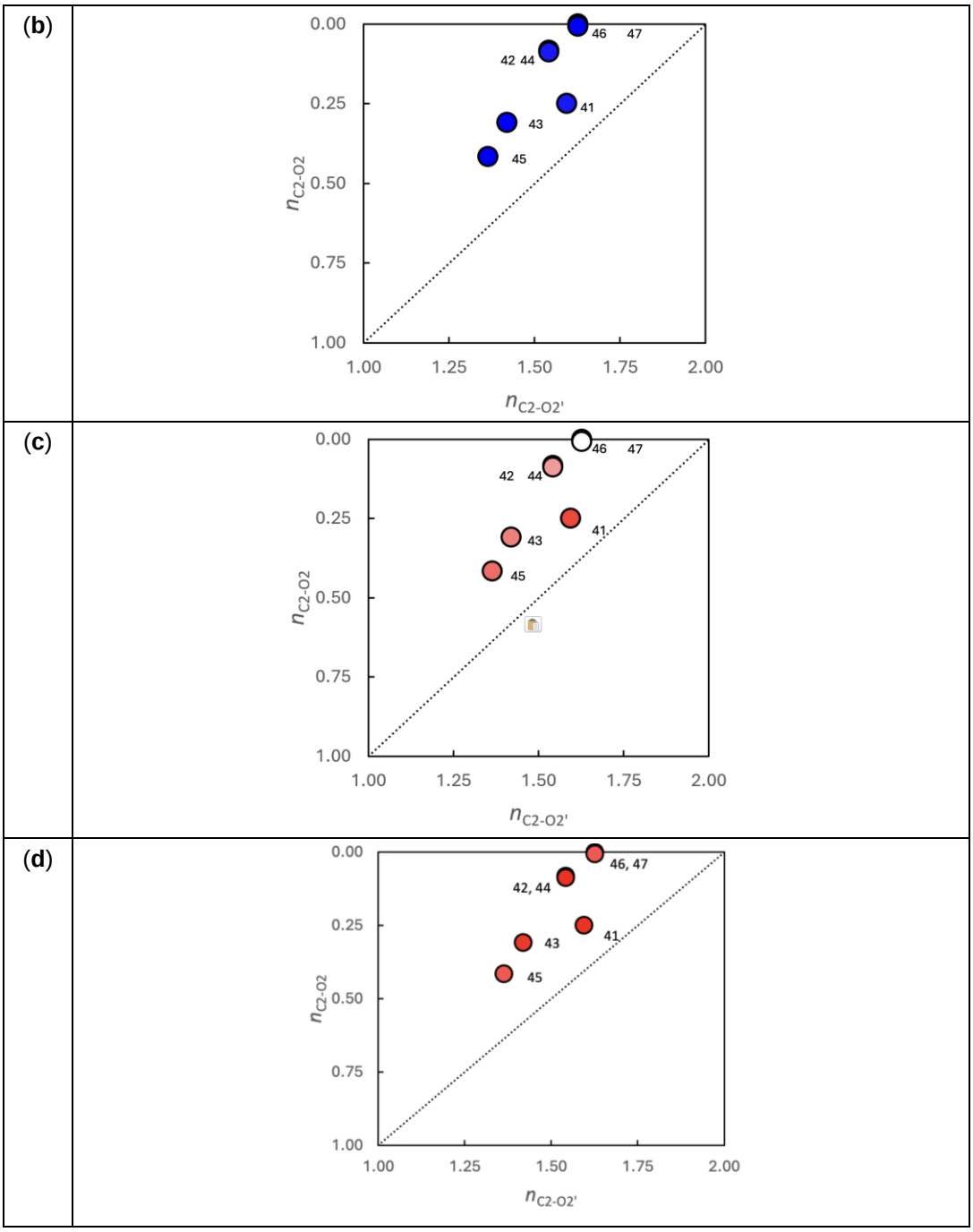


Figure 3.22: More O'Ferrall–Jencks plot for THI breakdown

The breaking of C2-O2 bond of the THI and the formation of the new C2-O2' bond is shown in Pauling bond orders are shown: nij=$e^{(r_1-r_{ij})/0.3}$ where $r_1$ is the bond length of a single bond between atoms of type i and j, and $r_{ij}$ is the observed bond length[209]. White symbols indicate calculated KIEs that match the experimental value. Red and blue showing the deviation between the experimental and calculated KIEs. **(a)** THI breakdown (**b**) 3-$^{13}$C KIEs: white symbol range = 1.023 ± 0.002 ; full range is 0.98 (blue) to 1.06 (red). (**c**) 2-$^{13}$C KIEs: white symbol range = 0.994 ± 0.007; full range = 0.95 (blue) to 1.03 (red) (**d**) 2-$^{18}$O KIEs: white symbol range = 0.999 ± 0.006; full range = 0.96 (blue) to 1.04 (red).

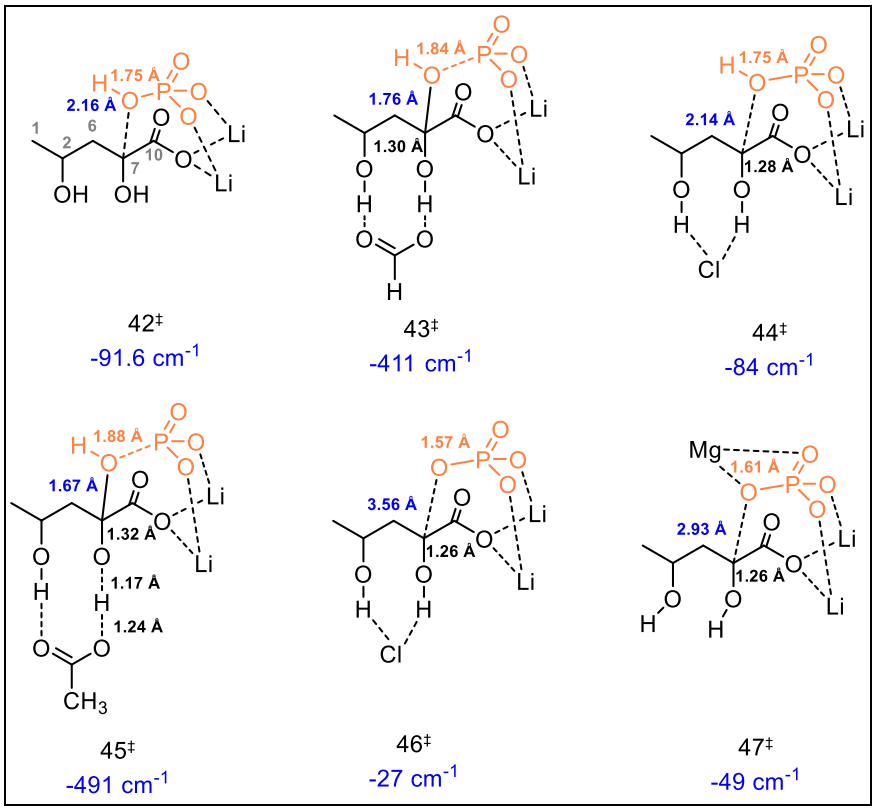


Figure 3.23: Computational TS structures for THI breakdown (**42‡**, **43‡**,**44‡**,**45‡**,**46‡**,**47‡**)

All six computational TS structures for THI breakdown (**Figure 3.23)** via either pathway gave inverse 3-$^{13}$C KIEs and normal 2-$^{18}$O KIEs. The calculated 2-$^{13}$C KIE ranged between inverse to normal (0.994 to 1.018) **(Table 3.10 & Table 3.11).**

Table 3.10: Calculated KIEs for THI breakdown.

| | Calculated KIE | | |
|---|---|---|---|
| **TS number** | 3-$^{13}$C | 2-$^{13}$C | 2-$^{18}$O |
| **42‡** | 0.988 | 1.011 | 1.034 |
| **43‡** | 0.983 | 1.018 | 1.037 |
| **44‡** | 0.989 | 1.010 | 1.039 |
| **45‡** | 0.982 | 1.015 | 1.030 |
| **46‡** | 0.993 | 0.994 | 1.035 |
| **47‡** | 0.984 | 0.996 | 1.030 |

Table 3.11: Summary of experimental and computational KIEs THI breakdown.

| Position | Exptl. KIEs | Calc KIEs (42‡, 43‡, 44‡, 45‡, 46‡ & 47‡) |
|---|---|---|
| 3-$^{13}$C | 1.023 | 0.982 → 0.989 |
| 2-$^{13}$C | 0.994 | 0.994 → 1.018 |
| 2-$^{18}$O | 0.999 | 1.030 → 1.039 |

## 3.4 Discussion

The experimental KIEs can be interpreted qualitatively to identify which step is the first irreversible transition state. If THI breakdown were the first irreversible step, then the 2-$^{18}$O KIE would be large and normal, due to the reaction coordinate being C2−O2 bond breakage, while the 2-$^{13}$C and 3-$^{13}$C KIEs would be inverse, due to their hybridization changing from $sp^2$ in PEP, to $sp^3$ in the THI and transition state. However, if the first irreversible transition state is THI formation, then the 2-$^{18}$O KIE would be unity as there is no change in bonding at O2 of PEP while 3-$^{13}$C KIE would be normal due to C3−C1' bond formation being in the reaction coordinate. The 2-$^{13}$C would be roughly unity for stepwise THI formation with only C3−C1' bond formation. It would be normal for concerted THI formation, with both the C3−C1' and C2−O2' bonds being formed in the reaction coordinate and for an anionic mechanism where only the C2−O2' bond is being formed.

The large normal 3-$^{13}$C KIE and roughly unity 2-$^{13}$C and 2-$^{18}$O experimental KIEs, indicate that THI formation is the first irreversible step of the NeuB reaction.

It was also possible that the THI would partition both forward and backward to a significant extent, that is $0.1 < k_3/k_2$ (**Figure 1.24**). In that case, the observable KIEs would

contain contributions from both steps, and they would be between the values for THI formation and breakdown. However, as discussed below, the excellent match of calculated to experimental KIEs for THI formation indicates that there is no significant contribution from THI breakdown to the experimental KIEs, and THI formation is mostly, or completely, irreversible.

### *3.4.1 What does the experimental TS structure look like?*

Three computational TS structures, **30‡, 31‡**, and **32‡** (**Figure 3.18**) were in good agreement with the experimental KIEs (**Table 3.9)**. A normal 3-$^{13}$C KIE implies that the C3-C1' bond is being formed at the TS, while the slightly inverse 2-$^{13}$C KIE shows that the nucleophile is yet to attack. In contrast, the calculated KIEs for a concerted TS structure, **27‡**, (**Figure 3.17)** agrees well with the experimental 3-$^{13}$C and 2-$^{18}$O KIEs, but not the 2-$^{13}$C KIE.

Other computational models for C3−C1' bond formation (**Figure 3.19 b)** were explored to see the effect of different metal ions ($Mg^{2+}$/$Li^{+}$) or hydrogen bonding to the carbonyl oxygen of acetaldehyde under similar reaction conditions. The calculated 3-$^{13}$C KIE for these TS structures ranged from 1.018 to 1.031, compared with the experimental value of 1.023 ± 0.002. The exact calculated values were influenced by the counter ions and the reaction coordinate motion, among other factors, but were all large and normal and in the same range as the experimental value. The calculated 2-$^{13}$C KIEs were unity compared to the slightly inverse experimental 2-$^{13}$C KIE. The difference was modest and likely arises from features of the NeuB active site that are not replicated in the computational models. The calculated unity 2-$^{18}$O KIE for these TS structures confirm that THI breakdown is not the first irreversible step. Although some of the computational TS structures (**Figure 3.19 b)** did not match fully agree with the

experimental values, they can be optimized further as they follow a stepwise mechanism with the attack of C3 of PEP on C1' of the aldose **(Figure 1.2 Figure 3.9).**

Computational TS structures for the concerted addition reaction were also found: **27**‡, **34**‡ (**Figure 3.17Figure 3.18**). In these structures the reaction coordinate motion was included both C3−C1' and C2−O2' bond formation, which caused normal 2-$^{13}$C KIEs. C3−C1' bond formation was also part of the reaction coordinate, but the inverse contribution to the KIE from C3 being rehybridized from $sp^2$ to $sp^3$ dominated the normal contribution from the reaction coordinate, giving an overall slightly inverse calculated KIE.

Computational TS structures **35**‡, **36**‡, **37**‡, **38**‡, **39**‡, and **40**‡ reflected nucleophile addition to the cationic intermediate; that is, breakdown of the cationic intermediate to the THI. The calculated 3-$^{13}$C KIEs were large and inverse, ≈ 0.985, reflecting the inverse structural contribution to the KIE, with no reaction coordinate contribution. The calculated 2-$^{13}$C KIEs were large and normal, ≈ 1.017, reflecting the reaction coordinate contribution. These calculated KIEs were not consistent with the experimental values.

#### *3.4.1.1 Why is there no accumulation of positive charge on the cationic centre?*

The experimental 2-$^{18}$O KIE was unity, which was unexpected considering the inverse $^{18}$O KIEs in other reactions that form oxacarbenium ion-like transition states. In glycoside hydrolysis reactions, the ring $^{18}$O KIE is inverse; for example, in acid-catalyzed AMP hydrolysis, when the C1'- N9 bond breaks and the bond to the nucleophile is still quite weak, the ribosyl ring contains a positive charge on C1' [211] (**Figure 3.24**). This is stabilized by development of partial double bond character between C1' and O4', making the 4'-$^{18}$O KIE inverse as the oxygen experiences a tighter vibrational environment at the transition state[211].

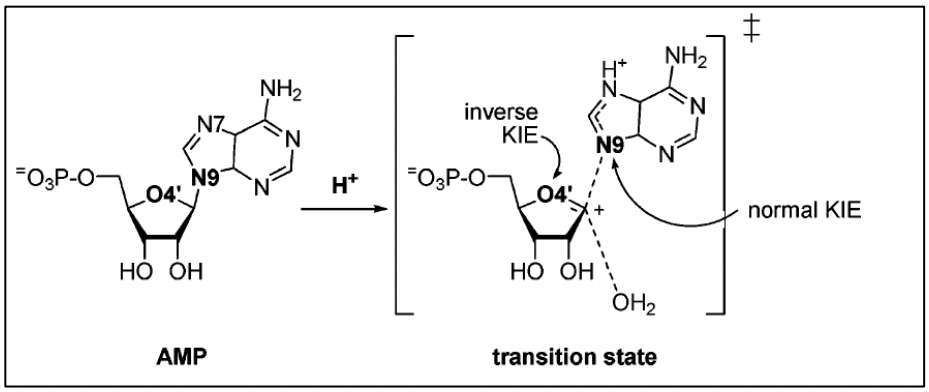


Figure 3.24: Acid-catalyzed AMP hydrolysis[211]

Similarly, the $^{18}$O KIE in enolpyruvyl group hydrolysis positive charge accumulates at the oxacarbenium ion centre (**Figure 3.25**)[161]. The difference appears to arise from the atoms bonded to O2, being P in the NeuB reaction versus C atoms in glycoside and enolpyruvul group. As the new C3−C1' bond forms in the NeuB reaction, the C2=C3 π-bond breaks and the C2−O2 bond order increases (**Figure 3.26).** This was as expected. What was not expected was that the O2−P bond order would decrease in response to the increased C2−O2 bond order, from 0.94 in the reactant to 0.50 in the cationic intermediate (Figure 3.26). This leaves the total bond order to O2, $\Sigma n_{O2}$, unchanged, which accounts for the 2-$^{18}$O KIE of near unity and the lack of positive charge at C2 in the cationic intermediate (**Figure 3.26**). In contrast, the cationic intermediate for enolpyruvyl group hydrolysis in the AroA-catalysed hydrolysis of enolpyruvylshikimate 3-phosphate (EPSP) [161], has increased bond order to O2, an inverse $^{18}$O KIE, and it accumulates positive charge at its cationic centre (**Figure 3.25**). This difference can be attributed to the P atom in a phosphate group being more polarizable than a carbon atom. Decreasing O2−P bond order is compensated by an increase in bond order to the non-bridging phosphate oxygens. As a result, the negative electrostatic potential on the phosphate group decreases as the C3−C1' bond forms.

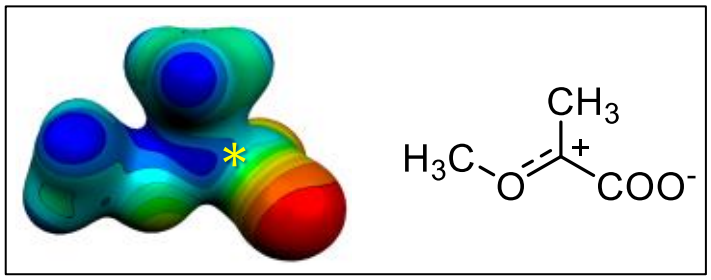


Figure 3.25: Cationic intermediate of AroA-catalysed EPSP hydrolysis

In this computational model of the oxacarbenium ion intermediate of EPSP hydrolysis, the positive charge is centred on the carbon atom (yellow asterisk). The colour range is −0.1 (red) to +0.25 (blue) Hartree[161]. (Figures from reference 161, used with permission from Journal of the American Chemical Society, ©2012).

### *3.4.2 Electrostatic potential map*

The cationic nature of a presumed cationic intermediate during THI formation has been a target of inhibitor design for αCKSs[25, 111-113, 119, 120]. Since the experimental TS structure demonstrates a stepwise mechanism leading to a cationic intermediate, it is worthwhile to consider the charge distribution of the experimental transition state and the presumed cationic intermediate. An electrostatic potential map for the reactant, transition state and presumed cationic intermediate of THI formation was created (**Figure 3.26**). The models of the reactant, TS, and hypothetical cationic intermediate contain only atoms from PEP and acetaldehyde. The solvent, nucleophile and counterions used during computational optimizations were removed to make the underlying electrostatic potentials visible. The models were trianions, so the overall electrostatic potential was negative. It was scaled to show the relative differences in electrostatic potential in each model, going from blue (-0.2 hartree) to red (-0.52 hartree). The yellow asterisk (*) highlights C2, where the cationic centre is expected to develop.

There is almost no accumulation of positive charge in TS model **31**‡, and even in the cationic intermediate there is little positive charge around C2.

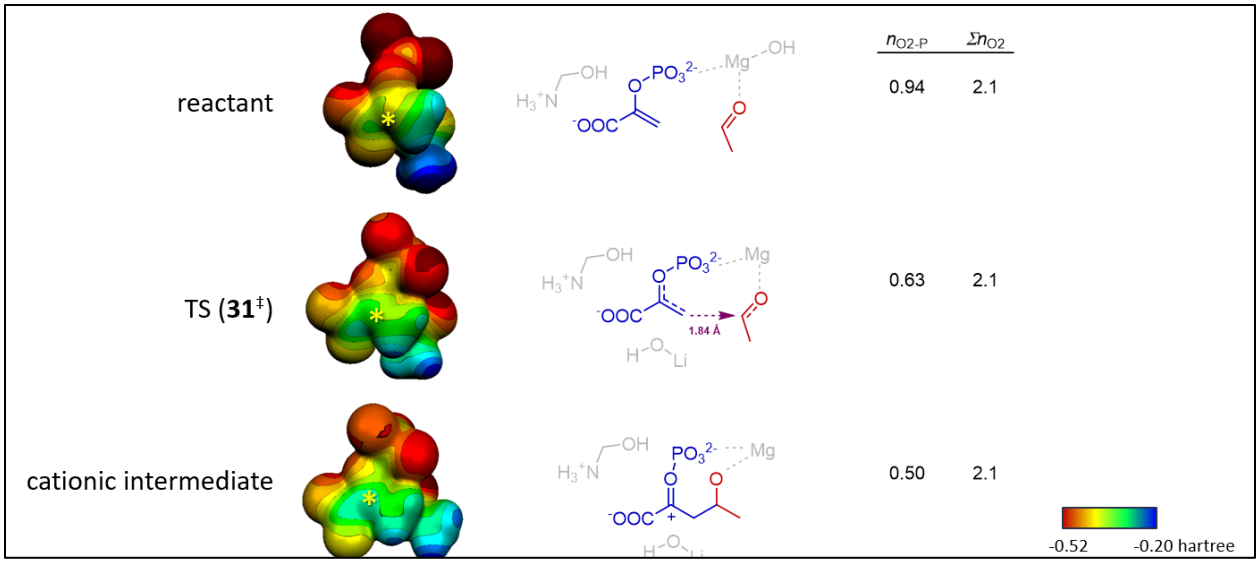


Figure 3.26: Electrostatic potential map for THI formation

The electrostatic potential for the reactant, TS model **31‡** and the cationic intermediate is scaled from most positive (-0.2 hartree) to most negative (-0.52 hartree). It represents the energy required to bring a proton from an infinite distance to the molecular surface. 1 hartree = 627 kcal/mol. Created by Dr. Paul. J. Berti.

### *3.4.3 Implications for catalysis and inhibitor design*

In NeuB, most of the contacts are made with the *si* face of PEP while minimal contacts are formed with the *re* face[15]. Reactions using *Z*-[3-$^2$H]PEP formed (3*S*)-[3-$^2$H]NeuNAc, indicating that the PEP *si* face attacks the ManNAc *si* face[63]. In the NeuB active site the divalent metal ion $Mn^{2+}$ forms an octahedral complex with two His residues (His-215, His-236), two water molecules, a non-bridging phosphate oxygen of PEP, and ManNAc's aldehyde oxygen [15, 118](**Figure 3.27 a**). The PEP phosphate group forms hydrogen bonds with the conserved residues Ser-132, Ser-154, Ser-213, and Asn-814 [15] and the PEP carboxylate can form ion pairs with the Lys-129 and Lys-53 side chains[15] (**Figure 3.27 b**). The PEP C2=C3 double bond does not interact with any active site residues as it is located in the centre of the cavity, making it freely accessible for interacting with ManNAc[1515]. ManNAc forms various ionic interactions and hydrogen bonds with highly conserved amino acid residues such as Asp-247, Gln-55, and Tyr-

186[15]. The distance of $Mn^{2+}$ from ManNAc (2.5 Å) suggests that the metal ion acts as an electrophilic catalyst. This differs from the role of metal ion in DAHPS and Kdo8PS where it is suggested that the metal ion plays a more structural role[49, 79, 80].

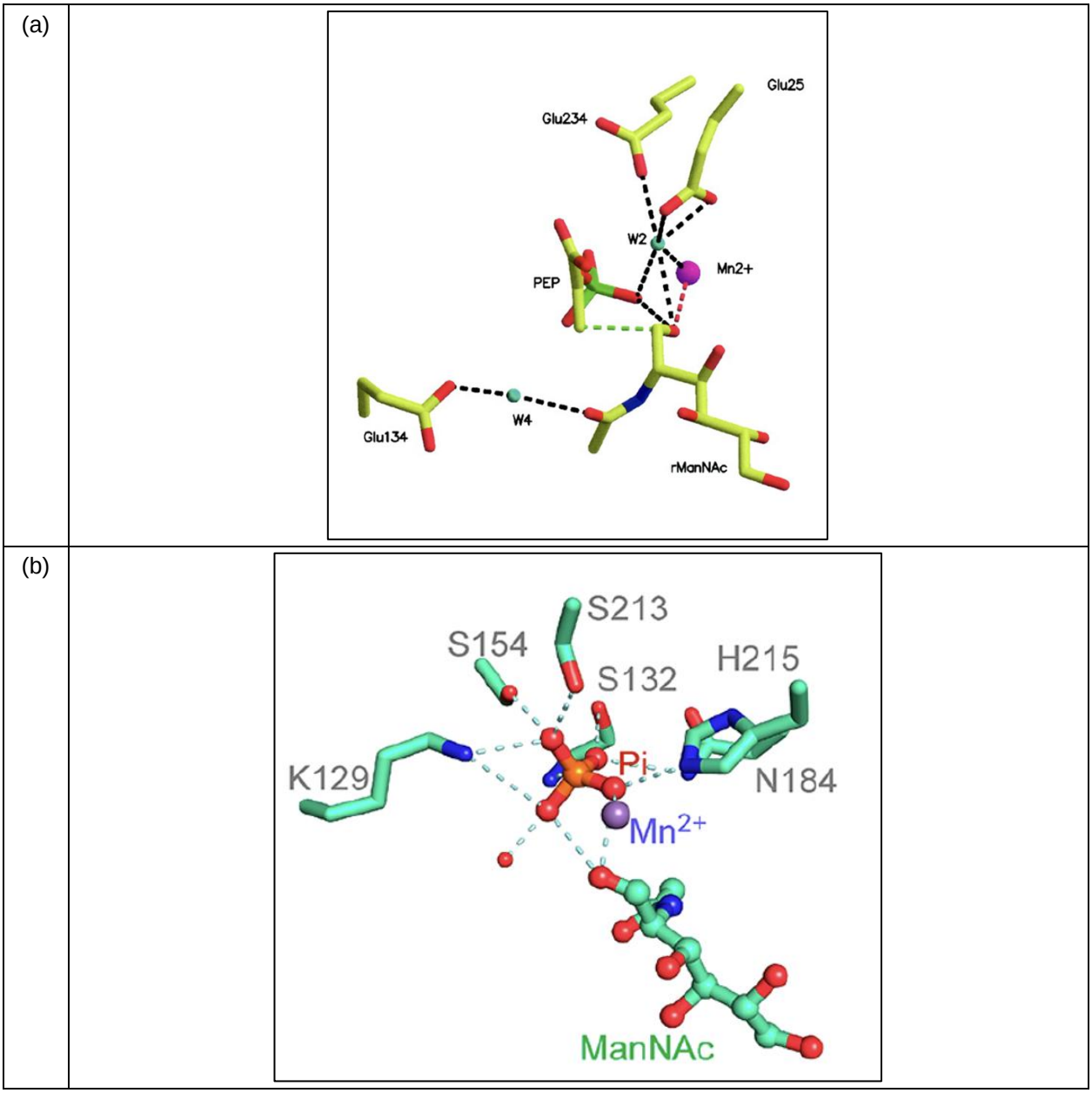


Figure 3.27: NeuB active sites

(**a**) Active site of the NeuB·$Mn^{2+}$·PEP·rManNAc complex (PDBID: 1XUZ)[15] (**b**) Active site of the NeuB· $Mn^{2+}$·Pi·ManNAc complex (PDBID: 6PPZ) displaying the polar interactions with $Mn^{2+}$ and $P_i$ as dashed lines[31]. (Figures from reference 15, 31, used with permission from ASBMB, and American Chemical Society, ©2005, 2019).

Inhibitors that focus on mimicking the presumed positive charge are not likely to be very successful since positive charge accumulation in the transition state and even the cationic intermediate is not large. That is a contrast to other enzymes, like glycosylases, where targeting the positive charge is effective. The fact that oximes (and hydrazone for DAHPS) are effective inhibitors of αCKSs shows that a positive charge at the reactive center is not necessary for effective inhibition[17, 90].

This TS structure raises the question of what the enzyme can do to promote catalysis. There is no proton transfer occurring in the experimental transition state, so there is no clear role for general acid/base catalysis in this step. Also, there is no major change in charge localization. This would tend to suggest that the enzyme's main catalytic role may be catalysis by approximation[33]. That is, the enzyme's main energetic contribution to catalysis is simply bringing the reactive groups into proximity. This would be consistent with the observation that mutations to DAHPS that cause changes in the specificity constant of up to $10^7$-fold have only minor effects on $k_{cat}$ of ≤100-fold[32]. In contrast, many or most other enzymes experience decreases in $k_{cat}$ on the order of $10^4$- to $10^5$-fold when catalytic residues are mutated[108]. This would argue that the enzyme's most important catalytic strategy is simply to bring the reactants together in the correct orientation to allow them to react.

The implications of the experimental transition state for inhibitor design are that cationic mimics are unlikely to be effective inhibitors. The effectiveness of the oxime-based inhibitors developed by the Berti lab[17, 30, 31], including NeuNAc oxime ($K_i^* \approx 0$)[31] may stem primarily from them bridging the length of the active site, from the proximal PEP/THI phosphate binding site to the distal O9 hydroxyl group[17]. Another useful feature of the oxime inhibitors is that they are able to occupy the phosphate binding site with a small, neutral phosphate mimic that does not

hinder membrane permeability in the way that other phosphate bioisosteres like phosphonate does[63]. The oxime inhibitors all display extended residence times that could be due to the inhibitors subverting the usual conformational changes the enzyme undergoes to catalyze product release[17, 30, 31]. The future of αCKS inhibitor design is an open question at this point, but it will certainly require strategies that do not rely on mimicking a non-existent positive charge on the transition state.

## 3.5 Conclusions

We have performed TS analysis on NeuB by measuring multiple KIEs to reveal the TS structure and provide a target for rational inhibitor design. We developed new methods for measuring the $^{18}O$ KIEs by NMR and measured the 3-$^{13}C$, 2-$^{13}C$, and 2-$^{18}O$ KIEs. We improved peak shape to decrease experimental errors by using autoshimming and EDTA to remove contaminating paramagnetic mal ions. The experimental 3-$^{13}C$ KIE was normal, while the 2-$^{13}C$ and 2-$^{18}O$ KIEs were close to unity. This reveals that the enzymatic transition state is for formation of the THI rather than its breakdown and that the TS involves formation of the C3···C1' bond with no involvement of the water nucleophile, and little charge development. This TS structure explains the ineffectiveness of previous cationic inhibitors and suggests a route forward for inhibitor design.

# 4 Transition state analysis of DAHP synthase

Many compounds are designed with TS mimicry in mind, but experimentally demonstrating TS mimicry is not straightforward. One experimental technique is linear free energy relationship (LFER) analysis to demonstrate a linear relationship between $\log(K_m/k_{cat})$ vs. $\log(K_i)$, which indicates that any perturbation that affects the free energy of TS stabilization has an equal or a proportional effect on the free energy of inhibitor binding[32]. LFER analysis of six DAHPS mutants demonstrates that DAHP oxime is a TS mimic[32], however, LFER analysis does not reveal which transition state is being mimicked. My third research project was to perform TS analysis on DAHPS by measuring multiple KIEs to understand the catalytic mechanism of the enzyme and to determine the TS structure, leading ultimately to the design of TS mimics based on the structure of the transition state. Experimental $^{13}C$ KIEs and $^{18}O$ KIEs were measured as described in Chapter 3.

## 4.1 Material and Methods

### *4.1.1 DAHPS$_{H6}$*

The expression plasmid for *N*-terminally $His_6$-tagged *E. coli* DAHPS(Phe) $DAHPS_{H6}$ was transformed into *E. coli* BL21(DE3) cells by heat shock, plated on an LB agar plate containing 25 μg/mL chloramphenicol and incubated at 37 °C overnight. The overnight 50 mL culture was transferred to 1 L of LB broth containing 25μg/mL of chloramphenicol and grown at 37 °C to $OD_{600}$ = 0.6. Overexpression of $DAHPS_{H6}$ was induced by adding 0.2 mM IPTG and incubating at 37 °C for 4 h. The cell pellet (2.5g) was resuspended in 15 mL of Buffer A (50 mM Tris-Cl, pH 7.5, 100 mM KCl, 25 mM imidazole) and protease cocktail inhibitor, and lysed using

CelLytic B (Sigma Aldrich). The lysate was centrifuged at 8,000 rpm for 30 min at 4 °C. The cell lysate was filtered through a 0.45 μm filter, and the supernatant was loaded onto a 1 mL pre-washed $Ni^{2+}$-charged Chelating-Sepharose Hi-trap (GE Life Sciences) column. The column was eluted with 10 column volumes (CV) of Buffer A, 20 CV of 10% Buffer B (50 mM Tris-Cl, pH 7.5, 100 mM KCl, 500 mM imidazole), and 10 CV of 80% Buffer B, then eluted with 10 CV of 100% Buffer B. The eluted protein was examined by SDS-PAGE and dialyzed against 1 L of dialysis buffer C (50mM Tris-Cl, pH 8.0, 150 mM KCl, 25 mM imidazole and 10% glycerol for 24 h, then 1 L dialysis buffer D (50 mM Tris-Cl, pH 7.5, 100 mM KCl, 1 mM TCEP, and 10% (v/v) glycerol) for 4 h. $DAHPS_{H6}$'s concentration was 40.3 μM, as determined from $A_{280}$ using $\varepsilon_{280}$ = 34,166 $M^{-1}$ $cm^{-1}$.[17] The overall yield was 7.9 mg/L of medium.

### *4.1.2 Synthesis of ppsA, labelled PEPs and E4P*

ppsA and labelled PEPs (3-$^{13}$C- , 2-$^{13}$C-, and 2-$^{18}$O PEPs) were synthesized and purified as described in Chapter 3. E4P was synthesized and purified as described in Chapter 2. However, due to the continued low yield in synthesizing E4P, even after significant optimization, it was decided to purchase E4P from Sigma Aldrich. The commercial E4P was quantified using RSA and MGAM assay.

### *4.1.3 Experimental KIEs and computational TS structures*

The MGAM colorimetric assay[181] was used to measure the DAHPS initial velocities ($v_0$) by following $P_i$ production. Typical reaction conditions were 20 nM DAHPS with 500 μM PEP, 250 μM E4P, 100 μM $MnCl_2$, and 100 μM TCEP in 50 mM K-HEPES, pH 7.0, in 200 μL. DAHPS shows maximum activity with $MnCl_2$ as the metal activator[82]. Aliquots (20 μL) of reaction mixture were added to 96 well plate containing 50 μL MGAM solution and 30 μL

dd$H_2O$ every 60 s and each reaction was quenched with 10 µL of 34 % trisodium citrate after 90 s. However, $MnCl_2$ cannot not be used to measure KIEs using NMR as it is paramagnetic and can reduce relaxation times, resulting in broader peaks. Therefore, the diamagnetic, divalent metal ions $ZnCl_2$, $CdCl_2$, and $CaCl_2$ were investigated. DAHPS reactions were run using different concentrations of the metal ion to select the one that gave the best and consistent rate under KIE reaction conditions.

The DAHPS reaction conditions selected for KIE measurement was 10 mM of labelled PEPs, 15 mM E4P, 50 – 100 nM DAHPS, 20 µM $CaCl_2$ (pre-incubated with DAHPS at 22 ℃ for 20 min), 100 µM TCEP in 50 mM K-HEPES, pH 7.0, in 600 µL. All buffers and substrates were treated with Chelex 100 (BioRad) except for $CaCl_2$ and DAHPS. Prior to each KIE measurement, a small-scale reaction in 35 µL volume was run at the same concentrations as the KIE reaction using MGAM assay to ensure the enzyme was fully active and to determine the concentration of DAHPS needed to run the reaction.

The $^{13}C$ and $^{31}P$ peaks showed some asymmetry in the KIE measurement conditions. In an attempt to improve peak shapes adding sub-stoichiometric EDTA was tested, since that was effective with the NeuB reaction. DAHPS rate assays were run with10 or 20 µM EDTA and 20 or 50 µM $CaCl_2$, respectively. However, addition of any amount of EDTA led to a complete loss of rate. Given that the [EDTA] < [$CaCl_2$], it was important to check if any impurity in the $CaCl_2$, or if a bound metal ion within DAHPS's active site was responsible for the observed rate. The DAHPS reaction was run under the same reaction conditions except with 20 µM ultrapure $CaBr_2$ pre-incubated with 80 nM DAHPS in absence of $CaCl_2$.

The final KIE reaction conditions for the DAHPS-catalyzed reaction consisted of 5 mM of each labelled PEP, 15 mM E4P, 80 – 100 nM DAHPS pre-incubated with 20 µM ultrapure $CaBr_2$, 10 % $D_2O$, and 100 µM TCEP in 50 mM K-HEPES (pH 7.0).

KIEs were measured competitively using quantitative $^{13}C$ and $^{31}P$ NMR using **Equation 15** and for $R_i$ and $RP_i$ **Equation 16**[142, 146, 156]. Labelled PEPs were synthesized, purified and confirmed as described in Chapter 3. The data was autophased, baseline corrected, FIDs were zero-filled using 1024k, and 'lb' was adjusted to 75 % of the line width at half height of the line of interest of the narrowest peak to improve the S/N[154]. Peak areas were calculated using Voigt peak deconvolution in PeakFit and the calculated peak areas were fitted to **Equation 12** to find $R_i/R_0$. $F_1$ was measured using the ratio of the PEP peak to the K-HEPES $C_2$ peak at 51.5 ppm in $^{13}C$ NMR spectra, or the P atom in glyphosate for $^{31}P$ spectra (**Equation 13**) (**Figure 4.7**).

All computational TS structures were found by Paul Berti using the methods described in Chapter 3.

## 4.2 Results

### *4.2.1 $DAHPS_{H6}$*

$DAHPS_{H6}$ was expressed, purified, flash frozen, and stored at -80 ℃ (**Figure 4.1**).

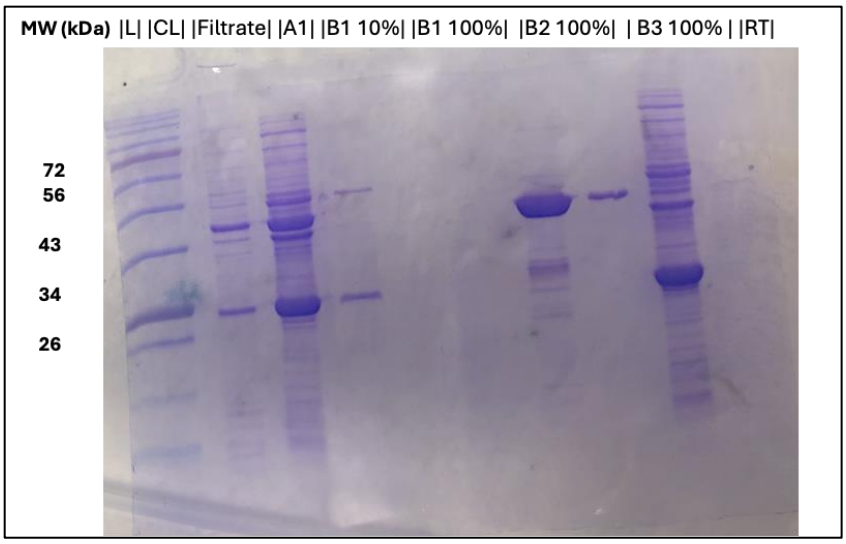


Figure 4.1: SDS-PAGE confirming $DAHPS_{H6}$ protein

Lanes :L: Protein standards; CL: Cell Lysate; Filtrate: Cell lysate after 0.2 µm filtration; A1: Wash buffer A-1; B1: Wash buffer B-1; B2 – B3: Elution buffer RT: Run-through

### *4.2.2 Measuring experimental KIEs*

Competitive 3-$^{13}$C, 2-$^{13}$C, and 2-$^{18}$O KIEs on PEP in the DAHPS reaction were measured using $^{13}$C- and $^{31}$P reporter nuclei. DAHPS requires a metal ion for its activity, and it shows maximum activity with $Mn^{2+}$.[82] However, as $Mn^{2+}$ is paramagnetic, it can reduce relaxation times, resulting in broader NMR peaks. Therefore, it was important to select a diamagnetic, divalent metal ion that would allow for the measurement of the isotopic ratio on the live DAHPS reaction for 6 – 8 h. DAHPS reactions were run with 20 µM $ZnCl_2$, and 20 µM and 1 mM $CaCl_2$ and $CdCl_2$, plus 100 µM $MnCl_2$ as a control reaction. However, a very low rate was observed with $ZnCl_2$. Previously, experiments with $ZnCl_2$ in this lab did not give reliable rates, and it has been reported that while $ZnCl_2$ can activate DAHPS, small excesses inactivate the enzyme[49]. Therefore, $ZnCl_2$ was not explored further. Reactions with 20 µM $CdCl_2$ did not give consistent results while 50 µM did give consistent rates. However, 20 µM $CaCl_2$ also gave consistent rates

when pre-incubated with DAHPS, so it was selected, as $Ca^{2+}$ is more physiologically relevant than $Cd^{2+}$.

Similar to NeuB, peak shape shoulders and inconsistency were also observed with the first two 3-$^{13}$C KIE measurements, even before DAHPS and metal ion were added (**Figure 4.2**). The labelled material in this reaction mixture, [2-$^{13}$C]PEP, showed symmetrical $^{13}$C peaks after purification and peak shape problems were not observed in the 2-$^{13}$C or 2-$^{18}$O KIE reaction mixtures, so this was an issue associated with the 3-$^{13}$C KIE. It was possible that something in the reaction mixture was interacting with the phosphate group of the labelled PEP and also affecting the 2-$^{13}$C reference peak due to two bond $^{31}$P:$^{13}$C coupling. It was also possible that some undesirable metal ion was present in the reaction mixture.

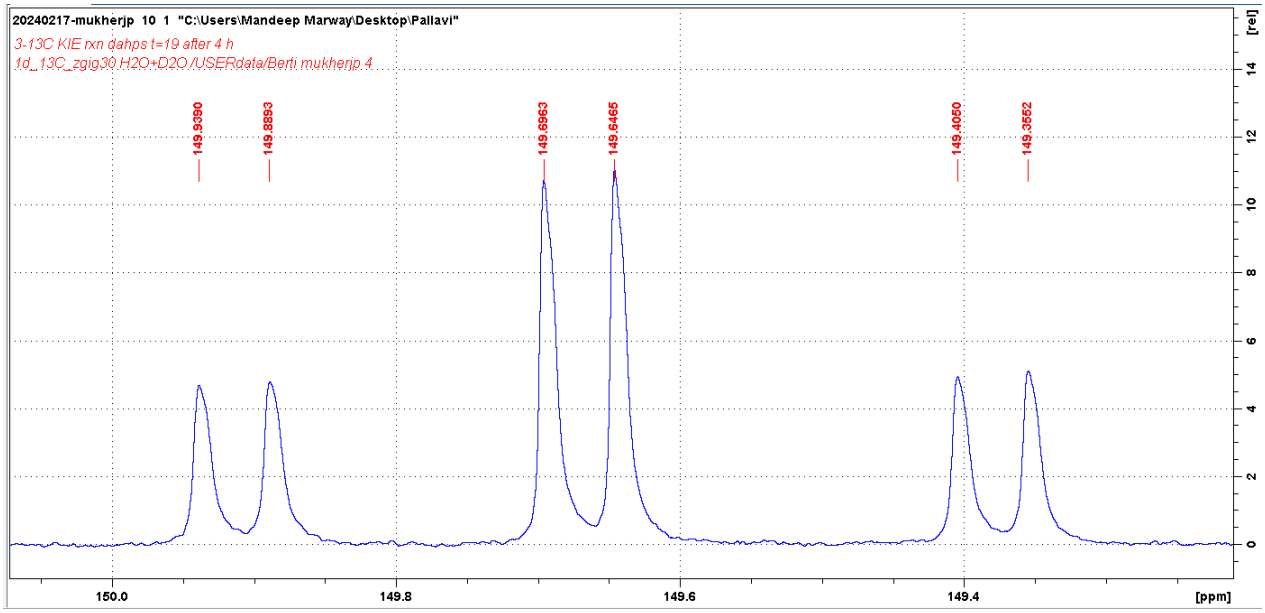


Figure 4.2 Asymmetrical 2-$^{13}$C peaks observed when measuring [3-$^{13}$C]PEP KIE

$^{13}$C NMR of a 3-$^{13}$C KIE reaction mixture containing [2-$^{13}$C]- and [2,3-$^{13}C_2$]PEP. The 2-$^{13}$C reference isotope peaks at ~140 ppm clearly show shouldering and asymmetrical peak shapes. The spectrum was processed using lb = 0 and SI = 1024k.

A similar problem in the NeuB reaction was solved using sub-stoichiometric EDTA. However, the DAHPS reaction rate went to zero with $CaCl_2$ in the presence of substoichiometric

concentrations of EDTA. Given that the DAHPS rate was zero even when [EDTA] < [$CaCl_2$], it was important to check whether the observed rate in the presence of 20 µM $CaCl_2$ was really due to $Ca^{2+}$ or some metal impurity present in $CaCl_2$. The DAHPS reaction was run under the same reaction conditions with 20 µM ultrapure $CaBr_2$ (99.99% on trace metal basis) and gave a rate comparable to $CaCl_2$. To continue our efforts to improve the peak shape using EDTA, the DAHPS reaction was run with 20 µM ultrapure $CaBr_2$ and 10 µM EDTA. Similar to the reaction with $CaCl_2$, there was no rate observed with ultrapure $Ca^{2+}$. To confirm that the observed rate was not due to a bound metal ion in the active site of DAHPS that did not exchange during dialysis with EDTA, the reaction was run without added metal ions. No rate was observed, confirming that DAHPS enzyme was dialysed successfully and required a metal ion for its activation. The complete loss of reaction rate in the presence of substoichiometric EDTA could not be explained. When the 3-$^{13}$C KIE was measured using ultrapure $CaBr_2$, the peak shapes had improved compared to the previous measurements performed, so $CaBr_2$ was used for all KIE measurements thereafter.

Before performing the next 3-$^{13}$C KIE reaction, the starting material 2-$^{13}$C PEP was treated with more Chelex100 and the peak shape were confirmed using $^{13}$C NMR. Adding Chelex100 did not improve peak shape significantly. It was observed that issues related to shimming affected the peak shape of the NMR spectrum, so the sample was re-shimmed every 2 – 3 h, in addition to autoshimming, to improve the peak shapes. This combination of re-shimming the sample as the reaction progressed, replacing $CaCl_2$ with ultrapure $CaBr_2$, and processing the data using a higher lb value improved peak shape and peak area calculations.

### *4.2.2.1 3-$^{13}$C KIE measurement*

The 3-$^{13}$C KIE was measured using a mixture of [2-$^{13}$C]- and [2,3-$^{13}$C]PEPs **(Figure 4.3).** The NMR data was processed on TopSpin. The data was auto phased by first selecting a range of chemical shift (absf1 = 152 ppm and absf2 = 148 ppm) and then autophasing that region using the 'apkf' command. The improved S/N spectrum was baseline corrected, zero-filled using 512k or 1024k points, and 'lb'= 0.6.

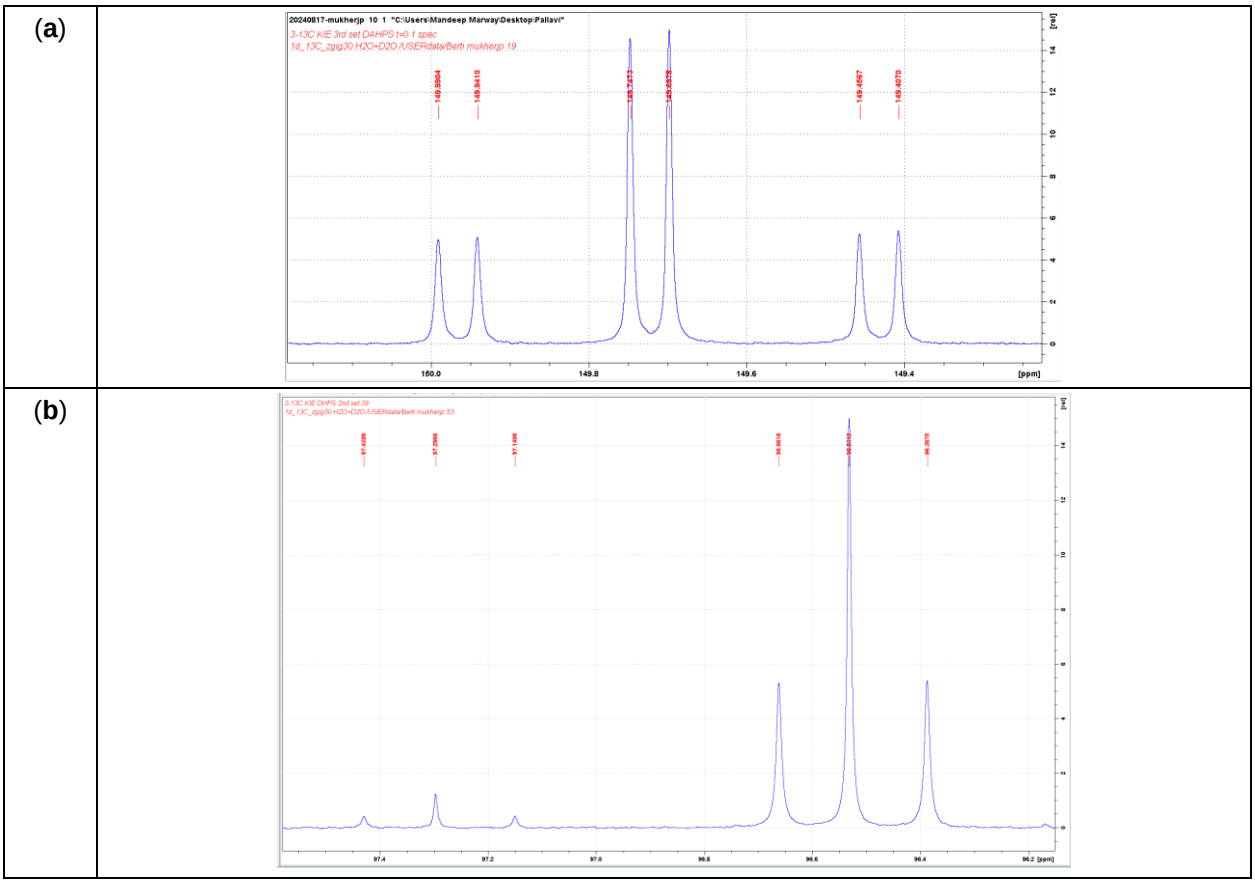


Figure 4.3: $^{13}$C-NMR of the 3-$^{13}$C KIE reaction mixture

(**a**) Substrate peaks, [2,3-$^{13}C_2$]PEP at 149.97 & 149.93 ppm and 149.44 & 149.40 ppm, and [2-$^{13}$C]PEP at 149.73 & 149.75 ppm. (**b**) Product peaks of α- and β-anomers of [2,3-$^{13}C_2$]DAHP at 97.42 & 97.14 ppm and 96.66 & 96.38 ppm, and [2-$^{13}$C]DAHP 97.3 & 96.50 ppm, processed using lb = 0.6 and SI = 1024k.

The isotope ratios, $R_i$ and $RP_i$, were measured in the reactant and product by calculating the peak areas for the reactant, product and K-HEPES (internal reference) using peak

deconvolution in PeakFit. $R_i$ and $F_1$ were calculated using **Equation 12Equation 13** described in Chapter 1**.** Fitting the isotope ratio data to (**Equation 15 & Equation** 16) gave an overall large, normal 3-$^{13}$C KIE of 1.024 ± 0.004 **(Table 4.1)**. A typical progress curve of isotope ratio versus $F_1$ is shown for reactant and product peaks (**Figure 4.4**).

Table 4.1 3-$^{13}$C Experimental KIEs

| Experiment no. | 3-$^{13}$C KIEs [a] | |
|---|---|---|
| | Reactant (**Equation 15**) | Product (**Equation 16**) |
| 1 | 1.0214 ± 0.005 | 1.0208 ± 0.018 |
| 2 | 1.0218 ± 0.006 | 1.0227 ± 0.010 |
| 3 | 1.0267 ± 0.005 | 1.0312 ±0.004 |
| Mean (± 95% C. I.) | 1.024 ± 0.004 | |

[a] For individual experiments, the reported experimental error is the standard error on the fitted KIE value in Equation 15 or 16. The overall experimental error is the 95% confidence interval on the mean of all measurements.

A normal 3-$^{13}$C KIE indicates that THI formation is the first irreversible step of the DAHPS-catalyzed reaction, i.e., the C3 of PEP is forming a bond with C1’ of E4P at the transition state **(Figure 4.4)**. As with the NeuB reaction, an inverse KIE would have been expected if the transition state was either water attack on the cationic intermediate during THI formation, or if it was THI breakdown.

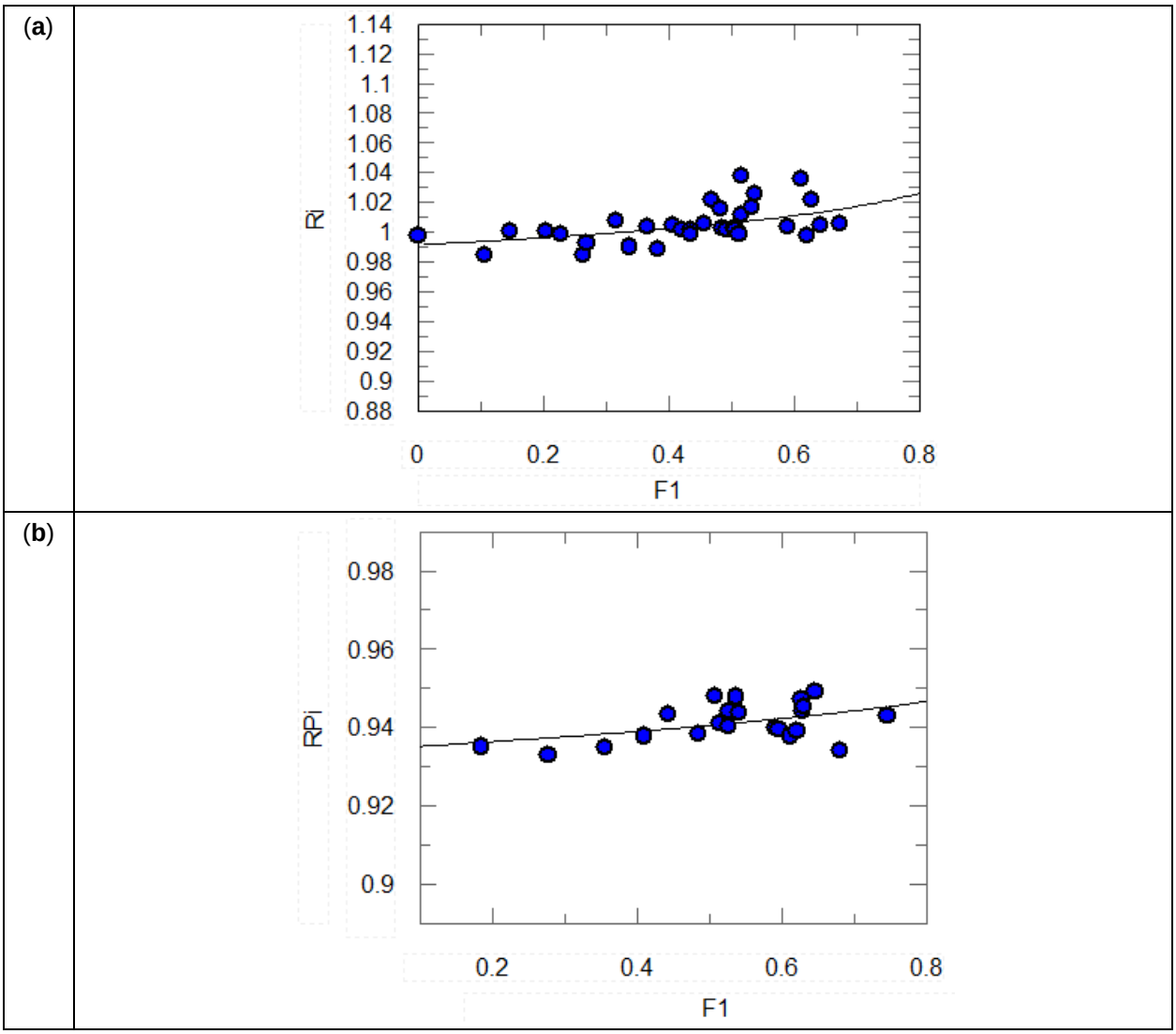


Figure 4.4: 3-$^{13}$C KIE measurements: isotope ratios vs. extent of reaction.

Isotope ratios for 3-$^{13}$C KIE measurement showing (a) $R_i$ vs $F_1$ for the PEP reactant and (b) $RP_i$ vs. $F_1$ for the DAHP product.

### *4.2.3 2-$^{13}$C-KIE Measurement*

The 2-$^{13}$C KIE was measured using a mixture of [3-$^{13}$C]- and [2,3-$^{13}$C]PEPs (**Figure 4.5**), using the same methods as the 3-$^{13}$C KIE.

(a)

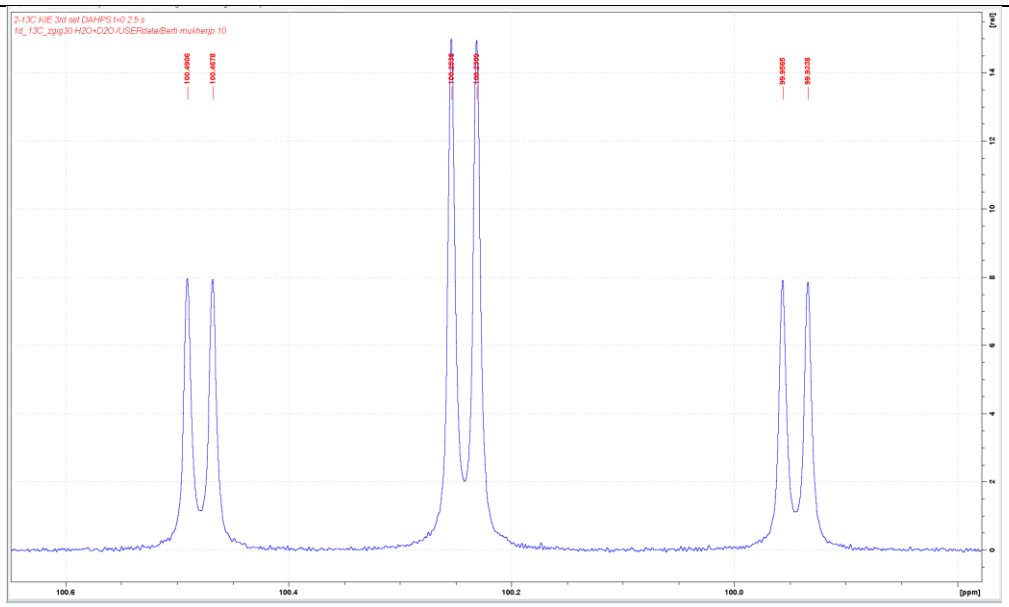


(b)

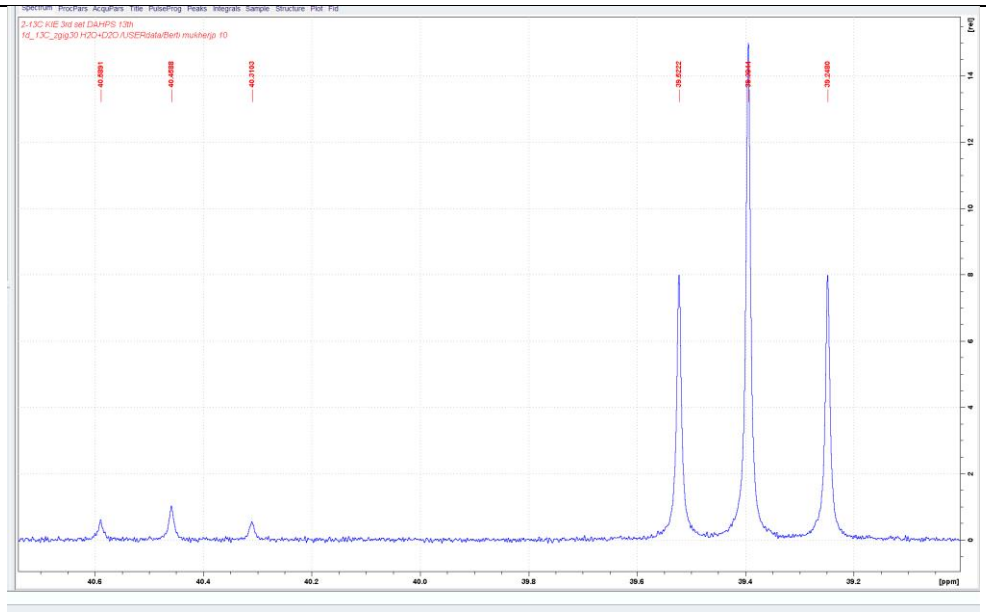


Figure 4.5: $^{13}$C-NMR of the 2-$^{13}$C KIE reaction mixture

(**a**) Substrate peaks, [2,3-$^{13}C_3$]PEP at 100.49 & 100.46 ppm and 99.95 & 99.93 ppm, and [2-$^{13}$C]PEP at 100.25 & 100.23 ppm. (**b**) Product peaks of the α- and β-anomers of [2,3-$^{13}C_2$]DAHP at 40.59 & 40.31 ppm and 39.52 & 39.24 ppm, and [3-$^{13}$C]DAHP at 40.45 & 39.38 ppm, processed using lb = 0, SI =1024k.

The data was processed similarly to the 3-$^{13}$C KIE measurement. Three KIE reactions, fitting substrate ratios to give three 2-$^{13}$C KIE measurements gave an inverse value of 2-$^{13}$C KIE

= 0.988 ± 0.005 (**Table 4.2**). The inverse 2-$^{13}$C KIE indicates that there is no bond formation between C2 of PEP and O2' of the nucleophilic $H_2O$ at the transition state (**Figure 4.6**).

Table 4.2: 2-$^{13}$C Experimental KIEs

| | 2-$^{13}$C KIEs [a] |
|---|---|
| Experiment no. | Reactant (**Equation 15)** |
| 1 | 0.986 ± 0.002 |
| 2 | 0.988 ± 0.002 |
| 3 | 0.990 ± 0.003 |
| Mean (± 95% C. I.) | 0.988 ± 0.005 |

[a] For individual experiments, the reported experimental error is the standard error on the fitted KIE value in Equation 15. The overall experimental error is the 95% confidence interval on the mean of all measurements.

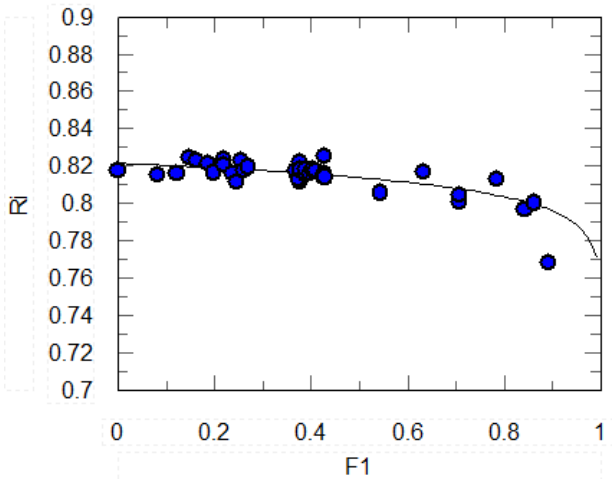


Figure 4.6: 2-$^{13}$C KIE measurements: isotope ratios vs. extent of reaction

Isotope ratios for 2-$^{13}$C KIE measurement showing $R_i$ vs $F_1$ for the PEP reactant.

### *4.2.4 Measuring 2-$^{18}$O-KIE*

The 2-$^{18}$O KIE was measured using a mixture of [2-$^{18}$O]- and unlabelled PEPs using $^{31}$P NMR (**Figure 4.7**)**.** To calculate the 2-$^{18}$O KIE, $F_1$, $R_i$, and $RP_i$ were calculated using **Equation 12Equation 13** on the reactant 2-$^{18}$O KIE was calculated using **Equation 15.**

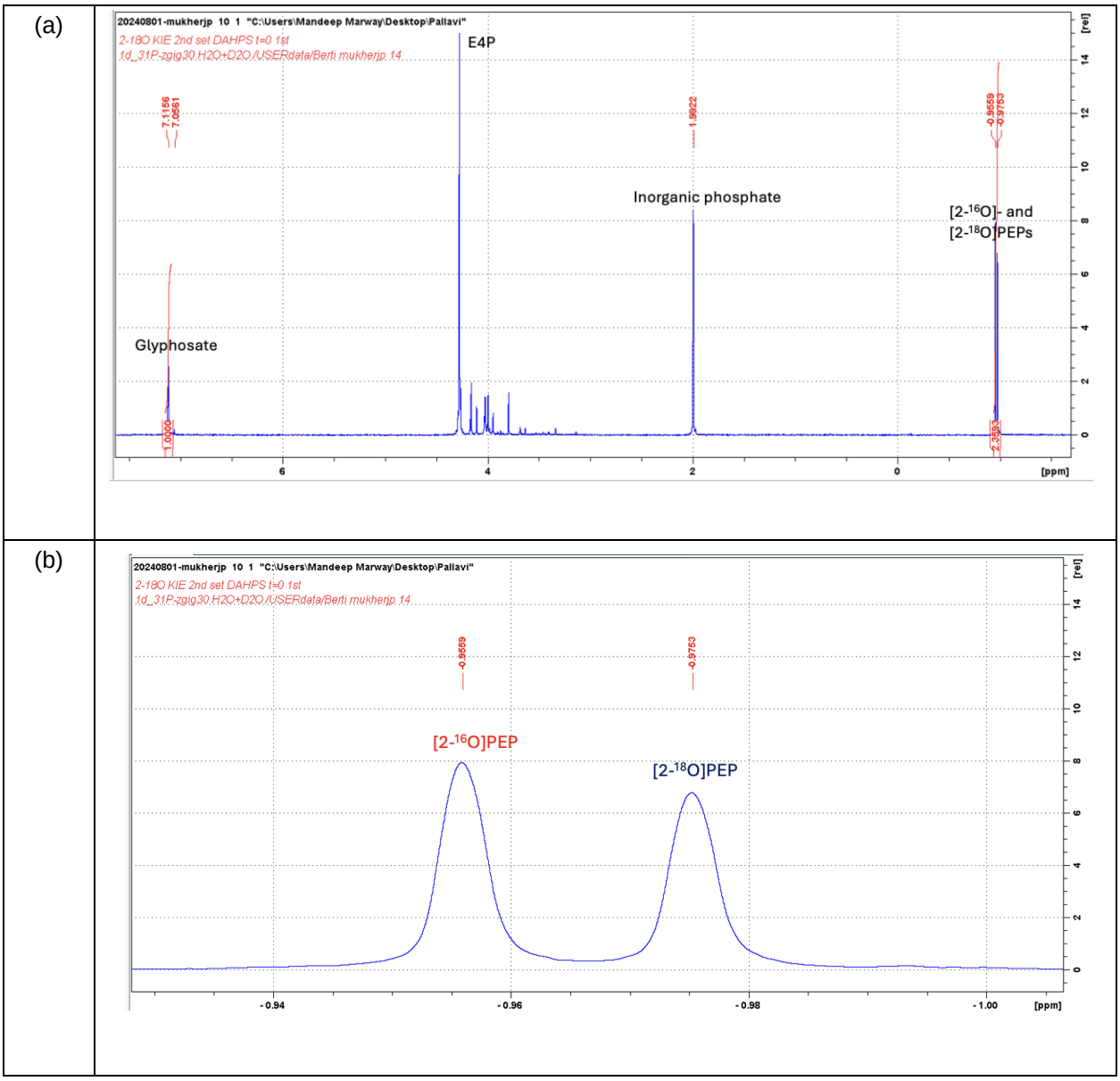


Figure 4.7: $^{31}$P-NMR of the 2-$^{18}$O KIE reaction mixture

(**a**) Zoomed out spectrum showing $^{18}$O and $^{16}$O PEP, Pi (1.99 ppm), E4P (4.36 to 3.13 ppm), and internal standard Glyphosate peaks (7.11, 7.05 ppm. (**b**) Zoomed in substrate peaks [2-$^{18}$O]PEP at -0.9752 ppm and unlabelled PEP at -0.9559 ppm (lb = 0, SI = 1024k).

The experimental 2-$^{18}$O KIE was 1.007 ± 0.006 **(Table 4.3)**. A small, normal 2-$^{18}$O KIE demonstrates that THI breakdown is not the first irreversible step since the C2−O2 bond cleavage would result in a large, normal KIE (**Figure 4.8**).

Table 4.3: 2-$^{18}$O Experimental KIEs

| Experiment no. | 2-$^{18}$O KIEs [a] |
|---|---|
| | Reactant (**Equation 15)** |
| 1 | 1.004 ± 0.007 |
| 2 | 1.009 ± 0.004 |
| 3 | 1.006 ± 0.004 |
| Mean (± 95% C. I.) | 1.007 ± 0.006 |

a For individual experiments, the reported experimental error is the standard error on the fitted KIE value in Equation 15. The overall experimental error is the 95% confidence interval on the mean of all measurements.

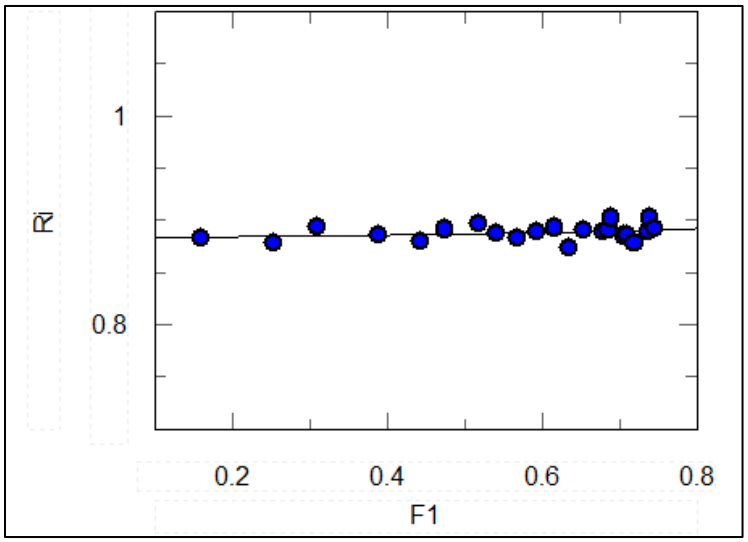


**Figure 4.8: 2-$^{18}$O KIE measurements: isotope ratios vs. extent of reaction**

Isotope ratios for 2-$^{18}$O KIE measurements showing $R_i$ vs $F_1$ for the PEP reactant.

The table below (**Table 4.4)** provides a consolidated list of all the experimental KIEs measured on the DAHPS reaction.

Table 4.4: Experimental KIEs for the DAHPS-catalyzed reaction.

| Isotopic label | Experimental KIEa | nb |
|---|---|---|
| 2-$^{13}$C | 0.988 ± 0.005 | 3 |
| 3-$^{13}$C | 1.024 ± 0.004 | 6 |
| 2-$^{18}$O | 1.007 ± 0.006 | 3 |

*a* Experimental error reported as the 95% confidence interval.

*b* Number of independent trials. For the 2-$^{13}$C and 3-$^{13}$C KIEs, this reflects three replicate reactions with KIEs calculated separately from isotope ratios on both the residual reactant and products. The 2-$^{13}$C KIE in product analysis is in progress. For 2-$^{18}$O KIE, the KIE was measured in four independent reactions using $^{31}$P as the reporter nucleus.

### *4.2.5 Computations*

In this study, the computational models needed to generate computational KIEs were built up from the models for the NeuB reaction. There is a difference in the metal ion interactions between NeuB and DAHPS. In NeuB crystal structures the metal ion bridges between the ManNAc's carbonyl oxygen and a non-bridging phosphate oxygen in PEP (**Figure 1.10**). In DAHPS, the metal ion is able to interact with the E4P's carbonyl oxygen but is distant from the PEP/THI phosphate group (**Figure 4.9**).

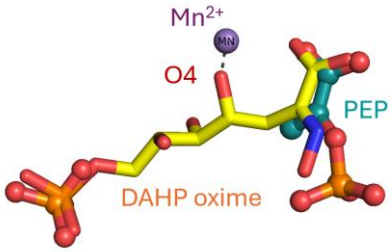


Figure 4.9: Metal ion interactions in DAHPS

Crystal structures of DAHP oxime (yellow) and PEP (teal) in the DAHPS active site showing $Mn^{2+}$'s (purple) potential interactions with DAHP oxime O4 (equivalent to E4P O1) and distance from the PEP/THI phosphate group PDBID: 5CKS and 8E0X)[17, 46].

The reactants used were PEP and acetaldehyde to model E4P (**25**), Li, $H_2O$, and $NH_4^+$ ions to mimic active site residues, and different divalent metal ($Mg^{2+}$, $Ca^{2+}$, $Mn^{2+}$) ions complexed with $^-OH$ and $H_2O$ molecules. Given a normal 3-$^{13}C$ KIE and an inverse 2-$^{18}O$ KIE, TS structures focused on THI formation. All but one of the computational TS models found were for stepwise formation of the cationic intermediate, i.e., C3−C1' bond formation. One TS model, **56**‡, reflected water attack on the cationic intermediate, i.e., C2−O2' bond formation (**Figure 4.11**).

A More O'Ferrall-Jencks plot was created to show all the computational TS structures for the DAHPS. The plot shows reactants on the bottom left corner and the THI on the top right

corner. The *y*-axis corresponds to the C3−C1' bond order, $n_{C3-C1'}$,between PEP C3 and E4P C1'. The *x*-axis corresponds to the bond order for the formation of the new C2−O2' bond between PEP C2 and the water nucleophile, O2'. The plot shows 19 computational TS structures **(Figure 4.10)**.

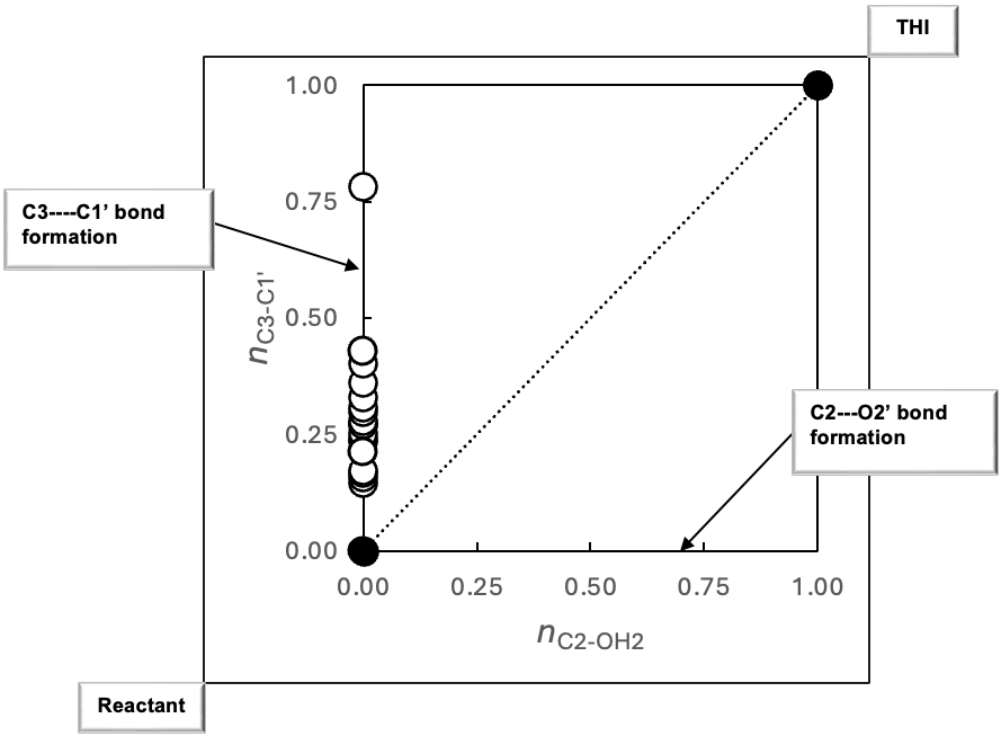


Figure 4.10: More O'Ferrall–Jencks plot for THI formation during DAHPS reaction

The bond order was calculated using Pauling bond order: $n_{ij}=e^{(r_1-r_{ij})/0.3}$ as described in Chapter 3.

Keeping in mind the differences in the active site interactions between NeuB and DAHPS, the first reaction model was created by appropriately orienting PEP and acetaldehyde with $Mg^{2+}$ placed away from the phosphate group, complexing with one of the oxygens of PEP's carboxylate group and the carbonyl oxygen of the acetaldehyde with all the computational TS structures (**Figure 4.11)** (**Table 4.5**). The phosphate non-bringing oxygens formed ionic interactions with two $Li^+$ ions. This gave an early computational TS structure (**48**‡) with an

imaginary frequency of -309 $cm^{-1}$ (**Figure 4.11)**. This reaction model was further optimized using $NH_4^+$ ions, $Li^+$ ions, water molecules, and hydroxide ions to mimic the interaction between PEP's non-bridging oxygens and carboxylate oxygens, the metal ion and the carbonyl oxygen of the acetaldehyde (**Figure 4.11**).The computational TS models were relatively insensitive to the nature of the counterions, and most had incoming bond orders, $n_{C3\text{-}C1'}$, from 0.15 to 0.43, in spite of significant differences in the surrounding atoms (**Figure 4.11**).

Table 4.5. Calculated KIEs for computational TS structures for DAHPS reaction.

| | | Calculated KIEs | | |
|---|---|---|---|---|
| **Structure no.** | $n_{C3\text{-}C1'}$ [a] | **3-$^{13}$C** | **2-$^{13}$C** | **2-$^{18}$O** |
| **51‡** | 0.15 | 1.030 | 1.002 | 1.004 |
| **49‡** | 0.16 | 1.030 | 0.999 | 1.010 |
| **48‡** | 0.17 | 1.030 | 0.999 | 1.007 |
| **50‡** | 0.17 | 1.031 | 0.999 | 1.004 |
| **61‡** | 0.21 | 1.029 | 0.999 | 1.005 |
| **52‡** | 0.24 | 1.032 | 1.001 | 1.005 |
| **63‡** | 0.24 | 1.030 | 0.999 | 1.005 |
| **53‡** | 0.25 | 1.027 | 1.002 | 1.005 |
| **65‡** | 0.27 | 1.016 | 0.998 | 1.001 |
| **66‡** | 0.27 | 1.026 | 0.998 | 1.004 |
| **54‡** | 0.28 | 1.029 | 1.002 | 1.005 |
| **59‡** | 0.30 | 1.023 | 1.000 | 1.002 |
| **55‡** | 0.31 | 1.031 | 0.999 | 1.005 |
| **62‡** | 0.33 | 1.032 | 1.000 | 1.006 |
| **64‡** | 0.36 | 1.027 | 1.001 | 1.002 |
| **57‡** | 0.40 | 1.031 | 1.000 | 1.006 |
| **58‡** | 0.43 | 1.031 | 1.000 | 1.006 |
| **60‡** | 0.43 | 1.028 | 1.001 | 1.005 |
| **56‡** | 0.78 | 1.002 | 1.014 | 1.016 |

[a] C3−C1' Pauling bond order, $n_{C3-C1'} = e^{\frac{r_1 - r_{ij}}{0.3}}$, where $r_1$ is the single bond length for a bond between atom types *i* and *j*, and $r_{ij}$ is the observed bond length.

To understand the importance of the metal ion in the active site of DAHPS and how it affects the TS structure, reaction models were created in absence of metal ion. Instead, weaker

acids like $NH_4^+$ (**53‡, 59‡ ,65‡, and 66‡)** and $CH_3{-}NH_3^+$ (**54‡ and 64‡)** were used to interact with the acetaldehyde carbonyl oxygen. Several $Li^+$ ions, $H_2O$, and $NH_4^+$ interacted with PEP's non-bridging oxygens and carboxylate oxygens (**Figure 4.11**).

Next, reaction models were created to understand the role of metal ion and its interaction in the active site of DAHPS, and its effects on the computational TS structures. While keeping other counter ions and solvation constant, metal ions $Mg^{2+}$, $Ca^{2+}$, and $Mn^{2+}$ complexed with the acetaldehyde carbonyl oxygen, water molecules, and hydroxide ions and their effects on TS structures were determined (**Figure 4.11**).

(a)

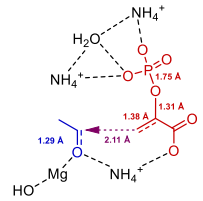

**51‡**
-311 cm$^{-1}$

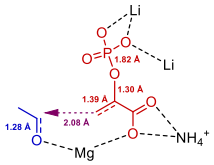

**49‡**
-306 cm$^{-1}$

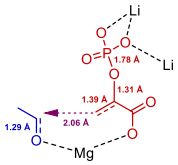

**48‡**
-309 cm$^{-1}$

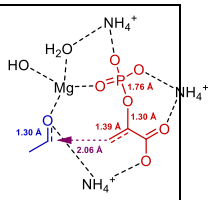

**50‡**
-313 cm$^{-1}$

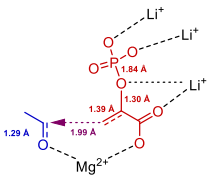

**61‡**
-341 cm$^{-1}$

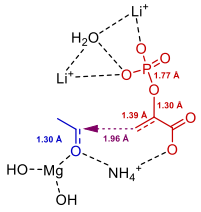

**52‡**
-331 cm$^{-1}$

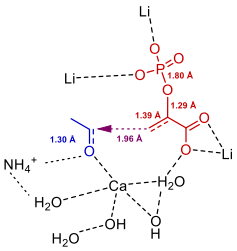

**63‡**
-360 cm$^{-1}$

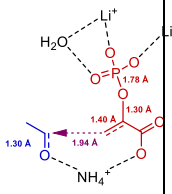

**53‡**
-418 cm$^{-1}$

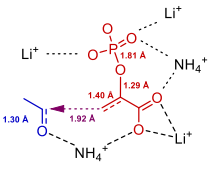

**66‡**
-447 cm$^{-1}$

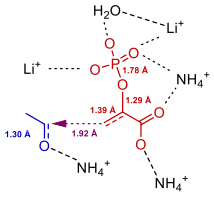

**65‡**
-689 cm$^{-1}$

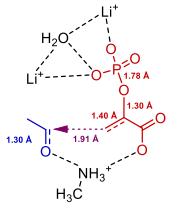

**54‡**
-379 cm$^{-1}$

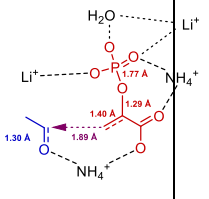

**59‡**
-495 cm$^{-1}$

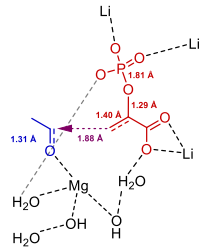

**55‡**
-323 cm$^{-1}$

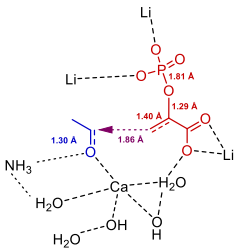

**62‡**
-297 cm$^{-1}$

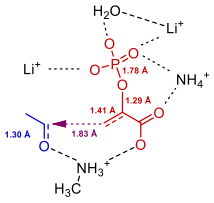

**64‡**
-368 cm$^{-1}$

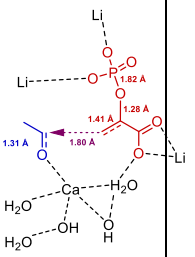

**57‡**
-255 cm$^{-1}$

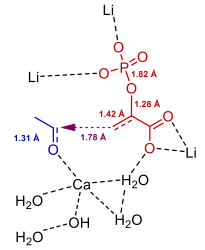

**58‡**
-274 cm$^{-1}$

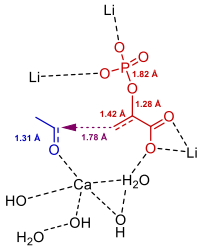

**60‡**
-195 cm$^{-1}$

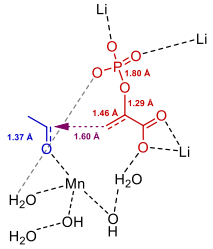

**56‡**
-217 cm$^{-1}$

(b)

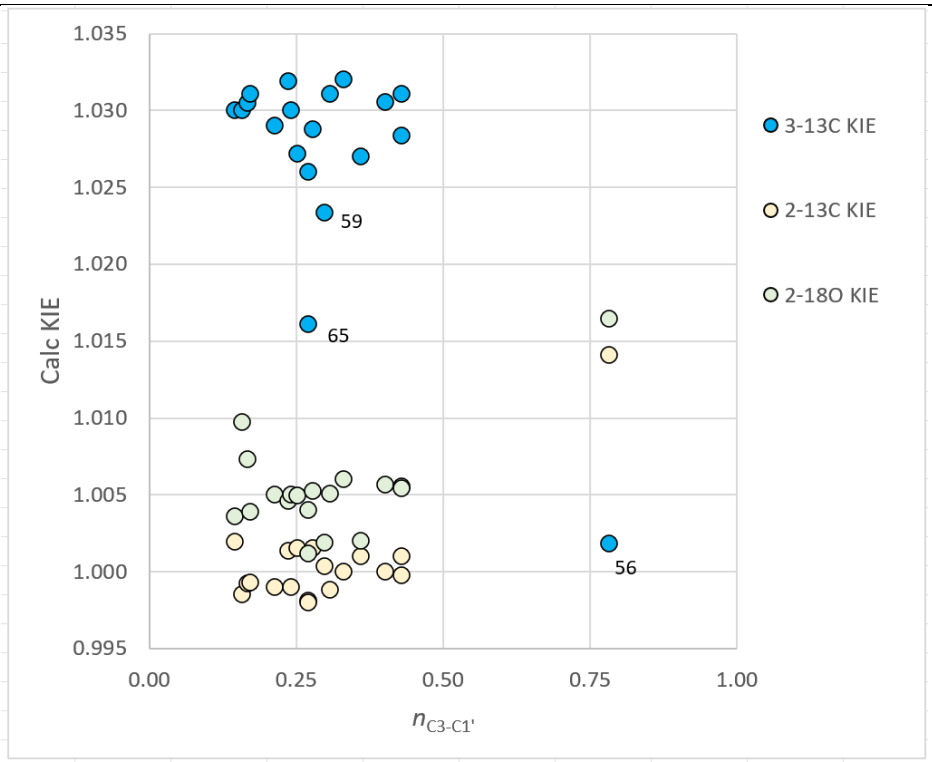


Figure 4.11: Complete computational TS structures

(a) Computational TS structures (**48‡, 49‡, 50‡, 51‡, 52‡, 53‡, 54‡, 55‡, 56‡, 57‡, 58‡, 59‡, 60‡, 61‡, 62‡, 63‡, 64‡, 65‡, and 66‡)** (**b**) Calculated KIEs vs. C3−C1' bond order, $n_{C3\text{-}C1'}$, for the computational TS structures. The TS structures are arranged from low to high *n*(C3-C1').

### *4.2.6 Experimental TS structure*

The experimental KIEs clearly indicate an experimental TS structure in which the C3−C1' bond is being formed during cationic intermediate formation.

The 3-$^{13}$C KIE was large and normal, 1.024 ± 0.004, demonstrating that C3−C1' bond formation is in the reaction coordinate. The computational TS structures have calculated KIEs in the range of 1.016 to 1.032, but the large majority had calculated KIEs > 1.028, the upper limit of the experimental value. The two exceptions were structures **59**‡, with a calculated 3-$^{13}$C KIE of 1.023, almost equal to the experimental value, and **65**‡, at 1.016 (**Figure 4.11**). What distinguished these TS structures were their higher reaction coordinate frequencies, -495 cm$^{-1}$

and -689 $cm^{-1}$, than the average of -320 $cm^{-1}$ for the other computational TS structures. These higher reaction coordinate frequencies were associated with proton transfer to the carbonyl oxygen atom, O1' from $NH_4^+$. There were other TS structures where proton transfer was occurring, namely **53**‡ and **54**‡ **(Figure 4.11)**, but the proton transfer was less pronounced. Their reaction coordinate frequencies were lower, -418 $cm^{-1}$ and -379 $cm^{-1}$, and the calculated 3-$^{13}$C KIEs were higher, 1.027 and 1.029. Based on these trends, the computational TS structures most consistent with the experimental 3-$^{13}$C KIE had O1' protonation in the reaction coordinate. The solvent deuterium KIE was not measured because, as a non-competitive KIE, it would reflect the rate-limiting step rather than the first irreversible step, and for DAHPS, the rate-limiting step is likely product release.[49]

The experimental 2-$^{13}$C KIE, 0.988 ± 0.005, was inverse, demonstrating that C2−O2' bond formation is not part of the reaction coordinate, and therefore that THI formation proceeds through a cationic intermediate rather than a concerted addition reaction to form the THI without any intermediates. The experimental 2-$^{13}$C KIE was more inverse than the calculated values (0.998 to 1.002), and more inverse than the experimental 2-$^{13}$C KIE for the NeuB reaction, 0.994 ± 0.007. The reason for this difference is not yet clear but could be related to DAHPS stabilizing a positive charge at the cationic centre better than NeuB and better than the computational models allow.

The experimental 2-$^{18}$O KIE was slightly normal 1.007 ± 0.006. It was higher than the NeuB value, 0.999 ± 0.006, but consistent with the calculated KIEs for the computational DAHPS TS structures, 1.001 to 1.010. The slightly higher computational KIEs compared with the NeuB computational models presumably reflects the differences in structure, particularly around the metal ion and its interactions with the phosphate group's bridging oxygen.

## 4.3 Discussion

Based on the experimental 3-$^{13}$C- and 2-$^{18}$O KIEs for the DAHPS catalyzed reaction, the first irreversible step is the THI formation. This means that at the transition state, the C3 of PEP is forming a bond with the C1' of E4P. The experimental 2-$^{13}$C KIE is more inverse for DAHPS-catalyzed reaction compared to NeuB reaction. This could mean that there is more cationic character at C2 compared to the NeuB counterpart. However, given the small extent of C3−C1' bond formation expected at the transition state (**Figure 4.10**), the amount of positive charge at C2 is still likely to be modest. The positive charge is likely not developed enough for cationic inhibitor **3** in Chapter 1 to be effective (**Figure 4.12**). This is evident by the inhibition displayed by fragment based inhibitor, pyruvate hydrazone ($K_i$ = 100 µM), and the full length inhibitor DAHP hydrazone ($K_i$ = 10 nM)[90] suggesting favourable interaction between the neutral hydrazone functional group and DAHPS's active site[90].

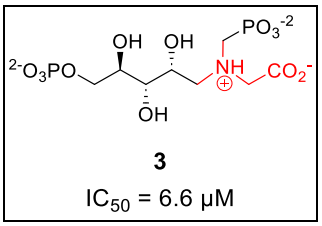


Figure 4.12: Oxacarbenium ion mimic inhibitor **3**

TS analysis not only provides an experimental TS structure, it also allows the charge and the geometric features of the TS structure to be examined[124, 125]. If we can mimic the charge and geometric features at the transition state, it can result in a highly potent inhibitor[131]. LFER analysis on DAHP oxime shows that it is a TS mimic inhibitor of DAHPS[17, 32]. However, it was not clear which transition state structure was being mimicked. LFER analysis was performed

using six DAHPS mutants which were generated and characterized to test for the TS mimicry of DAHP oxime. A linear relationship was obtained between log($K_{M,Mn}K_{M,PEP}K_{M,E4P}/k_{cat}$) and log($K_i$). The effect of mutation on $k_{cat}$ was smaller [32]. K186 is the presumed general acid catalyst during THI breakdown[16, 21, 89, 210]. The K186A mutation decreased $k_{cat}$ 100-fold, but decreased $k_{cat}/K_{M,Mn}K_{M,PEP}K_{M,E4P}$ $10^7$-fold [32]. Based on the crystal structure of DAHP oxime, previously it was proposed that DAHP oxime was mimicking the transition state of THI breakdown[32]. But the experimental KIEs clearly reveal that the first irreversible step in this reaction is THI formation, not breakdown. Similar to the NeuB-catalyzed reaction, it is possible that DAHPS catalyzes its reaction primarily using catalysis by approximation[32]. This means that most of the catalytic energy is employed to bring the reactants closer and in proper orientation[32, 33]. This would be consistent with the larger effect of mutation seen on $k_{cat}/K_{M,Mn}K_{M,PEP}K_{M,E4P}$ compared to $k_{cat}$[32]. It would also be consistent with DAHP oxime being a TS mimic inhibitor. DAHP oxime is able to occupy the whole catalytic site, from the proximal PEP/THI phosphate binding site to the E4P distal phosphate binding site. In this way, it bridges the whole catalytic site, bringing the active site residues into their catalytically active conformations, and thus mimics the transition state of a reaction being catalyzed primarily by approximation. Compound **3** could, in principle, function the same way, but its modest $K_i$ = 6.6 μM suggests that some other unfavourable interaction around its cationic center is reducing its affinity for the enzyme.

Several computational TS structures for THI formation were in close agreement with the experimental KIEs. More computational TS structures will be explored, particularly to explain the more inverse 2-$^{13}$C KIE. These computational TS structures have provided deep insight into the charge and geometric features at the transition state. They also provide a blueprint for developing future TS inhibitors against DAHPS.

As with NeuB, the design of TS mimic inhibitors is now an open question in light of the experimental TS structure. Inhibitors that fill the whole active site and contain small neutral phosphate mimics are one possible path forward, especially if inhibitors can be found that have long residence times.

## 4.4 Conclusion

We have performed TS analysis on DAHPS by measuring multiple KIEs to reveal the TS structure and provide a target for rational inhibitor design. We developed new methods of KIE measurement by NMR and measured the 3-$^{13}$C-, 2-$^{13}$C-, and 2-$^{18}$O KIEs. We improved peak shape to decrease experimental errors using a variety of approaches, including autoshimming and improved sample preparation and composition. The experimental KIEs showed that 3-$^{13}$C KIE is normal and 2-$^{18}$O KIEs were close to unity. However, the 2-$^{13}$C KIE was more inverse compared to the NeuB-catalyzed reaction. This reveals that the enzymatic transition state is for formation of the THI rather than its breakdown and that the TS involves formation of the C3···C1' bond during the formation of the cationic intermediate. There is no involvement of the water nucleophile. A more inverse 2-$^{13}$C KIE suggests that there is more cationic character at the C2 of the cationic intermediate formed during the DAHPS-catalyzed reaction, though it is still likely to be modest. Previously, it was demonstrated that DAHP oxime is a TS mimic inhibitor[17], and proposed it was mimicking the transition state for THI breakdown. This study clarified that the first irreversible in the reaction in THI formation and not its breakdown. However, since DAHPS's main catalytic strategy appears to be catalysis by approximation, that is consistent with DAHP oxime inhibiting the enzyme by filling the catalytic site and bringing it into a TS-like conformation. Several computational TS structures were found showing the C3···C1' bond formation at the transition state while no bond formation is observed between the C2 of PEP and

the nucleophilic water. Future work will involve finding more computational TS structures to explain the experimental inverse 2-$^{13}$C KIE better.

# 5 Concluding Remarks

## 5.1 Conclusions

TS analysis on the NeuB- and DAHPS-catalyzed reactions was performed using new methods of KIE measurement by NMR using $^{13}C$ and $^{31}P$ NMR. Although NeuB and DAHPS belong to the same superfamily of enzymes, there are structural and mechanistic differences. We performed TS analysis on these enzymes to understand their catalytic mechanisms, to provide a target for rational inhibitor design, and to discover any mechanistic differences between them. The experimental 3-$^{13}C$-, 2-$^{13}C$-, and 2-$^{18}O$ KIEs were measured. For NeuB, the experimental KIEs showed that that the enzymatic transition state is for THI formation rather than its breakdown, and that the TS involves formation of the C3···C1' bond but no bond was formed between the PEP C2 and the water nucleophile. There was also very little charge development at the cationic centre of the computational cationic intermediate formed as seen from the electrostatic potential maps. When the C2=C3 double bond breaks, there is are simultaneous and compensating changes in the phosphate group between the P atom and O atoms keep the overall bonding to O2 the same and prevent the accumulation of significant positive charge at C2. The overall effect was that the negative charge on the phosphate group decreased rather than C2 becoming cationic.

The experimental KIEs for the DAHPS-catalyzed reaction also showed that the enzymatic transition state is for THI formation rather than its breakdown. The transition state involves formation of the C3···C1' bond during THI formation. The inverse 2-$^{13}C$ KIE suggests there may be more cationic character at the C2 in the DAHPS-catalyzed reaction than the NeuB-catalyzed reaction. Several computational TS structures were found for the two reactions and KIEs were calculated for them. The computational candidate structures with calculated KIEs that

matched with the experimental KIEs were selected as the potential experimental TS structures. The TS structures explained the ineffectiveness of previous cationic inhibitors and suggests a route forward for inhibitor design.

## 5.2 Future work

Future work would involve finding more computational TS structures to explain the experimental inverse 2-$^{13}$C KIE better. Given the problems with peak shape and shouldering observed during the 3-$^{13}$C KIE measurement and although we optimized the method, it would be helpful to gain a better understanding of the factors affecting the NMR spectrum quality. TS analysis of NeuB and DAHPS-catalyzed reaction provides a blueprint for designing antibiotics/inhibitors based on the experimental TS structure.

# 6 References

(1) CDC. *Antibiotic Resistant Threats in the United States*; CDC, 2019.
(2) Gaynes, R. The Discovery of Penicillin—New Insights After More Than 75 Years of Clinical Use. *Emerg Infect Dis* **2017**, *23* (5), 849-853. DOI: 10.3201/eid2305.161556 PMC.
(3) Walsh, C.; Wright, G. Introduction: Antibiotic Resistance. *Chem. Rev.* **2005**, *105* (2), 391-394. DOI: 10.1021/cr030100y.
(4) Davies, J.; Davies, D. Origins and Evolution of Antibiotic Resistance. *Microbiol. Mol. Biol.* **2010**, *74* (3), 417–433. DOI: 10.1128/MMBR.00016-10.
(5) Sengupta, S.; Chattopadhyay, M. K.; Grossart, H. P. The multifaceted roles of antibiotics and antibiotic resistance in nature. *Front. Microbiol.* **2013**, *4*. DOI: 10.3389/fmicb.2013.00047.
(6) Munita, J. M.; Arias, C. A. Mechanisms of Antibiotic Resistance. *Microbiol Spectr* **2016**, *4* (2), 1-24. DOI: 10.1128/microbiolspec.VMBF-0016-2015 PubMed.
(7) Aslam, B., Wang, W., Arshad, M. I., Khurshid, M., Muzammil, S., Rasool, M. H., Baloch, Z. Antibiotic resistance: a rundown of a global crisis. *Infection and Drug Resistance* **2018**, *11*, 1645–1658. DOI: 10.2147/IDR.S173867.
(8) Appelbaum, P. C. 2012 and beyond: potential for the start of a second pre-antibiotic era? *J. Antimicrob. Chemother.* **2012**, *67*, 2062 –2068. DOI: 10.1093/jac/dks213.
(9) Projan, S. J. New (and not so new) antibacterial targets — from where and when will the novel drugs come? *Curr. Opin. Pharmacol.* **2002**, 513-522. DOI: 10.1016/s1471-4892(02)00197-2.
(10) Zhen, X.; Lundborg, C. S.; Sun, X.; Hu, X.; Dong, H. Economic burden of antibiotic resistance in ESKAPE organisms: a systematic review. *Antimicrob. Resist. Infect. Control.* **2019**, *8* (1), 137. DOI: 10.1186/s13756-019-0590-7.
(11) Pogue, J. M., Kaye, K., Cohen, D., Marchaim, D. . Appropriate antimicrobial therapy in the era of multidrug-resistant human pathogens. *Clin. Microbiol.* **2015**, *21* (4), 302–312. DOI: 10.1016/j.cmi.2014.12.025.
(12) Rice, L. B. Federal funding for the study of antimicrobial resistance in nosocomial pathogens: no ESKAPE. *J. Infect. Dis.* **2008**, *197*, 1079-1081. DOI: 10.1086/533452 PubMed.
(13) Kumarasamy, K.; Toleman, M. A.; Walsh, T. R.; Bagaria, J.; Butt, F.; Balakrishnan, R.; Chaudhary, U.; Doumith, M.; Giske, C. G.; Irfan, S.; et al. Emergence of a new antibiotic resistance mechanism in India, Pakistan, and the UK: a molecular, biological, and epidemiological study. *Lancet Infect Dis.* **2010**, *10*, 597-602. DOI: 10.1016/S1473-3099(10)70143-2 PubMed.
(14) Tacconelli, E.; Carrara, E.; Savoldi, A.; Harbarth, S.; Mendelson, M.; Monnet, D. L. Discovery, research, and development of new antibiotics: the WHO priority list of antibiotic-resistant bacteria and tuberculosis. *Lancet Infect. Dis* **2018**, *18*, 318–327. DOI: 10.1016/S1473-3099(17)30753-3.
(15) Gunawan, J.; Simard, D.; Gilbert, M.; Lovering, A. L.; Wakarchuk, W. W.; Tanner, M. E.; Strynadka, N. C. J. Structural and Mechanistic Analysis of Sialic Acid Synthase NeuB from *Neisseria meningitidis* in Complex with $Mn^{2+}$, Phosphoenolpyruvate, and *N*-Acetylmannosaminitol. *J Biol Chem* **2005**, *280*, 3555-3563. DOI: 10.1074/jbc.M411942200.
(16) Reichau, S.; Jiao, W.; Walker, S. R.; Hutton, R. D.; Baker, E. N.; Parker, E. J. Potent Inhibitors of a Shikimate Pathway Enzyme from *Mycobacterium tuberculosis* combining mechanism and modeling based design. *J Biol Chem* **2011**, *286*, 16197-16207. DOI: 10.1074/jbc.M110.211649.
(17) Balachandran, N.; Heimhalt, M.; Liuni, P.; To, F.; Wilson, D. J.; Junop, M. S.; Berti, P. J. Potent Inhibition of 3-Deoxy-D-arabinoheptulosonate-7-phosphate (DAHP) Synthase by DAHP

Oxime, a Phosphate Group Mimic. *Biochemistry* **2016**, *55*, 6617-6629. DOI: 10.1021/acs.biochem.6b00930.
(18) Liang, P.; Lewis, J.; Anderson, K. S.; Kohen, A.; D'Souza, F. W.; Benenson, Y.; Baasov, T. Catalytic Mechanism of Kdo8P Synthase: Transient Kinetic Studies and Evaluation of a Putative Reaction Intermediate. *Biochemistry* **1998**, *37*, 16390-16399. DOI: 10.1021/bi981374w.
(19) Li, Z.; Sau, A. K.; Shen, S.; Whitehouse, C.; Baasov, T.; Anderson, K. S. A snapshot of enzyme catalysis using electrospray ionization mass spectrometry. *J. Am. Chem. Soc.* **2003**, *125* (33), 9938-9939. DOI: 10.1021/ja0354768.
(20) DeLeo, A. B.; Sprinson, D. B. Mechanism of 3-Deoxy-D-arabino-heptulosonate 7-phosphate (DAHP) synthetase. *Biochem. Biophys. Res. Commun.* **1968**, *32*, 873–877. DOI: 10.1016/0006-291X(68)90322-7.
(21) König, V.; Pfeil, A.; Braus, G. H.; Schneider, T. R. Substrate and metal complexes of 3-deoxy-D-arabino-heptulosonate-7-phosphate synthase from *Saccharomyces cerevisiae* provide new insights into the catalytic mechanism. *J. Mol. Biol.* **2004**, *337*, 675-690. DOI: 10.1016/j.jmb.2004.01.055.
(22) Asojo, O.; Friedman, J.; Adir, N.; Belakhov, V.; Shoham, Y.; Baasov, T. Crystal Structures of KDOP Synthase in Its Binary Complexes with the Substrate Phosphoenolpyruvate and with a Mechanism-Based Inhibitor. *Biochemistry* **2001**, *40* (21), 6326-6334. DOI: 10.1021/bi010339d.
(23) Kaustov, L.; Kababya, S.; Belakhov, V.; Baasov, T.; Shoham, Y.; Schmidt, A. Inhibition Mode of a Bisubstrate Inhibitor of KDO8P Synthase: A Frequency-Selective REDOR Solid-State and Solution NMR Characterization. *J. Am. Chem. Soc.* **2003**, *125* (15), 4662-4669. DOI: 10.1021/ja028688y.
(24) Li, Z.; Sau, A. K.; Shen, S.; Whitehouse, C.; Baasov, T.; Anderson, K. S. A Snapshot of Enzyme Catalysis Using Electrospray Ionization Mass Spectrometry. *J. Am. Chem. Soc.* **2003**, *125* (33), 9938-9939. DOI: 10.1021/ja0354768.
(25) Du, S.; Faiger, H.; Belakhov, V.; Baasov, T. Towards the development of novel antibiotics: synthesis and evaluation of a mechanism-based inhibitor of Kdo8P synthase. *Bioorg. Med .Chem.* **1999**, *7* (12), 2671-2682. DOI: 10.1016/s0968-0896(99)00233-3 From NLM.
(26) Clark, M. E.; Berti, P. J. Enolpyruvyl Activation by Enolpyruvylshikimate-3-phosphate Synthase. *Biochemistry* **2007**, *46*, 1933-1940. DOI: 10.1021/bi0618316.
(27) Schofield, L. R.; Anderson, B. F.; Patchett, M. L.; Norris, G. E.; Jameson, G. B.; Parker, E. J. Substrate Ambiguity and Crystal Structure of *Pyrococcus furiosus* 3-Deoxy-D-arabino-heptulosonate-7-phosphate Synthase: An Ancestral 3-Deoxyald-2-ulosonate-phosphate Synthase? *Biochemistry* **2005**, *44*, 11950-11962. DOI: 10.1021/bi050577z.
(28) Subramaniam, P. S.; Xie, G.; Xia, T.; Jensen, R. A. Substrate ambiguity of 3-deoxy-D-manno-octulosonate 8-phosphate synthase from Neisseria gonorrhoeae in the context of its membership in a protein family containing a subset of 3-deoxy-D-arabino-heptulosonate 7-phosphate synthases. *J. Bacteriol.* **1998**, *180*, 119-127. DOI: 10.1128/JB.180.1.119-127.1998.
(29) Liu, F.; Lee, H. J.; Strynadka, N. C. J.; Tanner, M. E. Inhibition of Neisseria meningitidis Sialic Acid Synthase by a Tetrahedral Intermediate Analogue. *Biochemistry* **2009**, *48* (39), 9194-9201. DOI: 10.1021/bi9012758.
(30) Gama, S. R.; Balachandran, N.; Berti, P. J. Campylobacter jejuni KDO8P Synthase, Its Inhibition by KDO8P Oxime, and Control of the Residence Time of Slow-Binding Inhibition. *Biochemistry* **2018**, *57* (36), 5327-5338. DOI: 10.1021/acs.biochem.8b00748.
(31) Popović, V.; Morrison, E.; Rosanally, A. Z.; Balachandran, N.; Senson, A. W.; Szabla, R.; Junop, M. S.; Berti, P. J. NeuNAc Oxime: A Slow-Binding and Effectively Irreversible Inhibitor

of the Sialic Acid Synthase NeuB. *Biochemistry* **2019**, *58* (41), 4236-4245. DOI: 10.1021/acs.biochem.9b00654.
(32) Balachandran, N.; To, F.; Berti, P. J. Linear Free Energy Relationship Analysis of Transition State Mimicry by 3-Deoxy-d-arabino-heptulosonate-7-phosphate (DAHP) Oxime, a DAHP Synthase Inhibitor and Phosphate Mimic. *Biochemistry* **2017**, *56*, 592-601. DOI: 10.1021/acs.biochem.6b01211.
(33) Jencks, W. P. *Catalysis in Chemistry and Enzymology*; Dover, 1987.
(34) Smith, H. J.; Simons, C. Enzymes and their Inhibitors: Drug development. *S.l.. CRC PRESS* **2019**.
(35) Averesch, N. J. H.; Krömer, J. O. Metabolic Engineering of the Shikimate Pathway for Production of Aromatics and Derived Compounds-Present and Future Strain Construction Strategies. *Front Bioeng Biotechnol* **2018**, *6*, 32-32. DOI: 10.3389/fbioe.2018.00032.
(36) Tohge, T.; Watanabe, M.; Hoefgen, R.; Fernie, A. Shikimate and Phenylalanine Biosynthesis in the Green Lineage. *Front. Plant Sci.* **2013**, *4*, 62, Review. DOI: 10.3389/fpls.2013.00062.
(37) Herrmann, K. M.; Weaver, L. M. The Shikimate Pathway. *Annu Rev Plant Physiol Plant Mol Biol* **1999**, *50*, 473-503. DOI: 10.1146/annurev.arplant.50.1.473.
(38) Herrmann, K. M. The Shikimate Pathway: Early Steps in the Biosynthesis of Aromatic Compounds. *Plant Cell* **1995**, *7*, 907-919. DOI: 10.1105/tpc.7.7.907.
(39) Suzich, J. A.; Dean, J. F.; Herrmann, K. M. 3-Deoxy-d-arabino-Heptulosonate 7-Phosphate Synthase from Carrot Root (*Daucus carota*) Is a Hysteretic Enzyme. *Plant Physiol.* **1985**, *79*, 765. DOI: 10.1104/pp.79.3.765.
(40) Byng, G. S.; Johnson, J. L.; Whitaker, R. J.; Gherna, R. L.; Jensen, R. A. The evolutionary pattern of aromatic amino acid biosynthesis and the emerging phylogeny of pseudomonad bacteria. *J. Mol. Evol.* **1983**, *19*, 272-282. DOI: 10.1007/BF02099974.
(41) Light, S. H.; Anderson, W. F. The diversity of allosteric controls at the gateway to aromatic amino acid biosynthesis. *Protein Science* **2013**, *22*, 395-404. DOI: 10.1002/pro.2233.
(42) McCandliss, R. J.; Herrmann, K. M. Iron, an essential element for biosynthesis of aromatic compounds. *Proc. Natl. Acad. Sci. U.S.A.* **1978**, *75*, 4810-4813. DOI: 10.1073/pnas.75.10.4810.
(43) Park, O. K.; Bauerle, R. Metal-catalyzed oxidation of phenylalanine-sensitive 3-deoxy-D-arabino-heptulosonate-7-phosphate synthase from *Escherichia coli:* inactivation and destabilization by oxidation of active-site cysteines. *J. Bacteriol.* **1999**, *181*, 1636-1642. DOI: 10.1128/JB.181.5.1636-1642.1999.
(44) Shumilin, I. A.; Kretsinger, R. H.; Bauerle, R. Crystal structure of phenylalanine-regulated 3-deoxy-D-arabino-heptulosonate-7-phosphate synthase from *Escherichia coli. Structure.* **1999**, *7* (7), 865-875. DOI: 10.1016/S0969-2126(99)80109-9.
(45) Webby, C. J.; Jiao, W.; Hutton, R. D.; Blackmore, N. J.; Baker, H. M.; Baker, E. N.; Jameson, G. B.; Parker, E. J. Synergistic allostery, a sophisticated regulatory network for the control of aromatic amino acid biosynthesis in Mycobacterium tuberculosis. *J. Biol. Chem.* **2010**, *285* (40), 30567-30576. DOI: 10.1074/jbc.M110.111856.
(46) Balachandran, N.; Grainger, R. A.; Rob, T.; Liuni, P.; Wilson, D. J.; Junop, M. S.; Berti, P. J. Role of Half-of-Sites Reactivity and Inter-Subunit Communications in DAHP Synthase Catalysis and Regulation. *Biochemistry* **2022**, *61* (20), 2229-2240. DOI: 10.1021/acs.biochem.2c00465.
(47) Seydoux, F.; Malhotra, O. P.; Bernhard, S. A. Half-site reactivity. *CRC. Crit. Rev. Biochem.* **1974**, *2* (2), 227-257. DOI: 10.3109/10409237409105448.
(48) Bocedi, A.; Fabrini, R.; Lo Bello, M.; Caccuri, A. M.; Federici, G.; Mannervik, B.; Cornish-Bowden, A.; Ricci, G. Evolution of Negative Cooperativity in Glutathione Transferase Enabled

Preservation of Enzyme Function. *J. Biol. Chem.* **2016**, *291* (52), 26739-26749. DOI: 10.1074/jbc.M116.749507.
(49) Furdui, C.; Zhou, L.; Woodard, R. W.; Anderson, K. S. Insights into the mechanism of 3-deoxy-D-arabino-heptulosonate 7-phosphate synthase (Phe) from Escherichia coli using a transient kinetic analysis. *J. Biol. Chem.* **2004**, *279*, 45618-45625. DOI: 10.1074/jbc.M404753200.
(50) Shumilin, I. A.; Zhao, C.; Bauerle, R.; Kretsinger, R. Allosteric inhibition of 3-deoxy-D-arabino-heptulosonate-7-phosphate synthase alters the coordination of both substrates. *J.Mol. Biol* **2002**, *20*, 1147-1156. DOI: 10.1016/s0022-2836(02)00545-4.
(51) Blackmore, N. J.; Reichau, S.; Jiao, W.; Hutton, R. D.; Baker, E. N.; Jameson, G. B.; Parker, E. J. Three Sites and You Are Out: Ternary Synergistic Allostery Controls Aromatic Amino Acid Biosynthesis in Mycobacterium tuberculosis. *J. Mol. Biol.* **2013**, *425* (9), 1582-1592. DOI: 10.1016/j.jmb.2012.12.019.
(52) Yuan, C.; Rieke, C. J.; Rimon, G.; Wingerd, B. A.; Smith, W. L. Partnering between monomers of cyclooxygenase-2 homodimers. *Proc. Natl. Acad. Sci. U S A.* **2006**, *103* (16), 6142-6147. DOI: 10.1073/pnas.0601805103.
(53) Blobaum, A. L.; Xu, S.; Rowlinson, S. W.; Duggan, K. C.; Banerjee, S.; Kudalkar, S. N.; Birmingham, W. R.; Ghebreselasie, K.; Marnett, L. J. Action at a distance: mutations of peripheral residues transform rapid reversible inhibitors to slow, tight binders of cyclooxygenase-2. *J. Biol. Chem.* **2015**, *290* (20), 12793-12803. DOI: 10.1074/jbc.m114.635987.
(54) Cornish-Bowden, A. The physiological significance of negative cooperativity revisited. *J. Theor. Biol.* **2013**, *319*, 144-147. DOI: 10.1016/j.jtbi.2012.12.010.
(55) Miles, R. W.; Tyler, P. C.; Furneaux, R. H.; Bagdassarian, C. K.; Schramm, V. L. One-Third-the-Sites Transition-State Inhibitors for Purine Nucleoside Phosphorylase. *Biochemistry* **1998**, *37*, 8615-8621. DOI: 10.1021/bi980658d.
(56) Castellani, M.; Covian, R.; Kleinschroth, T.; Anderka, O.; Ludwig, B.; Trumpower, B. L. Direct demonstration of half-of-the-sites reactivity in the dimeric cytochrome bc1 complex: enzyme with one inactive monomer is fully active but unable to activate the second ubiquinol oxidation site in response to ligand binding at the ubiquinone reduction site. *J. Biol. Chem.* **2010**, *285* (1), 502-510. DOI: 10.1074/jbc.M109.072959.
(57) Mochalkin, I.; Miller, J. R.; Evdokimov, A.; Lightle, S.; Yan, C.; Stover, C. K.; Waldrop, G. L. Structural evidence for substrate-induced synergism and half-sites reactivity in biotin carboxylase. *Protein Science* **2008**, *17* (10), 1706-1718. DOI: 10.1110/ps.035584.108.
(58) Shi, J.; Dertouzos, J.; Gafni, A.; Steel, D.; Palfey, B. A. Single-molecule kinetics reveals signatures of half-sites reactivity in dihydroorotate dehydrogenase A catalysis. *Proc. Natl. Acad. Sci. U S A.* **2006**, *103* (15), 5775-5780. DOI: 10.1073/pnas.0510482103.
(59) Masson, L.; Holbein, B. E. Physiology of sialic acid capsular polysaccharide synthesis in serogroup B Neisseria meningitidis. *J. Bacteriol.* **1983**, *154* (2), 728-736. DOI: 10.1128/jb.154.2.728-736.1983.
(60) Varki, A. Biological roles of oligosaccharides: all of the theories are correct. *Glycobiology* **1993**, *3* (2), 97-130. DOI: 10.1093/glycob/3.2.97.
(61) Rosenberg, A. *Biology of the sialic acids*; Springer Science & Business Media, 1995.
(62) Linton, D.; Dorrell, N.; Hitchen, P. G.; Amber, S.; Karlyshev, A. V.; Morris, H. R.; Dell, A.; Valvano, M. A.; Aebi, M.; Wren, B. W. Functional analysis of the Campylobacter jejuni N-linked protein glycosylation pathway. *Mol. Microbiol.* **2005**, *55* (6), 1695-1703. DOI: 10.1111/j.1365-2958.2005.04519.x.

(63) Sundaram, A. K.; Pitts, L.; Muhammad, K.; Wu, J.; Betenbaugh, M.; Woodard, R. W.; Vann, W. F. Characterization of N-acetylneuraminic acid synthase isoenzyme 1 from Campylobacter jejuni. *Biochem. J.* **2004**, *383* (Pt 1), 83-89.
(64) Annunziato, P. W.; Wright, L. F.; Vann, W. F.; Silver, R. P. Nucleotide sequence and genetic analysis of the neuD and neuB genes in region 2 of the polysialic acid gene cluster of Escherichia coli K1. *J. Bacteriol.* **1995**, *177* (2), 312-319. DOI: 10.1128/jb.177.2.312-319.1995.
(65) Vann, W. F.; Tavarez, J. J.; Crowley, J.; Vimr, E.; Silver, R. P. Purification and characterization of the Escherichia coli K1 neuB gene product N-acetylneuraminic acid synthetase. *Glycobiology* **1997**, *7* (5), 697-701. DOI: 10.1093/glycob/7.5.697.
(66) Vimr, E. R.; Kalivoda, K. A.; Deszo, E. L.; Steenbergen, S. M. Diversity of Microbial Sialic Acid Metabolism. *Microbiol. Mol. Biol. R.* **2004**, *68*, 132-153. DOI: 10.1128/mmbr.68.1.132-153.2004.
(67) García García, M. I.; Lau, K.; von Itzstein, M.; García Carmona, F.; Sánchez Ferrer, Á. Molecular characterization of a new N-acetylneuraminate synthase (NeuB1) from Idiomarina loihiensis. *Glycobiology* **2014**, *25* (1), 115-123. DOI: 10.1093/glycob/cwu096 (acccessed 8/14/2021).
(68) Morrison E. NeuNAc oxime: A New Inhibitor for Sialic Acid Synthase. McMaster University, Hamilton, Canada, **2009**.
(69) Blacklow, R. S.; Warren, L. Biosynthesis of sialic acids by *Neisseria meningitidis*. *J. Biol. Chem.* **1962**, *237*, 3520-3526.
(70) Raetz, C. R.; Whitfield, C. Lipopolysaccharide endotoxins. *Annu. Rev. Biochem.* **2002**, *71*, 635-700. DOI: 10.1146/annurev.biochem.71.110601.135414.
(71) Anderson, L.; Unger, F. M.; Chemistry, A. C. S. D. o. C.; Meeting, A. C. S. *Bacterial Lipopolysaccharides: Structure, Synthesis, and Biological Activities*; American Chemical Society, 1983.
(72) Parish, J. H. *Bacterial Outer Membranes: Biogenesis and Functions*; 1982. DOI: 10.1016/0307-4412(82)90066-8.
(73) Raetz, C. R. Biochemistry of endotoxins. *Annu. Rev. Biochem.* **1990**, *59*, 129-170. DOI: 10.1146/annurev.bi.59.070190.001021.
(74) Duewel, H. S.; Radaev, S.; Wang, J.; Woodard, R. W.; Gatti, D. L. Substrate and metal complexes of 3-deoxy-D-manno-octulosonate-8-phosphate synthase from Aquifex aeolicus at 1.9-A resolution. Implications for the condensation mechanism. *J. Biol. Chem.* **2001**, *276* (11), 8393-8402. DOI: 10.1074/jbc.M007884200.
(75) Ahn, M.; Pietersma, A. L.; Schofield, L. R.; Parker, E. J. Mechanistic divergence of two closely related aldol-like enzyme-catalysed reactions. *Org. Biomol. Chem.* **2005**, *3* (22), 4046-4049, 10.1039/B511661A. DOI: 10.1039/B511661A.
(76) Wu, J.; Woodard, R. W. New Insights into the Evolutionary Links Relating to the 3-Deoxy-D-arabino-heptulosonate 7-Phosphate Synthase Subfamilies*. *J. Biol. Chem.* **2006**, *281* (7), 4042-4048. DOI: 10.1074/jbc.M512223200.
(77) Duewel, H. S.; Woodard, R. W. A metal bridge between two enzyme families. 3-deoxy-D-manno-octulosonate-8-phosphate synthase from Aquifex aeolicus requires a divalent metal for activity. *J. biol. chem.* **2000**, *275* (30), 22824-22831. DOI: 10.1074/jbc.M000133200.
(78) Ray, P. H. Purification and characterization of 3-deoxy-D-manno-octulosonate 8-phosphate synthetase from Escherichia coli. *J Bacteriol* **1980**, *141* (2), 635-644. DOI: 10.1128/jb.141.2.635-644.1980.

(79) Shumilin, I. A.; Bauerle, R.; Wu, J.; Woodard, R. W.; Kretsinger, R. H. Crystal Structure of the Reaction Complex of 3-Deoxy-d-arabino-heptulosonate-7-phosphate Synthase from Thermotoga maritima Refines the Catalytic Mechanism and Indicates a New Mechanism of Allosteric Regulation. *J. Mol. Biol.* **2004**, *341* (2), 455-466. DOI: 10.1016/j.jmb.2004.05.077.
(80) Shulami, S.; Furdui, C.; Adir, N.; Shoham, Y.; Anderson, K. S.; Baasov, T. A Reciprocal Single Mutation Affects the Metal Requirement of 3-Deoxy-d-manno-2-octulosonate-8-phosphate (KDO8P) Synthases from Aquifex pyrophilus and Escherichia coli. *J. Biol. Chem.* **2004**, *279* (43), 45110-45120. DOI: 10.1074/jbc.M404561200.
(81) Li, J.; Wu, J.; Fleischhacker, A. S.; Woodard, R. W. Conversion of Aquifex aeolicus 3-Deoxy-d-manno-octulosonate 8-Phosphate Synthase, a Metalloenzyme, into a Nonmetalloenzyme. *J. Am. Chem. Soc.* **2004**, *126* (24), 7448-7449. DOI: 10.1021/ja0480872.
(82) Stephens, C. M.; Bauerle, R. Analysis of the Metal Requirement of 3-Deoxy-D-arabino-heptulosonate-7-phosphate synthase from *Escherichia coli*. *J. Biol. Chem.* **1991**, *266*, 20810-20817. DOI: 10.1016/S0021-9258(18)54781-5.
(83) Chou, W. K.; Dick, S.; Wakarchuk, W. W.; Tanner, M. E. Identification and characterization of NeuB3 from Campylobacter jejuni as a pseudaminic acid synthase. *J. Biol. Chem.* **2005**, *280* (43), 35922-35928. DOI: 10.1074/jbc.M507483200.
(84) Krosky, D. J.; Alm, R.; Berg, M.; Carmel, G.; Tummino, P. J.; Xu, B.; Yang, W. Helicobacter pylori 3-deoxy-D-manno-octulosonate-8-phosphate (KDO-8-P) synthase is a zinc-metalloenzyme. *Biochim. Biophys. Acta, Protein Struct. Mol. Enzymol.* **2002**, *1594* (2), 297-306. DOI: 10.1016/S0167-4838(01)00319-3.
(85) Staub, M.; Dénes, G. Purification and properties of the 3-deoxy-D-arabino-heptulosonate-7-phosphate synthase (phenylalanine sensitive) of Escherichia coli K12. II. Inhibition of activity of the enzyme with phenylalanine and functional group-specific reagents. *Biochim Biophys Acta* **1969**, *178* (3), 588-598. DOI: 10.1016/0005-2744(69)90228-9.
(86) Ganson, R. J.; Jensen, R. A. The essential role of cobalt in the inhibition of the cytosolic isozyme of 3-deoxy-D-arabino-heptulosonate-7-phosphate synthase from Nicotiana silvestris by glyphosate. *Arch.Biochem.Biophys.* **1988**, *260* (1), 85-93. DOI: 10.1016/0003-9861(88)90427-4.
(87) Baasov, T.; Knowles, J. R. Is the first enzyme of the shikimate pathway, 3-deoxy-D-arabino-heptulosonate-7-phosphate synthase (tyrosine sensitive), a copper metalloenzyme? *J. Bacteriol.* **1989**, *171* (11), 6155-6160. DOI: 10.1128/jb.171.11.6155-6160.1989.
(88) Howe, D. L.; Duewel, H. S.; Woodard, R. W. Histidine 268 in 3-Deoxy-d-arabino-heptulosonic Acid 7-Phosphate Synthase Plays the Same Role as Histidine 202 in 3-Deoxy-d-manno-octulosonic Acid 8-Phosphate Synthase. *J. Biol. Chem.* **2000**, *275* (51), 40258-40265. DOI: 10.1074/jbc.M003585200.
(89) Shumilin, I. A.; Bauerle, R.; Kretsinger, R. H. The high-resolution structure of 3-deoxy-D-arabino-heptulosonate-7-phosphate synthase reveals a twist in the plane of bound phosphoenolpyruvate. *Biochemistry* **2003**, *42* (13), 3766-3776. DOI: 10.1021/bi027257p From NLM.
(90) Heimhalt, M.; Mukherjee, P.; Grainger, R. A.; Szabla, R.; Brown, C.; Turner, R.; Junop, M. S.; Berti, P. J. An Inhibitor-in-Pieces Approach to DAHP Synthase Inhibition: Potent Enzyme and Bacterial Growth Inhibition. *ACS Infectious Diseases* **2021**, *7* (12), 3292-3302. DOI: 10.1021/acsinfecdis.1c00462.
(91) Birck, M. R.; Woodard, R. W. Aquifex aeolicus 3-deoxy-D-manno-2-octulosonic acid 8-phosphate synthase: a new class of KDO 8-P synthase? *J. Mol. Evol.* **2001**, *52* (2), 205-214. DOI: 10.1007/s002390010149.

(92) Dotson, G. D.; Nanjappan, P.; Reily, M. D.; Woodard, R. W. Stereochemistry of 3-deoxyoctulosonate 8-phosphate synthase. *Biochemistry* **1993**, *32* (46), 12392-12397. DOI: 10.1021/bi00097a017.
(93) Cochrane, F. C.; Cookson, T. V.; Jameson, G. B.; Parker, E. J. Reversing evolution: re-establishing obligate metal ion dependence in a metal-independent KDO8P synthase. *J. Mol. Biol.* **2009**, *390* (4), 646-661. DOI: 10.1016/j.jmb.2009.05.014.
(94) Yeoman, J. A. Biochemical Characterization of Metal-Dependent 3-Deoxy- D - manno - Octulosonate 8-Phosphate Synthases from Chlorobium tepidum & Acidithiobacillus ferrooxidans. 120 p. Massey University, 2007.
(95) Shulami, S.; Yaniv, O.; Rabkin, E.; Shoham, Y.; Baasov, T. Cloning, expression, and biochemical characterization of 3-deoxy-D-manno-2-octulosonate-8-phosphate (KDO8P) synthase from the hyperthermophilic bacterium Aquifex pyrophilus. *Extremophiles* **2003**, *7* (6), 471-481. DOI: 10.1007/s00792-003-0346-3.
(96) Jensen, R. A.; Xie, G.; Calhoun, D. H.; Bonner, C. A. The correct phylogenetic relationship of KdsA (3-deoxy-d-manno-octulosonate 8-phosphate synthase) with one of two independently evolved classes of AroA (3-deoxy-d-arabino-heptulosonate 7-phosphate synthase). *J. Mol. Evol.* **2002**, *54* (3), 416-423. DOI: 10.1007/s00239-001-0031-z.
(97) Allison, T. M.; Hutton, R. D.; Cochrane, F. C.; Yeoman, J. A.; Jameson, G. B.; Parker, E. J. Targeting the Role of a Key Conserved Motif for Substrate Selection and Catalysis by 3-Deoxy-D-manno-octulosonate 8-Phosphate Synthase. *Biochemistry* **2011**, *50*, 3686-3695. DOI: 10.1021/bi200251f.
(98) Oliynyk, Z.; Briseño-Roa, L.; Janowitz, T.; Sondergeld, P.; Fersht, A. R. Designing a metal-binding site in the scaffold of Escherichia coli KDO8PS. *Protein Eng Des Sel* **2004**, *17* (4), 383-390. DOI: 10.1093/protein/gzh046.
(99) Sau, A. K.; Li, Z.; Anderson, K. S. Probing the Role of Metal Ions in the Catalysis of Helicobacter pylori 3-Deoxy-d-manno-octulosonate-8-phosphate Synthase Using a Transient Kinetic Analysis. *J. Biol. Chem.* **2004**, *279* (16), 15787-15794. DOI: 10.1074/jbc.M308989200 (acccessed 2024/09/26).
(100) Hopkins, A. L.; Groom, C. R. The druggable genome. *Nat. Rev. Drug Discov.* **2002**, *1*, 727-730. DOI: 10.1038/nrd892.
(101) Robertson, J. G. Mechanistic Basis of Enzyme-Targeted Drugs. *Biochemistry* **2005**, *44*, 5561-5571. DOI: 10.1021/bi050247e.
(102) Copeland, R. A. *Evaluation of enzyme inhibitors in drug discovery. A guide for medicinal chemists and pharmacologists.* Wiley-VCH; 2005.
(103) Copeland, R. A. *Enzymes: a practical introduction to structure, mechanism, and data analysis*; John Wiley & Sons, 2000.
(104) Albuquerque, E. X.; Santos, M. D.; Alkondon, M.; Pereira, E. F. R.; Maelicke, A. Modulation of Nicotinic Receptor Activity in the Central Nervous System: A Novel Approach to the Treatment of Alzheimer Disease. *Alzheimer Dis. Assoc. Disord.* **2001**, *15*, S19-S25. DOI: 10.1097/00002093-200108001-00004.
(105) Copeland, R. A.; Harpel, M. R.; Tummino, P. J. Targeting enzyme inhibitors in drug discovery. *Expert Opin. Ther. Targets.* **2007**, *11* (7), 967-978. DOI: 10.1517/14728222.11.7.967.
(106) Yocum, R. R.; Rasmussen, J. R.; Strominger, J. L. The mechanism of action of penicillin. Penicillin acylates the active site of Bacillus stearothermophilus D-alanine carboxypeptidase. *Journal of Biological Chemistry* **1980**, *255* (9), 3977-3986. DOI: 10.1016/S0021-9258(19)85621-1.

(107) Robertson, J. G. Enzymes as a special class of therapeutic target: clinical drugs and modes of action. *Curr. Opin. Struct. Biol.* **2007**, *17*, 674-679. DOI: 10.1016/j.sbi.2007.08.008.
(108) Fersht, A. *Enzyme structure and mechanism.*; 1985.
(109) Segel, I. H. *Enzyme kinetics : behavior and analysis of rapid equilibrium and steady state enzyme systems*; Wiley, 1993.
(110) Hendlin, D.; Stapley, E. O.; Jackson, M.; Wallick, H.; Miller, A. K.; Wolf, F. J.; Miller, T. W.; Chaiet, L.; Kahan, F. M.; Foltz, E. L.; et al. Phosphonomycin, a New Antibiotic Produced by Strains of Streptomyces. *Science* **1969**, *166* (3901), 122-123. DOI: 10.1126/science.166.3901.122.
(111) Walker, S. R.; Cumming, H.; Parker, E. J. Substrate and reaction intermediate mimics as inhibitors of 3-deoxy-d-arabino-heptulosonate 7-phosphate synthase. *Org. Biomol.* **2009**, *7*, 3031. DOI: 10.1039/B909241B.
(112) Walker, S. R.; Jiao, W.; Parker, E. J. Synthesis and evaluation of dual site inhibitors of 3-deoxy-D-arabino-heptulosonate 7-phosphate synthase. *Bioorg Med Chem Lett.* **2011**, *21*, 5092-5097. DOI: 10.1016/j.bmcl.2011.03.071.
(113) Walker, S. R.; Parker, E. J. Synthesis and evaluation of a mechanism-based inhibitor of a 3-deoxy-D-arabino heptulosonate 7-phosphate synthase. *Bioorg Med Chem Lett.* **2006**, *6*, 2951-2954. DOI: 10.1016/j.bmcl.2006.02.073.
(114) Heimhalt M. Mechanisms of Imine-Based Inhibitors of DAHP Synthase. McMaster University, Canada, 2018.
(115) Grison, C.; Petek, S.; Finance, C.; Coutrot, P. Synthesis and antibacterial activity of mechanism-based inhibitors of KDO8P synthase and DAH7P synthase. *Carbohydr. Res.* **2005**, *340* (4), 529-537. DOI: 10.1016/j.carres.2004.11.019.
(116) Erlanson, D. A. Introduction to fragment-based drug discovery. *Top. Curr. Chem.* **2012**, *317*, 1-32. DOI: 10.1007/128_2011_180.
(117) Reyes, A. C.; Amyes, T. L.; Richard, J. P. Enzyme Architecture: Self-Assembly of Enzyme and Substrate Pieces of Glycerol-3-Phosphate Dehydrogenase into a Robust Catalyst of Hydride Transfer. *J. Am. Chem. Soc.* **2016**, *138* (46), 15251-15259. DOI: 10.1021/jacs.6b09936.
(118) Popović, V.; Morrison, E.; Rosanally, A. Z.; Balachandran, N.; Senson, A. W.; Szabla, R.; Junop, M. S.; Berti, P. J. NeuNAc Oxime: A Slow-Binding and Effectively Irreversible Inhibitor of the Sialic Acid Synthase NeuB. *Biochemistry* **2019**, (41), 4236-4245. DOI: 10.1021/acs.biochem.9b00654.
(119) Du, S.; Tsipori, H.; Baasov, T. Synthesis and evaluation of putative oxocarbenium intermediate mimic in the KDO8P synthase-catalyzed reaction as a tool for the design of potent inhibitors for lipopolysaccharide biosynthesis. *Bioorganic & Medicinal Chemistry Letters* **1997**, *7* (19), 2469-2472. DOI: 10.1016/S0960-894X(97)10020-8.
(120) Belakhov, V.; Dovgolevsky, E.; Rabkin, E.; Shulami, S.; Shoham, Y.; Baasov, T. Synthesis and evaluation of a mechanism-based inhibitor of KDO8P synthase. *Carbohydr. Res.* **2004**, *339* (2), 385-392. DOI: 10.1016/j.carres.2003.10.007.
(121) Harrison, A. N.; Reichau, S.; Parker, E. J. Synthesis and evaluation of tetrahedral intermediate mimic inhibitors of 3-deoxy-d-manno-octulosonate 8-phosphate synthase. *Bioorg Med Chem Lett.* **2012**, *22* (2), 907-911. DOI: 10.1016/j.bmcl.2011.12.025.
(122) O'Ferrall, R. A. M. Relationships between E2 and E1cB mechanisms of β-elimination. *J. Chem. Soc. B.* **1970**, (0), 274-277, 10.1039/J29700000274. DOI: 10.1039/J29700000274.
(123) Berti, P. J. [14] Determining transition states from kinetic isotope effects. In *Methods in Enzymology*, Vol. 308; Academic Press, 1999; pp 355-397.

(124) Pauling, L. Molecular Architecture and Biological Reactions. *Chem. Eng. News.* **1946**, *24*, 1375-1377. DOI: 10.1021/cen-v024n010.p1375.
(125) Pauling, L. Nature of forces between large molecules of biological interest. *Nature* **1948**, *161*, 707-709. DOI: 10.1038/161707a0.
(126) Wolfenden, R. Transition State Analogues for Enzyme Catalysis. *Nature* **1969**, *223*, 704–705. DOI: 10.1038/223704a0.
(127) Wolfenden, R.; Snider, M. J. The Depth of Chemical Time and the Power of Enzymes as Catalysts. *Acc. Chem. Res.* **2001**, *34*, 938–945. DOI: 10.1021/ar000058i.
(128) Schramm, V. L.; Horensteins, B. A.; Kline, P. C. Transition State Analysis and Inhibitor Design for Enzymatic Reactions. *J. Biol. Chem.* **1994**, *269* (28), 18259–18262. DOI: 10.1016/S0021-9258(17)32294-9.
(129) O'Leary, M. H. Determination of Heavy-Atom Isotope Effects On Enzyme-Catalyzed Reactions. *Methods Enzymol. 64*, 83-104. DOI: 10.1016/s0076-6879(80)64006-3.
(130) Berti, P. J.; Blanke, S. R.; Schramm, V. L. Transition State Structure for the Hydrolysis of NAD+ Catalyzed by Diphtheria Toxin. *J. Am. Chem. Soc.* **1997**, *119*, 12079-12088. DOI: 10.1021/ja971317a.
(131) Berti, P. J. Determining transition states from kinetic isotope effects. *Methods. Enzymol.* **1999**, *308*, 355–397. DOI: 10.1016/S0076-6879(99)08016-7.
(132) Schramm, V. L.; Purich, D. L. *Enzyme kinetics and mechanism.*; **1999**.
(133) Berti, P. J.; McCann, J. A. B. Toward a Detailed Understanding of Base Excision Repair Enzymes: Transition State and Mechanistic Analyses of N-Glycoside Hydrolysis and N-Glycoside Transfer. *Chem. Rev.* **2006**, *106*, 506-555. DOI: 10.1021/cr040461t.
(134) Gandour, R. D.; Schowen, R. L. *Transition states of biochemical processes.*; New York: Plenum Press, **1978**.
(135) Janak, K. E.; Churchill, D. G.; Parkin, G. Kinetic and Equilibrium Deuterium Isotope Effects for C—H Bond Reductive Elimination and Oxidative Addition Reactions Involving the *Ansa*—Tungstenocene Methyl—Hydride Complex $[Me_2Si(C_5Me_4)_2]W(Me)H$. In *Activation and Functionalization of C—H Bonds*, ACS Symposium Series, Vol. 885; ACS, **2004**; pp 86-104.
(136) Schramm, V. L. Transition States, Analogues, and Drug Development. *ACS Chem. Biol.* **2013**, *8* (1), 71-81. DOI: 10.1021/cb300631k.
(137) Gu, H.; Zhang, S. Advances in kinetic isotope effect measurement techniques for enzyme mechanism study. *Molecules (Basel, Switzerland)* **2013**, *18* (8), 9278-9292. DOI: 10.3390/molecules18089278.
(138) Singleton, D. A.; Thomas, A. A. High-Precision Simultaneous Determination of Multiple Small Kinetic Isotope Effects at Natural Abundance. *J. Am. Chem. Soc.* **1995**, *117*, 9357-9358. DOI: 10.1021/ja00141a030.
(139) Chen, X.-Y.; Berti, P. J.; Schramm, V. L. Transition-State Analysis for Depurination of DNA by Ricin A-Chain. *J. Am. Chem. Soc.* **2000**, *122* (28), 6527-6534. DOI: 10.1021/ja992751a.
(140) Po-Huang, L.; Kohen, A.; Baasov, T.; Anderson, K. S. Catalytic mechanism of KDO8P synthase. Pre-steady-state kinetic analysis using rapid chemical quench flow methods. *Bioorg. Med. Chem. Lett.* **1997**, *7* (19), 2463-2468. DOI: 10.1016/S0960-894X(97)10021-X.
(141) Pascal, R. A.; Baum, M. W.; Wagner, C. K.; Rodgers, L. R.; Huang, D. S. Measurement of deuterium kinetic isotope effects in organic and biochemical reactions by natural abundance deuterium NMR spectroscopy. *J. Am. Chem. Soc.* **1986**, *108* (21), 6477-6482. DOI: 10.1021/ja00281a005.

(142) Chan, J.; Lewis, A. R.; Gilbert, M.; Karwaski, M.-F.; Bennet, A. J. A direct NMR method for the measurement of competitive kinetic isotope effects. *Nat. Chem. Biol.* **2010**, *6*, 405-407. DOI: 10.1038/nchembio.352.
(143) Claridge, T. D. W. Chapter 2 - Introducing High-Resolution NMR. In *High-Resolution NMR Techniques in Organic Chemistry (Third Edition)*, Claridge, T. D. W. Ed.; Elsevier, 2016; pp 11-59.
(144) Facey G. The Information Content of an FID. In *http://u-of-o-nmr-facility.blogspot.com/search/label/FID*, University of Ottawa NMR Facility, 2015.
(145) Pavia DL; Lampman GM; Kriz GS; Vyvyan JR. *Introduction to spectroscopy*; Brooks/Cole, Cengage Learning, 2009.
(146) Niu A. Toward Transition State Analysis of DAHP Synthase. Masters Thesis. McMaster University, Canada, 2020.
(147) Becker, E. D.; Ferretti, J. A.; Gambhir, P. N. Selection of optimum parameters for pulse Fourier transform nuclear magnetic resonance. *Anal. Chem.* **1979**, *51* (9), 1413-1420. DOI: 10.1021/ac50045a016.
(148) Pauli, G. F.; Jaki, B. U.; Lankin, D. C. Quantitative 1H NMR: development and potential of a method for natural products analysis. *J Nat Prod* **2005**, *68* (1), 133-149. DOI: 10.1021/np0497301 From NLM.
(149) Manning, K. A.; Sathyamoorthy, B.; Eletsky, A.; Szyperski, T.; Murkin, A. S. Highly Precise Measurement of Kinetic Isotope Effects Using 1H-Detected 2D [13C,1H]-HSQC NMR Spectroscopy. *Journal of the American Chemical Society* **2012**, *134* (51), 20589-20592. DOI: 10.1021/ja310353c.
(150) Claridge, T. D. W. Chapter 3 - Practical Aspects of High-Resolution NMR. In *High-Resolution NMR Techniques in Organic Chemistry (Third Edition)*, Claridge, T. D. W. Ed.; Elsevier, 2016; pp 61-132.
(151) Sannikova, N.; Lewis, A. R.; Bennet, A. J. Chapter Nineteen - Measurement of Kinetic Isotope Effects by Continuously Monitoring Isotopologue Ratios Using NMR Spectroscopy. In *Methods in Enzymology*, Harris, M. E., Anderson, V. E. Eds.; Vol. 596; Academic Press, 2017; pp 547-571.
(152) Sannikova, N.; Lewis, A. R.; Bennet, A. J. Measurement of Kinetic Isotope Effects by Continuously Monitoring Isotopologue Ratios Using NMR Spectroscopy. *Methods. Enzymol.* **2017**, *596*, 547-571. DOI: 10.1016/bs.mie.2017.06.034.
(153) Claridge, T. D. W. Chapter 4 - One-Dimensional Techniques. In *High-Resolution NMR Techniques in Organic Chemistry (Third Edition)*, Claridge, T. D. W. Ed.; Elsevier, 2016; pp 133-169.
(154) Facey, G. Exponential Line Broadening. In *University of Ottawa NMR Facility Blog*, Canada, 2007.
(155) Duggleby, R. G.; Northrop, D. B. The expression of kinetic isotope effects during the time course of enzyme-catalyzed reactions. *Bioorg. Chem.* **1989**, *17* (2), 177-193. DOI: doi.org/10.1016/0045-2068(89)90018-7.
(156) Lee, J. K.; Bain, A. D.; Berti, P. J. Probing the transition states of four glucoside hydrolyses with 13C kinetic isotope effects measured at natural abundance by NMR spectroscopy. *J. Am. Chem. Soc.* **2004**, *126* (12), 3769-3776. DOI: 10.1021/ja0394028.
(157) Patengill, M. D. Reaction rates of isotopic molecules (Melander, Lars; Saunders, William H.). *J. Chem. Educ.* **1981**, *58* (8), A247. DOI: 10.1021/ed058pA247.1.

(158) Glad, S. S.; Jensen, F. Basis set and correlation effects on transition state geometries and kinetic isotope effects. *J. Phys. Chem.* **1996**, *100* (42), 16892-16898. DOI: 10.1021/jp961559h.
(159) Scott, A. P.; Radom, L. Harmonic vibrational frequencies: an evaluation of Hartree− Fock, Møller− Plesset, quadratic configuration interaction, density functional theory, and semiempirical scale factors. *J. Phys. Chem.* **1996**, *100* (41), 16502-16513. DOI: 10.1021/jp960976r.
(160) Merrick, J. P.; Moran, D.; Radom, L. An evaluation of harmonic vibrational frequency scale factors. *J. Phys. Chem. A.* **2007**, *111* (45), 11683-11700. DOI: 10.1021/jp073974n.
(161) Lou, M.; Burger, S. K.; Gilpin, M. E.; Gawuga, V.; Capretta, A.; Berti, P. J. Transition State Analysis of Enolpyruvylshikimate 3-Phosphate (EPSP) Synthase (AroA)-Catalyzed EPSP Hydrolysis. *J. Am. Chem. Soc.* **2012**, *134* (31), 12958-12969. DOI: 10.1021/ja304339h.
(162) Lienhard, G. E. Enzymatic Catalysis and Transition-State Theory. *Science* **1973**, *180* (4082), 149. DOI: 10.1126/science.180.4082.149.
(163) Hosmane, R. Ring-Expanded ('Fat') Purines and their Nucleoside/Nucleotide Analogues as Broad-Spectrum Therapeutics. In *Progress in Heterocyclic Chemistry*, Gribble, G. W., Joule, J. A. Eds.; Vol. 21; ScienceDirect, 2009; pp 35-68.
(164) Holden, H. M.; Tronrud, D. E.; Monzingo, A. F.; Weaver, L. H.; Matthews, B. W. Slow- and fast-binding inhibitors of thermolysin display different modes of binding: crystallographic analysis of extended phosphonamidate transition-state analogs. *Biochemistry* **1987**, *26* (26), 8542-8553. DOI: 10.1021/bi00400a008.
(165) Kicska, G. A.; Long, L.; Hörig, H.; Fairchild, C.; Tyler, P. C.; Furneaux, R. C.; Schramm, V. L.; Kaufman, H. L. Immucillin H, a powerful transition-state analog inhibitor of purine nucleoside phosphorylase, selectively inhibits human T lymphocytes. *Proc. Natl. Acad. Sci. U.S.A.* **2001**, *98* (8), 4593. DOI: 10.1073/pnas.071050798.
(166) Schramm, V. L. Enzymatic Transition States and Drug Design. *Chem. Rev.* **2018**, *118* (22), 11194-11258. DOI: 10.1021/acs.chemrev.8b00369.
(167) Schramm, V. L. Enzymatic transition states and transition state analog design. *Annu. Rev. Biochem.* **1998**, *67* (1), 693-720. DOI: 10.1146/annurev.biochem.67.1.693.
(168) Schramm, V. L. Development of transition state analogues of purine nucleoside phosphorylase as anti-T-cell agents. *Biochim Biophys Acta.* **2002**, *1587* (2-3), 107-117. DOI: 10.1016/S0925-4439(02)00073-X.
(169) Kline, P. C.; Schramm, V. L. Purine nucleoside phosphorylase. Catalytic mechanism and transition-state analysis of the arsenolysis reaction. *Biochemistry* **1993**, *32* (48), 13212-13219. DOI: 10.1021/bi00211a033 From NLM.
(170) Kline, P. C.; Schramm, V. L. Purine nucleoside phosphorylase. Inosine hydrolysis, tight binding of the hypoxanthine intermediate, and third-the-sites reactivity. *Biochemistry* **1992**, *31* (26), 5964-5973. DOI: 10.1021/bi00141a003.
(171) Murray, C. W.; Rees, D. C. The rise of fragment-based drug discovery. *Nat Chem* **2009**, *1* (3), 187-192. DOI: 10.1038/nchem.217.
(172) Scott, D. E.; Coyne, A. G.; Hudson, S. A.; Abell, C. Fragment-based approaches in drug discovery and chemical biology. *Biochemistry* **2012**, *51* (25), 4990-5003. DOI: 10.1021/bi3005126.
(173) Davies, T.; Hyvoenen, M. Fragment-Based Drug Discovery and X-Ray Crystallography. *Top Curr Chem (Cham).* **2012**, *317*, IX-X. DOI: 10.1007/978-3-642-27540-1.
(174) Joseph-McCarthy, D.; Campbell, A. J.; Kern, G.; Moustakas, D. Fragment-based lead discovery and design. *J Chem Inf Model.* **2014**, *54* (3), 693-704. DOI: 10.1021/ci400731w.

(175) Sieben, A. S.; Perlin, A. S.; Simpson, F. J. An improved preparative method for D-erythrose 4-phosphate. *Can J Biochem* **1966**, *44* (6), 663-669. DOI: 10.1139/o66-083 From NLM.
(176) Balanchandran N. DAHP Oxime: A Transition State Mimic Inhibitor Of DAHP Synthase. PhD. Thesis. McMaster University, Canada, 2014.
(177) Peris-Tortajada, M.; Puchades, R.; Maquieira, A. Determination of reducing sugars by the neocuproine method using flow injection analysis. *Food Chemistry* **1992**, *43* (1), 65-69. DOI: 10.1016/0308-8146(92)90243-U.
(178) Dygert, S.; Li, L. H.; Florida, D.; Thoma, J. A. Determination of reducing sugar with improved precision. *Analytical Biochemistry* **1965**, *13* (3), 367-374. DOI: 10.1016/0003-2697(65)90327-1
(179) Brown M, B. M. Ultra-micro Sugar Determinations Using 2, 9-dimethyl-1,10-phenanthroline Hydrochloride (Neocuproine). *Diabetes* **1961**, *10*, 2.
(180) Hadjivassiliou, A. G.; Rieder, S. V. The enzymatic assay of pyruvic and lactic acids. A definitive procedure. *Clin. Chim. Acta.* **1968**, *19* (3), 357-361. DOI: 10.1016/0009-8981(68)90258-1.
(181) Lanzetta, P. A.; Alvarez, L. J.; Reinach, P. S.; Candia, O. A. An improved assay for nanomole amounts of inorganic phosphate. *Anal. Biochem.* **1979**, *100* (1), 95-97.
(182) Taylor, R.; Kennard, O. Hydrogen-bond geometry in organic crystals. *Acc. Chem. Res.* **1984**, *17* (9), 320-326. DOI: 10.1021/ar00105a004.
(183) WERNER, W.; DEPREUX, P. Reactions with formic acid. Part 2. Formohydrazides by azeotropic distillation. *Chemischer Informationsdienst* **1981**, *12* (8). DOI: 10.1002/chin.198108177.
(184) Cohn, M.; Hu, A. Isotopic (18O) shift in 31P nuclear magnetic resonance applied to a study of enzyme-catalyzed phosphate—phosphate exchange and phosphate (oxygen)—water exchange reactions. *Proc. Natl. Acad. Sci. U S A.* **1978**, *75* (1), 200-203. DOI: 10.1073/pnas.75.1.200.
(185) Mullins, L. S.; Raushell, F. M. [15] Positional isotope exchange as probe of enzyme action. In *Methods Enzymol.*, Vol. 249; Academic Press, 1995; pp 398-425.
(186) Vallurupalli, P.; Sekhar, A.; Yuwen, T.; Kay, L. E. Probing conformational dynamics in biomolecules via chemical exchange saturation transfer: a primer. *J. Biomol. NMR.* **2017**, *67* (4), 243-271. DOI: 10.1007/s10858-017-0099-4.
(187) Becker, W.; Bhattiprolu, K. C.; Gubensäk, N.; Zangger, K. Investigating Protein-Ligand Interactions by Solution Nuclear Magnetic Resonance Spectroscopy. *ChemPhysChem* **2018**, *19* (8), 895-906. DOI: 10.1002/cphc.201701253.
(188) Liu, C. T.; Neverov, A. A.; Maxwell, C. I.; Brown, R. S. Demonstration of Prominent Cu(II)-Promoted Leaving Group Stabilization of the Cleavage of a Homologous Set of Phosphate Mono-, Di-, and Triesters in Methanol. *J. Am. Chem. Soc.* **2010**, *132* (10), 3561-3573. DOI: 10.1021/ja910111q.
(189) Parmar, D.; Sugiono, E.; Raja, S.; Rueping, M. Complete Field Guide to Asymmetric BINOL-Phosphate Derived Brønsted Acid and Metal Catalysis: History and Classification by Mode of Activation; Brønsted Acidity, Hydrogen Bonding, Ion Pairing, and Metal Phosphates. *Chem. Rev.* **2014**, *114* (18), 9047-9153. DOI: 10.1021/cr5001496.
(190) Howe, G. W.; van der Donk, W. A. 18O Kinetic Isotope Effects Reveal an Associative Transition State for Phosphite Dehydrogenase Catalyzed Phosphoryl Transfer. *J. Am. Chem. Soc.* **2018**, *140* (51), 17820-17824. DOI: 10.1021/jacs.8b06301.

(191) Metz, K. R.; Lam, M. M.; Webb, A. G. Reference deconvolution: A simple and effective method for resolution enhancement in nuclear magnetic resonance spectroscopy. *Concepts Magn. Reson.* **2000**, *12* (1), 21-42. DOI: 10.1002/(SICI)1099-0534(2000)12:1.
(192) Keeler, J. *Understanding NMR spectroscopy*; John Wiley & Sons, 2010.
(193) *Gaussian 16 Rev. B.01*; 2016. (accessed.
(194) Becke, A. D. Density-functional exchange-energy approximation with correct asymptotic behavior. *Phys. Rev. A.* **1988**, *38* (6), 3098-3100. DOI: 10.1103/PhysRevA.38.3098.
(195) Perdew, J. P.; Wang, Y. Accurate and simple analytic representation of the electron-gas correlation energy. *Phys. Rev. B.* **1992**, *45* (23), 13244-13249. DOI: 10.1103/PhysRevB.45.13244.
(196) Wong, M. W. Vibrational frequency prediction using density functional theory. *Chem. Phys. Lett.* **1996**, *256* (4), 391-399. DOI: 10.1016/0009-2614(96)00483-6.
(197) Cossi, M.; Rega, N.; Scalmani, G.; Barone, V. Energies, structures, and electronic properties of molecules in solution with the C-PCM solvation model. *J Comput Chem.* **2003**, *24* (6), 669-681. DOI: 10.1002/jcc.10189.
(198) Peng, C.; Bernhard Schlegel, H. Combining Synchronous Transit and Quasi-Newton Methods to Find Transition States. *Isr. J. Chem.* **1993**, *33* (4), 449-454. DOI: 10.1002/ijch.199300051.
(199) Saunders, M.; Laidig, K. E.; Wolfsberg, M. Theoretical calculation of equilibrium isotope effects using ab initio force constants: application to NMR isotope perturbation studies. *J. Am. Chem. Soc.* **1989**, *111* (25), 8989-8994. DOI: 10.1021/ja00207a001.
(200) Bell, R. P. The tunnel effect correction for parabolic potential barriers. *Trans. Faraday Soc.* **1959**, *55* (0), 1-4. DOI: 10.1039/TF9595500001.
(201) Hirschi, J. S.; Takeya, T.; Hang, C.; Singleton, D. A. Transition-state geometry measurements from (13)c isotope effects. The experimental transition state for the epoxidation of alkenes with oxaziridines. *J Am Chem Soc* **2009**, *131* (6), 2397-2403. DOI: 10.1021/ja8088636.
(202) Meyer, M. P.; DelMonte, A. J.; Singleton, D. A. Reinvestigation of the isotope effects for the Claisen and aromatic Claisen rearrangements: The nature of the Claisen transition states. *J. Am. Chem. Soc.* **1999**, *121* (47), 10865-10874. DOI: 10.1021/ja992372h.
(203) Wong, K. Y.; Richard, J. P.; Gao, J. Theoretical analysis of kinetic isotope effects on proton transfer reactions between substituted alpha-methoxystyrenes and substituted acetic acids. *J. Am. Chem. Soc.* **2009**, *131* (39), 13963-13971. DOI: 10.1021/ja905081x.
(204) Parkin, D. Enzyme mechanism from isotope effects. CRC Press, Boca Raton, FL: 1991.
(205) Berti, P.; Tanaka, K. Transition State Analysis Using Multiple Kinetic Isotope Effects: Mechanisms of Enzymatic and Non-Enzymatic Glycoside Hydrolysis and Transfer. *Adv. Phys. Org. Chem.* **2002**, *37*, 239-314. DOI: 10.1016/S0065-3160(02)37004-7.
(206) Klepach, T.; Carmichael, I.; Serianni, A. S. 13C-Labeled N-Acetyl-neuraminic Acid in Aqueous Solution: Detection and Quantification of Acyclic Keto, Keto Hydrate, and Enol Forms by 13C NMR Spectroscopy. *Journal of the American Chemical Society* **2008**, *130* (36), 11892-11900. DOI: 10.1021/ja077565g.
(207) Severi, E.; Müller, A.; Potts, J. R.; Leech, A.; Williamson, D.; Wilson, K. S.; Thomas, G. H. Sialic Acid Mutarotation Is Catalyzed by the Escherichia coli β-Propeller Protein YjhT. *J. Biol. Chem.* **2008**, *283* (8), 4841-4849. DOI: 10.1074/jbc.M707822200.
(208) Vinarov, D. A.; Nowak, T. pH Dependence of the Reaction Catalyzed by Yeast Mg−Enolase. *Biochemistry* **1998**, *37* (43), 15238-15246. DOI: 10.1021/bi981047o.
(209) Beckey, H. D. *Gas phase reaction rate theory*; Ronald Press Company, 1967.

(210) Loncke, P. G.; Berti, P. J. Implications of Protonation and Substituent Effects for C−O and O−P Bond Cleavage in Phosphate Monoesters. *J. Am. Chem. Soc.* **2006**, *128* (18), 6132-6140. DOI: 10.1021/ja057435c.
(211) Parkin, D. W.; Schramm, V. L. Catalytic and allosteric mechanism of AMP nucleosidase from primary, beta-secondary, and multiple heavy atom kinetic isotope effects. *Biochemistry* **1987**, *26* (3), 913-920. DOI: 10.1021/bi00377a036.